

Separations and Waste Forms Research and Development FY 2013 Accomplishments Report

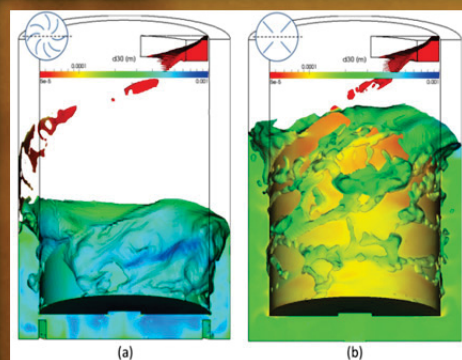
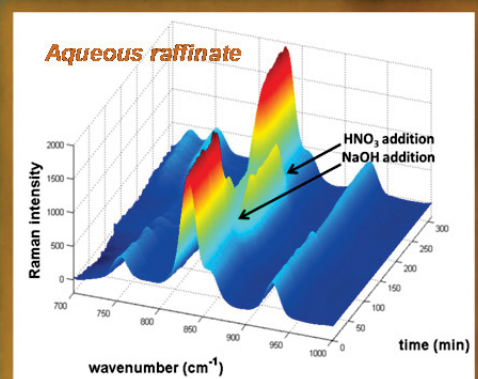
December 2013



The INL is a U.S. Department of Energy National Laboratory
operated by Battelle Energy Alliance

Separations and Waste Forms Research and Development FY 2013 Accomplishments Report

December 2013



DISCLAIMER

This information was prepared as an account of work sponsored by an agency of the U.S. Government. Neither the U.S. Government nor any agency thereof, nor any of their employees, makes any warranty, expressed or implied, or assumes any legal liability or responsibility for the accuracy, completeness, or usefulness, of any information, apparatus, product, or process disclosed, or represents that its use would not infringe privately owned rights. References herein to any specific commercial product, process, or service by trade name, trade mark, manufacturer, or otherwise, does not necessarily constitute or imply its endorsement, recommendation, or favoring by the U.S. Government or any agency thereof. The views and opinions of authors expressed herein do not necessarily state or reflect those of the U.S. Government or any agency thereof.

Cover Graphics:

[background] Treated uranyl nitrate hydrate fuel from the Dresden reactor. ;
[Insets] *Top right* – Real-time Raman spectroscopic measurements of the aqueous raffinate phase, *Bottom right* – Assembly to determine iodine loading capacity, and *Left* – Comparison of liquid holdup and drop size for prediction for simulations in the annular mixing zone of a centrifugal contactor.

**FCRD-SWF-2014-000022
INL/EXT-13-30961**

**Separations and Waste Forms
Research and Development
FY 2013 Accomplishments Report**

December 2013

**Idaho National Laboratory
Idaho Falls, Idaho 83415**

<http://www.inl.gov>

**Prepared for the
U.S. Department of Energy
Office of Nuclear Energy
Under DOE Idaho Operations Office
Contract DE-AC07-05ID14517**

This page intentionally left blank.

Separations and Waste Forms Research and Development FY 2013 Accomplishments Report

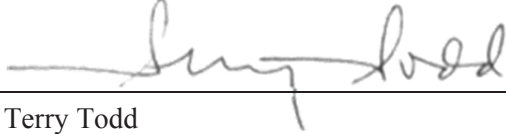
FCRD-SWF-2014-000022
INL/EXT-13-30961

December 2013

Compiled and Edited by:

Jason Schulthess (jason.schulthess@inl.gov)
Douglas Hamelin (douglas.hamelin@inl.gov)
INL Systems Analyses

Approved by:



Terry Todd
Separations and Waste Forms Campaign
National Technical Director

12/21/2013

Date

This page intentionally left blank.

Separations and Waste Forms
2013 Accomplishments Report

EXECUTIVE SUMMARY

The Separations and Waste Form (S&WF) Campaign under the U.S. Department of Energy (DOE) Fuel Cycle Research and Development Program (FCRD) is responsible for developing advanced separation and waste form technologies to support the various fuel cycle options defined in the *DOE Nuclear Energy Research and Development Roadmap, Report to Congress, April 2010*. The fiscal year (FY) 2013 accomplishments report provides a highlight of the results of the research and development (R&D) efforts performed within the S&WF Campaign in FY 2013. Each section contains a high-level overview of the activities, results, technical point of contact, applicable references, and documents produced during the fiscal year.

This report briefly outlines campaign management and integration activities, but the intent of the report is to highlight the many technical accomplishments made during FY 2013. The campaign continued to develop a more science-based approach, while keeping the balance of an engineering-driven program to maintain relevance and focus. There was an increased focus on development of technologies that support near-term applications and that are relevant to the current once-through fuel cycle.

The S&WF Campaign management and integration activities included international coordination activities (France, China, Russia, Japan, European Union, and the International Atomic Energy Agency [IAEA]), integration of S&WF Campaign activities with other FCRD campaigns, (Advanced Fuels, Used Fuel Disposition, Systems Options, and Material Protection, Accountancy and Control Technology), and integration with DOE Office of Environmental Management (EM). The Campaign also provided support in planning and executing of a joint DOE Office of Nuclear Energy (NE)-EM-National Nuclear Security Administration Separations Workshop, aimed at developing a Roadmap for Separations Technology across the DOE mission areas.

Technical accomplishments are reported under the following R&D categories:

- Advanced Aqueous Technologies
- Domestic Electrochemical Separation Technologies
- Sigma Team for Minor Actinide Separations
- Off-Gas Sigma Team
- Fundamental Science, Modeling and Simulation
- Advanced Separation Process Alternatives
- Advanced Waste Forms and Processes
- Waste Form Performance over Geologic Timescales
- Fuel Resources

Advanced Aqueous Technologies

Work performed within Advanced Aqueous Technologies was primarily the development of capabilities to support generic aqueous separation technologies (i.e., areas of development that will be needed and important for any aqueous technology). These included spectrophotometric monitoring of key process parameters (e.g., U, Pu, Np, nitrate, acid concentration) in near-real time. Additionally, the same techniques were applied to detecting and monitoring solvent degradation products. A solvent degradation test loop, to allow hydrolysis and/or radiolysis of process solvents was used to test the solvent degradation behavior of the TRUEX process. The test loop, which is one of only two in the world, gives the S&WF Campaign the ability to test the solvent degradation of any process solvent planned for future testing or implementation. Testing of a robotic sampling system and alternative sample chip designs was completed in FY 2013. Lab-scale testing of candidate separation processes identified in the Case Study activity was initiated.

Separations and Waste Forms
2013 Accomplishments Report

Domestic Electrochemical Separation Technologies

Work performed under this area includes U/transuranic (TRU) codeposition development, TRU/Ln drawdown from spent salt by electrolysis, process monitoring of metals in molten salt using volumetric and spectrophotometric techniques, molten salt extraction of TRU and reactive fission products, and fission product removal from used salt using ion selective ceramics. These are areas that fall outside of the Joint Fuel Cycle Studies project and are focused on long term improvements for the electrochemical processing technology.

Sigma Team for Minor Actinide Separations

This multi-lab, multidisciplinary Sigma Team is taking a number of approaches at trying to develop a simplified, economic and robust separation scheme for Am from Cm and lanthanides, or Am and Cm from lanthanides. This is without a doubt one of the most difficult chemical separations in the nuclear industry and represents tens of millions of dollars of R&D spent each year worldwide. Significant progress has been made in the Sigma team in its first five years, setting the foundation for development and testing of minor actinide flowsheets in the next few years. The team has demonstrated outstanding collaboration and teamwork, while maintaining individual research projects.

Off-Gas Sigma Team

This team has been in existence for four years and has already made important discoveries relative to the capture and immobilization of iodine and krypton. The team has demonstrated key fundamentals for iodine capture on silver mordenite (the reference case) including the effects of silver aging and the fundamental sorption mechanics. Performance of the reference waste form for iodine, glass composite material, were initiated and early results show higher performance than borosilicate waste glass with lower dependence on environmental variables. Novel new sorbents such as silica aerogels, chalcogide glass gels, and metal organic frameworks (MOFs) have also been demonstrated.

Fundamental Science, Modeling and Simulation

This activity is focused on developing the tools and methods to better understand the fundamental properties and driving forces behind the separation processes and waste form behavior. This work is closely tied to the applied R&D effort to support process development as well as subscale and first principle models. This work includes studies on the thermodynamics and kinetics of solvent extraction processes, study of non-ideality in separation processes, fundamental radiation chemistry and the effects of radiation on separation chemistry (e.g., speciation of multivalent cations), generation of data and models for the first principle modeling of metal-water interactions, and understanding decay impacts on waste form stability.

Advanced Separation Process Alternatives

This area was focused on two efforts in FY 2013; defining and documenting a case-study flowsheet for a TRU-recycle option, and testing of fuel pretreatment technology for the removal of tritium from fuel, prior to dissolution. The case study flowsheet effort was completed by a team of experts from several national laboratories and participants from industry. The case-study flowsheets allows for objective comparison of technologies under development, as well as identifying better understanding of interfaces between processes, identifying knowledge gaps, and identifying potential regulatory issues.

Advanced Waste Forms and Processes

The objective of the advanced waste management activity is to develop the next generation waste forms and processes with higher performance suitable for advanced separations. By higher performance, these technologies are aimed at order of magnitude improvement in chemical durability for troublesome radionuclides, fifty percent reduction in waste management costs, and/or thirty percent reduction in waste volumes. Six projects were selected in FY 2010 by a peer review process from laboratory generated white papers and were first funded in FY 2011: (1) glass ceramics for mixed fission products waste 50% higher waste loading relative to borosilicate glass using essentially the same process, (2) zirconium purification and recycle to reduce the waste

Separations and Waste Forms
2013 Accomplishments Report

requiring deep geologic disposal by ~25% and reuse nuclear grade zirconium, (3) epsilon metal for Tc, undissolved solids, and noble metals with 100% waste loading and ~2 orders of magnitude higher durability than waste glass, (4) titanate ceramics for Tc with four orders of magnitude increase in durability, (5) titanate ceramics for mixed fission product waste for 50% higher waste loading and 2 orders of magnitude higher durability, and (6) engineered passivation layers on borosilicate glass waste forms for increased durability and improved durability prediction with reference waste form. Development on these six technologies began in FY 2011 and already significant progress has been made, in particular, on the glass ceramics, titanate ceramics, and epsilon metal. Four of these technologies were continued to FY 2013 (glass ceramics, titanate ceramics for high-level waste [HLW], zirconium purification, and epsilon metals. In addition, advancement of the cold-crucible induction melter (CCIM) for fabrication of the advanced HLW forms (ceramics and glass-ceramics) was initiated. Successful proof-of-principle tests were performed for Zr purification by chloride chemical degrading method and glass ceramics fabrication by CCIM. A melt processed titanate ceramic which immobilizes all of the radionuclides and chemical component from HLW without the formation of water soluble minor phases was formulated. The initial performance measurements of the epsilon metal phase were made.

Waste Form Performance Over Geologic Timescales

The primary objective of a waste form is to prevent the release of the immobilized radionuclides from release to the environment during disposal. As the half-lives of radionuclides being immobilized are as long as millions of years, the waste form should be stable for at least that long in the environment. This activity is focused on developing the tools and science necessary to predict the performance of waste

forms for geologic timescales with sufficient confidence to be effective in convincing the public, regulators, and stakeholders in the safety of nuclear waste disposal. Two example waste forms are used for the development – borosilicate glass and iron based alloys. These two waste forms are both likely candidates for long-lived radionuclide immobilization and serve to give a range of processes that need to be understood for the prediction of repository performance. A conceptual model for alloy waste form performance was developed and reviewed and a database of electrochemical and emersion test results was developed for the parameterization of this model. Data gaps were identified and prioritized in a performance model development roadmap. For glass performance, a number of advanced measurement techniques were developed and demonstrated. These techniques give unprecedented resolution into the mechanisms that control long-term performance. An improved performance model was developed that accounts for both the affinity and transport control mechanisms dominant under different circumstances during glass disposal. The affinity control approach differs significantly from previous models in that it accounts for the coupling of secondary phase precipitation with the glass corrosion. In FY 2014, this model will be refined and parameterized and brought forward to the international community to gain consensus.

Fuel Resources

The objective of the fuel resources activity is to improve the extraction efficiency and reduce cost and uncertainty for the separation of uranium from seawater. In FY 2013 progress was made in demonstrating performance improvements greater than the original goal of doubling the current Japanese capacity for uranium on a sorbent material. In addition, an independent review of the project was performed in FY 2013.

Separations and Waste Forms
2013 Accomplishments Report

This page intentionally left blank.

Separations and Waste Forms
2013 Accomplishments Report

CONTENTS

Executive Summary	v
Chapter 1: Introduction	2
Campaign Objective	2
Campaign Structure	2
Response to Campaign Relevance Review	3
Chapter 2: Collaborations	6
IAEA-DOE Collaboration	6
EU-DOE Collaboration	6
CEA-DOE Collaboration.....	7
JAEA-DOE Collaboration.....	7
Rosatom-DOE Collaboration	7
China-DOE Collaboration	8
JNFL-AREVA-DOE Collaboration on Iodine Management	9
EM Collaboration	9
Chapter 3: Advanced Aqueous Technology	12
Online Monitoring	12
Microfluidic Based Sampling	12
Spectroscopic Online Monitoring for Real-time pH and Metal Concentration	14
Solvent Degradation	18
Radiolysis/Hydrolysis Test Loop.....	18
Spectroscopic Multivariate Analysis for Online Monitoring of the Degradation Products of Tributyl Phosphate.....	19
Lab-Scale Testing of Case-Study Processes.....	23
Case Study Tests for Co-Decontamination Process.....	23
Radiation Stability of Advanced TALSPEAK Solvent.....	24
Lab-scale Testing of Tritium Concentration	26
Advanced TALSPEAK Process for Minor Actinide Separation	28
Chapter 4: Domestic Electrochemical Separations Technology.....	34
Solid Cathode Co-deposition Prototype Development.....	34
Actinide and Lanthanide Drawdown by Electrolysis	34
Evaluation of Molybdate Melts for Used Fuel Treatment.....	35
Molten Salt Extraction.....	36
Codeposition Lab-Scale Testing.....	38
Ion Selective Ceramics for Waste Separations.....	39
Spectroelectrochemical Monitoring Under Electrochemical Processing Conditions.....	43
Chapter 5: Sigma Team for Minor Actinide Separations.....	50
Significance	50
Approach	51

Separations and Waste Forms
2013 Accomplishments Report

Technical Strategy.....	51
Highlights of Research Progress.....	53
Aqueous Complexes for Americium-Curium Separation	53
Advancing TALSPEAK Systems	54
ALSEP Process Development for An/Ln Separation.....	54
Mixed-Donor Extractants.....	56
DPAH Flowsheet Concept for Minor Actinide Separations	56
Separation of Americium from Curium and Trivalent lanthanides Using Bis-triazinyl Pyridine Derivatives.....	57
Exploiting the Higher Oxidation States of Americium.....	57
Oxidation of Am(III) with Cu(III) Periodate	58
Catalyzed Oxidation of Am(III) to Am(VI) Using Ozone.....	59
Minor Actinide and Lanthanide Separations by Ion Exchange.....	60
Future Progress	60
Chapter 6: Off-gas Sigma Team	68
Effects of Sorbent Aging on Iodine Adsorption.....	68
Humid Aging of Silver Functionalized Aerogel	68
NO ₂ Aging of Reduced Silver Mordenite.....	68
Silver-Functionalized Silica Aerogel for Iodine Adsorption and Immobilization	69
Summary Highlights	69
Preparation and Sorption Performance of Functionalized Aerogels.....	70
Consolidation of Ag ⁰ -Functionalized Silica Aerogel into Dense Product	70
Deep Bed Iodine Adsorption Testing.....	71
Introduction.....	71
FY 2013 Methyl Iodide Test Results	72
Chalcogels for Iodine Adsorption and Immobilization	74
Iodine / Tritium Co-Adsorption.....	75
Determination of Baseline Iodine Waste Form Performance Characteristics	77
Investigation Hot Pressing of Iodine Loaded Silver Mordenite	79
New Kr Adsorbents – Part 1 – INL Krypton Capture Accomplishments	82
Introduction.....	82
Preparation and Delivery of AgZ-PAN.....	82
Engineered Form Ni-DOBDC MOF	82
AgZ-PAN Capacity Data for Modeling Support.....	83
Pressure Swing Testing.....	83
New Kr Adsorbents – Part 2 – Metal Organic Frameworks.....	84
Kr Removal using Two Bed Approach.....	84
Radiation Stability of NiDOBDC	85
Scale-up.....	86
Off-Gas Adsorption Modeling.....	87
Assessment of the Iodine Pathways and Off-Gas Stream Characteristics.....	88
Chapter 7: Fundamental Science, Modeling and Simulation.....	92
Metal Corrosion Mechanisms.....	92
Deterministic Modeling of Metal Alloy Passivation and Corrosion Properties.....	92
R&D Overview	92
Results	92

Separations and Waste Forms
2013 Accomplishments Report

Technitium Incorporation into Iron Oxides	94
Thermodynamics and Kinetics	97
Thermodynamics and Kinetics of Advanced Separations Systems	97
Thermodynamics for Actinides and Lanthanides Separation	98
Computational and Spectroscopic Investigations of DTPA Complexes	101
Solvent Extraction Studies Using a Microfluidic Chip	104
Fundamental Radiation Chemistry	106
Significant Work Accomplished	106
Contactors Modeling and Validation Data	108
R&D Overview	108
Accomplishments	108
1 st Principles Modeling of Hydrolysis Reactions	110
Non-Ideality in Solvent Extraction Systems	111
Experimental / Theoretical Inquiry into Non-Ideal Chemistry of Solvent Extraction	111
Thermodynamics of Trivalent Lanthanides in Concentrated Aqueous Solutions	114
Extractant Design by Covalency	117
Importance of Work and Context to DOE-NE Mission	117
Summary of Research Accomplishments and FY 2013 Results	117
Decay Impacts in Waste Forms	120
Transmutation of Radionuclides to Chemically Distinct Daughter Products on Crystalline Waste Form Stability	120
Chemical and Charge Imbalance Induced by Radionuclide Decay: Effects on Waste Form Structure	122
Nano-Continuum Modeling of Nuclear Waste Glass Corrosion	127
Summary of 25 Year French Glass SON68 Leaching Experiment	128
Kinetic-Microscopic-Continuum Model (K μ C)	129
Model Setup for 25 Year French Glass Experiment	130
Simulation Results	131
Discussion	132
Plant-Scale Model Development for Fuel Recycling	133
Publications	134
Plant-Scale Model Integration	135
Comprehensive Corrosion Model	136
Summary of GCMT Accomplishments for FY 2013	136
Chapter 8: Advanced Separation Process Alternatives	140
Define and Document Case Study Flowsheet	140
Scope	140
Team Members	141
Flowsheet Development	141
Mass Balance Development	141
Conclusions	142
Tritium Pretreatment	143
Status	145
Future Work	145
Planning for H-Canyon Testing	146
Process Monitoring	146

Separations and Waste Forms
2013 Accomplishments Report

Off-Gas Treatment	147
Chapter 9: Advanced Waste Forms and Processes	150
Ceramic Waste Forms	150
Ceramics for High Level Waste Raffinate	150
Characterization and Stability Test of Ceramic Waste Forms	152
Glass Ceramics Waste Forms	155
Glass Ceramic Waste Form Development	155
Glass Ceramic Process Engineering Studies and Product Testing Support	157
Characterization and Stability Test of Glass Ceramic Waste Forms	160
Cold Crucible Induction Melter.....	163
Results of CCIM Modifications and Testing	164
Conclusions.....	166
Epsilon Metal Waste Form Development	167
Zirconium Recycle	168
Introduction.....	168
State of Technology Development.....	169
Flowsheet Alternatives.....	170
Summary	171
Chapter 10: Waste Form Performance Over Geologic Timescales	174
Alloy Long-term Corrosion	174
Testing Roadmap for Alloy Waste Forms	174
Corrosion Experiments with RAW-1(Tc).....	176
Model Development and Corrosion Experiments with RAW-1(Tc)	177
Electrochemical Impedance Spectroscopy of Alloy Waste Form.....	180
Effects of Waste Stream Composition on Phases Formed in Alloy Waste Forms.....	181
Glass Long-term Corrosion	183
Small –Angle X-ray Scattering.....	185
Examinations of Surface Alteration Layers	186
Determining the Analytical Form of the Reaction Affinity Term in Concentrated Solutions	188
ALTGLASS Database.....	189
Characterization of Extensively Corroded Glass and Secondary Phases.....	190
Incorporating Monte Carlo Techniques into Corrosion Modeling.....	191
Modeling the Effects of Secondary Phase Precipitation on Glass Dissolution Using a Linear Rate Law.....	192
Modeling the Onset of Secondary Phase Precipitation and Effect on Glass Dissolution Using Non-Linear Rate Laws	193
Collaborations	196
Conclusions.....	197
Chapter 11: Fuel Resources	200
Thermodynamic and Kinetic Studies (U from Seawater).....	200
Objectives.....	200
Complexation of U(VI) with Phthalimidedioxime in Comparison with Glutarimidedioxime	200
Complexation of U(VI) with Glutarimidecarbonyloxime (Ligand C) in Comparison with Ligands A and B	201

Separations and Waste Forms
2013 Accomplishments Report

Absorbent Development, Ligand Design, and Nanosynthesis	202
Advanced Adsorbent Development	202
Functional Ligand Development.....	202
Nanosynthesis	203
Thermodynamic, Kinetic, and Structural Studies.....	204
Marine Testing and Durability Studies.....	204
Introduction.....	204
Adsorption Capacity and Adsorption Rate Determinations.....	205
Adsorbent Characterization.....	205
Toxicity Testing.....	206
Material Durability.....	207
Potential Impact of Adsorbent Deployment on Ocean Current and Tidal Circulation.....	207
Appendix: Acronyms.....	210

FIGURES

Figure 1. Prototype disposable sample chips estimated to cost <\$15 each.....	12
Figure 2. 10 μ l disposable chip designs.....	13
Figure 3. Conceptual design of 10 μ l chip loading/unloading station.....	13
Figure 4. Raman signatures of 1 M lactate at an ionic strength of 1 M with a pH range from 1.66 to 4.99. The arrow indicates the trend with increasing pH.....	15
Figure 5. Organic and aqueous phase reagents used in TALSPEAK extraction system (left panel). The extraction of Nd is highly favored at low pH values (pH ~ 3), and is less favored at higher pH values (pH ~4), (right panel).	15
Figure 6. Schematic showing conceptual experimental design for the A) variable pH and B) corresponding Nd ³⁺ extraction.....	16
Figure 7. Real-time Raman spectroscopic measurements of the aqueous raffinate phase. The Raman spectra are shown over the entire experiment from time = 0 to 300 min, the addition of NaOH and HNO ₃ are indicated on the figure.....	16
Figure 8. Prediction of Nd ³⁺ concentration for aqueous feed, aqueous raffinate, organic feed and organic product phases as a function of run time during continuous centrifugal contactor test. Times for NaOH and HNO ₃ additions to feed, as well as ICP confirmation measurements are indicated within this figure.....	17
Figure 9. FTIR spectral layouts of the irradiated aqueous Sample 5 containing variable concentrations of UO ₂ (NO ₃) ₂ (dark blue, red, green, purple, and light blue traces in the order of increasing UO ₂ ²⁺ concentration from 0.1 to 1.9M).....	21
Figure 10. FTIR spectra of the irradiated organic TBP/n-dodecane sample 5 before (orange trace) and after loading (dark blue, red, green, purple, and light blue traces in the order of increasing UO ₂ ²⁺ loading) with UO ₂ ²⁺ at variable concentrations.....	22
Figure 11. PLS model (blue symbols) and prediction of HDBP concentration (green, red, and pink symbols) in the irradiated UO ₂ (NO ₃) ₂ /TBP/HDBP/n-dodecane solvent. Black line represents the modeling results. Solid red lines indicate 95% confidence interval.....	22

Separations and Waste Forms
2013 Accomplishments Report

Figure 12. Centrifugal Contactor Test Bed.....	23
Figure 13. Reference Codecontamination Flowsheet	23
Figure 14. The change in concentration for HEH[EHP] (boxes) or HDEHP (diamonds) when irradiated as components of either the Advanced TALPEAK or TALSPEAK process solvents, in contact with the same aqueous phase with air-sparging. Error bars shown are $\pm 5\%$ based on replicate analyses.	25
Figure 15. The increase in peak area with absorbed dose of radiolysis-product species for γ -irradiated samples of HEH[EHP] or HDEHP when irradiated as components of either the Advanced TALPEAK or TALSPEAK process solvents, in contact with the same aqueous phase with air-sparging.....	25
Figure 16. The solvent extraction of Am and Eu with 1.0 M HEH[EHP]/dodecane from pH 3.5, 0.05 M DTPA/1.5 M lactic acid irradiated aqueous phase. Error bars shown are $\pm 10\%$. Both phases were irradiated in contact with each other with air-sparging.	26
Figure 17. Tritium in Cladding as a Function of Local Burnup.....	27
Figure 18. Tritium in Cladding as a Function of Linear Heat Rate.	27
Figure 19. Chemical structures of the TALSPEAK (HDEHP) and Advanced TALSPEAK (HEH[EHP]) extractants.....	28
Figure 20. Chemical structures of the aqueous-phase complexants and buffers used in the TALSPEAK and Advanced TALSPEAK processes.	29
Figure 21. Extraction of Am and the lanthanides from 0.125 mol/L HEDTA + 0.2 mol/L citrate solutions with 1.0 mol/L HEH[EHP] in n-dodecane (left) and the corresponding reverse extraction into 0.125 mol/L HEDTA + 0.2 mol/L citrate solutions (right); SF (separation factor) = D_{Ln}/D_{Am}	30
Figure 22. Equilibrium potentials as a function of natural log of molar fraction. Marked points are values calculated for the initial salt composition.....	35
Figure 23. Distribution ratios of selected fission products between Mo melt (liquid phase) and U precipitate (solid phase) after one wash with ~ 30 g of Na_2MoO_4 for different initial composition of UO_2 , and Na_2MoO_4 . The initial content of MoO_3 was kept constant at 30%.	36
Figure 24. Crushed and sieved oxidized EBR-II (top) and BR3 (bottom) fuels used in molten salt extraction experiments.....	37
Figure 25. HFDA (top) and salt distillation apparatus/furnace (bottom) in the main cell of HFEF.	38
Figure 26. CDCSC stripping cycles.....	39
Figure 27. Gd/Sc deposits	39
Figure 28. Correlation between gadolinium content in metal deposit and OCP measured.....	39
Figure 29. Scheme for electrochemical removal of Cs^+ from LiCl-KCl molten salt. Chloride ions in the molten salt have been omitted for clarity.....	40
Figure 30. Schematic illustration of electroreduction of copper (left) or lithium (right) in a pellet stack using electrolyte binder pellets and an ion-conducting separator.....	41
Figure 31. a) Galvanostatic discharge curves for the electroreduction of copper using KSICON (KZP) and LBLTO separators at $100^\circ C$. Curves were obtained at a constant current	

Separations and Waste Forms
2013 Accomplishments Report

density of 100 mA/cm². b) Photograph of a dissected test cell showing dissolution of Cu anode and cathodic plating of Cu metal using a KSICON separator. 42

Figure 32. EDXS spectra and inset SEM micrographs from a) CsLK-EB and b) CuLK-EB pellet cross-sections after copper electroreduction at 500°C with a KSICON separator. The presence of Cu in the CsLK-EB pellet indicates solubility of the oxidized copper anode. Absence of Cs in the CuLK-EB pellet indicates ion transport selectivity against Cs⁺. 42

Figure 33. (A), Plot of the molar absorptivity (M⁻¹cm⁻¹) vs. wavelength (nm) for ErCl₃, HoCl₃, NdCl₃, PrCl₃, SmCl₃ and TmCl₃ in the 3LiCl – 2 CsCl eutectic melt at 723 K; and (B), Graph of the PLS prediction for NdCl₃. 44

Figure 34. (A) Absorption spectra of EuCl₃ in LiCl–KCl eutectic mixture at 773 K, recorded as a function of increasing potential. (B) Nernst plot of the E_{app} vs. log [Ox]/[Red] at 325 nm (Nernst equation is inset within figure). 45

Figure 35. A: Double potential step chronoabsorptometry at 324 nm of 10.3 mM EuCl₃ in LiCl – KCl eutectic mixture at 773K. The potential was stepped from -0.1 V to -0.70 V for 40 s and then to of -0.10 V for 40 s. B: Graph of the log of the diffusion coefficients for EuCl₃ in LiCl– KCl as a function of temperatures. 46

Figure 36. Strategies for achieving selectivity in two-phase separation systems and corresponding questions. 52

Figure 37. Agreement between calculated and experimental binding energy difference (selectivity) for complexation reactions of BP18C6 in 1 M NaNO₃ at T = 25 °C. 54

Figure 38. New DPA derivatives. 54

Figure 39. Effect of aqueous mPIPDPA on the selectivity of lanathanide and americium extraction by HDEHP. 54

Figure 40. Neutral chelating extractants (left) and acidic extractant (right) used in the ALSEP process. 55

Figure 41. Extraction of Am and the lanthanides from nitric acid with 0.05 M T2EHDGA + 0.75 M HEH[EHP] in n-dodecane (top) and selective stripping of Am with 0.125 M HEDTA in 0.2 M citrate (bottom) 55

Figure 42. Preorganization of picolinamide extractant increases extraction efficiency by 8 orders of magnitude. Variation of the distribution ratios of Am(III) and Eu(III) as a function of the initial ligand concentration in 1,2 DCE. Aqueous phase: [Eu(NO₃)₃] = 10⁻⁴ M, [HNO₃] = 10⁻⁴ M, and [LiNO₃] = 7.0 M containing a spike of Am-241 and Eu-152/154. Slope analysis indicates a ligand:metal ratio of 2:1 for 1 and 3:1 for 2. 56

Figure 43. Distribution ratios for the extraction of americium (open circles) and europium (open squares) by 0.5 M “0” + 0.1 M TOPO dissolved in mesitylene as a function nitric acid concentration. 57

Figure 44. Results for Am, Cm, Cf, and Eu extraction from nitric acid. 57

Figure 45. The solvent extraction of Am, Eu and Cm from bismuthate-treated COEX raffinate simulant using DAAP. 58

Figure 46. Photograph of KNa₄Cu(HIO₆)₂·xH₂O compound. 58

Separations and Waste Forms
2013 Accomplishments Report

Figure 47. Ozone-catalyzed oxidation of Am(III) to Am(VI) in 1 M HNO ₃ in the presence of Catalyst X.....	59
Figure 48. Iodine loading curves for humid-air aged aerogels	68
Figure 49: Test specimen holder for NO ₂ aging of Ag ⁰ Z	69
Figure 50: Iodine loading curves for 2% NO ₂ aged Ag ⁰ Z	69
Figure 51. Assembly to determine iodine loading capacity of thiolated silica aerogel; iodine vapors at 150°C for 24 hr.	70
Figure 52. Apparent density and open porosity of SPS samples vs. increased concentration of added silica. Red-filled circle and blue-filled square represent sample SPS-1 (Ag ⁰ -functionalized aerogel with organic moiety).	71
Figure 53. Backscattered electron images of fused silica grains for SPS samples; white spots are nanoparticles and μm-sized nodules of silver.....	71
Figure 54. A schematic (left) and photo (right) of the Deep-bed Sorbent Test System used in these studies.	72
Table 13. Testing accomplishments.....	73
Figure 55. Cross-sectional SEM micrographs of the pure PAN (PAN) and various chalcogel-PAN sorbents, SnS ₃₃ , SnS ₅₀ , and SnS ₇₀	74
Figure 56. Iodine uptake in desiccator experiments for (a) PAN hybrid sorbents and (b) pure chalcogels.	75
Figure 57. Co-adsorption of water and iodine (feed gas water dewpoint 0 °C (solid line), iodine 0 (red square symbols) or 25 ppmV (green diamond symbols)).	75
Figure 58. (a) Water and (b) iodine desorption from 3AMS during a slow approach to 150°C.....	76
Figure 59. Concept for implementation of system to separately confine iodine and tritium.	76
Figure 60. top, CGM of AgI-Z/Glass/Ag, 12 mm diameter; bottom, Single Pass Flow Through Test apparatus.	77
Figure 61. (top) An SEM photomicrograph of the sintered microstructure of a GCM containing AgI-Z (7.8% iodine). (bottom) Effluent iodine levels from SPFT tests of GCM containing various iodine loadings on AgI-Z at 25°C; data scatter is due to uncertainty in the leachant flow rate and the ICP-MS analyses.	78
Figure 62. Compacts from pellet form Ag ⁰ Z (left) and crushed Ag ⁰ Z (right) after sintering in a HUP.	80
Figure 63. Side view of I-Ag ⁰ Z loaded capsule	81
Figure 64. A photograph of the HIP capsule containing Ag ⁰ Z.....	81
Figure 65. A photograph of the cross-sectioned HIP capsule containing iodine loaded Ag ⁰ Z.....	81
Figure 66. Xenon adsorption isotherm on AgZ-PAN at 220K	83
Figure 67. Crystal structures for MOFs after removing solvent molecules. Left: Ni/DOBDC; and right: FMOFCu.....	84
Figure 68. Breakthrough curves for gas mixtures using two bed adsorption modules at 233K. Adsorbents in bed 1 and 2 are NiDOBDC. a) Gas mixture [Xe (400 ppm), Kr (40 ppm)	

Separations and Waste Forms
2013 Accomplishments Report

in air] into bed-1, b) gas breakthrough from bed 1, c) Gas mixture from bed 1 (Xe removed) introduced to bed 2 d) breakthrough of Kr from bed-1.	85
Figure 69. Xenon (top) and Kr (bottom) adsorption measurements after exposed to radiation.....	86
Figure 70. Schematic of typical unit operations for an aqueous-process-based UNF reprocessing plant.	88
Figure 71. Summary iodine pathways and distribution throughout an aqueous reprocessing facility.....	90
Figure 72. First-principles models for the initial growth of oxides on technetium metal (a) half-monolayer, (b) full mono-layer and (c) a bilayer.....	93
Figure 73. Pourbaix diagrams plotting the equilibrium potential (E) as a function of pH in pure water (top) and the system Tc-O-H (bottom) at 1.0 M, 298.15K, and 1.0 atm. In pure water, two possible cathodic reactions are $O_2 + 4H^+ + 4e^- = 2H_2O$ (long dashed line) and $2H^+ + 2e^- = H_2$ (short dotted line). In the system Tc-O-H, two possible reactions, in equilibrium with solid Tc, are $TcO_2 + 4H^+ + 4e^- = Tc + 2H_2O$ (blue) and $TcO_4^- + 8H^+ + 7e^- = Tc + 4H_2O$ (red). The potential plotted on the y-axis is in units of volts relative to the standard hydrogen electrode. Solid circle, square, and diamond are from experimental data, representing for Tc, TcO_2 , and TcO_4^- , respectively.....	93
Figure 74. Schematic illustrating one possible charge-compensated substitution scheme where Tc^{4+} and Fe^{2+} replace two lattice Fe^{3+} in bulk goethite.....	95
Figure 75. Goethite super cell illustrating a charge-compensated substitution of two Fe(II) (green) and Tc(IV) (yellow) pairs for four Fe(III) lattice atoms (purple). Red and white spheres are oxygen and hydrogen, respectively.	96
Figure 76. Measured heat of extraction for the lanthanide series. Aqueous phase= 0.05 M $Ln(NO_3)_3$, 0.1M HNO_3 and 3.9 M $NaNO_3$. Organic phase = 0.2M TOPO in toluene.....	98
Figure 77. Optimized structures of DTPA complexes with An(III) and Ln(III). (a) HML^- with proton on the carboxylate O that is not bonded to the metal center. The position of the proton is indicated with a red arrow. (b) ML^{2-} with second water in the second solvation shell.	99
Figure 78. Fluorescence emission spectra of Cm(III)/Lactate solutions at 25°C. Initial solution: V = 1 mL, $[Cm(III)] = 0.0192$ mM, $[H^+] = 1.0$ mM. Titrant: 0.2/0.8 M $NaL/NaClO_4$, L = lactate, total addition of 0.21 mL.....	100
Figure 79. Possible coordination modes in Cm(III)/lactate complexes. (a) “End-on” mode; (b) “side-on” mode.	101
Figure 80. Structural information of the nitrogen fragments for the three lowest energy species in $HDTPA^{4-}$. The other atoms were removed for clarity. The bond distances are shown in Angstroms. The ADFView program generated the bond distances to 0.001 Å but accuracy is only to 0.01 Å.	102
Figure 81. Structural information about the transition geometry between 2 and 3. The bond distances are shown in Angstroms. The ADFView program generated the bond distances to 0.001 Å but accuracy is only to 0.01 Å.....	102
Figure 82. View of the optimized structure of $[La^{III}(DTPA)(H_2O \cdot 2OMe_2)]^{2-}$. Hydrogen atoms on the $DTPA^{5-}$ ligand are removed for clarity.	103
Figure 83. Preliminary Raman spectra of La-DTPA complexes at various pHs.	103

Separations and Waste Forms
2013 Accomplishments Report

Figure 84. Lanthanide extraction system monitored by fluorescence spectroscopy. The pressure-driven droplet microfluidic system will include a droplet generator chip, an initial optical chip, capillary extraction tubing, a second optical chip, and a phase separator chip.	105
Figure 85. The optical chips have lenses that are focused to a common focal point in the middle of the microfluidic channel making it possible to examine the concentrations and fluorescent emission lifetimes of metal ion species at specific points in the two phase flow.	105
Figure 86. The decrease in the radiolytic degradation (G-value in $\mu\text{mol J}^{-1}$) of CMPO, when gamma-irradiated as 0.1 M CMPO/dodecane in contact with aqueous solutions of increasing nitric acid concentration.	106
Figure 87. The solvent extraction (solid symbols) and strip distribution ratios (open symbols) of Am from 2 M HNO_3 , for initially 0.1 M CMPO/dodecane irradiated using 244Cm in 0.1 M HNO_3 . The CMPO concentration was diluted to 0.16 M prior to the extraction contacts.	107
Figure 88. The wavelength and intensity shift of Nd absorbance at initially 796 nm in t-butanol upon addition of CMPO.	107
Figure 89. Comparison of liquid holdup and drop size for prediction for simulations in the annular mixing zone of a centrifugal contactor with (a) eight curved vanes and (b) four straight vanes.	109
Figure 90. Snapshot of simulated organic phase flow in the lower collector ring of a centrifugal contactor. The liquid surface is colored by velocity magnitude.	109
Figure 91. Sample image set (lower shows identified droplets) and droplet size distributions for locations in the 4V and CV contactor geometries. Measurements are in a CINC V05 at 10 L/min and an O/A of 1/3.	110
Figure 92. Structures of (a) bulk and (b) surface of sodium borosilicate glass and (c) hydrolysis reaction barriers calculated with first-principles methods.	111
Figure 93. Solvent extraction studies on the pH dependence for europium and americium distribution, where (a) aqueous solution consists of 5 mmol kg^{-1} DTPA, 10 mmol kg^{-1} malonate, 10 $\mu\text{mol kg}^{-1}$ M^{3+} traced with ^{154}Eu and ^{243}Am , and ionic strength is fixed at 0.25, 0.5, 0.75, 1.00 and 1.25 mol / kg using NaNO_3 and the organic solution is 0.04 M HDEHP in n-dodecane system, (b) aqueous and organic solutions are representative of typical Talspeak-type liquid-liquid distribution system.	113
Figure 94. Water activity (left panes) and osmotic coefficient (right panes) data for the binary lanthanide nitrate systems at 25°C. Green and blue symbols correspond to the data collected using VPO and water activity meter, respectively. The solid red line is literature values obtained using isopiestic technique [Rard, et al., 1979].	115
Figure 95. Dependence of the water activity (left pane) and osmotic coefficient (right pane) on the $\text{Ln}(\text{NO}_3)_3$ molality in the aqueous binary systems.	116
Figure 96. Dependence of the water activity on the Ln^{3+} ionic radii in the isomolal $\text{Ln}(\text{NO}_3)_3$ binary systems. The $m^{1/2}$ for each system is specified in the plot legend. Lanthanide ion radius data taken from Marcus [1997].	116

Separations and Waste Forms
2013 Accomplishments Report

Figure 97. Solid-state sulfur K-edge XAS spectra of a range of dithiophosphinate extractant ligands, showing that the ligand with the largest An/Ln separation factor has a very distinct electronic structure profile compared to ligands with lower separation factors. 117

Figure 98. Diagram of circulation system that was implemented for solution-phase S K-edge XAS experiments at SSRL. 118

Figure 99. Direct comparison of solution phase versus solid-state data for the [S2P(o-CF3C6H4)2]1- extractant (top), which is reported to exhibit the largest An/Ln separation factors; comparison of the solution phase (in dichloromethane) sulfur K-edge XAS spectra of dithiophosphinate extractant molecules bearing different substituents on the aryl ring (bottom). 118

Figure 100. EXAFS spectrum of Np(S₂PPh₂)₄ (left), and sulfur K-edge XAS comparison of Np(S₂PPh₂)₄ with Nd and U analogues (right). 119

Figure 101. Reactivity scheme depicting the synthetic steps en route to successful synthesis of product **5**, in which the phenyl rings are ‘tethered’ to confer favorable orbital mixing for actinide binding. 120

Figure 102. Two examples of DFT predictions, where (a) describes the formation of rocksalt BaCl from the decay of ¹³⁷Cs in CsCl, and (b) describes the formation of bixbyite Hf₂O₃ from the decay of ¹⁷⁷Lu in Lu₂O₃. In both examples, the yellow atoms refer to the parent atom, green to the daughter, and black to stable lattice anions. 121

Figure 103. Preliminary TEM results for ¹⁷⁷Lu₂O₃, which suggest the formation of non-intuitive phases. 122

Figure 104. (a) Low-resolution HAADF STEM for Cs_{0.9}Ba_{0.1}AlSi₂O₆ pollucite implanted with 1.2 MeV F⁺ ions to 1.36×10¹⁷ F⁺/cm² at 673 K and annealed at 1073 K. The pollucite is amorphized from surface to the depth of 1.7 μm. (b) SRIM simulation of depth profiles of lattice displacement rates. 123

Figure 105. (a) Low-resolution HAADF STEM for Cs_{0.9}Ba_{0.1}AlSi₂O₆ pollucite implanted with 1.2 MeV F⁺ ions to 2.73×10¹⁶ F⁺/cm² at 873 K. (b) Bright-field TEM image of the implanted sample in (a) after annealing at 1073 K. (c) High-resolution HAADF STEM image of the annealed sample showing the crystalline-amorphized interface. 124

Figure 106. (a) HAADF STEM image showing a 460 nm thick amorphized layer from the surface of Cs_{0.9}Ba_{0.05}AlSi₂O₆ implanted with 1.2 MeV F⁺ ions to 2.73×10¹⁶ F⁺/cm² at 873 K. (b) A magnified view showing a thin Cs-rich layer on the surface. 125

Figure 107. SRIM simulation of ionization rates as a function of depth in CsAlSi₂O₆ pollucite irradiated with 1.2 MeV F⁺ ions. 125

Figure 108. (a), (b) and (c) Low-resolution HAADF STEM images of a Ba-containing precipitate in Ba-doped pollucite Cs_{0.9}Ba_{0.1}AlSi₂O₆ observed along three zone axes. (d), (e) and (f) The corresponding high-resolution HAADF STEM images of the precipitate. (g), (h) and (i) Lattice simulations of monoclinic Ba₂Si₃O₈ projected along the [-2,0,1], [-4,8,1] and [-1,2,0] axes, which matches the observed lattice patterns, respectively. 126

Figure 109. (a), (b) and (c) The corresponding electron diffraction patterns from the Ba-containing precipitate shown in Figs. 5 (a), (b) and (c). (d), (e) and (f) show simulated diffraction patterns of Ba₂Si₃O₈ projected along the [-2,0,1], [-4,8,1] and [-1,2,0] axes, which match the observed diffraction patterns, respectively. 126

Separations and Waste Forms
2013 Accomplishments Report

Figure 110. Experimental setup for the 25 year SON68 glass leaching experiment [Guittonneau, et al, 2011]	129
Figure 111. Schematic of modeling setup showing nanometer-scale reaction and diffusion zones	131
Figure 112. Schematic of the disposition of elemental leaching zones based on atom probe tomography (from Gin et al, 2013).....	131
Figure 113. High resolution histogram of elemental abundance across the pristine glass-hydrated glass interface (from Gin et al, 2013).....	131
Figure 114. Simulation results using the K μ C model. Note the position of the B release front further from the pristine glass than the Li-H interdiffusion front, in qualitative agreement with the observations	132
Figure 115. Simulated corrosion front position versus time. Note the linear (constant) rate of front propagation.	132
Figure 116. Rotary dissolver module Nitron [2].....	134
Figure 117. Rotary pretreater module Pulvox [3].....	134
Figure 118. Simplified SSPM (Sandia) front end for Nitron integration testing.	135
Figure 119. Nitron stand-alone output for 12 hours of dissolution. Top-Liquid volume flow rate (L/min); Middle-Uranium nitrate concentration (g/L); Bottom-Plutonium nitrate concentration (g/L)	135
Figure 120. Results after integration with the SSPM; Top-Liquid volume flow rate (L/min); Middle-Uranium nitrate concentration (g/L); Bottom-Plutonium nitrate concentration (g/L).....	136
Figure 121. Representative fits of GRAAL model to SON68 data at a) no solution flow and b) at high solution flow.....	137
Figure 122. Total dissolved Al, B and Si (solid lines) and linear fits of the data (dashed lines) for the NeB3 glass on a 8x8x128 lattice.....	137
Figure 124. Treated UNF from the Dresden reactor. Uranyl nitrate hydrate on the top and UO ₃ on the bottom.....	144
Figure 125. Closed loop treatment of natural uranium pellets at 1 Kg scale, mix oxide (red) and nitrate (green) product	144
Figure 126. UO ₃ phase fractions	144
Figure 127. Modified H Canyon Sampler Piping	147
Figure 128. Dissolver Off Gas Flow Schematic	148
Figure 129. Hot Canyon Process Vessel Vent System	148
Figure 130. Multiphase Waste Form Cr/Al/Fe Hollandite with Ti/TiO ₂ Processing Comparison- Backscattered Electron Micrograph	151
Figure 131. Cr and Fe XANES and EXAFS spectra of CAF-Hol: Ba _{1.0} Cs _{0.3} Cr _{1.0} Al _{0.3} Fe _{1.0} Ti _{5.7} O ₁₆ processed in air (SPH); processed in air with Ti/TiO ₂ (SPH-Ti); processed in 1%H ₂ (SPHR); processed in 1%H ₂ with Ti/TiO ₂ (SPHR-Ti), according to the guide. The insets show the moduli and real components of the EXAFS in the (R) representation.....	153

Separations and Waste Forms
2013 Accomplishments Report

Figure 132. XRD results (top) of CSLNTM-2 before and after irradiations, Cross-sectional TEM micrograph (bottom) of irradiated zirconolite phase with corresponding selected area diffraction patterns..... 154

Figure 133. TEM image (left) of the He ion irradiated SFM sample with corresponding selected area diffraction patterns; high resolution TEM image (right) shows nano-crystallized secondary phase in the irradiated area. 155

Figure 134. Waste Loading as a Function of Cooling Time 159

Figure 135. Schematic for powder/monolithic leach test configuration. 160

Figure 136. TEM and XRD observations of oxyapatite phase under irradiations. 161

Figure 137. Thermal conductivity data calculated using the product of the thermal diffusivity, specific heat capacity, and density..... 162

Figure 138 Schematic of a CCIM. Compared to a Joule-Heated-Melters, the lack of in-melt electrodes and refractory in a CCIM allow for greater mixing, less corrosion, longer life, greater throughput, less footprint and therefore melting temperatures exceeding 1700⁰C-which is 50% higher than that achievable with the JHMs..... 163

Figure 139 The INL’s CCIM Pilot Plant’s 26.5 cm dia. crucible, surrounded by its 6 –turn induction coil-all inside a Faraday cage 163

Figure 140. Glass Ceramic Melt Pouring from the INL CCIM during the FY2012 Proof-of-Principle Test..... 163

Figure 141. CCIM Drain Assembly as viewed from below the melter..... 164

Figure 142. Observed damage to existing bottom drain tube and drain clamshell heater when exposed (for over an hour) at high temperatures (>1100°C) as required to melt solid crystals. 164

Figure 143 Tube shell heater with potted coils around a Hastelloy drain tube with a wider diameter. Drain tube diameter increased from ½” to ¾”..... 164

Figure 144. Complete new drain assembly on test stand. 164

Figure 145. One dimensional CFD model of new crucible with the graphite susceptor drain (left – bottom green square) in the closed (cold) position..... 165

Figure 146. Different sized test specimens for the new crucible’s graphite susceptor bottom drain tube. 165

Figure 147. New CCIM Pilot Plant remote arm for graphite susceptor drain control and stopping with R, Z, and Θ range 165

Figure 148. New exhaust blower. 165

Figure 149. New variable capacitor to replace one of two fixed capacitors. 166

Figure 150. Power Efficiency vs. Frequency for various Resistances 166

Figure 151. Recycle of zirconium from Zircaloy cladding is a major element of waste reduction. 168

Figure 152. Roadmap for zirconium recovery/purification from UNF cladding..... 169

Figure 153. Potential insertion of purified recycle zirconium into the process for zirconium alloy cladding manufacture. 170

Figure 154. Potential flowsheet applications. 170

Separations and Waste Forms
2013 Accomplishments Report

Figure 155. Chemical decladding test results, Dresden-1 BWR (24 Gwd/MT, discharge 1975).	171
Figure 156. Results of solution exchange tests with RAW-1 under immersion conditions.....	176
Figure 157. Pseudo-radial distribution function from EXAFS analysis of Mo K absorption edge for surface (red) and bulk (green) material.....	177
Figure 158. Comparison of potentiodynamic responses of (left) RAW-1(Tc) and (right) RAW-2(UTc) under conditions of (top) argon purge and (bottom) air in standard solutions: acidic (black), acid brine (red), neutral (blue), brine (green), alkaline (violet), and alkaline brine (orange).....	178
Figure 159. Comparison of potentiodynamic responses of surrogate EWF) in 0.1 mmolal NaCl solutions spiked with: 1×10^{-2} M H_2O_2 , (violet), 1×10^{-4} M H_2O_2 , (blue), 1×10^{-2} M H_2O_2 , (aqua), 1×10^{-6} M H_2O_2 , (green), 1×10^{-8} M H_2O_2 , (red), and without H_2O_2 , (black).	179
Figure 160. Results of SECM of RAW-1 surface during corrosion in 0.1 mmolal H_2SO_4	179
Figure 161. (a) Evolution of open circuit potential as RAW-2 corrodes in 1 mmolal H_2SO_4 and (b) EIS measurements made after various reaction times.	180
Figure 162. SEM photomicrograph of alloy made with 6.7 at% Mo showing MoFe ₂ phases distributed in steel matrix. (scale bar = 20 μ m)	182
Figure 163. Cyclic potentiodynamic polarization scans of alloys with 1.8 at% Mo (red) and with 6.7 at% Mo (black).	182
Figure 164. Alloy made with HT9 steel and simulated waste having a low Pd content showing four compositionally distinct ZrFe ₂ phases. (scale bar = 20 μ m).....	183
Figure 165. Schematic reaction progress plot for glass corrosion.	184
Figure 166. Small angle X-ray scattering from AFCI glass and International Simple Glass.	186
Figure 167. SAXS analyses of SON68 glass reacted in ASTM C1220 tests at pH 10 for 1.5 day (green) and 20 days (turquoise) and pH 11 for 9 days (gold/brown), 11 days (violet), and 19 days (blue). Red curve for AFCI glass reacted in C1308 test for 77 days at pH 8.5 with 7-day exchange interval.....	186
Figure 168. ToF-SIMS profiles of lithium diffusing into CJ-6 glass.....	187
Figure 169. Nano-SIMS cross-section of corroded SON68 glass showing (left) uptake of ²⁹ Si from solution, (center) total depletion of B, and (right) inner layer theorized to act as a transport barrier	188
Figure 170. SEM photomicrograph of SON-68 glass reacted 791 days at 200°C.	190
Figure 171. Boron leached thickness as a function of Al ₂ O ₃ content for a series of aluminoborosilicate glasses with varying B ₂ O ₃ content.	191
Figure 172. Amidoxime-related ligands (from left to right: H ₂ ^I L, glutarimidedioxime; H ₂ ^{II} L, phthalimidedioxime; and H ₂ ^{III} L, 2-(1,3-bis (hydroxyimino)isoindolin-5-ylamino)ethane-sulfonate (^{III} L was prepared at ORNL).....	200
Figure 173. A series of amidoxime-related ligands. (from left to right) A – glutarimidedioxime; B – glutardiamidoxime; C – glutarimidecarbonyloxime.....	201
Figure 174: Screening capacities of different monomers that add hydrophilicity.	202
Figure 175: The grafting methodology using "Click" chemistry for designed ligands.....	203
Figure 176: Batch seawater analysis with the nanoporous polymer adsorbent.....	203

Separations and Waste Forms
2013 Accomplishments Report

Figure 177: Scheme for producing high capacity sorbents with carbon trunks..... 203

Figure 178: Uranium(VI) complexation with the cyclic (H2A) and non-cyclic (H2B) forms of glutardiamidoxime..... 204

Figure 179. Summary of seawater exposure experiments conducted at PNNL with the ORNL 38H amidoxime-based uranium adsorbent material to determine adsorption capacity and kinetic uptake rate. One-site ligand saturation modeling indicates an adsorption capacity of $4890 \pm 830 \mu\text{g U/ g adsorbent}$ (when normalized to a salinity of 35 psu and a half-saturation time of 28 ± 10 days). 205

Figure 180. Time series measurements of selected trace element adsorption on the ORNL 38H adsorbent material..... 206

Figure 181. Example of a Microtox Test conducted with solid uranium adsorbent material obtained from the University of North Carolina. Toxicity was observed only when the concentration of the adsorbent reached levels greater than 5 mg/mL. 207

Figure 182. Characteristics of the removal of uranium from the ORNL amidoxime-based adsorbent material with HCl. Top Panel: Sequential extraction of uranium from the adsorbent using increasing HCl acid concentrations. Bottom Panel: Kinetics of uranium removal as a function of time at room temperature..... 207

Figure 183. Predicted reduction in ambient velocity through (a) kelp forest with a frond density of $0.08 \text{ fronds / m}^2$ and (b) braided adsorbent uranium extraction factor with a mooring density of $0.00178 \text{ moorings/ m}^2$ 208

TABLES

Table 1. Flow through filling versus dipping of glass chips..... 12

Table 2. Plastic chip dip and flow-through filling tests. 13

Table 3. G-values determined for the static irradiation of the aqueous TRUEX strip reagent in contact with TRUEX solvent..... 19

Table 4. G-values determined for the test loop irradiation of the aqueous TRUEX strip reagent in contact with TRUEX solvent..... 19

Table 5. Summary of G-values determined for the test loop irradiation of TRUEX solvent in contact with 4.4 M HNO₃. 19

Table 6. Description of Irradiated Samples. Initial pre-irradiation composition of the organic solvent was 30 v/v% TBP/n-dodecane for all samples..... 21

Table 7. Compositions of electrolyte binder pellets used for electroreduction studies. All values are weight percents. 41

Table 8. Values of Enthalpy, Entropy and Activation Energy of the Eu³⁺²⁺ Redox Couple for Various Eutectic Melt Compositions..... 46

Table 9. Participating Institutions and PIs in the Sigma Team for Minor Actinide Separations in FY 2013..... 53

Separations and Waste Forms
2013 Accomplishments Report

Table 10. Americium and Europium Distribution Values, K_d , (mL/g) for Potassium Titanosilicates (K- TSP) Prepared using a Microwave-Accelerated Reaction System and Commercially Available MWCNT Materials from pH 3 to pH 6.....	60
Table 11. Iodine loading for humid-air aged aerogels	68
Table 12: Iodine loadings for 2% NO ₂ aged Ag ⁰ Z.....	69
Table 14. Kr capacities of two MOF materials at 233K from 40 ppm Kr in Air with and without Xe.	85
Table 15. Distribution coefficients and separation factors for Ce ³⁺ , Eu ³⁺ , Am ³⁺ and Cm ³⁺ from different lactate buffer systems into 0.17 M HDEHP in n-dodecane. [lactate buffer] = 1.0 M, pH 3.6, 50 mM DTPA, all metal ions at tracer quantities.....	97
Table 16. Summary of the separation factors for Ln / An as a function lactate buffer systems into 0.17 M HDEHP in n-dodecane. [lactate buffer] = 1.0 M, pH 3.6, 50 mM DTPA, all metal ions at tracer quantities.	97
Table 17. Thermodynamic data on the formation of Cm(dtpa) ²⁻ (I = 1.0 M NaClO ₄). ^a Values of ΔH obtained by Van't Hoff equation. Method: sp – spectrophotometry, cal – calorimetry).	99
Table 18. Formation constants of the DTPA complexes	99
Table 19. Thermodynamic data on Cm(III)/lactate complexation at different temperatures (I = 1.0 M NaClO ₄).....	100
Table 20. Tabulation of Pitzer parameters of binary lanthanide nitrate solutions at 25°C obtained in this work.	115
Table 21. Ceramic Waste Form Compositions for SRNL Multiphase Melt Samples compared to SYNROC-C [2]; weight percent of oxide component ^a SYNCROC-C cited was material prepared by melting of an oxide-nitrate mixture. Crystalline oxides of Ca,Ba,Fe,Ni,Al,Mo,Ti and Zr and nitrates of Cs,Sr,Nd,Gd and Ce were mixed and melt processed. SYNROC-C samples also contained oxide additions of Si, Mg, Co, Ni, Na, and K.	150
Table 22. Multiphase Waste Form Cr/Al/Fe Hollandite with Ti/TiO ₂ Processing Comparison - Summary of Elements and Crystalline Phases (*Crystalline phases determined from XRD measurements and EDAX elemental analysis)	151
Table 23. First-order mixture model coefficients fitted separately to A and B Arrhenius coefficients.....	156
Table 24. Glass Ceramic Waste Form (GCWF) Canister Mass and Decay Heat Limits.....	158
Table 25. GCWF Total Project Cost Estimate Summary	159
Table 26. Summary of radiation stability of major crystalline phases in glass ceramic and ceramic waste forms.....	161
Table 27. Compositions of MoFe ₂ Phases in Alloys, in at%.....	182
Table 28 - Maximum/minimum values of selected durability test parameters for tests in the ALTGLASS database.....	190
Table 29. Thermodynamic parameters of the protonation and complexation of phthalimidedioxime (H ₂ ^{II} L) and 2-(1,3-bis (hydroxyimino)isoindolin-5-ylamino)	

Separations and Waste Forms
2013 Accomplishments Report

ethanesulfonate ($H_2^{III}L$) with U(VI), in comparison with glutarimidedioxime ($H_2^I L$). 25 °C, I = 0.5 M (NaCl) 200

Table 30. Protonation and complexation of Ligand C with U(VI) (25 °C, I = 0.5 M NaCl) 201

Table 31. Adsorption capacities for several trace elements on the ORNL 38H uranium adsorbent material 206

Separations and Waste Forms
2013 Accomplishments Report

This page intentionally left blank.

CHAPTER 1

INTRODUCTION

Separations and Waste Forms
2013 Accomplishments Report

CHAPTER 1: INTRODUCTION

T. Todd, terry.todd@inl.gov

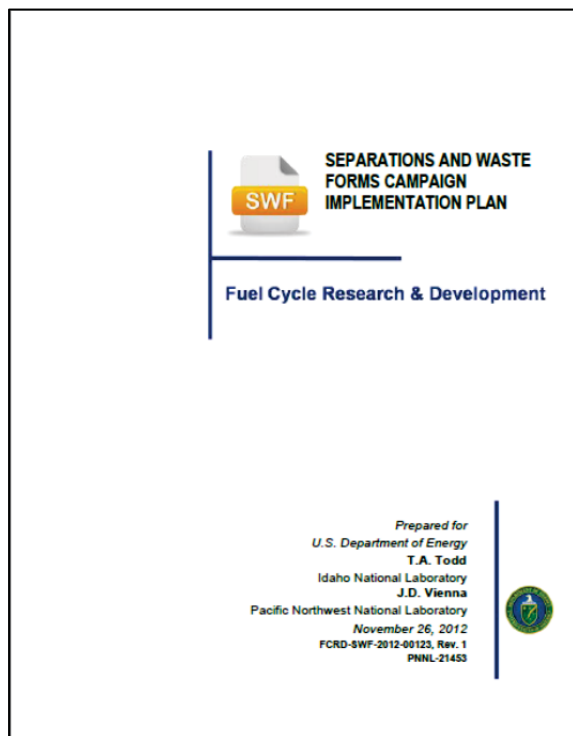
Campaign Objective

T. Todd, terry.todd@inl.gov

The objective of the Separations and Waste Forms (S&WF) campaign was updated in FY 2013 to include the focus on near-term support for the current fuel cycle:

Develop advanced fuel cycle separation and waste management technologies that improve current fuel cycle performance and enable a sustainable fuel cycle, with minimal processing, waste generation, and potential for material diversion.

The development of this objective and a description of the campaign strategy to implement this objective is described in the *Campaign Implementation Plan*, issued in November 2012.



Campaign Structure

T. Todd, terry.todd@inl.gov

The campaign is organized in a flat structure to facilitate campaign integration. Federal Project Directors are responsible for oversight and approval of all S&WF work activities. The National Technical Director (NTD) and Deputy NTD are responsible for work prioritization, integration, and management. Control account managers are responsible for integration of work packages within the control account, as well as monthly progress and budget status reporting.

Campaign Leadership

Campaign leadership is as follows:

- National Technical Director, Dr. Terry Todd, Idaho National Laboratory (INL)
- Deputy National Technical Director, Dr. John Vienna, Pacific Northwest National Laboratory (PNNL)
- Federal Project Director, Separations and Waste Forms, Dr. James Bresee
- Federal Project Director, Fuel Resources and Domestic Electrochemical Separations Technology, Dr. Stephen Kung
- Federal Project Director, Waste Forms, Kimberly Gray.

Control Accounts

Control accounts under the S&WF campaign are as follows:

- Advanced Aqueous Technology
- Domestic Electrochemical Separations Technology
- Sigma Team for Minor Actinide Separations

Separations and Waste Forms
2013 Accomplishments Report

- Off-Gas Sigma Team
- Fundamental Science, Modeling and Simulation
- Advanced Separation Process Alternatives
- Advanced Waste Forms and Processes
- Waste Form Performance over Geologic Time-scales
- Fuel Resources.

**Response to Campaign Relevance
Review**

T. Todd, terry.todd@inl.gov

In June 2012, a panel of independent experts in the S&WF area evaluated several aspects of the campaign to assess their relevance in responding to overall U.S. Department of Energy (DOE) guidance [Harmon, 2012]. The recommendations of the relevancy review panel were used to update the *Campaign Implementation Plan* (described

above) and to refocus efforts in some specific areas of research. Primarily, a study was undertaken to define a transuranic (TRU) recycle case study and near-term target case complete with mass balance and technology descriptions. This study, described in Chapter 8, allows for objective comparison of technologies currently under development, as well as future “improvements,” facilitates an understanding of the interfaces between specific processes, and aids in identifying knowledge gaps and areas for process improvements. An additional recommendation was for the development of specific targets and requirements for technologies being developed. To address this recommendation, roadmaps for completion of various research efforts were developed. In addition, the panel was skeptical about the usefulness of the so-called modified open fuel cycle technologies. These technologies were not further developed in FY 2013.

Separations and Waste Forms
2013 Accomplishments Report

This page intentionally left blank.

CHAPTER 2

COLLABORATIONS

CHAPTER 2: COLLABORATIONS

T. Todd, terry.todd@inl.gov

IAEA-DOE Collaboration

J. D. Vienna, john.vienna@pnnl.gov

The United States has a long history of nuclear energy research and development (R&D) collaboration with the international community through the International Atomic Energy Agency (IAEA). Specific areas of S&WF collaboration in FY 2013 include:

- Development of a technical handbook of “High Level Waste and Spent Fuel Processing”
- Development of a technical handbook of “Gaseous Waste Management”
- Participation in the Coordinated Research Project, “Processing Technologies for High-Level Waste, Formulation of Matrices, and Characterization of Waste Forms.”

These collaborations share methods, technologies, and research among practitioners from the member states. As such, there is a distinct advantage to campaign participation in that researchers gain valuable insight into the results from a wide range of member states that can be leveraged in conducting campaign R&D.

EU-DOE Collaboration

T. Todd, terry.todd@inl.gov

The European Union (EU) Framework Safety of Actinide Separation ProceSses (SACSESS) program is a 3-year effort that follows the very successful EU Actinide reCycling by SEPAraTion (ACSEPT) program that ran for the four previous years and developed and demonstrated a number of new minor actinide separation processes. This program includes most of the leading European separation experts from the Commissariat à l’Énergie Atomique (CEA) in France; National Nuclear Laboratory (NNL) in the United Kingdom (UK); Forschungszentrum Juelich, Karlsruhe

Institute of Technology, and the Institute for Transuranium Elements in Germany; Chalmers University in Sweden; and Czech Technical University and the Nuclear Research Institute in the Czech Republic, along with about 15 other European Universities.

The SACSESS program and the U.S. Fuel Cycle Research and Development (FCRD) S&WF campaign are both interested in collaborating in this field. Scientists from the United States have been asked to participate in a number of ACSEPT and SACSESS meetings, but there is a mutual desire to have a more formal collaboration.

One of the key areas of interest by the SACSESS team is in the radiolysis and hydrolysis of organic solvents. This has very important safety ramifications for any solvent extraction process since many of the extractants and solvents being studied are new and there is only limited information on their behavior under realistic process conditions.

Additionally, the team plans to have three workshops, one each year. The first workshop on the topic of “Separation of Higher Oxidation States of Americium” was held in Reading, UK, in September 2013. This is a major focus of the U.S. Sigma Team for Minor Actinide Separations. The second workshop (2014) will be on the kinetics of solvent extraction processes. The theme of this meeting will be how to connect the fundamental kinetic data with the more applied data obtained from running laboratory-scale tests (e.g., in centrifugal contactors). Finally, the third workshop (2015) will be on modeling and simulation, with the focus on modeling of solution non-ideality. The information exchange in all three of these workshops will be of great benefit to both the EU and the U.S. programs.

A draft Memorandum of Understanding (MOU; or an action plan amendment to a current DOE-EU MOU) has been prepared and reviewed by DOE and the EU and is pending final approval.

Separations and Waste Forms
2013 Accomplishments Report

CEA-DOE Collaboration

T. Todd, terry.todd@inl.gov

The United States and France share a long history of nuclear energy R&D collaboration, particularly in the area of separations and waste management. In particular, DOE and CEA have had a very successful nuclear technology interchange for several decades. A *Nuclear Energy Cooperative Action Plan* was drafted in 2012, and a joint planning meeting was held in October 2012 at Argonne National Laboratory (ANL). The Action Plan is organized into four working groups (WG):

- WG 1: Next Generation Reactors
- WG 2: Separations and Waste Forms
- WG 3: Advanced Fuels and Materials
- WG 4: Modeling and Simulation.

Breakout sessions at the October meeting at ANL led to the identification of a number of actions for further definition of future collaborative activities. The general areas jointly identified for future collaboration are: glass corrosion, solvent degradation, off-gas capture, and on-line process monitoring. Further consideration will be given to collaborating on studies to elucidate minor actinide selectivity. Additional actions, to be included later in the year, will (1) benchmark separation approaches with the objective of providing constructive feedback to each country's approaches, (2) evaluate possible future flowsheet tests with actual used fuel in the Atalante facility at Marcoule, and (3) evaluate the possibility to perform joint research in off-gas management and waste form development.

Follow on meetings between technical leads in each of the WG 2 areas were held during the year, identifying specific activities to be performed in each technical area. These were reviewed and summarized by a meeting between French and US WG 2 leads (France: B. Boullis and C. Poinssot; US: T. Todd and R. Versluis).

Separate meetings were held to discuss collaborative research in the areas of waste form development (Pont du Gard France) and off-gas capture and immobilization of iodine (Richland,

WA). Draft working plans were developed and will be completed in early FY 2014.

JAEA-DOE Collaboration

T. Todd, terry.todd@inl.gov

Collaboration with Japan on separations technology is carried out by the Civil Nuclear Working Group (CNWG), chartered under the *United States – Japan Bilateral Commission on Civil Nuclear Cooperation*. Japanese technical participation in the activities of the working group comes primarily from the Japan Atomic Energy Agency (JAEA), with occasional involvement of the Central Research Institute of the Electric Power Industry (CRIEPI). The responsible Japanese ministry is the Ministry of Education, Culture, Sports, Science and Technology.

The Fuel Cycle and Waste Management sub-working group developed action plans in FY 2013 to guide future collaborative efforts. Three action plans were developed as part of the S&WF Campaign: (1) extraction of uranium from seawater, (2) aqueous separations of oxide fuels, and (3) borosilicate glass dissolution.

The first meeting of the CNWG of the was held in Washington D.C., on November 1, 2013. A follow-on meeting, which will include sub-working groups, will be held in Japan in February 2014 to review action plans and initiate discussions on detailed collaboration topics.

Rosatom-DOE Collaboration

T. Todd, terry.todd@inl.gov

The *United States – Russia Civil Nuclear Energy Cooperation Action Plan* provides a framework with agreed upon areas of joint civil nuclear energy R&D cooperation for possible future collaborative activities. The *United States – Russia Civil Nuclear Energy Action Plan* is comprised of four technical elements:

1. Reactor Demonstration Projects
2. R&D for Innovative Nuclear Energy Technology Options
3. Global Civil Nuclear Energy Framework Development
4. Modeling and Simulation.

Separations and Waste Forms
2013 Accomplishments Report

The *Action Plan* identifies specific technical activity areas of mutual interest within each of these technical elements.

The long-term objectives of the *Action Plan* are to leverage U.S. and Russian scientific and engineering resources and facilities to advance the growth of clean, safe, secure, and affordable nuclear energy through the development of innovative nuclear energy technologies, systems, and services. Both parties understand that the initial collaborative activities will be limited to those that do not require entry into force of the *Agreement between the Government of the United States of America and the Government of the Russian Federation for Cooperation in the Field of Peaceful Uses of Nuclear Energy*.

Russian scientists (primarily from the Research Institute of Atomic Reactors) visited ANL and INL in December 2012. A number of technical presentations were given by both Russian and U.S. researchers, and tours were provided of ANL and INL research facilities. This meeting represents the third workshop on S&WF Technologies. A fourth technical workshop was planned in the United States following the Global Fuel Cycle Conference in October 2013.

China-DOE Collaboration

R. T. Jubin, jubinrt@ornl.gov

The *China–United States Bilateral Civil Nuclear Energy Cooperation Action Plan* (BCNECAP) signed in Vienna, Austria, on September 18, 2007, is a programmatic commitment for both countries to further facilitate joint long-term R&D collaborative activities in advanced civilian nuclear technologies. Presently, seven technical working groups have been established and organized under the BCNECAP cooperation framework. They are: (1) Advanced Separation Technologies, (2) Fast Reactor Technologies, (3) Advanced Fuels and Materials Development, (4) Safeguards, and Physical Protection Technologies, (5) Nuclear Safety Enhancement, (6) Spent Fuel Storage and Repository Sciences, and (7) High Temperature Reactor Technologies.

The Separations Technology Working Group's mission is the collaborative development

of advanced reprocessing and waste form production methods that reduce proliferation risk, provide economic benefits, and reduce environmental impacts. The working group's objective is achieving a mutually beneficial and equitable program of technological collaboration on the back end of the nuclear fuel cycle. Collaborative activities have focused on:

- Tritium and iodine management for advanced reprocessing
- Development of advanced aqueous product conversion methods
- Pyrochemical recycling research facilities and technology development
- Advanced on-line process monitoring and control instrumentation developments.

A technical information exchange meeting was held in Beijing, China, in February 2012 to discuss iodine and tritium management. A follow-on discussion on the same topics took place on December 10–11, 2012, at the Oak Ridge National Laboratory (ORNL). These two successful meetings provided detailed discussion on topics related to head-end tritium capture, including requirements and regulatory issues and iodine waste forms. Potential joint projects on iodine and tritium management for solid spent fuel were identified. Both sides agreed that a multi-year collaboration proposal will be developed by the working group co-chairs. The proposal will outline key tasks that must be accomplished to lead to joint tests in a hot-cell facility in China.

It was agreed that both sides will continue iodine and tritium management joint project development in future meetings. Potential topics for joint projects may include: iodine capture from dilute off-gas streams, iodine distribution and speciation, co-adsorption of iodine and tritium, iodine waste forms, and tritium management from aqueous streams. The Chinese side will prepare a detailed plan for possible exchange of research personnel. The proposed timing for the initiation of such an exchange would be 2014–2015. Potential research areas include tritium removal from aqueous streams and iodine removal from dilute gaseous streams.

Separations and Waste Forms
2013 Accomplishments Report

JNFL-AREVA-DOE Collaboration on Iodine Management

R. T. Jubin, jubinrt@ornl.gov

As part of the Advisory and Assistance Contract (A&AC; DE NE 0000291 [IDIQ Task 10]), AREVA facilitated visits for a team of U.S. researchers in the area of off-gas treatment to reprocessing facilities at Rokkasho, Japan, in May 2012 and La Hague in January 2013. Extensive facility tours were included as well as in-depth discussions that focused on facility operations in general and on the waste treatment and volatile emissions specifically.

As a result of these visits, a series of follow-on discussions have been held between DOE, AREVA, and laboratory personnel to explore several ideas for follow-on collaborations that would draw upon AREVA's experience and could possibly be accomplished under the existing IDIQ Task 10 or similar mechanism. One of the areas of joint interest is to examine in greater detail the release of volatile species from the facilities. Of particular interest are efforts to gain a better understanding of the iodine pathways through the reprocessing plants, the speciation of the iodine, and how the speciation is related to the iodine emitted from the facility. Initial discussions with AREVA indicate it may be possible to install a sampling system to specifically determine iodine species (i.e., elemental, organic, and specific organic iodide compounds) and/or particulate released at the main stack. Such studies would potentially lead to the installation of additional monitoring and sampling equipment on the main stack as well as reviewing historic stack data.

Comparable data requests directed to Japan Nuclear Fuel Limited (JNFL), a partner of AREVA, and to Energy Solutions would be equally valuable and might be accomplished under a similar approach.

EM Collaboration

J. D. Vienna, john.vienna@pnnl.gov

A long-standing interaction exists between the DOE Office of Nuclear Energy (NE) and the DOE

Office of Environmental Management (EM), particularly in the areas of S&WF. Many laboratory researchers work jointly for NE and EM, and many of the program objectives are similar. This close collaboration was formalized in 2011 by an MOU entitled, *Memorandum of Understanding between The Department of Energy Office of Environmental Management and The Department of Energy Office of Nuclear Energy for Used Nuclear Fuel and Radioactive Waste Management and Processing Research and Development*. The MOU, signed by Assistant Secretaries P. Lyons and I. Triay in March 2011, describes a policy of collaborative research and highlights several collaborative research tasks.

Three joint NE-EM-National Nuclear Security Administration nuclear separations technologies workshops were held to identify common needs and requirements in separations as well as opportunities for partnerships between the three offices. The first such workshop was held in July 2011, the second in September 2012, and the third in December 2012. The outcome of these workshops are being documented in meeting reports (the first published in 2012, the second in 2013, and the third scheduled to be published in early 2014) and in a joint roadmap that describes the individual and collaborative research areas that will be pursued as part of this joint effort. The roadmap is scheduled to be completed in 2014.

A joint EM-NE-International glass corrosion study that started in 2010 was continued through 2013. Details of the testing and modeling progress are given in Chapter 10. An international consensus glass corrosion rate law for a reference glass reacting in pure water is scheduled to be completed in FY 2014. That model will be updated and expanded to glass as a function of composition and disposal environment and is scheduled for completion in FY 2020.

A joint EM-NE project to develop and mature cold-crucible induction melter (CCIM) technologies was started in FY 2012 but discontinued in FY 2013.

Separations and Waste Forms
2013 Accomplishments Report

This page intentionally left blank.

CHAPTER 3
ADVANCED AQUEOUS TECHNOLOGY

Separations and Waste Forms
2013 Accomplishments Report

CHAPTER 3: ADVANCED AQUEOUS TECHNOLOGY

J. Law, jack.law@inl.gov

Online Monitoring

J. Law, jack.law@inl.gov

Microfluidic Based Sampling

J. Law, jack.law@inl.gov, and J. L. Tripp

The scope of this effort in FY 2013 was to evaluate disposable sample chips and complete the evaluation of sample accuracy through evaluation of chip filling methods. In FY 2012, the glass sample chips were tested by filling with capillary action when they were dipped into the solutions being sampled either by hand or by the robotic sampling system. Issues were noted that many of the channels were not completely filled. Therefore, testing was conducted on filling the glass sample chips by use of a flow-through header. Additionally, disposable sample chip designs were evaluated as an alternative to the more expensive glass sample chips tested. Results of testing with the glass chips indicate issues with cleaning and reuse due to plugging of the channels. Therefore, less expensive one use chips were evaluated.

Results

In FY 2012, the glass sample chips were filled by capillary action when they were dipped into the solutions being sampled either by hand or by the robotic sampling system. Issues were noted at the end of FY 2012 that many of the channels were not completely filling (10–15% of the 10 µl channels and up to 40% of the 2 µl channels). Therefore, testing was conducted in FY 2013 on filling the glass sample chips by use of a flow-through header (Table 1). Results indicate flow through filling is better at completely filling the chip channels, although some amount of solution can be lost when the chip is removed from the filling header.

Table 1. Flow through filling versus dipping of glass chips.

	Glass Chips Flow Fill (UV-vis) 1 g/L solution		Glass Chips Flow Fill (UV-vis) 100 g/L solution		Glass Chips Dip Fill (UV-vis) 100 g/L solution	
	2µl	10µl	2µl	10µl	2µl	10µl
% channels not filled	~1-5%	~1-5%	D-1.1.1	D-1.1.2	D-1.1.3	D-1.1.4
% RSD*	12.9%	11.4%	D-1.1.5	D-1.1.6	D-1.1.7	D-1.1.8
# channels	12	12	12	12	D-1.1.9	D-1.1.10

*does not include channels noted as not full

Several prototype “disposable” sample chips were manufactured by embedding SS capillary tubing into a plastic framework (Figure 1). Although this design will allow capillary filling, the design limits the volume of the sample to 2 µl.

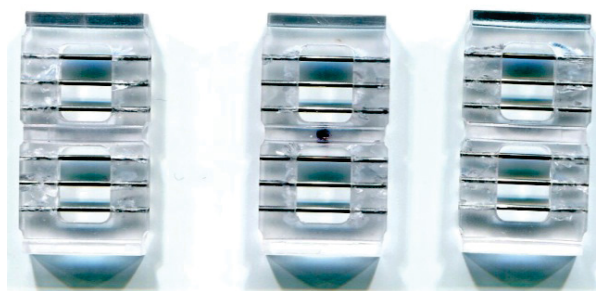


Figure 1. Prototype disposable sample chips estimated to cost <\$15 each.

The results of some of the testing with these chips are shown in Table 2.

Separations and Waste Forms
2013 Accomplishments Report

Table 2. Plastic chip dip and flow-through filling tests.

	Plastic chip w/ SS channels – Flow Fill – UV VIS 1 g/L solution	Plastic chip w/ SS channels – Dip Fill – UV VIS 1 g/L solution	Plastic chip w/ SS channels – Flow Fill – UV VIS 100 g/L solution	Plastic chip w/ SS channels – Dip Fill – UV VIS 100 g/L solution
	2µl	2µl	2µl	2µl
% RSD	34.1%	44.6%	14.8%	79.01%
# channels	36	36	36	36

Since the sample channels are stainless steel, it is not possible to visually determine if the channels are completely filled. The results in Table 2 indicate that flow-through filling provided less relative standard deviation in the results than by dip filling. However, even with flow-through filling the standard deviation is still too high. This seems to indicate, that a slightly larger sample size is needed to reduce the variation in the analyses. Therefore, different chip designs were conceptualized (Figure 2) that had a minimum 10 µl sample size.

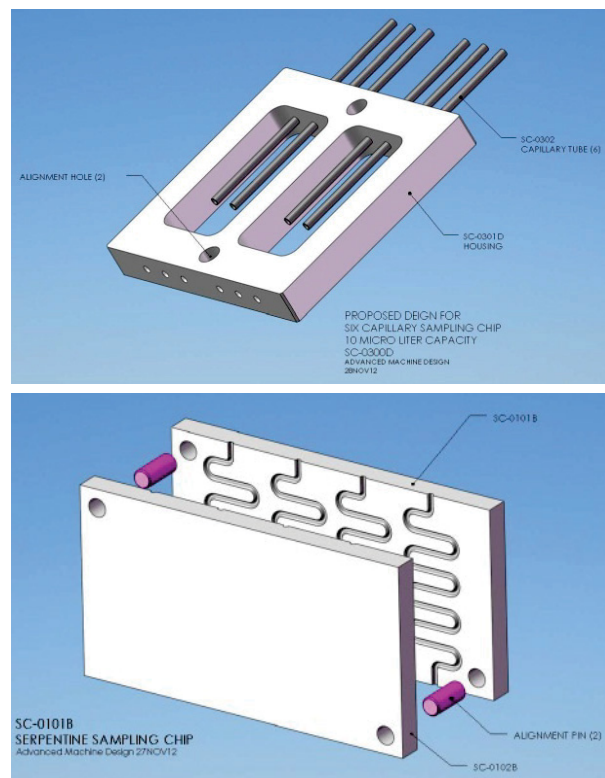


Figure 2. 10 µl disposable chip designs.

It was decided that since the flow-through filling generated more consistently filled chips, that the channels in these chips could be a slightly

larger diameter (do not have to fill with capillary action but have to hold the solution in the channels when disconnected from the fill station. To get the 10 µl size the flow-through loading and unloading stations on the robotic system would have to be slightly redesigned (Figure 3). Funding was not available to have the chips made and the loading/unloading station modified.

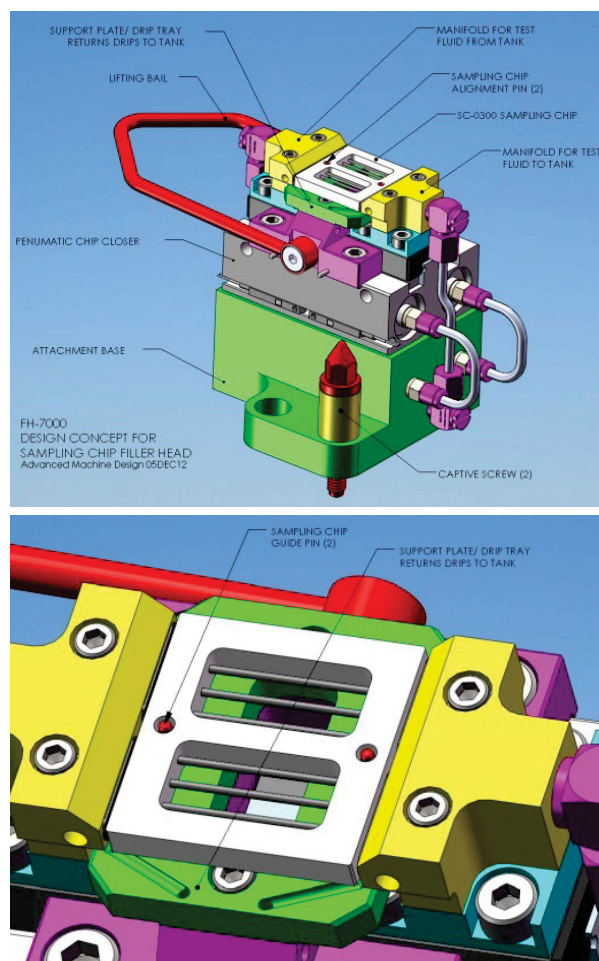


Figure 3. Conceptual design of 10 µl chip loading/unloading station.

Additional testing with both the glass and 2 µl prototype chips was completed using an Inductively Coupled Plasma-Optical Emission Spectroscopy (ICP-OES) instead of the ultraviolet-visible (UV-vis) previously used. To better evaluate the effectiveness of the robotic system, Inductively Coupled Plasma-Mass Spectroscopy (ICP-MS) will be used in place of the UV-Vis. ICP-MS is less impacted by volume changes and air bubbles when compared to the UV-Vis. Chips were filled by flow through

Separations and Waste Forms
2013 Accomplishments Report

primarily (with one dipped). Tests were conducted with 100 g/L $\text{Ho}(\text{NO}_3)_3$ and with a stock La solution. After the chip was filled it was placed by hand in the spare sample unloading header and transported to the sample unloading system attached to the ICP-OES. After analysis was complete, the process was repeated once with the same chip (i.e. two runs). Results from the ICP-OES are still being evaluated and will be reported in the end of year report.

Publications

1. Tripp, J. L., J. D. Law, and T. Smith (2013). "Recent Results of the Investigation of a Microfluidic Sampling Chip and Sampling System for Hot Cell Aqueous Processing Streams," *Proceedings from GLOBAL 2013*, Salt Lake City, UT, Sept 29-Oct 4.
2. Law, J. D., J. L. Tripp, T. E. Smith, J. M. Svoboda, V. J. Rutledge, T. G. Garn, and L. Macaluso (2013). "Development and Testing of A Microfluidic Based Robotic Sampling System for Remote Sampling and Analysis of radioactive solutions," Accepted for publication in *Nuclear Technology*, June.
3. Tripp, J. L., J. D. Law, T. E. Smith, V. J. Rutledge, W. Bauer, D. Ball, and P. Hahn, (2013). "Microfluidic-based Sample Chips for Radioactive Solutions," submitted to *Nuclear Technology*.

Spectroscopic Online Monitoring for Real-time pH and Metal Concentration

S. A. Bryan, sam.bryan@pnnl.gov, and A. J. Casella

The overall objective of this task is to obtain fundamental information needed for on-line, real-time, process spectroscopic instrumentation to be designed for use in monitoring and controlling fuel reprocessing flowsheets. The previously conducted work included measuring Raman and ultraviolet-visible near-infrared (UV-vis-NIR) spectroscopic responses of U, Pu, and Np in matrix simulants; evaluating sensitivity and detection limits of U, Pu, Np, and NO_3^- in each simulant for available in-house spectroscopy instrumentation; and developing and verifying chemometric models. The key results from FY 2013 work are:

- The developed weak acid monitor based on lactic acid/lactate specific Raman bands was expanded for inclusion of additional Trivalent Actinide Lanthanide Separation by Phosphorous reagent Extraction from Aqueous Komplexes (TALSPEAK) solution components and coupled with monitoring of metal extraction using UV/vis-NIR spectroscopy
- The weak acid monitoring technique using spectroscopic on-line monitoring was demonstrated and validated by simultaneous measurement of pH and lanthanide extraction using on-line process monitoring within a centrifugal contactor system

Process Monitoring of pH and Lanthanide Extraction Simultaneously using On-line Counter Current Centrifugal Contactor System

The goal of this work in FY 2013 is the development of spectroscopic measurement of pH in a weak acid extraction system, and the implementation of this method into an on-line process monitoring using centrifugal contactors. In this application, pH monitoring is performed using a Raman spectroscopic technique while the measurement of the lanthanide metal ion concentration is performed using UV-vis-NIR spectroscopy. The use of multiplexer systems, which allow for monitoring multiple locations within a process stream with both Raman and UV-vis-NIR techniques, allows for simultaneous monitoring of mass balance of metals within a counter-current extraction system, as well as the pH of the feed and raffinate streams.

For this demonstration, the team used the TALSPEAK system as the pH sensitive extraction system for study. The aqueous phase of the TALSPEAK process consisted of a lactic acid buffer and diethylenetriamine-N,N,N',N',N''-pentaacetic acid (DTPA) as the actinide hold back reagent while the organic phase contains the extractant di(2-ethylhexyl)phosphoric acid (HEDHP). The TALSPEAK separation is strongly affected by solution pH, and requires careful control to maintain optimal operating conditions.

As lactate/lactic acid is Raman active (Figure 4), it provides a spectroscopic signature for pH measurement in solution. As the lactate/lactic acid

Separations and Waste Forms
2013 Accomplishments Report

Raman spectra contains numerous peaks resulting from attributes such as methyl and CH stretching and deformation, intermolecular hydrogen bonding between hydrogen and carboxyl groups, and intramolecular hydrogen bonding, the alterations to these peaks resulting from changing pH can be used to develop a chemometric method for on-line measurement of pH by Raman spectroscopy.

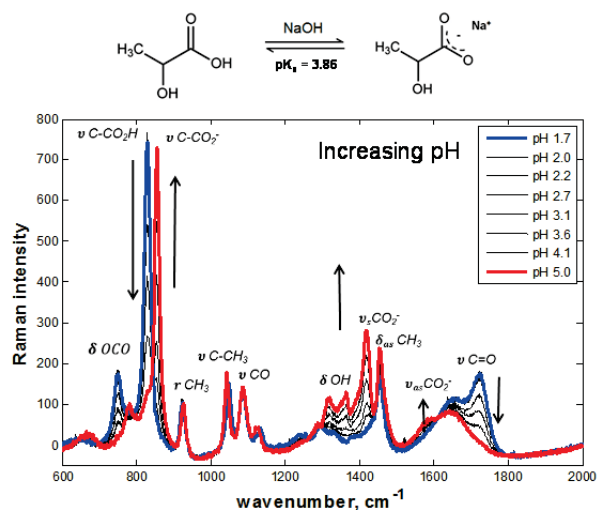


Figure 4. Raman signatures of 1 M lactate at an ionic strength of 1 M with a pH range from 1.66 to 4.99. The arrow indicates the trend with increasing pH.

The extraction of Nd(III) was monitored during an on-line flow experiment using a centrifugal contactor system. During the extraction experiment, the pH was purposely altered to change the distribution of Nd(III) between the aqueous and organic phases, after which the pH was restored to its original value. The extraction of Nd(III) was monitored on-line by UV-vis-NIR spectroscopy, while the pH of the system was monitored using Raman spectroscopy. Figure 5 (left panel) shows the organic and aqueous phase reagents used in TALSPEAK extraction system. The extraction of neodymium is favored at low pH values, pH ~ 3, and is less favored at higher pH values, pH ~4 (right panel).

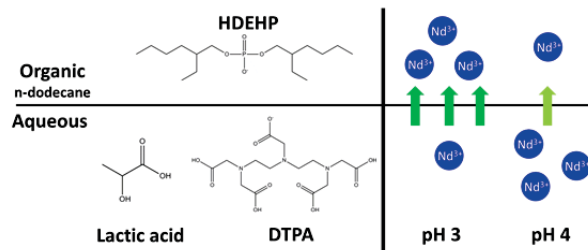


Figure 5. Organic and aqueous phase reagents used in TALSPEAK extraction system (left panel). The extraction of Nd is highly favored at low pH values (pH ~ 3), and is less favored at higher pH values (pH ~4), (right panel).

The schematic shown in Figure 6A depicts the conceptual design for the experiment. This figure shows the relative pH of the aqueous feed as a function of time during the course of flow extraction using a centrifugal contactor system. At the beginning of the experiment, the pH of the feed was set at pH ~3, a value chosen for optimal extraction of neodymium. At a predetermined time, the pH was increased to pH ~ 4 , at which neodymium extraction would be less favored. Time was allowed for steady state extraction conditions to be reestablished; then the pH was reduced to the original pH value (pH ~3), to reestablish conditions more favorable to the extraction of neodymium. The schematic in Figure 6B shows the expected response to the pH swing; when the pH is low, the neodymium is preferentially extracted into the organic phase; when the pH is increased, the neodymium extraction into the organic phase is less preferential, and the neodymium is retained in the aqueous phase. When the pH was decreased at the end of the experiment, the neodymium extraction returned to its original value, and the organic phase concentration of neodymium increased correspondingly as the neodymium in the aqueous phase decreased.

Separations and Waste Forms
2013 Accomplishments Report

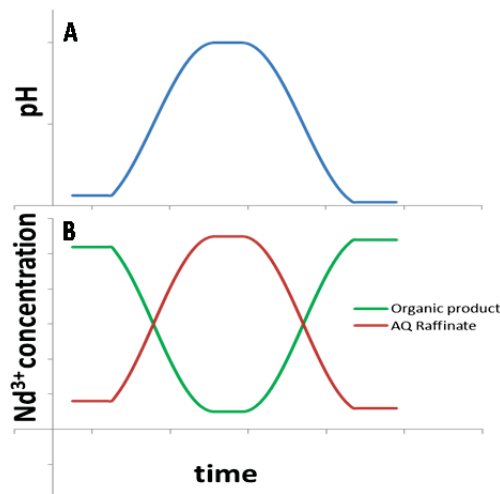


Figure 6. Schematic showing conceptual experimental design for the A) variable pH and B) corresponding Nd^{3+} extraction.

Contactor Demonstration

The centrifugal contactor system test was initially started with an aqueous feed composed of 28 mM $\text{Nd}(\text{NO}_3)_3$ at pH 3.09. The other components in the aqueous phase include the TALSPEAK system components (50 mM DTPA and 1.5 M lactate/lactic acid buffer). The aqueous phase and organic phase flow rates were set at approximately 10 mL/min each. After approximately 90 minutes of stable flow through the system, the feed solution was adjusted by the addition of NaOH to induce a pH change to achieve a final solution pH of 4.37. The centrifugal contactor system was allowed to flow at the same flow rate (10 mL/min) until a run time of approximately 200 minutes, whereupon the feed solution was adjusted to a lower pH by the addition of nitric acid (HNO_3), resulting in a final pH of 3.01.

Raman and UV-vis-NIR spectroscopic monitoring of the feed, raffinate, solvent, and organic product streams were recorded during the entire flow test. The real-time Raman spectroscopic measurement of the aqueous raffinate phase is shown in Figure 7.

For the aqueous raffinate, shown in Figure 7, the Raman band located at approximately 830 cm^{-1} associated with the protonated lactic acid ($\nu\text{C-COOH}$) is the most intense band in this region at the beginning of the flow experiment (times 0 to

approximately 90 minutes). When the pH is increased by the addition of NaOH to the feed, at time 90 minutes, the Raman band associated with lactic acid decreases in intensity, and a new band associated with the deprotonated lactate ($\nu\text{C-CO}_2^-$ at approximately 860 cm^{-1}) becomes the prominent Raman band. When the pH of the feed was decreased upon addition of nitric acid at 220 minutes, the lactate band in the raffinate diminishes and the lactic acid band is once again the most prominent band in this region, with a resulting measured pH of 2.78.

The spectroscopic measurements from the flow test were analyzed using the chemometric model developed under this task. The predicted pH and Nd concentrations for the raffinate stream are shown in Figure 8A and Figure 8B respectively. As an independent confirmation of the predictive model, grab samples were taken during the flow experiment and analyzed for pH and neodymium concentrations and are also shown in Figure 8.

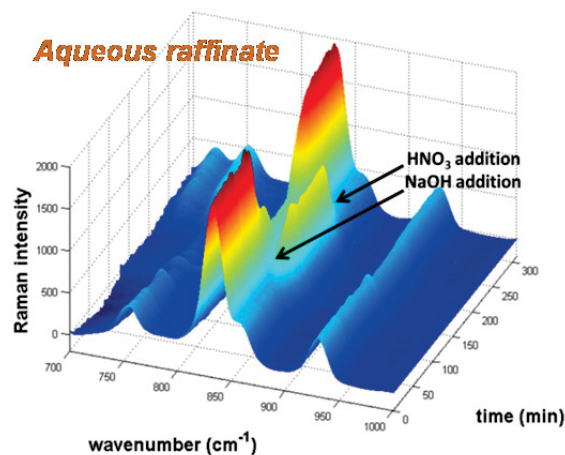


Figure 7. Real-time Raman spectroscopic measurements of the aqueous raffinate phase. The Raman spectra are shown over the entire experiment from time = 0 to 300 min, the addition of NaOH and HNO_3 are indicated on the figure.

Separations and Waste Forms
2013 Accomplishments Report

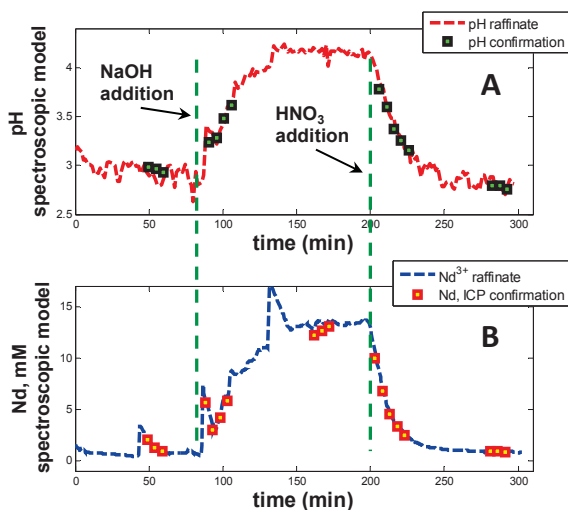


Figure 8. Prediction of Nd^{3+} concentration for aqueous feed, aqueous raffinate, organic feed and organic product phases as a function of run time during continuous centrifugal contactor test. Times for NaOH and HNO_3 additions to feed, as well as ICP confirmation measurements are indicated within this figure.

The time for addition of NaOH to the feed solution is marked on Figure 8 and coincides with the detected increase in pH (Figure 8A) and decrease in extraction of Nd^{3+} into the TALSPEAK organic phase, with the concurrent increase in the concentration of Nd^{3+} in the raffinate stream (Figure 8B). The addition of nitric acid is also marked in this figure and coincides with the decrease in pH, and decrease in Nd^{3+} in the raffinate stream. Several samples were taken from the aqueous feed and aqueous raffinate streams during the process for traditional pH and ICP analysis, which are also shown on this figure. In all instances, the pH and ICP (Nd) confirmation agrees with the flow model prediction.

In general, the extraction of Nd^{3+} follows the pH swing in the system, as observed in Figure 8 and confirmed by real-time, on-line process monitoring.

Summary of On-Line Centrifugal Contactor Experiment

The extraction of lanthanides in the TALSPEAK process is highly dependent upon the solution's pH, which is controlled by the lactic acid/lactate buffer system. The team carried out an on-line, real-time process monitoring demonstration using pH control to selectively partition a lanthanide metal (Nd^{3+}) from the

aqueous phase to the organic phase. The test was designed to follow both metal extraction (using vis-NIR spectroscopy) and changes in pH (using Raman spectroscopy) during the continuous cross-flow extraction process. The aqueous feed contained Nd^{3+} as the model lanthanide metal, DTPA, and lactic acid/lactate buffer; the organic phase contains the bis-(2-ethylhexyl) phosphoric acid (HDEHP) extractant in *n*-dodecane. The aqueous feed was buffered at a pH of 3 for an initial baseline extraction measurement. After the initial baseline measurement period, a swing to a higher pH (4.3) was induced by the addition of the strong base, NaOH , to show off-normal operating conditions, resulting in less efficient extraction of Nd^{3+} . After approximately two hours at this off-normal condition, the addition of the strong acid, nitric acid was implemented to bring the pH back to its normal operating pH of 3. The change in the Nd^{3+} concentration in the loaded organic and raffinate extraction phases was apparent from the observed absorbance bands for Nd^{3+} using UV-visible spectroscopy. By use of Raman spectroscopy, the pH of the aqueous feed and raffinate streams were also monitored during this on-line extraction demonstration to assess the system's swing to off-normal and the return to normal conditions. Samples were obtained from the aqueous feed and raffinate stream during testing and independently analyzed for pH and Nd^{3+} . These results verified the accuracy of the predictive model for both pH and Nd^{3+} concentration.

Publications

1. Casella, A. J., T. G. Levitskaia, J. M. Peterson, and S. A. Bryan (2103). "Water O-H Stretching Raman Signature for Strong Acid Monitoring via Multivariate Analysis". *Anal. Chem.* 85, 4120-4128. dx.doi.org/10.1021/ac4001628
2. Levitskaia, T. G., J. M. Peterson, E. L. Campbell, A. J. Casella, D. R. Peterman, and S. A. Bryan (2013). "FTIR Spectroscopy and Multivariate Analysis for Online Monitoring of Dibutyl Phosphate Degradation Product in Tributyl Phosphate /*n*-Dodecane/Nitric Acid Solvent" *Industrial & Engineering Chemistry Research*, accepted November 5, 2013, DOI: 10.1021/ie402722n

Separations and Waste Forms
2013 Accomplishments Report

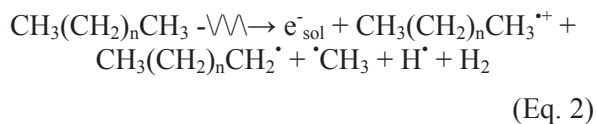
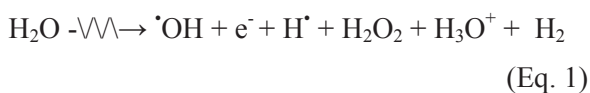
Solvent Degradation

Radiolysis/Hydrolysis Test Loop

D. Peterman, dean.peterman@inl.gov, and J. Law

The radiolysis/hydrolysis test loop, located at INL, was utilized to study the impacts of radiolytic and hydrolytic degradation processes on the performance of the stripping section of the TRansUranic EXtraction (TRUEX) process. The current TRUEX flowsheet concept considered by the Fuel Cycle Research Development program is intended to separate the trivalent actinides and lanthanides from the raffinate of a U/Pu separation process. The trivalent actinides would then be separated from the lanthanides using the TALSPEAK. The TALSPEAK process requires an aqueous phase containing a polyaminopolycarboxylate actinide holdback reagent and an organic acid buffer. This TALSPEAK flowsheet employs 1.5 M DTPA as the holdback reagent and 0.050 M lactic acid (LA) as the buffer in the aqueous phase of the extraction section. Therefore, the TRUEX flowsheet conditions evaluated during FY 2013 used a mixture of 1.5 M DTPA and 0.050 M LA as the aqueous stripping reagent.

The successful deployment of any solvent extraction ligand proposed for use in fuel cycle separations will depend upon the stability of that ligand in an acidic, radioactive environment. Irradiation of the ligand occurs due to the decay energy of actinides and fission products in the dissolved nuclear fuel solution. The radiation types are predominantly low linear energy transfer (LET) beta/gamma radiation from fission product decay, and high LET alpha radiation from actinide decay. The major reactive species formed by radiolysis of water, alkane diluent, and nitric acid are shown in Equations 1–3, respectively.



Equations 1 – 3 show that radiolysis of aqueous and organic phases generates a range of

oxidizing ($\cdot\text{OH}$, $\cdot\text{NO}_3$, $\cdot\text{NO}_2$) radicals, reducing (H^\cdot) radicals, the reducing aqueous electron (e^-_{aq}), and reactive molecular species (H_2O_2 , HNO_2 , H_2).

The effects of gamma radiolysis upon the efficacy of the strip section of a TRUEX flowsheet for the recovery of trivalent actinides and lanthanides from acidic solution were determined by a combination of static and test loop irradiations. The compositions of the irradiated aqueous and organic solutions were determined using a suite of analytical techniques. In addition, Electrospray Ionization-Mass Spectrometry (ESI-MS) was used to identify some of the products of the radiolytic degradation of lactic acid, DTPA, octyl(phenyl)-N,N-diisobutylcarbonylmethylphosphine oxide (CMPO), and tributyl phosphate (TBP).

For lactic acid, the major degradation products detected by ESI-MS were pyruvic acid and a species corresponding to a lactic acid-pyruvic acid cluster. The major product of DTPA degradation was determined by ESI-MS to be a DTPA lactam resulting from the radiolytic loss of glycolic acid. Acetate and several other unknown degradation products of both lactic acid and DTPA were detected by high-performance liquid chromatography analysis. Several species arising from the degradation of CMPO ($[(\text{iBu})_2\text{NPrH}]^+$, $[(\text{iBu})_2\text{PrH}_2]^+$ and CMPO-carboxylic acids) were determined by ESI-MS; which is consistent with products identified in previous studies.

The extent of radiolytic degradation of any particular species in solution may be described by a *G*-value, in units of $\mu\text{mol}\cdot\text{L}^{-1}\cdot\text{Gy}^{-1}$. As the magnitude of the *G*-value for a particular radiolytic degradation process increases, the amount of degradation product formed increases. The *G*-values determined for the static irradiation of the aqueous TRUEX strip reagent in contact with TRUEX solvent are summarized in Table 3. The *G*-values for several species determined for the test loop irradiation of the aqueous TRUEX strip reagent in contact with TRUEX solvent are summarized in Table 4. For comparison, the *G*-values determined for test loop irradiation of TRUEX in contact with 4.4 M HNO_3 (extraction conditions) are summarized Table 5. Comparison of the *G*-values determined for these irradiation conditions indicate that degradation due to

Separations and Waste Forms
2013 Accomplishments Report

radiolysis occurs via differing processes in these systems.

Table 3. *G*-values determined for the static irradiation of the aqueous TRUEX strip reagent in contact with TRUEX solvent.

Species	<i>G</i> -value, $\mu\text{mol}\cdot\text{L}^{-1}\cdot\text{Gy}^{-1}$	R ²
Lactic Acid	-0.585 ± 0.040	0.97
DTPA	$-6.65 \times 10^{-2} \pm 2.82 \times 10^{-3}$	0.99
CMPO	-0.527 ± 0.108	0.88
TBP	$-7.04 \times 10^{-2} \pm 3.96 \times 10^{-3}$	0.21
HDBP _{tot}	6.16×10^{-3}	na
H ₂ MBP	$5.22 \times 10^{-4} \pm 2.39 \times 10^{-5}$	0.99
Phosphate	$1.16 \times 10^{-3} \pm 2.19 \times 10^{-4}$	0.87

Table 4. *G*-values determined for the test loop irradiation of the aqueous TRUEX strip reagent in contact with TRUEX solvent.

Species	<i>G</i> -value, $\mu\text{mol}\cdot\text{L}^{-1}\cdot\text{Gy}^{-1}$	R ²
Lactic Acid	$-5.18 \times 10^{-2} \pm 2.37 \times 10^{-2}$	0.39
DTPA	$-4.75 \times 10^{-2} \pm 9.46 \times 10^{-3}$	0.86
CMPO	$-3.67 \times 10^{-2} \pm 5.07 \times 10^{-3}$	0.88
TBP	$-3.00 \times 10^{-2} \pm 1.06 \times 10^{-4}$	0.29
HDBP _{tot}	6.25×10^{-3}	na
H ₂ MBP	$4.39 \times 10^{-4} \pm 1.06 \times 10^{-5}$	0.89
Phosphate	$8.15 \times 10^{-4} \pm 1.37 \times 10^{-4}$	0.90

Table 5. Summary of *G*-values determined for the test loop irradiation of TRUEX solvent in contact with 4.4 M HNO₃.

Species	<i>G</i> -value, $\mu\text{mol}\cdot\text{L}^{-1}\cdot\text{Gy}^{-1}$	R ²
TBP	-0.115 ± 0.031	0.62
CMPO	-0.159 ± 0.016	0.97
HDBP _{tot}	0.118 ± 0.007	0.97
H ₂ MBP	$1.56 \times 10^{-3} \pm 8.06 \times 10^{-5}$	0.99
Phosphate	$5.66 \times 10^{-3} \pm 3.94 \times 10^{-4}$	0.98

Comparison of the test loop irradiations of the TRUEX extraction and stripping sections revealed surprising differences in the radiolytic degradation of TBP and di-*n*-butyl phosphoric acid (HDBP). Based upon research results, an unidentified process is responsible for the degradation of HDBP which results from the radiolysis of TBP,

for irradiation in the presence of lactic acid/DTPA aqueous phase. Further study would be necessary to develop a detailed understanding of the radiation chemistry of TBP and HDBP in contact with a lactic acid/DTPA aqueous solution. The generally lower *G*-values determined for test loop irradiation compared to static irradiation experiments clearly points out the importance of performing radiolytic degradation studies using oxygenated, mixed aqueous and organic solutions.

Gamma radiolysis results in a small increase the distribution ratios in the strip section of the TRUEX flowsheet ($D_{Am} = <0.001$ at 0 kGy absorbed dose to $D_{Am} = 0.015$ at 1300 kGy absorbed). Even the distribution ratio determined for the highest absorbed dose is not expected to adversely impact operation of the stripping section of the TRUEX flowsheet. However, the generation of degradation products in the aqueous phase and the radiolytic destruction of lactic acid and DTPA may have serious impacts on a subsequent TALSPEAK process. Close coupling of the TRUEX and TALSPEAK operations may help to mitigate these effects by limiting the dose to the aqueous and subsequent degradation.

Publications

- Peterman, D. R., L. G. Olson, G. S. Groenewold, R. G. McDowell, R. D. Tillotson, and J. D. Law (2013). "Characterization of radiolytically generated degradation products in the strip section of a TRUEX flowsheet." FCRD-SWF-2013-000202, Idaho National Laboratory.

Spectroscopic Multivariate Analysis for Online Monitoring of the Degradation Products of Tributyl Phosphate

T. G. Levitskaia, tatiana.levitskaia@pnnl.gov, J. M. Peterson, and S. A. Bryan

Pacific Northwest National Laboratory is investigating the applicability of online spectroscopic instrumentation for identification and quantification of radiolytic and hydrolytic degradation products accumulating in extraction organic solvents with time. The goal of this work is to establish the spectroscopic capabilities necessary for real-time online monitoring of solvent degradation. This capability will allow

Separations and Waste Forms
2013 Accomplishments Report

plant operators to take appropriate actions to restore the solvent quality on an as-needed basis.

For proof-of-concept that spectroscopic detection of the realistic quantities of degradation products is feasible in the matrix containing significantly greater concentrations of the parent material, TBP/*n*-dodecane solvent was selected. The radiolytic degradation chemistry of the TBP/*n*-dodecane solvent system has been extensively studied and recently reviewed [Bryan and Levitskaia, 2011; and references therein]. HDBP is generated by the direct degradation of TPB in relatively high yield and has been identified as major radiolytic degradation product of the TBP extractant under the acidic conditions.

FY 2010–2011 PNNL scope effort was focused on the development of the predictive chemometric partial least squares (PLS) regression models for the quantification of the main degradation products of the TBP/*n*-dodecane organic solvent contacted with nitric acid and testing them against gamma-irradiated solvent samples generated by INL researchers. The solvent samples received from INL were contacted with aqueous 0.5–4 M HNO₃ solutions and varied in accumulated dose for each sample. These studies identified the spectroscopic signatures of the TBP-based solvent and its main degradation product HDBP in the extraction phases contacted with nitric acid solutions of the variable concentrations. Developed PLS models successfully predicted HDBP, TBP, and HNO₃ concentrations in the irradiated samples obtained from INL [Levitskaia et al, 2013]. This work continued in FY 2012 [Levitskaia et al., 2012] to increase solvent complexity by including UO₂(NO₃)₂ in the system, and expand respective spectral databases. It was demonstrated that developed PLS models are capable of quantitative prediction of HDBP, TBP, and UO₂²⁺ in the TBP/*n*-dodecane solvent. Further, translation of the three-component PLS model to the flow conditions in the centrifugal contactor tests was performed.

The experimental scope of FY 2013 has been focused on the expanding spectral database and

testing PLS models developed previously using irradiated TBP/HNO₃/*n*-dodecane samples upon introduction of UO₂(NO₃)₂ in the system and re-equilibrating the contact irradiated phases thus further increasing complexity of the solvent containing the actual degradation components generated by the external gamma irradiation. The results of this investigation are summarized in this report.

Five HNO₃/TBP/*n*-dodecane solvent samples 1–5 irradiated to 500–2160 kGy (Table 6) were used to test PLS models developed for the HDBP quantification in the presence of UO₂(NO₃)₂. Solid UO₂(NO₃)₂ was dissolved in aqueous HNO₃ solutions, which were previously irradiated to the variable gamma dose during the contact with 30% TBP/*n*-dodecane solvent, to prepare 0.1–1.9 M UO₂(NO₃)₂ solutions. The representative Fourier transform infrared (FTIR) spectral layouts corresponding the resulting solutions of the irradiated Sample 5 are shown in Figure 9 (top). The observed vibrational bands were ascribed to UO₂²⁺, HNO₃, and H₂O. No bands due to the organic components were identified in the spectra. Intensities of both UO₂²⁺ and NO₃⁻ bands increase as the UO₂(NO₃)₂ concentration of the in the feed increases. The prepared aqueous solutions were re-equilibrated with the corresponding irradiated TBP/*n*-dodecane phases, and the FTIR spectra of the post-contact aqueous and organic solutions were acquired. Figure 9 (bottom) shows FTIR spectral layouts of the aqueous post-contact solutions of the Sample 5

It was observed that aqueous pre- and post contact solutions exhibited dissimilar spectral profiles, the main difference being the presence of the bands due to the organic constituents in the post-contact phases. The identified bands included POC, P=O, and CH vibrations and were ascribed to the HDBP. This result was supported by the split of the UO₂²⁺ stretch band into two components at 962 and 940 cm⁻¹ corresponding to the UO₂²⁺ and UO₂²⁺•2DBP complex, formation of which is the driving force for the partitioning of HDBP from the organic to aqueous phase.

Separations and Waste Forms
2013 Accomplishments Report

Table 6. Description of Irradiated Samples. Initial pre-irradiation composition of the organic solvent was 30 v/v% TBP/*n*-dodecane for all samples.

Sample ID	Accumulated dose, kGy	Post-irradiation concentration, v/v%, ^{a)}		Post-contact HNO ₃ concentration, M ^{b)}	
		TBP	HDBP	Aqueous phase	Organic phase
R1	506	28.43 ± 0.43	1.64 ± 0.10	1.13	0.28
R2	649	27.95 ± 0.55	2.11 ± 0.13	1.48	0.35
R3	540	28.29 ± 0.46	1.75 ± 0.10	2.25	0.51
R4	2048	23.4 ± 1.8	6.77 ± 0.40	1.83	0.35
R5	2158	23.2 ± 1.8	7.01 ± 0.42	0.84	0.23

^{a)} Calculated based on G values taken from Peterman et al, 2012; $G_{\text{TBP}} = -0.115 \pm 0.031$ and $G_{\text{HDBP}} = 0.118 \pm 0.007 \mu\text{mol L}^{-1} \text{Gy}^{-1}$.

^{b)} Experimentally determined by the potentiometric titration.

Sample 5 contains mostly $\text{UO}_2^{2+} \cdot 2\text{DBP}$, and the largest concentration of HDBP as evident from the highest intensities of the POC, P=O, and CH vibrations among other post-contact aqueous samples. This can be attributed to two cooperative effects, the largest irradiation dose of the Sample 5 leading to the significant conversion of TBP to HDBP and the relatively small HNO₃ concentration in the system promoting deprotonation of HDBP and therefore facilitating $\text{UO}_2^{2+} \cdot 2\text{DBP}$ complex formation.

traces in the order of increasing UO_2^{2+} concentration from 0.1 to 1.9M).

The FTIR spectroscopy spectra of the irradiated TBP/*n*-dodecane solutions loaded with $\text{UO}_2(\text{NO}_3)_2$ show several changes as the organic concentration of $\text{UO}_2(\text{NO}_3)_2$ increases (Figure 10). One noticeable change is slight narrowing accompanied by the slight red shift of the P-O-C stretch at 1033 cm^{-1} . The P=O vibration band undergoes significant narrowing and shifted to 1190 cm^{-1} due to the TBP complexation of the UO_2^{2+} cation. Also several bands appeared in the spectrum due to the presence of extracted $\text{UO}_2(\text{NO}_3)_2$ including 748 cm^{-1} O-N-O bend and 1280 cm^{-1} O-N-O symmetric stretch of the nitrate in the complex $\text{NO}_3^- \cdot \text{UO}_2^{2+} \cdot 2\text{TBP}$ as well as 939 cm^{-1} UO_2^{2+} stretch. The FTIR spectra corresponding to the organic samples 1–5 with the similar UO_2^{2+} loading were found to be nearly identical. This finding suggests the organic solutions irradiated to the different gamma doses and contacted with the corresponding aqueous phases containing the same $\text{UO}_2(\text{NO}_3)_2$ concentration have a similar final post-contact species present due to the partitioning of HDBP degradation product into the aqueous phases. This result is in agreement with the FTIR analysis of the aqueous post-contact solutions demonstrating presence of the $\text{UO}_2^{2+} \cdot 2\text{DBP}$ complex.

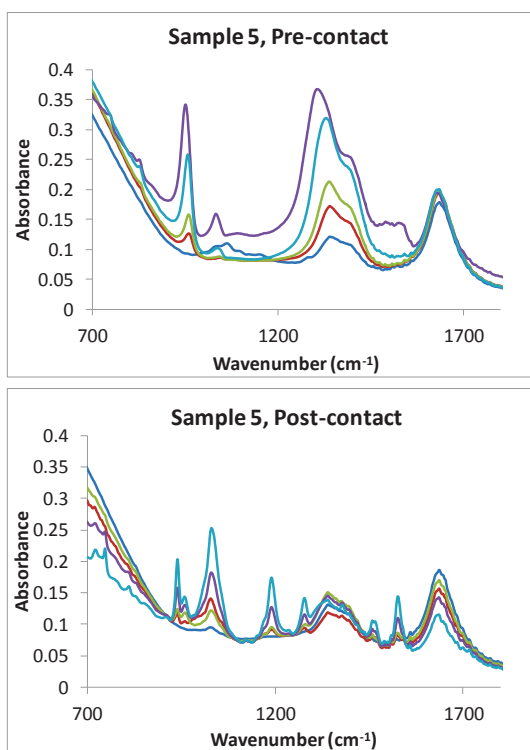


Figure 9. FTIR spectral layouts of the irradiated aqueous Sample 5 containing variable concentrations of $\text{UO}_2(\text{NO}_3)_2$ (dark blue, red, green, purple, and light blue

Separations and Waste Forms
2013 Accomplishments Report

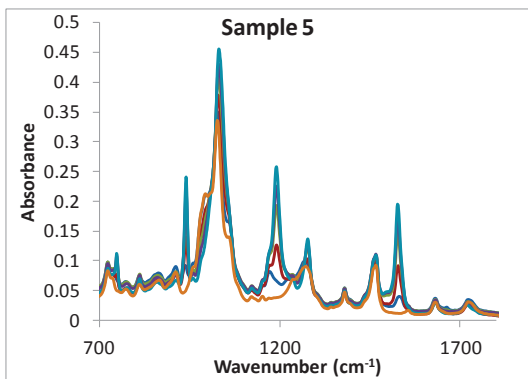


Figure 10. FTIR spectra of the irradiated organic TBP/*n*-dodecane sample 5 before (orange trace) and after loading (dark blue, red, green, purple, and light blue traces in the order of increasing UO_2^{2+} loading) with UO_2^{2+} at variable concentrations.

The PLS developed model previously developed using FTIR measurements of the TBP/HDBP/*n*-dodecane solvent containing various concentrations of $\text{UO}_2(\text{NO}_3)_2$ was used to estimate the post-contact HDBP concentration in the irradiated organic solvent containing $\text{UO}_2(\text{NO}_3)_2$. The resulting prediction is shown in Figure 3. In this plot, blue symbols indicate HDBP concentration in the simulated $\text{UO}_2(\text{NO}_3)_2$ /TBP/HDBP/*n*-dodecane solvent solution used for the PLS model development. Green and red symbols correspond to the PLS-predicted HDBP concentrations in the irradiated to the low dose post-contact organic samples loaded with UO_2^{2+} (Samples 1, 2, and 3 in Table 1) plotted versus HDBP concentration estimated using G_{HDBP} value assuming no partitioning into the aqueous phase.

Interestingly for the samples containing low UO_2^{2+} concentrations, the PLS-predicted and G_{HDBP} -estimated organic HDBP concentrations are in excellent agreement (green symbols) suggesting negligible HDBP partitioning into the aqueous phase. As total UO_2^{2+} concentration in the extraction system increases, $D(\text{UO}_2^{2+})$ decreases, and significant amount of UO_2^{2+} remains in the aqueous post-contact raffinate forcing HDBP partitioning into the aqueous phase and reducing its concentration in the organic product (red symbols). The same conclusion is drawn upon examination of the FTIR spectra of the aqueous raffinate phases of the Samples 1, 2, and 3 (Figure 11).

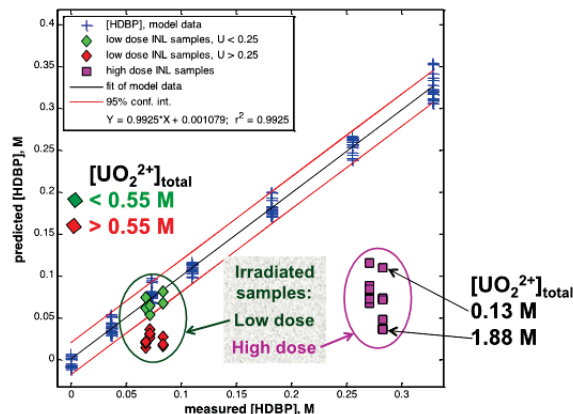


Figure 11. PLS model (blue symbols) and prediction of HDBP concentration (green, red, and pink symbols) in the irradiated $\text{UO}_2(\text{NO}_3)_2$ /TBP/HDBP/*n*-dodecane solvent. Black line represents the modeling results. Solid red lines indicate 95% confidence interval.

Similar results were obtained for the Samples 4 and 5 irradiated to the high dose (see Table 6), the PLS-predicted organic HDBP concentration in these samples is shown by the pink symbols (Figure 11). For these samples due to the high conversion of TBP to HDBP leading to the significant increase in the total HDBP concentration, the HDBP partitioning into the aqueous phase was observed for the entire UO_2^{2+} concentration range. Similarly to the low-dose samples, this HDBP transport correlated with the UO_2^{2+} concentration. As a result, the predicted organic HDBP concentration was significantly lower than estimated based on G_{HDBP} value.

The PLS regression model predicts similar HDBP concentration in the post-contact organic solvent with similar UO_2^{2+} loading. This result is in agreement with the conclusion drawn based on the comparison of FTIR spectra corresponding to the organic post-contact Samples 1–5 containing similar concentrations of UO_2^{2+} . Overall it was concluded that PLS modeling using FTIR spectra is capable of predicting realistic quantities of the primary degradation product HDBP in the $\text{UO}_2(\text{NO}_3)_2$ /TBP/HDBP/*n*-dodecane solvent.

Publications

- Levitskaia T. G., J. M. Peterson, E. L. Campbell, A. J. Casella, D. R. Peterman, and S. A. Bryan (2013). “FTIR Spectroscopy and Multivariate Analysis for Online Monitoring of Dibutyl Phosphate Degradation Product in

Separations and Waste Forms
2013 Accomplishments Report

Tributyl Phosphate /n-Dodecane/Nitric Acid Solvent.” *Industrial & Engineering Chemistry*. In press.

**Lab-Scale Testing of
Case-Study Processes**

Case Study Tests for Co-Decontamination Process

C. Pereira, pereira@anl.gov

The experimental work for the Co-decontamination flowsheet for FY 2013 was to be centered on running a modified version of the case study flowsheet (Figure 13) using cold chemicals and radiotracers on prototypic equipment. The planned tests are to be run on an instrumented centrifugal contactor (Figure 12).

The testing would verify that the expected elemental distributions among the effluent streams were observed and provide bounds on detectable limits. Experimental work that was planned for FY 2013 in support of the co-decontamination process flowsheet mass balance could not be done due to

the shutdown in late March 2013 of all laboratories in ANL Building 205 where the contactor was located. As a result, the work done in support of this effort was refocused on examining the impact of changes to the baseline assumptions used to select the final flowsheet based on a review of the available literature on TBP-nitric acid systems and supported with simulation studies using the Argonne Model of Universal Solvent Extraction (AMUSE). A review of literature on ancillary processing on denitration and actinide solidification processes was also done.

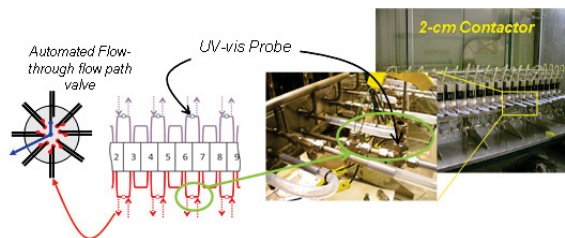


Figure 12. Centrifugal Contactor Test Bed

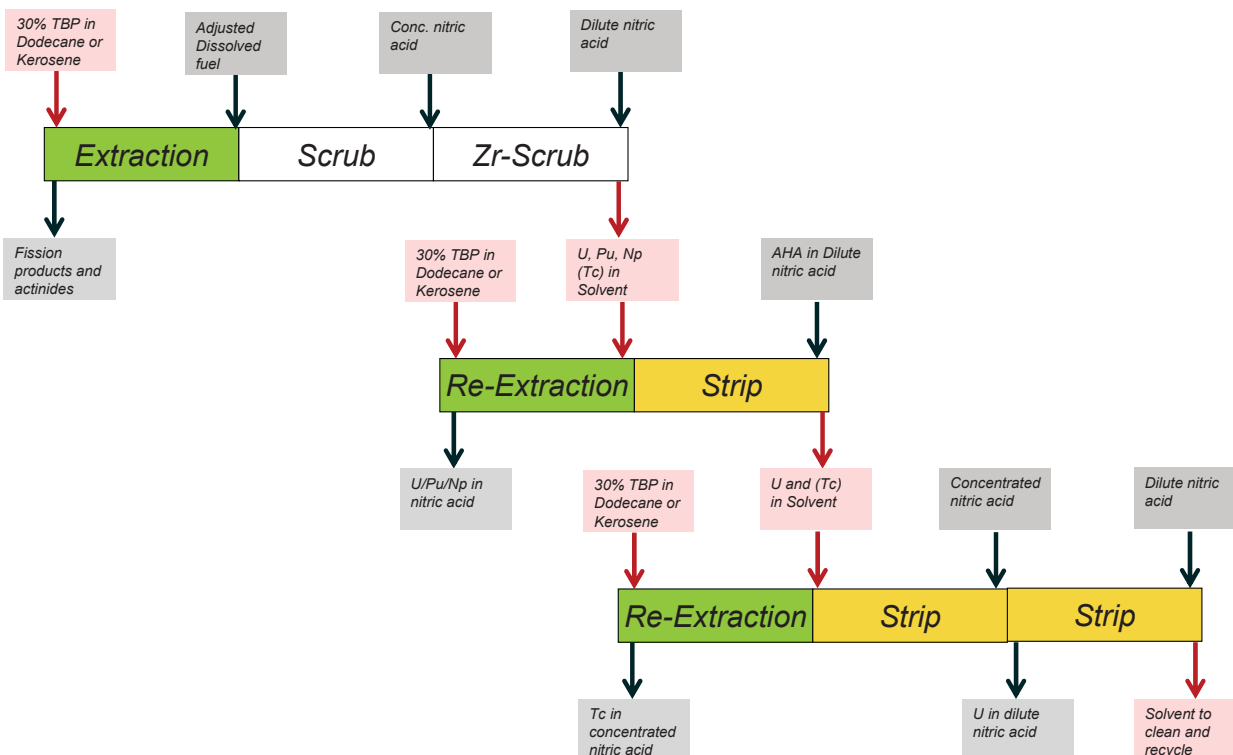


Figure 13. Reference Codecontamination Flowsheet

Separations and Waste Forms
2013 Accomplishments Report

In developing the reference case study flowsheet, a number of flowsheet options were examined using AMUSE, where the behavior of key actinide and fission product species was tracked as a function of acid concentration, stage number, flow rate, and complexant concentration. The goal of the testing program was to verify the predicted behavior for the case study flowsheet and to verify the assumptions made for the case study. These flowsheets studies provide an overview of the expected behavior.

Other than the two key actinides of interest, uranium and plutonium, the species that are most impacted by process conditions include neptunium, technetium, ruthenium, molybdenum, and zirconium. The oxidation state of neptunium was a particular concern because the oxidation state distribution is a strong function of the conditions under which the extraction process is run, including the radiation environment. Consequently, there is significant variation in the literature on the manner in which neptunium oxidation is controlled at the process-scale. In particular, there has been a significant amount of recent work reported on controlling neptunium behavior in process because of its impact on products of so-called advanced plutonium uranium reduction extraction (PUREX) processes. In the AMUSE code, the neptunium valence distribution is imposed by the user based on the process stream compositions, assumed pretreatment conditions and additives. Therefore, verification of the predicted neptunium behavior in the case study flowsheet was of particular interest.

One of the areas in which AMUSE can be augmented is in modeling the behavior of species that undergo kinetically limited reactions and species that change oxidation state under conditions that are encountered in aqueous solution under process conditions. DyAMUSE, the dynamic version of AMUSE was developed to allow simulation of species that can undergo changes oxidation state as a test progresses. The code currently models reduction of Pu⁴⁺ to Pu³⁺ by HAN. It is desirable to develop and implement a similar model for neptunium based on the literature data, augmented with data collected to support the case study. In particular, it is desirable to develop a kinetics-based neptunium oxidation

model based on Np-HNO₂-HNO₃ interaction kinetics.

A second study area was the development of primary and secondary processes for the case study. A literature review of candidate mixed actinide solidification processes was undertaken. Limited data exist on mixed oxide solidification as the literature is focused on uranium and plutonium denitration and/or oxidation. Proposed mixed oxide processes tend to settle on the assumption that behavior will be similar to that of pure-phase systems, and dominated by uranium. Minor actinide solidification studies are very limited in number; the best initial approach would seem to be to focus on candidate matrix materials that can be co-solidified with the minor actinides while retaining these species. Options include precipitation using complexants, or isolation and co-oxidation with predominant matrix metal elements for target fabrication. A second solvent extraction separation is a possibility though with addition of significant added processing.

Radiation Stability of Advanced TALSPEAK Solvent

B. J. Mincher, bruce.mincher@inl.gov

Separating the minor actinide elements (americium and curium) from the fission product lanthanides is an important step in closing the nuclear fuel cycle. Until now, a two-step method has been adopted by the FCRD program to separate the minor actinides, with the first step involving co-extraction of the lanthanides and minor actinides using the TRUEX process and the second step using the TALSPEAK process. However, TALSPEAK suffers the disadvantages of slow extraction kinetics and high sensitivity to the aqueous phase pH. To overcome these disadvantages, a variation of the TALSPEAK process was proposed which replaces the HDEHP extractant with 2-ethylhexylphosphonic acid mono-2-ethylhexyl ester (HEH[EHP]). This is referred to as an *Advanced TALSPEAK* process. The key advantages of switching to the HEH[EHP] extractant are: less dependence on the aqueous solution pH, more predictable extraction behavior, and more rapid extraction kinetics. However, the radiation stability of any process used in fuel cycle separations is a key parameter that could limit its utility. Therefore, lab scale

Separations and Waste Forms
2013 Accomplishments Report

testing of the radiation stability of this Advanced TALSPEAK reference process was performed.

Results

The effect of γ -rays on the concentration of HEH[EHP] irradiated as a component of the aerated, biphasic Advanced TALSPEAK process is shown in Figure 14. Also shown is the change in concentration for the conventional HEDHP extractant as a function of absorbed dose for irradiation under identical conditions. In both cases there appears to be no concentration change due to irradiation, suggesting that both have adequate stability for fuel cycle applications. However, products analysis is also important, since small amounts of radiolysis products may be deleterious to system performance.

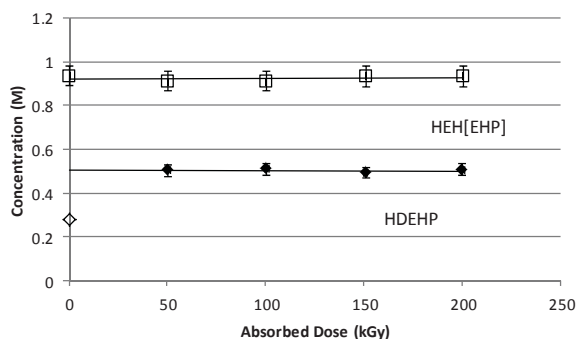


Figure 14. The change in concentration for HEH[EHP] (boxes) or HDEHP (diamonds) when irradiated as components of either the Advanced TALSPEAK or TALSPEAK process solvents, in contact with the same aqueous phase with air-sparging. Error bars shown are $\pm 5\%$ based on replicate analyses.

Small amounts of products were indeed detectable by a gas chromatography-flame ionization detector as peaks appearing at new retention times (RT). During the analyses of both the conventional TALSPEAK and Advanced TALSPEAK solvents a new peak was found (RT = 8.7 min) in irradiated samples; indicating its origin in the radiolysis of both HDEHP and HEH[EHP]. This is shown in Figure 15. Additionally, an unknown peak appeared in samples of only the Advanced TALSPEAK solvent with RT = 9.61 min, also shown in Figure 15. This peak was present in unirradiated solution, but increased with absorbed dose. The product of HDEHP irradiation is H_2MEHP , resulting from rupture of the ethylhexyl ether linkage and this is the most probable species corresponding to RT =

8.7 min. The product at 9.61 min RT is found only in Advanced TALSPEAK solutions with a non-zero concentration is probably an impurity associated with either synthesis or degradation of HEH[EHP] that is also produced by radiolytic degradation of that compound. It may be monoethylhexylphosphonic acid, which would be the product of the rupture of the single ether linkage in HEH[EHP]. Future work should involve mass spectrometric confirmation of this proposed product.

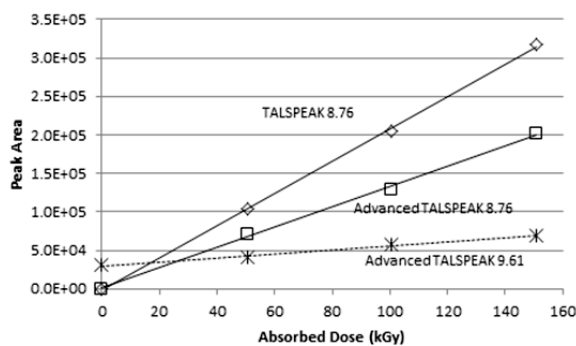


Figure 15. The increase in peak area with absorbed dose of radiolysis-product species for γ -irradiated samples of HEH[EHP] or HDEHP when irradiated as components of either the Advanced TALSPEAK or TALSPEAK process solvents, in contact with the same aqueous phase with air-sparging.

Samples of the Advanced TALSPEAK organic phases that were irradiated in the presence of the lactic acid aqueous phase were used in solvent extraction contacts. The results are shown in Figure 16. Despite the nearly constant concentration of HEH[EHP] in these irradiated samples it can be seen that the distribution ratios for both Am and Eu increased with absorbed dose; at a slightly faster rate for Am. The separation factor α_{EuAm} decreased moderately from ~ 90 – 100 at 0–50 kGy to 74 at 200 kGy absorbed dose. The moderately increasing distribution ratios shown may be attributed to the accumulation of mono-(2-ethylhexyl) phosphoric acid (H_2MEHP) and/or the proposed phosphonic acid radiolysis product. Similar results were obtained when this irradiated Advanced TALSPEAK organic phase was used to perform solvent extraction experiments from a freshly prepared citric acid buffered aqueous phase. The TALSPEAK and Advanced TALSPEAK systems behaved substantially similarly under irradiation.

Separations and Waste Forms
2013 Accomplishments Report

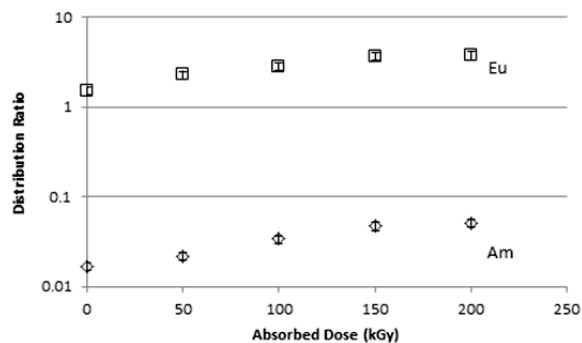


Figure 16. The solvent extraction of Am and Eu with 1.0 M HEH[EHP]/dodecane from pH 3.5, 0.05 M DTPA/1.5 M lactic acid irradiated aqueous phase. Error bars shown are $\pm 10\%$. Both phases were irradiated in contact with each other with air-sparging.

Future work will also include an irradiation of the optimized Advanced TALSPEAK process using the INL Irradiator Test Loop. The irradiation will be biphasic, and will use the HEH[EHP]/dodecane organic phase and the N-(2-hydroxyethyl)-ethylenediaminetriacetic acid (HEDTA)/citrate aqueous phase. The effects of irradiation on distribution ratios, product formation and post-irradiation pH will be measured.

Publication

1. Mincher, B. J., Lumetta, G., Peterman, D. R., McDowell, R. G., and Olson, L. G. (2013). "Radiation Chemistry of Advanced TALSPEAK Reference Flowsheet." Report, FCRD-SEPA-2013-000295, U.S. Department of Energy.

Lab-scale Testing of Tritium Concentration

R. T. Jubin, rubinrt@ornl.gov, R. M. Robinson, and S. H. Bruffey

Review of Tritium in Zircaloy Cladding from Light Water Reactors

Zircaloy® cladding makes up roughly 25% by mass of used nuclear fuel (UNF) in the United States. In the future, reprocessing may be the option of choice for disposition of UNF from light water reactors (LWRs). Treatment options for Zircaloy cladding include recycling to recover the significant cost of the zirconium and to eliminate the disposal costs associated with transuranic-contaminated Zircaloy. To design and operate the reprocessing plants in a safe and environmentally compliant manner, the quantity

and form of tritium in the UNF must be understood and its distribution among components of the UNF assembly must also be understood.

For Zircaloy-clad fuels from LWRs, the tritium produced from ternary fission and other sources is expected to be divided between the fuel where it is generated and the cladding. It has been previously documented that a fraction of the tritium produced in uranium oxide fuel from a LWR can migrate and become trapped in the cladding. If the fuel is dissolved without tritium pretreatment during reprocessing, this fraction of the tritium will remain bound to the cladding and reduce the rate at which the tritium accumulates in the aqueous streams within the plant. If tritium pretreatment is included in the flowsheet, at least a portion of the tritium in the cladding will be volatilized along with the tritium from the fuel meat. Tritium volatilized in the pretreatment process is recovered in the tritium pretreatment off-gas system.

The fraction of tritium in Zircaloy cladding from LWR UNF has been reported in the literature to range from 0–95%. Presently, the behavior of tritium in fuel rods and cladding is not fully understood. Since addressing the tritium in the cladding could be an important step in the development of treatment processes for cladding recycle and/or fuel recycle treatment processes, a study was undertaken to gain a better understanding of tritium in LWR Zircaloy-clad fuel rods as a function of burnup and fuel history (temperature, power, etc.) and how the tritium concentration varies within a single fuel pin due to variations in temperature profiles, heat rates, etc. Information on how tritium is released from the clad during heating and/or dissolution is also included.

Examination of the literature indicates that data characterizing tritium content of actual samples of Zircaloy-clad fuel rods and cladding irradiated in LWRs are rather sparse, and limited details were given on the related fuel history, making interpretation of the reported data difficult. The behavior of tritium in fuel rods and claddings is by no means fully understood, and the presently available data are scattered as shown in Figure 17 and Figure 18 [Robinson and Jubin, 2013].

Separations and Waste Forms
2013 Accomplishments Report

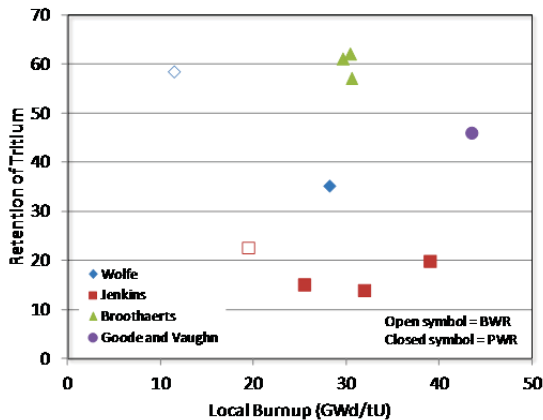


Figure 17. Tritium in Cladding as a Function of Local Burnup.

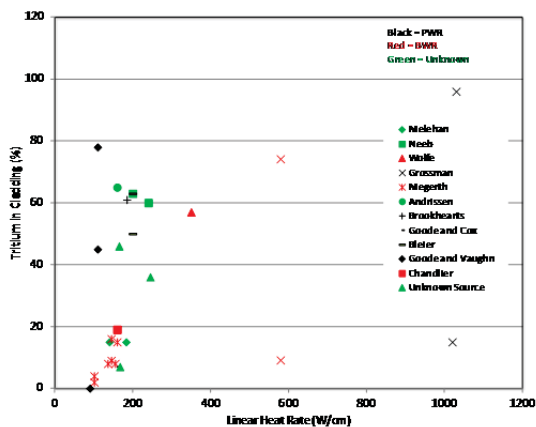


Figure 18. Tritium in Cladding as a Function of Linear Heat Rate.

The primary variables that are thought to impact tritium concentration in cladding are cladding temperature, linear heat rating (power density), burnup, and/or physical condition of the fuel rod or fuel pellets. Literature references indicated that the location of samples along the length of a fuel rod and the analytical procedures used to determine the tritium content could significantly impact the measurement of tritium in the cladding. To obtain a better understanding of how tritium in cladding will behave during treatment processing, it is recommended that a more in-depth analysis of the existing literature data be performed to evaluate such variables as analytical procedures and physical condition of the fuel rods tested. In addition, it would be highly desirable to obtain additional experimental data using the latest analytical techniques available to fill in the gaps in existing data.

Laboratory-Scale Testing of Tritium Concentration in Hulls from Light Water Reactor Fuel Rods

The behavior of tritium in fuel rods and claddings is by no means fully understood, and the data reported in the literature are scattered and sometimes conflicting. The estimates of the percentage of tritium in the cladding typically ranged from 0–96%. In order to obtain a better understanding of how tritium in cladding will behave during processing, scoping tests are being performed to determine the tritium content of pre- and post-tritium pretreated cladding.

Initial test results for tritium in H. B. Robinson pressurized water reactor cladding indicates that the cladding that received no heat treatment had a tritium concentration of $\sim 5 \mu\text{Ci/g}$; heating at $500\text{--}600^\circ\text{C}$ for 24 hr removes approximately 65% of the tritium from the cladding.

The amount of tritium in the unheated sample was unexpectedly low. The literature indicates that the cladding from LWR can contain 0–95% of the tritium in the fuel rod, many researchers have reported seeing 30–50% of the tritium in the cladding [Robinson and Jubin, 2013]. Many of these references reported tritium concentrations in the cladding in the range of 100s of $\mu\text{Ci/g}$. A rough estimate of the total tritium that would be expected from a fuel rod with an average burn-up of 60–70 GWd/MTU cooled for 20 years is $\sim 1000 \mu\text{Ci/g}$. If only 10% of the tritium was in the cladding, it would have resulted in $\sim 100 \mu\text{Ci/g}$ in the unheated cladding.

Additional evaluations will be needed to address the unexpectedly low value of tritium in the original H. B. Robinson sample. Similar tests are presently being performed on Surry-2 cladding.

Iodine Capture Performance of Silver Exchanged Mordenite exposed to High levels of NO₂

One of the case studies included an advanced head-end unit operation that involved the use of high concentrations of NO_2 and elevated temperatures to remove tritium from the UNF. Initial studies of this head-end process also showed that significant fractions of iodine may be volatilized during the treatment of the UNF. The

Separations and Waste Forms
2013 Accomplishments Report

treatment process also included a recycle loop for the NO₂. If the iodine is released into the vapor phase it would be desirable to remove the iodine from the circulating NO₂ stream. One of the materials currently under evaluation for iodine removal is reduced silver substituted mordenite (Ag⁰Z). Previous studies have examined the effects of extended exposure of Ag⁰Z to both dry, humid air streams, and low levels of NO₂ (~2%). The aim of this study was to determine the effects of limited exposure (1 week to 1 month) to high levels of NO₂ vapor used in this process on the iodine capture capacity of exposed Ag⁰Z.

Iodine loading following exposure to NO₂ was determined by both using a thermogravimetric analyzer (TGA) and neutron activation analysis (NAA). Both the 1 week and 1 month sample showed very small weight gains (≤0.5 wt%). This represents an apparent 93% loss in capacity. However, should there be any residual NO₂ some additional loss may have occurred during the iodine loading process that would confound the results from the TGA. NAA of the 1 week exposed Ag⁰Z showed significantly higher iodine loading (~1.4%) but still very low compared to fresh Ag⁰Z. The 1 month NAA results are still pending.

Publication

1. Robinson, S. M., and R. T. Jubin (2013). "Review of Tritium in Zircaloy Cladding from Light Water Reactor," FCRD-SWF-2013-000288, U.S. Department of Energy, September.

Advanced TALSPEAK Process for Minor Actinide Separation

G. J. Lumetta, gregg.lumetta@pnnl.gov

Separating the lanthanide fission product elements from the minor actinide elements (Am and Cm) at an industrial scale is one of the most daunting challenges to fully closing the nuclear fuel cycle [Hudson, et al., 2013; Todd, 2010] Achieving this separation is necessary if the minor actinide elements are to be converted to short-lived or stable isotopes in fast reactors because of the relatively large neutron cross sections of the light lanthanide elements. Nearly all methods under investigation for separating the minor actinides from the lanthanides exploit the apparent

slightly softer character of the trivalent actinide ions compared to the trivalent lanthanide ions. Thus, ligands containing nitrogen or sulfur donors have received considerable attention [Hudson, et al., 2013; Ekberg, et al., 2008; Wang, et al., 2001; Law, et al. 2006]. The ligands can be deployed in either the organic phase (as extractant) or in the aqueous phase (as an actinide-holdback reagent) in liquid-liquid extraction systems.

The Full Recycle Case Study that was performed in FY 2013 identified the TALSPEAK process [Weaver and Kappelmann, 1968; Milsoon and Nash, 2007] as the primary candidate for separating the lanthanides from the minor actinides. The TALSPEAK process has previously been demonstrated at a laboratory scale to separate the minor actinides from the lanthanides.^[8] However, the Case Study also identified a variation of the TALSPEAK process for potential near-term insertion into the fuel recycle flowsheet. In this variant of TALSPEAK, the traditionally used extractant, HDEHP (Figure 19), is replaced with HEH[EHP] (Figure 19). Three key advantages of switching to the HEH[EHP] extractant were claimed: less dependence of the process performance on the aqueous solution pH, more predictable extraction behavior, and more rapid extraction kinetics [Braley, et al., 2012]. This variant of the TALSPEAK process is now referred to as *Advanced TALSPEAK*. In FY 2013, work was conducted at PNNL to characterize the process chemistry relevant to Advanced TALSPEAK so as to further evaluate whether this process should replace the conventional TALSPEAK process in the FCRD program's full recycle flowsheet.

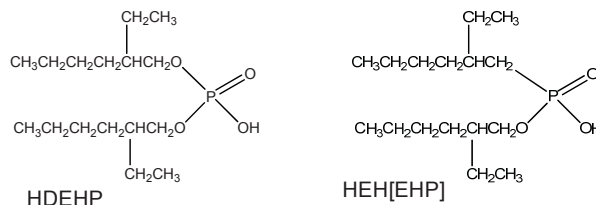


Figure 19. Chemical structures of the TALSPEAK (HDEHP) and Advanced TALSPEAK (HEH[EHP]) extractants.

Process Overview

The TALSPEAK and Advanced TALSPEAK processes operate by extracting the lanthanide ions

Separations and Waste Forms
2013 Accomplishments Report

into an aliphatic hydrocarbon phase containing HDEHP or HEH[EHP], respectively. A polyaminocarboxylate ligand is added to the aqueous phase to suppress the extraction of Am and Cm. In this case, the soft amine donor groups in the polyaminocarboxylate ligand preferentially bind the softer actinide ions, keeping them in the aqueous phase. A carboxylate buffer such as citric acid or lactic acid (Figure 20) is also added to the aqueous phase to control the solution pH. In the conventional TALSPEAK process, DTPA (Figure 20) is typically used as the actinide-holdback reagent. In the Advanced TALSPEAK process, a weaker aqueous-phase complexant is needed to allow adequate extraction of the lanthanides because of the weaker extraction power of HEH[EHP] compared to HDEHP. Hence, HEDTA (Figure 20) is used as the actinide-holdback reagent in the Advanced TALSPEAK process.

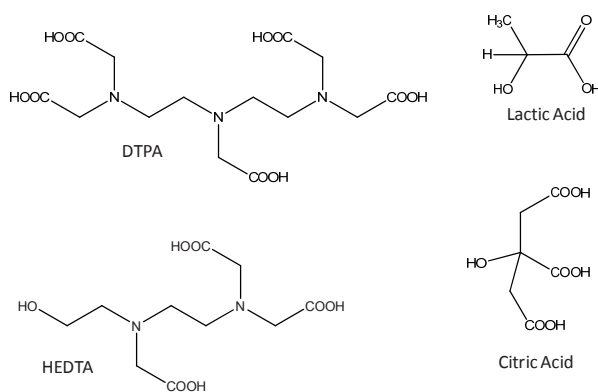


Figure 20. Chemical structures of the aqueous-phase complexants and buffers used in the TALSPEAK and Advanced TALSPEAK processes.

Objectives

The objective of this work was to generate the data required for designing and testing the Advanced TALSPEAK flowsheet. The first step was to determine an HEH[EHP] concentration that would serve as a basis for scale-up and testing of the process. Second, the composition of the aqueous phase was examined, including dependence on the HEDTA concentration, dependence on pH, and comparison of lactate and citrate buffers. Finally, equilibrium distribution measurements were made for Am and the relevant lanthanides.

Results

In FY 2013, an Advanced TALSPEAK solvent formulation consisting of 1.0 mol/L HEH[EHP] dissolved in *n*-dodecane was chosen for continued process development. Comparison of lactic acid to citric acid for use as the aqueous-phase buffer indicated that the extraction kinetics for the citrate system was faster, so citrate was chosen for subsequent studies. These experiments also revealed that the extraction kinetics slowed as the pH was increased; this trend was especially evident for the heavier lanthanides examined (Sm, Eu, and Gd). The nominal aqueous-phase conditions for the Advanced TALSPEAK process were established to be 0.125 mol/L HEDTA + 0.2 mol/L citrate buffer.

One of the major advantages of Advanced TALSPEAK, originally suggested by Braley et al. [Braley, et al., 2012], is its reported insensitivity to the aqueous solution pH relative to that seen for the conventional TALSPEAK process [Nilsson and Nash, 2007]. The team sought to verify this by examining the extraction of Am and the lanthanide ions relevant to fuel recycling (La through Gd, excluding Pm) as a function of the aqueous solution pH. The distribution ratios were measured in both the forward direction (metal ions initially in the aqueous phase) and the reverse direction (metal ions initially in the organic phase). Figure 21 presents the results of this study. As pH increases there is a trend of slight decrease in distribution ratio (D = ratio of a component's concentration in the organic phase to that in the aqueous phase), but the results show that the Advanced TALSPEAK process is less sensitive to pH than the conventional TALSPEAK process. For example, slopes of the best fit lines through the Nd and Am data in Figure 21 are approximately -0.25 , whereas the slopes for analogous TALSPEAK data from the literature are -2 [Svantesson, et al., 1979]. The separation factors ($SF = D_{Ln}/D_{Am}$) achieved are independent of pH above pH ~ 3 with the Nd/Am SF being approximately 20.

Separations and Waste Forms
2013 Accomplishments Report

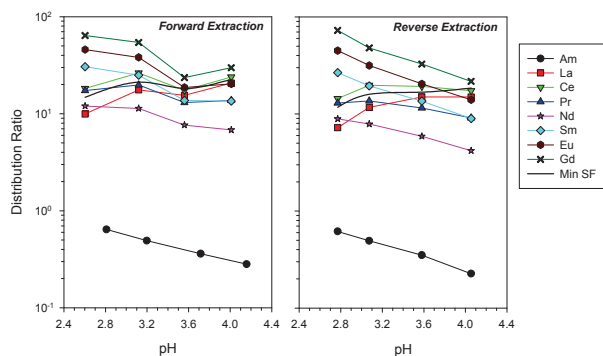


Figure 21. Extraction of Am and the lanthanides from 0.125 mol/L HEDTA + 0.2 mol/L citrate solutions with 1.0 mol/L HEH[EHP] in *n*-dodecane (left) and the corresponding reverse extraction into 0.125 mol/L HEDTA + 0.2 mol/L citrate solutions (right); SF (separation factor) = D_{Ln}/D_{Am} .

The data in Figure 21 show reasonable agreement between the distribution ratios measured in the forward and reverse directions. However, examination of the data obtained under other experimental conditions indicated wide scatter in the data for the reverse extractions, and the D values obtained in the reverse direction tended to be lower than those obtained in the forward direction. The reason for this observation is not yet clear. Since the Advanced TALSPEAK process is envisioned to operate only in the forward direction, the impact of this observation is expected to be minimal.

Conclusions

In this work, the team initiated a study of the process chemistry related to the Advanced TALSPEAK process. A solvent formulation consisting of 1.0 mol/L HEH[EHP] in *n*-dodecane, and an aqueous phase consisting of 0.125 mol/L HEDTA in a 0.2 mol/L citrate buffer, were chosen for further process development. The process should easily operate in the pH range of 3 to 4, although slow extraction kinetics is still a concern for the heavier lanthanides Sm, Eu, and Gd. Future work will examine single-stage extraction efficiencies using centrifugal contactors to get a more realistic indication of the separation factors that can be achieved with this process. This information can then be used to develop the AMUSE flowsheet model for the Advanced TALSPEAK process.

References

- Hudson, M. J., L. M. Harwood, D. M. Laventine, and F. W. Lewis (2013), "Use of Soft Heterocyclic N-Donor Ligands to Separate Actinides and Lanthanides." *Inorg. Chem.*, 52, 3414-3428.
- Todd, T. A. (2010). "Separations Research for Advanced Nuclear Fuel Cycles." In *Nuclear Energy and the Environment*, C. M Wai and B. J. Mincher, Eds; Washington, DC: American Chemical Society, pp 13-18.
- Ekberg, C., A. Fermvik, T. Retegan, G. Skarnemark, M. R. S. Foreman, M. J. Hudson, S. Englund, and M. Nilsson (2008). "An Overview and Historical Look Back at the Solvent Extraction using Nitrogen Donor Ligands to Extract and Separate An(III) From Ln(III)." *Radiochim. Acta*, 96, 225-233.
- Wang, X., Y. Zhu, and R. Jiao (2001). "Separation of Am from Macro Amount of Lanthanides by a Countercurrent Multistage Extraction with Purified Cyanex 301 and TBP." *Solvent Extr. Ion Exch.*, 19, 1007-1015.
- Law, J. D., D. R. Peterman, T. A. Todd, and R. D. Tillotson (2006). "Separation of Trivalent Actinides from Lanthanides in an Acetate Buffer Solution using Cyanex 301." *Radiochim. Acta*, 94, 261-266.
- Weaver, B., and F. A. Kappelmann (1968). "Preferential Extraction of Lanthanides Over Trivalent Actinides by Monoacidic Organophosphates from Carboxylic Acids and From Mixtures of Carboxylic Acids and Aminopolyacetic Acids." *J. Inorg. Nucl. Chem.*, 30, 263-272.
- Nilsson, M., and N. L. Nash (2007). "Review Article: A Review of the Development and Operational Characteristics of the TALSPEAK Process." *Solvent Extr. Ion Exch.*, 25, 665-701.
- Regalbuto, M. C. (2011). "Alternative Separation and Extraction: UREX+ Processes for Actinide and Targeted Fission Product Recovery." In *Advanced Separation Techniques for Nuclear Fuel Reprocessing and Radioactive Waste Treatment*, K. L. Nash

Separations and Waste Forms
2013 Accomplishments Report

- and G. J. Lumetta, Eds; Oxford: Woodhead Publishing, pp 176-200.
9. Braley, J. C., T. S. Grimes, and K. L. Nash (2012). "Alternatives to HDEHP and DTPA for Simplified TALSPEAK Separations." *Ind. Eng. Chem. Res.*, 51, 629-638.
10. Svantesson, I., I. Hangström, G. Persson, and J. O. Liljenzin (1979). "Separation of Americium and Neodymium by Selective Stripping and Subsequent Extraction with HDEHP Using DTPA-Lactic Acid Solution in a Closed Loop." *Radiochemical and Radioanalytical Letters*, 37, 215-222.

Separations and Waste Forms
2013 Accomplishments Report

This page intentionally left blank.

CHAPTER 4
DOMESTIC ELECTROCHEMICAL
SEPARATIONS TECHNOLOGY

CHAPTER 4: DOMESTIC ELECTROCHEMICAL SEPARATIONS TECHNOLOGY

M. A. Williamson, williamson@cmt.anl.gov

Solid Cathode Co-deposition Prototype Development

J. T. Willit, willit@anl.gov

With successful demonstration of U/TRU co-deposition at a solid cathode at the gram-scale, the emphasis this year was on the development of a kg-scale prototype unit for evaluating engineering aspects of U/TRU co-deposition. This versatile new electrorefiner prototype was designed with two types of cathodes with each having the appropriate anode-to-cathode area ratios for either U or U/TRU deposition where rare earths will be used as TRU simulants. With respect to the U-rare earth co-deposition cathode, the multiple planar anodes in the prototype provide a sufficiently high anode-to-cathode area ratio to achieve co-deposition at the U-rare earth cathode. With respect to uranium deposition cathodes, the anode-to-cathode area ratio is sufficiently low for the three pairs of cathode rods interleaved between the anode baskets that only uranium will deposit on them.

This prototype will be used to study the performance of a multi-electrode planar electrode electrorefiner for recovery of uranium metal while simultaneously recovering U-rare earth at the separate, specially designed co-deposition cathode.

Actinide and Lanthanide Drawdown by Electrolysis

J. T. Willit, willit@anl.gov

Electrolysis is a “back-end” process operation in the electrochemical process flowsheets for used LWR oxide and advanced reactor fuels. Electrolysis in a molten salt electrolyte has been used effectively for many years on an industrial scale for magnesium production. However, in the electrochemical recycling of used reactor fuels it has had considerably less study and development compared to “front-end” electrochemical process

operations such as electrorefining or electrolytic reduction. The focus of this project is to demonstrate the viability of electrolysis for removal (drawdown) of actinides and lanthanides from the rest of the molten salt matrix. In electrolysis, a sufficiently negative voltage is applied to the cathode to reduce the actinides and/or lanthanides to metals while chloride ions are oxidized to form chlorine gas at the anode. In the electrochemical flowsheet, the recovered actinides are later re-chlorinated and returned to the electrorefiner. The recovered lanthanides, on the other hand, are passed on to the ceramic wastefrom preparation step where they are mixed with zeolite, glass, and concentrated active metal fission product chlorides to form a durable ceramic wastefrom.

The extent of completion of electrolysis and selection of the metals that are reduced at the cathode is set by the cathode potential, and therefore it must be carefully monitored and controlled vs. a stable reference voltage. The value of the potential that needs to be applied in order to electrochemically separate two species depends on their thermodynamic properties, concentrations, salt conditions, etc.

Thus, the work this year involved developing an equilibrium electrochemical model to predict the extent of separation of actinides and lanthanides from the salt and determine the maximum possible degree of removal. The model was constructed using literature values for the formal redox potentials for the M^{+n}/M^0 reaction for the actinides and lanthanides. For a given applied cathode potential, the equilibrium concentrations of selected lanthanide or actinide cations can be determined using the formal potential of the species and the Nernst equation. A plot of equilibrium concentration (mole fraction) as a function of cathode potential is shown in Figure 22. The plotted lines show how the equilibrium concentration for a given species changes with cathode potential. The points on the lines are the predicted concentrations of a given

Separations and Waste Forms 2013 Accomplishments Report

species at steady state in the flowsheet before starting actinide drawdown by electrolysis.

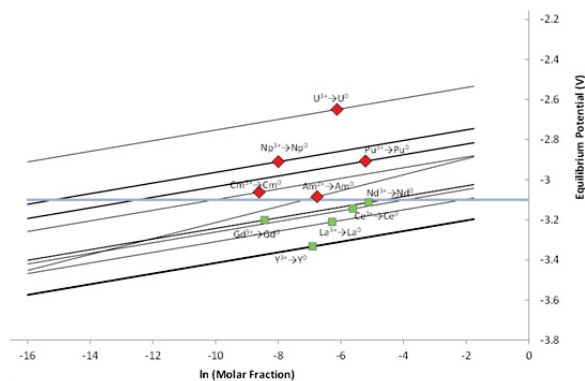


Figure 22. Equilibrium potentials as a function of natural log of molar fraction. Marked points are values calculated for the initial salt composition.

This model predicts that all of the lanthanides except samarium and europium can be recovered from the electrolyte during lanthanide drawdown. Samarium and europium could potentially be recovered along with the active metal fission products in a subsequent separation step. The model also predicts that a significant amount of the less stable lanthanide chlorides likely will be deposited along with the actinides during actinide drawdown. However, this prediction is extremely sensitive to the value used for the americium (Am) formal potential, the activity of Am in the cathode co-deposit, and the relative stability of the Am^{2+} and Am^{3+} species in the electrolyte under actual processing conditions. To more accurately predict the amount of lanthanides in the actinide drawdown product, better data for the chemical activity of Am in the co-deposit, the $\text{Am}^{2+}/\text{Am}^{3+}$ equilibrium, and the respective formal potentials is needed.

In addition to the modeling work, an electrolysis cell and chlorine scrubber was fabricated this year. The electrochemical cell design is a modification of a cell that was used for similar work in the past [Laplace, et al., 2008]. The primary crucible material in the new cell is graphite. The modified design uses multiple vertical anodes arranged around a central vertical cathode. Because the deposit is not expected to adhere to the vertical cathode, a beryllia crucible was attached to the bottom of the cathode assembly to retain the cathode deposit. This crucible sits directly beneath the cathode and is

separable from the rest of the assembly. This configuration makes it possible to quickly remove the cathode from the cell.

Electrolysis was proposed as the reference method for actinide and lanthanide recovery from the electrorefiner salt at the back end of the electrochemical flowsheets for both LWR oxide and advanced (metal) fast reactor fuels because it can potentially provide the needed separations, is scalable, and is used industrially. The modeling and preliminary tests conducted this year show that better characterized formal potential values are needed along with a determination of the activity of the depositing species, particularly for the species like Am and Np. If Am deposits at unit activity, it will be difficult to achieve an actinide electrolysis product with minimal lanthanide content. If however, the formal potential data contains errors or if Am rapidly forms a solution at the cathode, the likelihood of achieving minimal lanthanide content in the actinide electrolysis product is greatly increased. Future experimental work will address these questions.

Reference

1. Laplace, A. F., J. Lacquement, J. L. Willit, R. A. Finch, G. A. Fletcher, and M. A. Williamson (2008). "Electrodeposition of Uranium and Transuranics Metals (Pu) on Solid Cathode." *Nuclear Technology*, 163(3): 366-372.

Evaluation of Molybdate Melts for Used Fuel Treatment

J. T. Willit, willit@anl.gov

An alternative process studied last year [1] is based on the difference in solubility of most of the fission product metal oxides in a molybdate melt compared to UO_2 and PuO_2 . Uranium oxide containing fission products dissolves in molten molybdate salt at 1000–1200°C, where molybdenum trioxide serve as an oxidizer for the fission products that are in a metallic state. Uranium can be precipitated by lowering the temperature, while fission products remain dissolved in the molybdate melt. The very simple separation process is based on physical separation (filtration) of (U, Pu) from fission products that

Separations and Waste Forms
2013 Accomplishments Report

remain dissolved in the molybdate melt. Because there is no change in oxidation state of uranium or plutonium, it does not require use of any electrochemical equipment or chemical reductants/oxidants. Results on speciation of uranium in the presence of MoO₃ and Na₂MoO₄ salts and partitioning of selected fission products simulants were reported earlier [Tkac, et al., 2012].

This year's work focused on the partitioning of selected fission products in a molybdate melt containing 20% UO₂. Experiments were performed to look at partitioning of selected fission product between the molybdate melt and the uranium precipitate. Several compositions of salt were investigated to determine the optimum composition for best purification of a uranium product from selected fission product simulants. The partitioning of fission products (FP) between melt (liquid phase) and U product (solid phase) is defined by distribution ratio as follows:

$$D = \frac{FP_{melt}}{FP_{U\ product}} \cdot U(\%)$$

The amount of FP in the melt was determined as a difference between the initial quantity of FP metal and the quantity present in the U precipitate after dissolution. Since the recovery of uranium varied, yield of uranium was included in the distribution ratio. Thus, if low a U recovery was obtained, the reported D value was lower than actually measured because it was assumed that amount of uranium not recovered contained the same amount of fission products.

Distribution ratios for other fission products from the system containing 20% and 30% UO₂ were the best for molybdate melts containing 30% MoO₃. The data for the melt containing 30% MoO₃ are shown in Figure 23. In general, no significant difference in distribution ratios of selected fission products was observed for mixtures containing 20% or 30% UO₂. Therefore, 30% UO₂ loading allows processing more uranium without affecting the purity of the product. Slightly better D values for heavier lanthanides were observed for the system containing 20% UO₂. Higher D values for heavier lanthanides are observed when higher initial loading of MoO₃ was used. Thus, if further purification of U precipitate

from heavier lanthanides is necessary, washing with a molybdate salt containing MoO₃ may be beneficial.

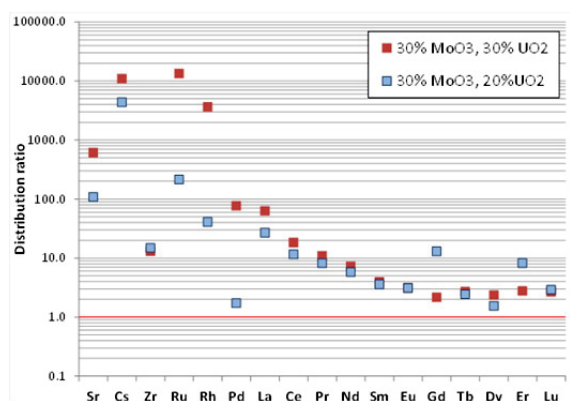


Figure 23. Distribution ratios of selected fission products between Mo melt (liquid phase) and U precipitate (solid phase) after one wash with ~30g of Na₂MoO₄ for different initial composition of UO₂, and Na₂MoO₄. The initial content of MoO₃ was kept constant at 30%.

Reference

1. Tkac, P., J. L. Willit, and M. A. Williamson (2012). "Evaluation of Molybdate Melts for Used Fuel Treatment, Argonne National Laboratory," FCRD-SWF-2012-000230, U.S. Department of Energy, September.

Molten Salt Extraction

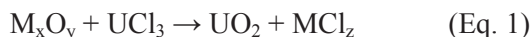
S. D. Herrmann, steven.herrmann@inl.gov

In the course of developing an electrochemical treatment process comprised of electrolytic reduction in LiCl-Li₂O at 650°C and electrorefining in LiCl-KCl-UCl₃ at 500°C for used uranium oxide fuels, the extraction of transuranic and reactive fission products from the fuels into the respective molten salt systems has been observed. Specifically, the extraction of alkali, alkaline earth, group 16, and group 17 fission products from used oxide fuel has been observed with and without an applied electric potential in LiCl-Li₂O at 650°C. The extraction of transuranic and lanthanide fission products from partially and fully reduced used oxide has been observed in subsequent uranium electrorefining operations in LiCl-KCl-UCl₃ at 500°C. However, the kinetics and mechanisms of such extractions has not been well understood. Thus, the objective of this study was to investigate the extraction of transuranic and reactive fission products from

Separations and Waste Forms
2013 Accomplishments Report

different forms of used uranium oxide fuels into LiCl-KCl-UCl₃ at 500°C.

The extraction of transuranic and reactive fission products from used uranium oxide fuel is based on the following general reaction mechanism,



where M represents transuranic and reactive fission product metals. Fission products that are nobler than uranium trichloride at 500°C (e.g., Zr, Mo, Ru, Pd, Tc, and Rh) are not expected to extract into the molten salt phase. Although the above reaction mechanism is thermodynamically favored, conditions may exist that impede the prescribed extractions. Thus, an experimental study was conducted to investigate these issues.

Three different forms of used oxide fuel were prepared for this laboratory-scale experimental study, including oxidized fast reactor fuel from Experimental Breeder Reactor (EBR)-II, LWR fuel from Belgium Reactor – 3 (BR3), and pretreated (i.e., exposed to oxygen bearing atmosphere at elevated temperature) BR3 fuel. Each was crushed, as necessary, and sieved to a particle size range of 0.045 to 0.6 mm. Each fuel form was loaded into a permeable steel basket and immersed in succession into a common pool of LiCl-KCl-UCl₃ at 500°C. Time-at-temperature salt samples were withdrawn at specified intervals after the immersion of each basket. At the end of each run, the fuel baskets were removed and placed in sealed storage containers. The three post-test fuel baskets were then collectively subjected to reduced pressure and elevated temperature to distill away salt adhering to the fuel. Post-test fuel samples were taken for analysis along with pre-test fuel samples and time-at-temperature salt samples to determine the rate and extent of transuranic and reactive fission product extraction from the oxide fuels to the prescribed molten salt. Figure 24 shows oxidized EBR-II and BR3 fuels following crushing and sieving.

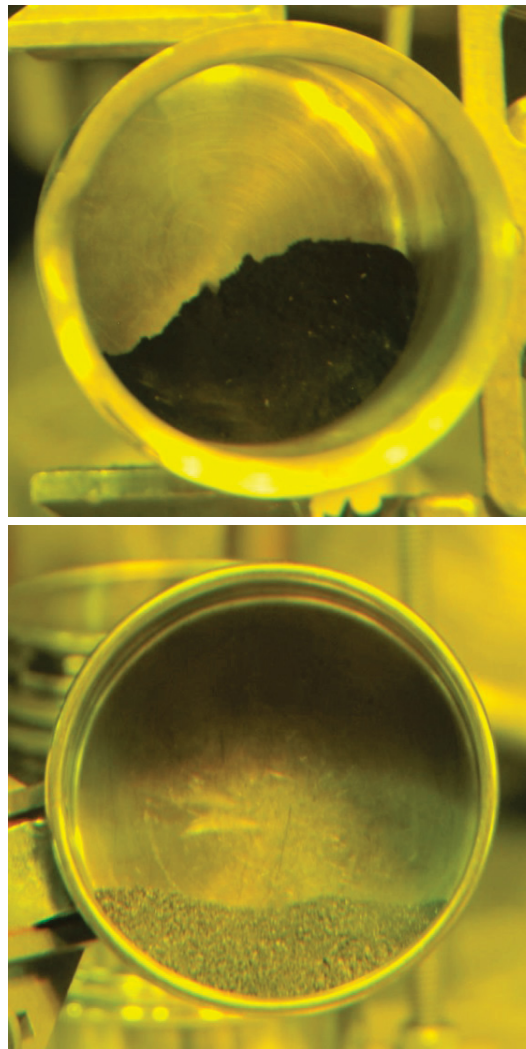


Figure 24. Crushed and sieved oxidized EBR-II (top) and BR3 (bottom) fuels used in molten salt extraction experiments.

Figure 25 (top) shows the Hot Fuel Dissolution Apparatus (HFDA), in which the molten salt extraction experiments were conducted. The salt distillation apparatus and accompanying furnace that were used to remove adhering salt from the fuel are also shown in Figure 25 (bottom). The molten salt extractions and salt distillation were conducted in a dry inert atmosphere hot cell at the Hot Fuel Examination Facility (HFEF).

Separations and Waste Forms
2013 Accomplishments Report

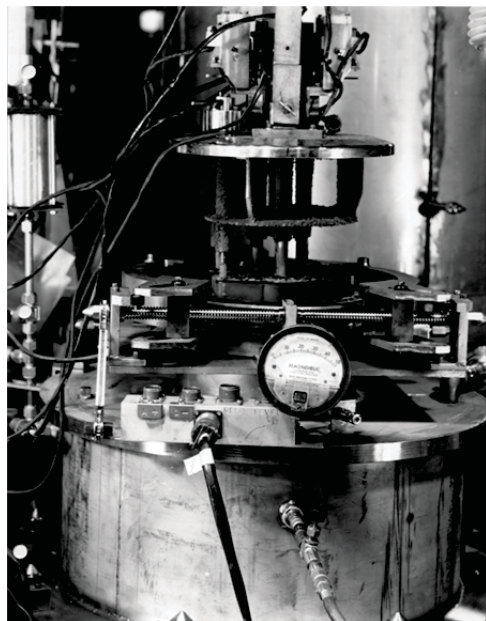


Figure 25. HFDA (top) and salt distillation apparatus/furnace (bottom) in the main cell of HFEF.

Salt and fuel samples from this experimental study will be subjected to ICP-OES, ICP-MS, and gamma spectroscopy. All sample analyses will be completed and reported in 2014.

Codeposition Lab-Scale Testing

G. Frederickson, guy.frederickson@inl.gov

During FY 2013, two different LiCl-KCl-based electrolytes were used to study the fundamental electrochemistry governing the cathodic codeposition of uranium and TRU from

molten chloride electrolytes onto a solid cathode. The first series of experiments were performed using an electrolyte that contained uranium and plutonium in chloride form as the species of interest, as well as several rare earth chlorides. These experiments were carried out in the HFDA located in an inert atmosphere hot cell at HFEF. The second series of experiments were performed in an inert atmosphere glovebox located in the Engineering Development Laboratory (EDL). Gadolinium and scandium were used as surrogates for plutonium and uranium respectively.

Four different electrochemical techniques were employed in the HFDA to study the system before and after U/TRU electrorefining activities. The U/TRU electrorefining was done using a liquid cadmium cathode (LCC). These LCC tests were performed as part of the Joint Fuel Cycle Studies' Laboratory-Scale Feasibility Study. The four techniques used were: constant deposition coulombs open circuit potential chronopotentiometry (CDCOCPC), constant deposition potential open circuit potential chronopotentiometry (CDPOCPC), constant deposition coulombs stripping chronoamperometry (CDCSC) and constant deposition time stripping chronoamperometry (CDTSC). Figure 26a shows a comparison of the CDCSC stripping cycle before LCC Test #1 and after LCC Test #2. The cycles shown are after a deposition using the onset potential for the reduction of plutonium. Figure 26b shows the CDCSC stripping cycles after a deposition using a potential slightly less negative than the onset potential for the reduction of rare earths. In both figures, the peak on the left corresponds to the oxidation of plutonium and the peak on the right to the oxidation of uranium. The peaks reflect the changes in plutonium and uranium concentrations in the electrolyte after two LCC tests. According to analytical results the plutonium concentration decreased as the uranium concentration increased.

Separations and Waste Forms
2013 Accomplishments Report

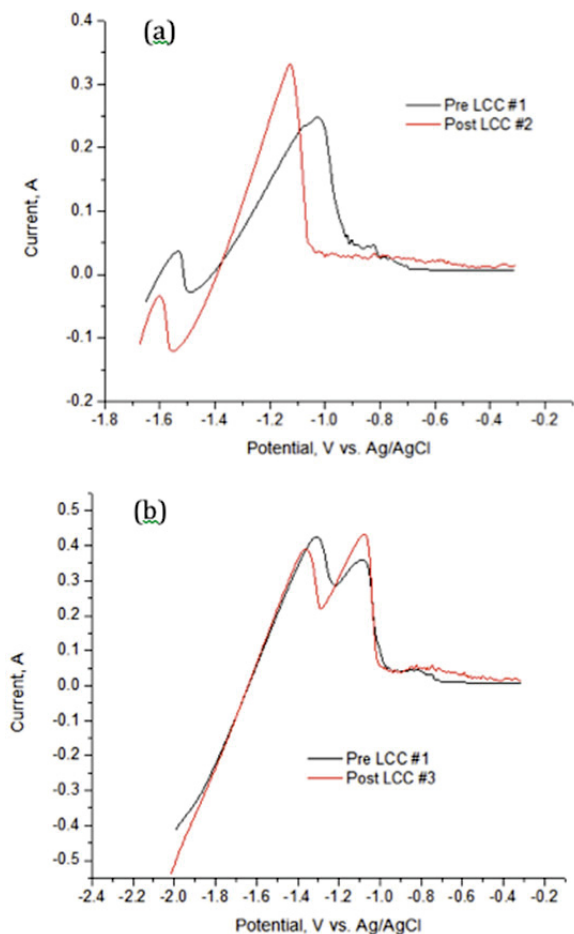


Figure 26. CDCSC stripping cycles

One of the advantages of working with surrogate systems in EDL is the ease of taking samples and handling them to perform chemical analyses. Figure 27 presents five different deposits collected using different deposition potentials. The deposits were analyzed via ICP-MS. The amount of gadolinium metal present in the deposit increased as the deposition potential became more negative. The open circuit potential (OCP) at the cathode was measured before the deposit samples were taken. Figure 28 shows a correlation between the OCP measured and the gadolinium content in the metal deposit. As expected, the gadolinium content in the deposit decreased as the OCP became less negative.


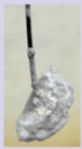



Test	1	2	3	4	5
Composition	No Gd	No Gd	12.7 wt% Gd	62.5 wt% Gd	74.2 wt% Gd
Morphology					

Figure 27. Gd/Sc deposits

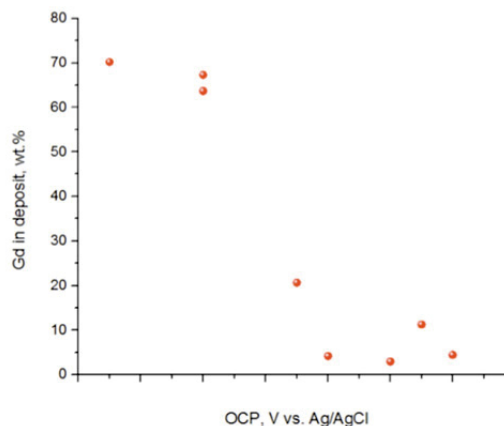


Figure 28. Correlation between gadolinium content in metal deposit and OCP measured

Ion Selective Ceramics for Waste Separations

E. Spoerke, edspoer@sandia.gov

In the course of the electrochemical process, spent nuclear fuel is introduced to a molten salt bath, where uranium is electrochemically dissolved and ultimately reductively replated and recaptured as pure uranium. Left behind in the molten salt electrolyte, however, are residual fission products, transuranics, and other contaminants that can degrade the electrochemical efficiency of the system and pose significant challenges to ultimate waste packaging and disposal.

The research program, “Ion Selective Ceramics for Waste Separations” is focused on developing ion-conducting ceramics that could be used to selectively, electrochemically filter target fission product waste from the molten salts used in electrochemical processing. In FY 2013, program objectives focused on investigating the feasibility of this concept, specifically exploring the segregation of cesium from molten LiCl-KCl eutectic electrolytes. This summary provides an overview of the technical approach proposed for

Separations and Waste Forms
2013 Accomplishments Report

this electrochemical separation, highlights the tailored synthesis of two target ion-conducting ceramics, and demonstrates the preliminary feasibility of the system for the segregation of target fission products from LiCl-KCl molten salts.

Figure 29 schematically illustrates how ion-selective ceramics would be used to electrochemically remove Cs⁺ from a LiCl-KCl molten salt.

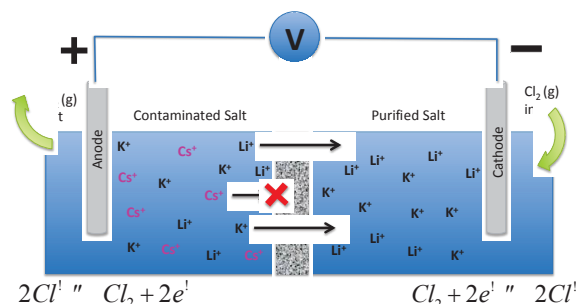


Figure 29. Scheme for electrochemical removal of Cs⁺ from LiCl-KCl molten salt. Chloride ions in the molten salt have been omitted for clarity.

In this scheme, Cs⁺-contaminated LiCl-KCl salt is placed opposite purified LiCl-KCl electrolyte, separated by an ion-selective solid state ceramic electrolyte. Under an applied electrical bias, Li⁺ and K⁺ ions are transported through the crystallographic lattice of the ceramic, ion-conducting membrane. Based on size-exclusion limitations to ion transport through these ceramics, larger Cs⁺ ions are effectively filtered and ultimately concentrated on the anode-side of the cell. Ultimately, the resulting heavily Cs⁺-enriched salt would be processed for disposal, but the volume of salt waste would be reduced. This approach takes specific advantage of the fact that the ionic radius of Cs⁺ is significantly larger than either Li⁺ or K⁺. ($r_{\text{Li}} = 0.090\text{\AA}$, $r_{\text{K}} = 1.52\text{\AA}$, $r_{\text{Cs}} = 1.81\text{\AA}$). To maintain charge balance on the anodic side of the cell, “excess” chloride ions in the molten salt will be electrochemically oxidized to form chlorine gas. Meanwhile, chlorine gas (Cl₂), ideally that produced at the anode, is bubbled into the cathode where it will be reduced to chloride ions, balancing the influx of K⁺ and Li⁺ coming through the ceramic membrane.

Naturally, the properties of the ceramic separator will strongly influence the effectiveness

of this approach. This ceramic material must serve as a stable physical barrier between contaminated and purified salts at 500°C, it must be resistant to radiation damage, it must be electrical insulating, and it must enable efficient, selective ion transport of Li⁺ and K⁺. Although a number of candidate ion-conducting materials were synthesized in FY 2013, this report will highlight the two candidate ion-conducting materials most extensively studied: KZr₂P₃O₁₂ (KSICON) and Li₆BaLa₂Ta₂O₁₂ (LBLTO).

KSICON is a K⁺-substituted derivative of the well-known sodium ion conductor NaSICON (Na Super Ion CONductor: NaZr₂P₃O₁₂). In the sodium-based model, atomically-defined channels within the crystal structure promote the rapid, selective transport of sodium ions, while preventing transport of larger ions or multivalent ions. In FY 2013, solid-state ceramic syntheses were developed to create the potassium-analog to NaSICON, forming a crystal structure with ion-transport channels designed to favor desirable K⁺ and Li⁺ transport, while excluding the transport of larger ions such as Cs⁺. The second ceramic material synthesized was based on a garnet-structured lithium lanthanum tantalate with the base composition Li₅La₃Ta₂O₁₂. This material is a known lithium ion-conductor, but substitution of Ba²⁺ ($r = 1.49\text{\AA}$) for La³⁺ ($r = 1.174\text{\AA}$) to create LBLTO produced a lattice expansion intended to facilitate transport of K⁺ as well as Li⁺. By tailoring the amount of Ba²⁺ added, it was possible to control the amount of lattice expansion in these materials, providing a handle to potentially tune ion-selectivity. Both of these materials were successfully synthesized, crystal structures were confirmed by x-ray diffraction (XRD), and they were formed into ceramic pellets for chemical stability and electrochemical characterization.

Both KSICON and LBLTO ceramics showed good chemical and structural stability against eutectic molten salts of KCl-LiCl (56-44 wt%) and KCl-LiCl-CsCl. (18-25-57 wt%). In addition, room temperature impedance spectroscopy (with blocking electrodes) indicated reasonable ionic conductivities in these materials ($\sim 3 \times 10^{-5}$ S/cm for LBLTO and 2×10^{-4} S/cm for in-grain KSICON). Collectively, these results motivated high temperature (500°C) electrochemical evaluation of

Separations and Waste Forms
2013 Accomplishments Report

selective ion transport through these ceramics in molten salts.

Ideally, these tests would have been conducted according to the scheme shown in Figure 29, in which charge balance is maintained through the oxidation and reduction of chlorine. While this is a potentially elegant, efficient, and self-contained approach to salt purification, the design and production of a system capable of safely managing chlorine chemistry at 500°C proved beyond the scope of the present effort. While the materials and processes needed for the chlorine chemistry are still under development, an alternative scheme was devised to more safely and immediately assess the selective ion-transport properties of the KSICON and LBLTO ceramics at 500°C. This alternative scheme utilized stacks of molten salt pellets separated by ceramic ion conductors, all sandwiched by a copper anode and a stainless steel cathode. A stainless steel current collector was also placed in contact with the copper anode. In this system, charge balance was maintained not through the oxidation and reduction of chlorine, but through the oxidation of copper metal at the anode and the reduction of copper at the cathode (Figure 30).

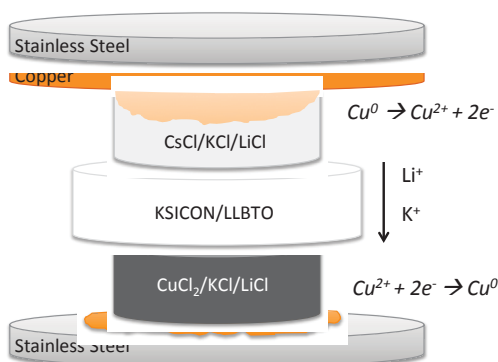


Figure 30. Schematic illustration of electroreduction of copper (left) or lithium (right) in a pellet stack using electrolyte binder pellets and an ion-conducting separator.

The assembly shown in Figure 30 is designed to mimic the configuration that would be used to remove Cs from a KCl-LiCl molten salt. The molten salt pellets used for this process were pressed from mixtures of target salts (Table 7) and an electrochemically inert, inorganic electrolyte binder that allowed the pellets to maintain their shape and integrity within the assembled testing

stacks at 500°C, even after melting of the molten salt.

Table 7. Compositions of electrolyte binder pellets used for electroreduction studies. All values are weight percents.

	LiCl	KCl	CsCl	CuCl ₂
LK-EB	44	56	0	0
CsLK-EB	40.1	48.7	11.2	0
CuLK-EB	32.7	41.6	0	25.7

The ion-transport properties of both KSICON and LBLTO ceramics were determined by galvanostatic electroreduction through these pellet stacks, heated to 500°C. Discharge curves generated during the cathodic electroreduction of Cu²⁺ at a current density of 100 mA/cm² using both LBLTO and KSICON ion-conductors are shown in Figure 31a. The discharge potential for the electroreduction of copper was a consistent 0.3V, and was similar for both LBLTO and KSICON, evidence of facile ion flow through these ceramics at the relatively high current density applied. The small overpotential (relative to 0V expected for the balanced oxidation and reduction of copper in this system) likely represents a small activation energy required to drive ionic transport across interfaces or through the ion-conducting ceramics.

The electroreduction resulted in macroscopic changes in the device structure, evidenced Figure 31b, which shows a photograph of a galvanostatic discharge cell, disassembled after the electroreduction of copper reduction using KSICON. (Similar results were observed for copper plating with LBLTO.) At the cathode, reduced copper plated visibly at the interface between the stainless steel cathodes and the CuLK-EB or LK-EB pellets. In addition, the copper anodes, originally disks, were etched into rings with the electrochemical dissolution of the anode into CsLK-EB pellets. Clearly, the anodic oxidation of Cu and the cathodic reduction of Cu²⁺, supported by ionic transport through the ceramic membranes, were remarkable efficient processes. With both the KSICON and LBLTO tests, the ceramic separators remained stable and intact. These macroscopic changes to the device structure during the discharge provide compelling evidence of the highly effective ion transport

Separations and Waste Forms
2013 Accomplishments Report

properties of these ceramics at 500°C. The significant ion mass transport through these ceramics, evidenced by the macroscopic changes to the test cells, provides promising insight into the feasibility of using these materials for molten salt purification.

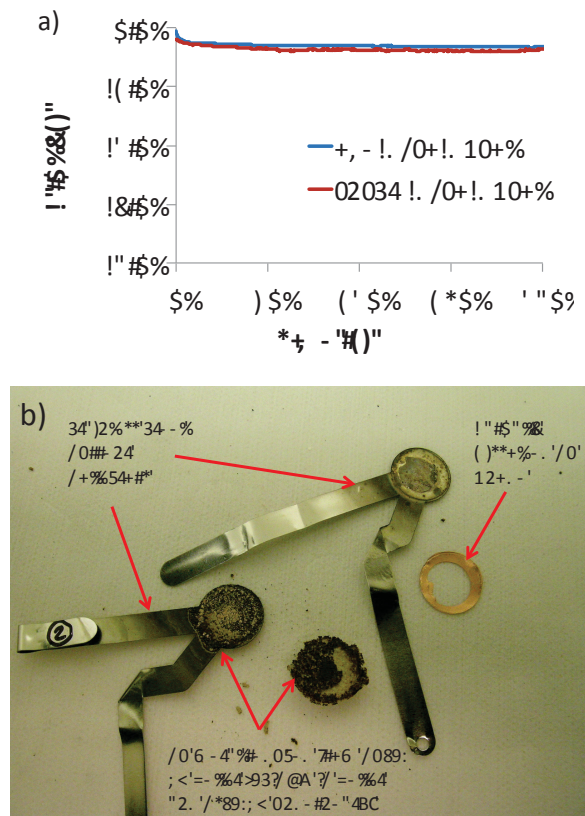


Figure 31. a) Galvanostatic discharge curves for the electroreduction of copper using KSICON (KZP) and LBLTO separators at 100°C. Curves were obtained at a constant current density of 100 mA/cm². b) Photograph of a dissected test cell showing dissolution of Cu anode and cathodic plating of Cu metal using a KSICON separator.

While the evidence in Figure 31 showed that ion transport through these ceramics was feasible, the energy dispersive x-ray spectroscopy (EDXS) data in Figure 32 provided additional, critical insight into the ion selectivity of KSICON and LBLTO during these galvanostatic discharge experiments. Figure 32 shows the EDXS spectra collected from molten salt pellet cross-sections (insets) after electroreduction of copper. The spectrum in Figure 32a was collected from the CsLK-EB pellet after discharge through a KSICON separator and shows evidence of the KCl salt (Li is not visible in EDXS), the CsCl salt, the

inorganic binder, and copper, confirming the dissolution of anodically oxidized copper into the pellet during discharge. The data in Figure 32b were collected from the CuLK-EB pellet in the same experiment. This spectrum shows expected peaks from KCl, residual CuCl₂, the inorganic binder, and a minor Fe contaminant believed to come from the stainless steel current collector. Critically, though, there is no evidence of Cs present, indicating that the Cs did not cross the ceramic separator in any measureable quantities. This important evidence of ionic selectivity during the electrochemical discharge was consistent when both KSICON and LBLTO membranes were used.

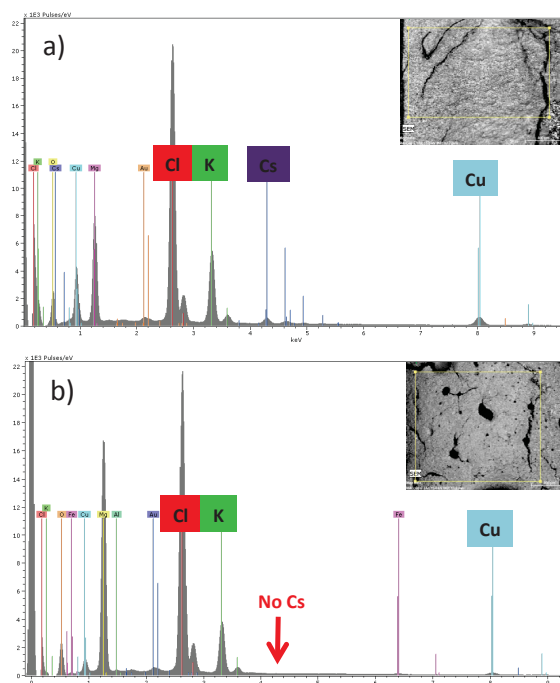


Figure 32. EDXS spectra and inset SEM micrographs from a) CsLK-EB and b) CuLK-EB pellet cross-sections after copper electroreduction at 500°C with a KSICON separator. The presence of Cu in the CsLK-EB pellet indicates solubility of the oxidized copper anode. Absence of Cs in the CuLK-EB pellet indicates ion transport selectivity against Cs⁺.

The primary purpose of the FY 2013 research described above was to establish the feasibility of using ion-selective ceramics to electrochemically remove contaminants such as Cs⁺ from LiCl-KCl molten salts. Several key FY 2013 highlights support the suitability of this approach:

1. Ion-conducting ceramics, KSICON and LBLTO, were successfully synthesized

Separations and Waste Forms
2013 Accomplishments Report

with crystal structures tailored to promote Li^+ and K^+ ion transport while inhibiting Cs^+ ion transport.

- Both KSICON and LBLTO demonstrated chemical and structural stability against LiCl-KCl molten salts up to 500°C .
- KSICON and LBLTO ceramics demonstrated meaningful ionic conductivity (particularly at elevated temperatures) of Li^+ and/or K^+ .
- Ion conducting ceramics demonstrated selectivity against Cs^+ transport, both under passive conditions and under DC bias at elevated temperatures (up to 500°C).
- The rapid, macroscopic dissolution of Cu metal anodes, and the cathodic plating of Cu metal during galvanostatic discharge experiments (at $100\text{mA}/\text{cm}^2$) indicate that this approach may be able to support meaningful mass transport needed to make this a scalable and viable salt purification approach.

Collectively these results support the conclusion that electrochemical purification of molten salts using ion-selective ceramics is feasible.

Fully realizing the potential of this system will involve continued characterization of the materials and ion transport phenomena. In addition, evaluation of the system's capacity and efficiency of waste separation will be enabled through the expansion beyond the small-scale "pellet stack" test cells to a bulk molten salt test configuration.

Publications

- Spoerke, E. D., J. Ihlefeld, J. S. Wheeler, M. A. Blea, K. Waldrip, and L. Johnson (2013). "Ion Selective Ceramics for Waste Separations: EOFY Project Assessment" Level 3 Milestone M3FT-13SN0311032, submitted to FCRD Management, September.
- Spoerke, E. D., J. Ihlefeld, J. S. Wheeler, and M. A. Blea (2013). "Ion Selective Ceramics for Waste Separations: Cumulative Summary of Ion Selective Results to Date" Level 4

Milestone: M4FT-13SN0311031, submitted to FCRD Management, April.

Sandia Technical Advance (IP)

- Spoerke, E. D., J. Ihlefeld, K. Waldrip, and J. S. Wheeler (2013). "Methods and Materials for Electrochemical Ion Separation." SNL SD# 12921, filed September.

Spectroelectrochemical Monitoring Under Electrochemical Processing Conditions

S. A. Bryan, sam.bryan@pnnl.gov, and W. R. Heineman, Univ. of Cincinnati

The overall objective of this task is to obtain the fundamental information needed for on-line, real-time, process spectroscopic instrumentation to be designed for use in monitoring and controlling fuel reprocessing flowsheets. The goal of this work is to establish quantitative optical detection of U, Pu, and Np in molten salt media to support electrochemical process monitoring under electrochemical processing conditions (LiCl/KCl eutectic, 500°C). Experiments are designed to demonstrate this ability using vis-NIR spectroscopy on molten salt systems. While the goal is to measure actinides in LiCl/KCl molten salt media, initial work was focused on molten salt systems and using lanthanide chlorides as non-radioactive surrogates for the actinides. The key results from the FY 2013 work are:

- Performed vis-NIR spectroscopy of various lanthanide chloride salts using single and multi-component mixtures of praseodymium, neodymium, samarium, holmium, erbium, and thulium in LiCl/CsCl molten salt matrix.
- Developed quantitative predictive models for spectroscopic process monitor application using PLS chemometric analysis for lanthanides in molten-salt media.
- Measured the electrochemistry and spectroelectrochemistry of EuCl_3 in four eutectic mixtures (LiCl/NaCl , LiCl/KCl , LiCl/RbCl , and LiCl/CsCl) under variable temperature conditions (643 K to 1173 K). This allowed the electrochemical properties,

Separations and Waste Forms
2013 Accomplishments Report

including redox potential, diffusion coefficients, Gibbs free energy, enthalpy and entropy for the $\text{Eu}^{2+/3+}$ redox couple, to be determined under electrochemical processing conditions.

Demonstration of Quantitative spectroscopic Measurement of Lanthanides under Pyroprocessing Conditions

This project has demonstrated the capability of vis-NIR for the quantitative measurement of lanthanides and actinides within a molten-salt media. This effort was initiated in FY 2012, and concluded in FY 2013. UV-vis spectroscopy was performed on single-component mixtures of six different lanthanide(III) chlorides within a LiCl/CsCl eutectic melt to obtain the dependence of their absorbance based on their concentration in solution and the value of each lanthanide's molar absorptivities for its various peaks.

In order to quantify lanthanides in complex mixtures, researchers initially obtained the UV-Vis spectra for six different lanthanides (erbium(III) chloride, holmium(III) chloride, neodymium(III) chloride, praseodymium(III) chloride, samarium(III) chloride and thulium(III) chloride) in single-component solutions at different concentrations (0 - ~120 mM) in the eutectic molten-salt $3\text{LiCl} - 2\text{CsCl}$ matrix. Beer's law analysis was performed by establishing the absorbance vs. concentration relationship for each lanthanide to determine the molar absorptivity of the peaks for each analyte. A series of multi-component mixtures were also prepared and measured using UV-Vis spectroscopy, and a multivariate regression model for each lanthanide was produced using both the single- and multi-component mixtures.

Figure 33A contains the plot of the molar absorptivity ($\text{M}^{-1}\text{cm}^{-1}$) vs. wavelength for six lanthanides ErCl_3 , HoCl_3 , NdCl_3 , PrCl_3 , SmCl_3 and TmCl_3 in $3\text{LiCl} - 2\text{CsCl}$ at 723 K. The combined data set containing the mixtures of single component and multiple-component mixtures were used to form predictive models for the series of six lanthanide chloride salts in this study. The PLS prediction vs measure concentrations for NdCl_3 , shown in Figure 33B, is representative of all the metals evaluated in molten salt media. The slope of the fitted line is

close to unity and an intercept value close to zero (slope = 1, and intercept = 0 is optimum). In addition, with few exceptions, the predicted values fall within the 95% confidence interval plotted in each figure.

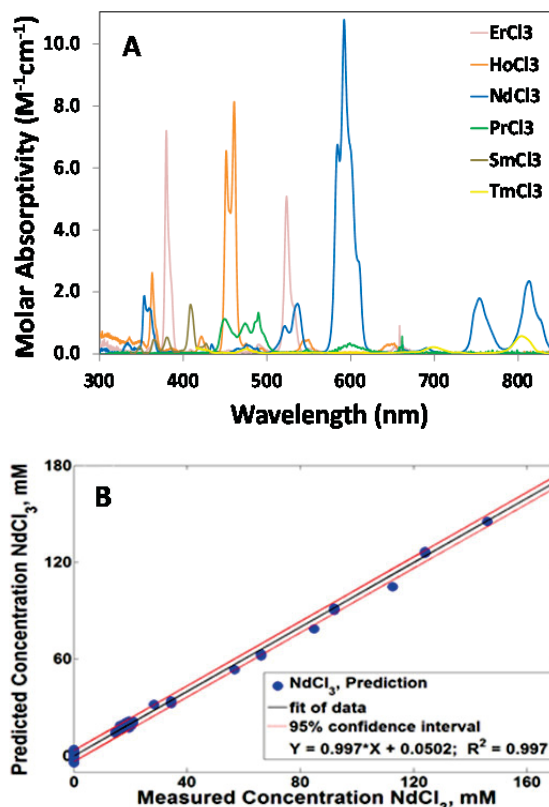


Figure 33. (A), Plot of the molar absorptivity ($\text{M}^{-1}\text{cm}^{-1}$) vs. wavelength (nm) for ErCl_3 , HoCl_3 , NdCl_3 , PrCl_3 , SmCl_3 and TmCl_3 in the $3\text{LiCl} - 2\text{CsCl}$ eutectic melt at 723 K; and (B), Graph of the PLS prediction for NdCl_3 .

Electrochemical and spectroelectrochemical Measurements of Selected Lanthanides in Molten Salt

The goal of this work is to enable the real-time spectroscopic analysis of lanthanides and actinides in molten-salt media under electrochemical processing conditions. In order to determine the various thermodynamic properties of the metal ion interaction in solution, researchers have studied the dependence within various eutectic melts, and at variable temperatures. These conditions include molten salts ranging from 500 K to 1173 K, under applied electrochemical potentials, enabling the availability of multiple metal redox states. In order to accomplish this, researchers have studied the

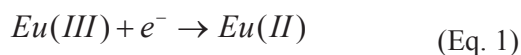
Separations and Waste Forms
2013 Accomplishments Report

combined spectroscopic and electrochemical behavior of $\text{Eu}^{2+/3+}$ as a model lanthanide ion.

Absorbance spectra, redox potentials and electron-transfer stoichiometries were determined by thin-layer spectroelectrochemistry. In the experimental technique, Eu^{3+} is converted to Eu^{2+} by a series of applied potentials so that the ratio of Eu^{3+} to Eu^{2+} in the thin-layer cell is varied according to the Nernst equation. Figure 34A shows the absorption spectra for EuCl_3 in the LiCl–KCl eutectic at 773 K when various potentials are applied. The spectrum with the least absorbance at 330 nm is at $E_{\text{app}} = -0.1$ V when europium is fully oxidized to Eu^{3+} , while the spectrum with the most absorbance at 330 nm is at $E_{\text{app}} = -0.7$ V is the fully reduced form, Eu^{2+} .

The plot of the E_{app} vs the $\log[\text{ox}]/[\text{red}]$ (Figure 34B) shows linearity according to the Nernst analysis (Nernst equation shown in inset to Figure 34B). The y -intercept indicates that the formal potential for $\text{Eu}^{3+/2+}$ is -0.34 V. The E° values for the $\text{Eu}^{3+/2+}$ couple were determined under variable temperatures between 643 K and 1173 K, and under various eutectic melts.

The effect of temperature on the redox potential of EuCl_3 was examined further in an effort to understand the trend and to predict the thermodynamic properties of EuCl_3 in the various eutectic melts. As the temperature of the melt was increased, a positive shift in the redox potential was observed. To understand the shift in redox potentials with increasing temperature, the Gibbs free energy for the reaction,



was calculated in each of the melts using the Gibbs free energy equation,

$$\Delta G_{\text{Eu}^{3+/2+}}^0 = -nFE_{\text{Eu}^{3+/2+}}^0 \quad (\text{Eq. 2})$$

where ΔG^0 is the standard Gibbs free energy of the reduction process.

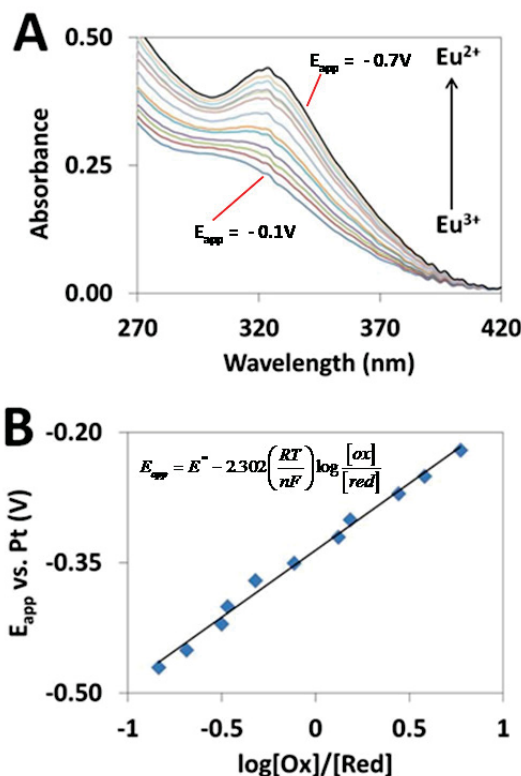


Figure 34. (A) Absorption spectra of EuCl_3 in LiCl–KCl eutectic mixture at 773 K, recorded as a function of increasing potential. (B) Nernst plot of the E_{app} vs. $\log [\text{Ox}]/[\text{Red}]$ at 325 nm (Nernst equation is inset within figure).

In using Equation 2, and measuring the redox potentials as a function of temperature, the Gibbs free energy values for the reduction of EuCl_3 was obtained as a function of temperature. In turn, the temperature dependence of the Gibbs free energy (ΔG°) allowed the determination of the enthalpy (ΔH°), entropy (ΔS°) of this redox reaction, according to the equation

$$\Delta G_{\text{Eu}^{3+/2+}}^0 = \Delta H_{\text{Eu}^{3+/2+}}^0 - T\Delta S_{\text{Eu}^{3+/2+}}^0 \quad (\text{Eq. 3})$$

The enthalpy (ΔH°) and entropy (ΔS°) of the system was determined for each eutectic melt, and is summarized within Table 8.

Separations and Waste Forms
2013 Accomplishments Report

Table 8. Values of Enthalpy, Entropy and Activation Energy of the $\text{Eu}^{3+/2+}$ Redox Couple for Various Eutectic Melt Compositions

Eutectic melt	$\Delta H^\circ_{\text{Eu}^{3+/2+}}$ (kJ mol ⁻¹)	$\Delta S^\circ_{\text{Eu}^{3+/2+}}$ (J K ⁻¹ mol ⁻¹)	E_a (kJ · mol ⁻¹)
LiCl - NaCl	-103	-48.4	55.0
LiCl - KCl	-127	-47.9	62.6
LiCl - RbCl	-138	-47.6	81.0
LiCl - CsCl	-137	-46.1	76.6

The general trend of a highly negative enthalpy term ($\Delta H^\circ_{\text{Eu}^{3+/2+}}$) and a large negative entropy term ($\Delta S^\circ_{\text{Eu}^{3+/2+}}$) for all the eutectics is consistent with Equation 1, where EuCl_3 changes coordination number from a six-coordinate octahedral complex to a nine-coordinate orthorhombic complex when reduced to europium(II).

Double potential step chronoabsorptometry (CA) was performed in EuCl_3 in 3LiCl – 2 KCl at 773 K to determine the diffusion coefficient for Eu^{3+} . Absorbance spectra were recorded over time, during both reduction and oxidation steps. Figure 35A shows the increase in absorbance at 330 nm upon lowering the potential to -0.7 V, indicating a reduction of Eu^{3+} to Eu^{2+} . After 40 s the applied potential was stepped to -0.1 V; which resulted in the oxidation of the electro-generated Eu^{2+} back to parent Eu^{3+} , as exemplified by the decrease in the absorbance at 330 nm.

The diffusion coefficient for Eu^{3+} was determined from the slope of the plot of absorbance versus the square root of time. Diffusion coefficients were similarly determined over the 643 K to 1173 K range, and under variable alkali chloride salt eutectic compositions (Li/Na, Li/K, Li/Rb, and Li/Cs). Figure 35B shows the plot of the log D of Eu^{3+} versus the inverse of the temperature and confirms that as the temperature increases, the diffusion rate of Eu^{3+} increases with the melt as expected.

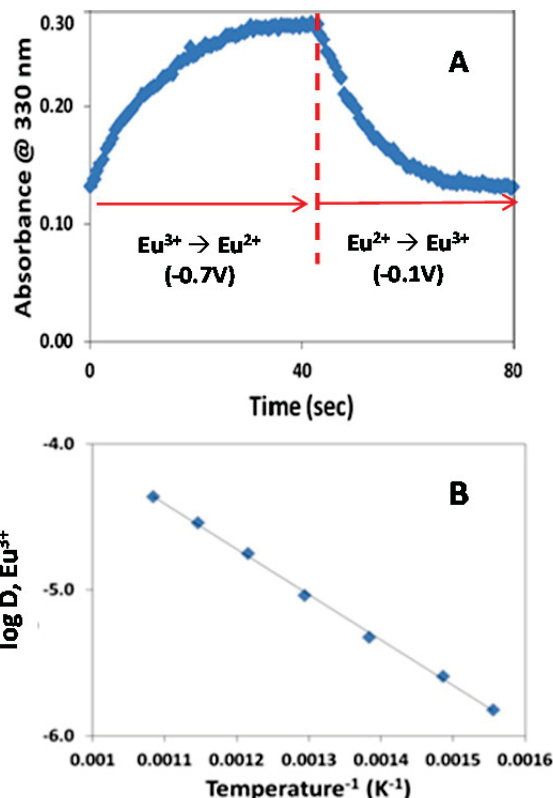


Figure 35. A: Double potential step chronoabsorptometry at 324 nm of 10.3 mM EuCl_3 in LiCl –KCl eutectic mixture at 773K. The potential was stepped from -0.1 V to -0.70 V for 40 s and then to of -0.10 V for 40 s. B: Graph of the log of the diffusion coefficients for EuCl_3 in LiCl– KCl as a function of temperatures.

The variation of diffusion coefficient with temperature can be related to the activation energy for diffusion, based on the Arrhenius equation,

$$-\frac{\log D}{1/T} = \frac{E_a}{2.303R} \quad (\text{Eq 4})$$

where D is the diffusion coefficient, T is the absolute temperature, R is the gas constant, and E_a is the activation energy. The activation energies have been calculated and are listed in 8. The measured values for the E_a term for these two techniques are in close agreement. The activation energy required for the diffusion of Eu^{3+} in molten salt eutectic media has been attributed to the “hopping” mechanism whereby the Eu^{3+} “hops” between vacancies within the molten salt matrix.

Separations and Waste Forms
2013 Accomplishments Report

Summary of Quantitative Spectroscopic Measurement of Lanthanides under Electrochemical Processing Conditions

UV-Vis spectroscopy was performed on six different lanthanide(III) chlorides in LiCl–CsCl. In the single-component solutions, researchers were able to determine the molar absorptivities of each of the lanthanide(III) chlorides. Researchers used the single- and multi-component mixtures to create multivariate regression models for use in prediction of lanthanide(III) chloride concentrations in unknown molten-salt solutions. The models had excellent linearity and the slopes were close to unity, indicating a nearly perfect model. These results indicate that UV-Vis absorbance spectroscopy, combined with the multivariate data analysis, is an appropriate method for the quantification of the lanthanide ions in the molten-salt media.

Using the spectroelectrochemical technique, researchers performed the first diffusion coefficient measurements of Eu^{3+} based on chronoabsorptometry, and showed with great precision, that it is a viable technique to use in molten salts. Researchers used cyclic voltammetry, differential pulse voltammetry and spectroelectrochemistry to obtain E° , $D_{\text{Eu}^{3+}}$, and n values for EuCl_3 over a temperature range of 500 K and have measured relevant thermodynamic

parameters extending the ability to develop quantitative spectroelectrochemical sensors for lanthanides and actinides in molten salt media.

Publication

1. Schroll, C. A., S. Chatterjee, T. G. Levitskaia, W. R. Heineman, and S. A. Bryan (2013). "Electrochemistry and Spectroelectrochemistry of Europium(III) chloride in 3 LiCl – 2 KCl from 643 K to 1123 K." I., accepted September 9. DOI: 10.1021/ac402518p.

Patent

1. Bryan, S. A., C. Schroll, W. Heineman, and S. D. Chatterjee (2011). "Method and Apparatus for Simultaneous Spectroelectrochemical Analysis". U.S. Patent and Trademark Office; Notice of Allowance issued for U.S. Patent Application Number 13/246,090, filed on September 27 (Notice of Allowance 2013).

Ph.D. Dissertation

1. Schroll, C. A. (2013). "Spectro-electrochemical Real-Time Monitoring of f-block Elements during Nuclear Fuel Reprocessing." Ph.D. Thesis, University of Cincinnati,

Separations and Waste Forms
2013 Accomplishments Report

This page intentionally left blank.

CHAPTER 5
SIGMA TEAM FOR MINOR ACTINIDE
SEPARATIONS

CHAPTER 5: SIGMA TEAM FOR MINOR ACTINIDE SEPARATIONS

B. A. Moyer, moyerba@ornl.gov

The Sigma Team for Minor Actinide Separation (STMAS) was formed at the beginning of FY 2009 with the overarching goal to lay the scientific basis for more efficient separation methods for americium and other minor actinides in order to greatly improve the overall benefit of fuel recycle. Specific aims of the STMAS as elaborated previously [Moyer, 2009, 2010] are to develop a robust, more efficient actinide/lanthanide (An/Ln) separation process and to develop an efficient separation of americium from curium, preferably as a single process. While the emphasis in the first years of the STMAS was focused on developing applicable science behind germinating technology concepts, the scope of the program has advanced to include the development of functional separations systems, testing, and bench-scale demonstration. Demonstration activities targeted to begin 2015 or later will employ simulated feeds using small-scale, continuous prototype equipment.

The above aims are being pursued mainly within the paradigm of aqueous reprocessing of used oxide nuclear fuel dissolved in nitric acid. Given that an array of previously matured separation technologies for minor actinide separations had been brought successfully through demonstrations in the context of the Uranium Extraction Plus (UREX+) suite of processes [Regalbuto, 2011; Gelis, 2009; Laidler, 2008], the overarching question now before us is not the feasibility of separating MAs, but rather the efficiency and economy with which these separations can be achieved toward a manageable and affordable fuel cycle. The magnitude of this problem will require unprecedented simplification and compaction of separations processes, preferably eliminating and combining steps. It is anticipated that this will entail new chemistry and likely altogether new separation agents.

Significance

The major long-term benefit of this research is expected to be a significant simplification of aqueous- reprocessing schemes that rely on the separation of MAs, leading to overall better economics and increased acceptability of nuclear fuel recycle. As recognized widely by the national and international scientific community [Salvatores, 2011; Tachimori, 2010; Hill, 2010; Boullis, 2008; Arm, 2008; Todd, 2006; Nash, 2006], the major benefit of minor actinide separation in general lies mainly in the reduced heat load on a repository, effectively increasing repository capacity. At the same time, the recycle of the recovered MAs provides additional energy utilization of the UNF, offsetting the cost of performing the separation. International arguments have stressed the reduced long-term radiotoxicity of the waste stored in geologic repositories, reducing the timeframe for storage.

As described in the Introduction, the STMAS has two aims, namely to develop

efficient An/Ln and Am/Cm separations. Given that an effective chemistry already exists for manipulating Np in contemporary solvent-extraction systems employing TBP, the need for Np separations research therefore seems relatively less urgent than the need for Am and Cm separations research. On the other hand, An/Ln or Am/Cm separations have been especially difficult because the chemistry of their common trivalent oxidation states is very similar. Although the team can point to significant progress, a fully satisfactory solution has not yet been found [Hill, 2010, 2011]. An efficient An/Ln separation is important because the lanthanides are strong thermal neutron absorbers and thus cannot be recycled in light-water reactor fuel, though fast-reactor fuel is more tolerant. A separation of Am from Cm has been viewed as a desirable process option [Laidler, 2008], as Cm presents difficulties in fuel fabrication due to the greater neutron shielding requirements, though this is not a universally agreed upon opinion [Arm, 2008].

Separations and Waste Forms
2013 Accomplishments Report

A clear need to simplify separations in fuel recycle is universally recognized. Although the successful demonstrations of UREX+ [Regalbuto, 2011; Gelis, 2009; Laidler 2008] increased overall confidence in the ability to reprocess used light-water reactor fuel at a commercial scale to meet a variety of potential objectives, the level of complexity and projected cost of deploying multiple process steps was unprecedented. Whether to separate the MAs in the first place and what types of streams the MAs are best suited to fuel fabrication or waste disposal must be a result of a comprehensive fuel-cycle systems analysis. While such guidance is being formulated, a chemical toolbox approach has been undertaken by STMAS under the philosophy that the chemical understanding in the context of potential separation methods will be available for exploitation as systems goals are more clearly defined. At the most fundamental level, the major product of STMAS effort is intended to be a family of chemical principles and corresponding test data enabling the design of efficient Am and Cm separation processes, one or more of which will be demonstrated at the laboratory scale.

Specific outcomes can be anticipated from achieving one or both of the STMAS aims. The most straightforward scenario dominant in STMAS strategy follows from within the UREX+ paradigm [Regalbuto, 2011] (or COEX™ [Herbst, 2011]) in which minor actinide separation must be performed on a highly acidic raffinate stream from which U, Pu, and Np have already been removed. A major advance by itself would be a one-step An/Ln separation [Hill, 2010, 2011; Lumetta, 2010a,b]. Two of the most selective solvent-extraction methods were incorporated into the framework of the UREX+ suite in the form of the TRUEX-TALSPEAK tandem processes or the TRUEX-Selective Actinide Extraction (SANEX) tandem processes using Cyanex® 301 as the SANEX extractant [Regalbuto, 2011].

Demonstrations showed a successful separation of Am and Cm from Ln using either technology. On the other hand, both approaches require two separate processes using disparate solvents and chemistries, and Cyanex® 301 is

unstable at practical nitric acid concentrations. Both technologies present major challenges in process control, that is, robustness. These challenges involve narrow processing envelopes, complex chemistry, empirical knowledge bases with limited understanding, reagent stability, voluminous effluent streams, and unknown impacts on downstream processes and waste disposition. Control of pH has been especially problematic for TALSPEAK and related systems employing aqueous-phase buffers and complexants, as distribution ratios are not constant over the expected operating range. Despite these already known challenges, the demonstrations of these technologies confirm the selectivity principles employed, which are outlined further below. Thus, appropriate extractants and aqueous-phase complexants can discriminate between An(III) and Ln(III), and a solution to developing a suitable technology should therefore be within the reach of research that can successfully address the major shortcomings. Given the evident challenge of the task, however, it is also clear that the prior understanding of extraction mechanisms and molecular behavior has been inadequate to generate the needed breakthrough. In the long term, a very attractive though ambitious minor actinide separation meeting both STMAS aims simultaneously would be one in which Am and Cm are separated together and split into separate streams, that is, a co-extraction followed by selective stripping. Potentially such a process could eliminate three separate processes in UREX+, with a high degree of potential UREX+ flowsheet simplification. If Pu and Np could also be co-extracted with Am and Cm followed by stripping of all, or certain combinations of, these actinides, the landscape of fuel recycle could be even further simplified.

Approach

Technical Strategy

As shown in Figure 36, dual strategies for Am separation are being pursued by STMAS based on either complexation or the higher oxidation states of Am. Complexation presents particular challenges in that the trivalent 4f and 5f elements have very similar bonding

Separations and Waste Forms
2013 Accomplishments Report

characteristics, dominated by electrostatics. For Am(III)/Cm(III) separations, the ionic radii differ very slightly, and these fall within the much wider size range of the lanthanides. Regarding the second strategy, the higher oxidation states of Am that can be exploited require aggressively high oxidation potentials and are unstable once formed [Runde, 2011].

Feed types: Dissolver solution; UREX (CoEX) raffinate; or TRUOX (DIAMEX) strip solution

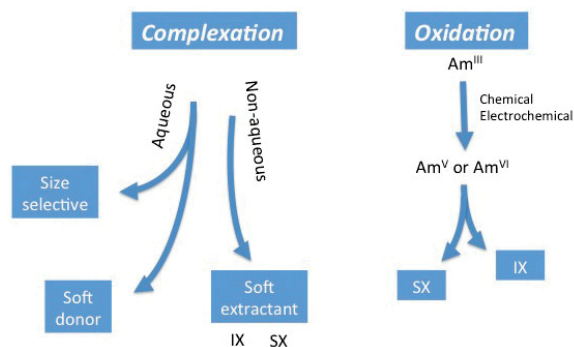


Figure 36. Strategies for achieving selectivity in two-phase separation systems and corresponding questions.

Both strategies can be used in either phase of a separation system. For example, by use of the extractant HDEHP, which is slightly selective for Ln(III), and addition of the An(III)-selective complexant DTPA to the aqueous phase, the Ln(III) are rendered significantly more extractable than An(III). This principle can be made to operate in an extraction of Ln(III) away from Am(III) (TALSPEAK) or in stripping Am(III) from extracted Ln(III) (reverse TALSPEAK). Alternatively, the actinide-selective complexant can be the extractant, as is the approach in the SANEX processes. One could employ the same ideas in the use of inorganic ion exchangers. For example, an inorganic exchanger with affinity for both An(III) and Ln(III) is used in the presence of an appropriate aqueous-phase complexant that has an affinity for An(III) vs Ln(III), such that only the Ln(III) are removed from the feed stream. Or the complexant can be added to the eluent after the combined uptake of Am(III) and Ln(III) to selectively desorb the Am(III). Complexation strategies can be sophisticated, taking advantage of subtle effects due to even small differences in ionic radii. Manipulation of the Am oxidation

state is in principle a powerful approach for a selective Am separation, either in the context of solvent extraction or ion exchange, but the very high oxidation potentials required for oxidation of Am(III) to Am(V) and Am(VI) [Runde, 2011] present a formidable challenge. Indeed, if this were not such a challenge, the two aims of the STMAS likely would have been preempted long ago.

The major questions being pursued within the dual strategy described above naturally sort themselves as follows:

1. Can aqueous complexation provide sufficient discrimination and operational control?
2. Can the higher oxidation states of americium be formed and stabilized for separation?
3. Can soft-donor extractants be made sufficiently robust and effective under desired conditions?
4. Does ion exchange have the selectivity and robustness to operate effectively?

In most cases, research inquiry focuses on obtaining the desired An/Ln or Am/Cm selectivity. However, in some cases, selectivity is often not so much in question as such issues as robustness, ability to operate under expected conditions, kinetics, etc. For example, ion-exchange materials have not been strong enough nor stable enough under acidic conditions, and soft-donor extractants like bis(dithiophosphinic) acids have presented stability issues of their own.

In general, pursuing the above strategy requires a team effort often involving more than one laboratory. Administratively, work packages are laboratory-centered. Nine principal investigators (PIs) from six national laboratories and one university were involved in addressing the above questions in FY 2013, as reported in the corresponding annual reports cited in the Sigma Team Publications and Reports section. The participants are listed in Table 1 together with the questions that their projects are primarily concerned with. It should be noted that each principal investigator leads a team of

Separations and Waste Forms
2013 Accomplishments Report

collaborators, some through subcontract, whose contributions are properly acknowledged in the corresponding annual reports. Questions are crosscutting, as shown in the middle column of Table 9. The composition of the STMAS was selected based on the experience of the PIs in conducting both basic and applied research, having demonstrated success in employing the results of basic research in technology development and in collaborating with engineers in scale-up and implementation. All specialize in separation science and technology, with backgrounds in solvent extraction, resin ion exchange, inorganic ion exchange, crystallization, and dissolution techniques.

Table 9. Participating Institutions and PIs in the Sigma Team for Minor Actinide Separations in FY 2013

Institution	Questions Addressed	Lead PI
Argonne National Laboratory (ANL)	#1	Mark P. Jensen
Argonne National Laboratory	#1, #4	Artem V. Gelis
Idaho National Laboratory (INL)	#2	Bruce J. Mincher
Idaho National Laboratory (INL)	#3	Dean R. Peterman
Los Alamos National Laboratory (LANL)	#1, #2,	George S. Goff
Oak Ridge National Laboratory (ORNL)	#1, #2, #3	Benjamin P. Hay
Oak Ridge National Laboratory (ORNL)	#3	Lætitia H. Delmou
Pacific Northwest National Laboratory (PNNL)	#1, #2	Gregg J. Lumetta
Savannah River National Laboratory (SRNL)	#1, #4	David T. Hobbs
Washington State University (WSU)	#1, #3	Kenneth L. Nash

Highlights of Research Progress

The reader is referred to the annual reports of individual principal investigators of the STMAS for a more complete account of research progress (See Sigma Team Publications and Reports section). Below are given summary reports on the Sigma Team's major accomplishments.

Aqueous Complexes for Americium-Curium Separation

M. P. Jensen, mjensen@anl.gov

Separating americium from curium could greatly simplify plans for recycling UNF, but the very similar chemistries of Am and Cm make their efficient separation quite difficult. To date, chemical separations of Am from Cm have relied either on selective oxidization of Am³⁺ to particularly unstable oxidation states, or on inefficient use of the very small size differences between the Am³⁺ and Cm³⁺ cations. The team is exploring a different way to separate Am and Cm using sterically constrained ligands that amplify the very small thermodynamic differences between Am³⁺ and Cm³⁺ complexes which arise from the slightly different radii of these two actinide ions. By pairing a sterically constrained crown ether ligand designed to selectively bind the larger Am³⁺ cation in the aqueous phase with an extractant that preferentially carries smaller cations such as Cm³⁺ into the organic phase, Am can be separated from Cm (and the lanthanides) in a limited number of solvent extraction stages without the difficult oxidation of Am³⁺. Combining the experimental measurements of Am, Cm, and lanthanide binding thermodynamics of a prototype sterically constrained ligand *N,N'*-bis[(6-carboxy-2-pyridyl)methyl]-4,13-diaza-18-crown-6 (BP18C6) with theoretical calculations of the strain energy in the complexes that were performed by the Sigma Team's Dr. Ben Hay, the team has discovered that the correlation between ligand strain and Am/Cm selectivity originally hypothesized by the team does indeed hold. Although the prototype ligand is already an efficient Am³⁺/Cm³⁺ separation agent, this critical insight into the modes of Am/Cm selectivity opens the way to rational and computationally guided design of still more efficient sterically constrained ligands. Further strain computations have already identified a modification to the prototype ligand that should increase selectivity for larger cations such as Am. Efforts to synthesize this molecule are underway.

Separations and Waste Forms
2013 Accomplishments Report

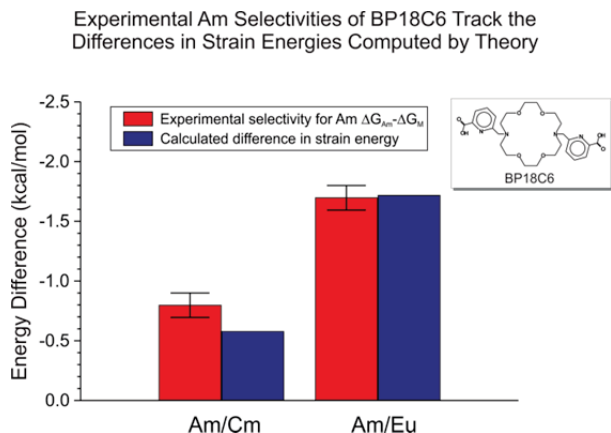


Figure 37. Agreement between calculated and experimental binding energy difference (selectivity) for complexation reactions of BP18C6 in 1 M NaNO₃ at T = 25 °C.

Advancing TALSPEAK Systems

K. L. Nash, knash@wsu.edu; G. J. Lumetta and S. Sinkov (PNNL)

Previous studies of the Advanced TALSPEAK Process established the potential utility of 2,6-dicarboxypyridine (dipicolinic acid, DPA) as an actinide-selective complexant. Preliminary tests indicated that DPA can enhance the actinide-lanthanide selectivity of the Advanced TALSPEAK process. Unfortunately, this powerful actinide-selective complexant suffers limited solubility in the acidic solutions needed for process-scale actinide-lanthanide separations. To overcome this limitation, the team has synthesized structural analogs of dipicolinic acid that exhibit dramatically increased solubility in acidic, aqueous media. The team has developed procedures to functionalize DPA at the 4-position on the pyridine ring in a fashion that allows tailoring of properties of the pyridine-dicarboxylate chelating agent. The team has successfully synthesized, purified, and characterized four new DPA derivatives, hydroxymethyl-DPA (HMDPA), quaternary methyl ammonium-DPA (QDPA), 4-morpholino-DPA (mor-DPA), and 4-methyl-piperidinyl-DPA (mPIP-DPA). Each derivative is 10–200 times more soluble than DPA in acidic solutions.

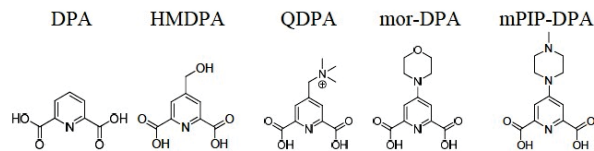


Figure 38. New DPA derivatives.

The direct-substituted derivatives mor-DPA and mPIP-DPA are significantly more acidic than the HMDPA and QBPA derivatives, as expected, a result that suggests further adjustments could result in greater tunability. Tests of the lanthanide-actinide selectivity in a TALSPEAK-like system (operating in more acidic conditions than conventional TALSPEAK) indicates group (Am/Nd) separation factors greater than 12 in a less than fully optimized set of experiments, as shown to the left. These reagents with tunable properties have promise for wide applicability in actinide-lanthanide separations. Further adjustments are planned.

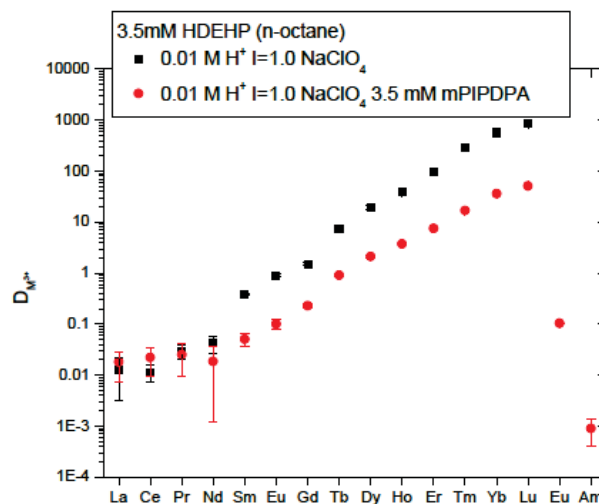


Figure 39. Effect of aqueous mPIPDPDA on the selectivity of lanthanide and americium extraction by HDEHP.

ALSEP Process Development for An/Ln Separation

G. J. Lumetta, gregg.lumetta@pnl.gov, and A. V. Guelis (ANL)

The Actinide-Lanthanide Separation (ALSEP) process combines an acidic extractant with a neutral chelating extractant to yield a single process for recovering the trivalent minor actinide elements (Am and Cm) from acidic

Separations and Waste Forms
2013 Accomplishments Report

high-level waste raffinate. This single process replaces two separate processes previously required to achieve this separation, thus significantly simplifying the closed fuel cycle concept. In the past year, the team has made significant progress in developing the process chemistry of the ALSEP system.

In FY 2013, ALSEP solvent systems consisting of TODGA or T2EHDGA and HEH[EHP] were investigated (see Figure 40).

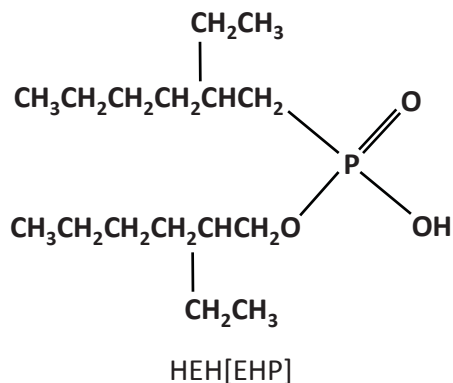
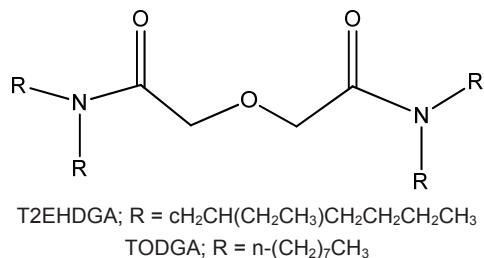


Figure 40. Neutral chelating extractants (left) and acidic extractant (right) used in the ALSEP process.

Although either TODGA or T2EHDGA could be used in the ALSEP process, the latter has been chosen as a reference case for further process development. The reason for this choice is that T2EHDGA is a slightly less powerful extractant than TODGA, resulting in weaker extraction of the light lanthanides. This can be exploited to achieve separation of La from the minor actinides in the extraction step of the process. In turn, this makes selective stripping of the minor actinides from the loaded solvent easier.

Figure 41 presents the distribution ratios for Am and the relevant lanthanide elements under both extraction conditions and minor-actinide

stripping conditions. For extraction, the aqueous solution consists of nitric acid media, as represented by the top of Figure 41.

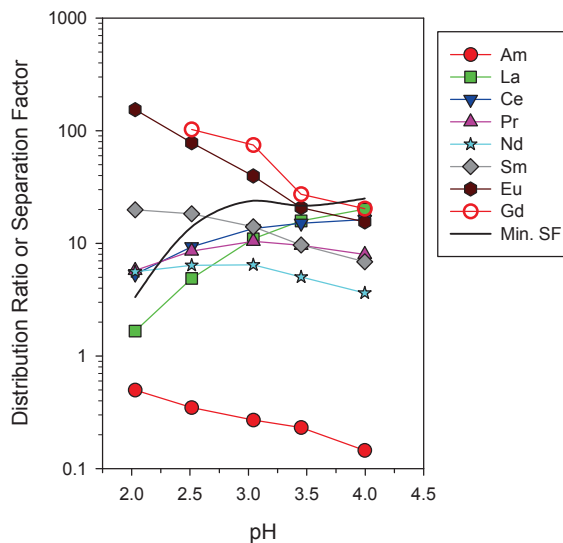
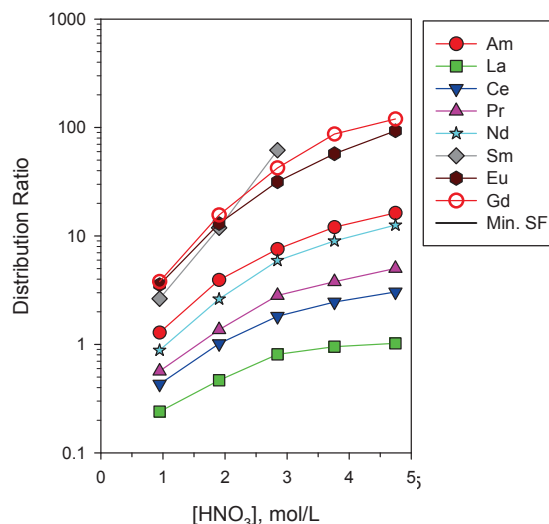


Figure 41. Extraction of Am and the lanthanides from nitric acid with 0.05 M T2EHDGA + 0.75 M HEH[EHP] in *n*-dodecane (top) and selective stripping of Am with 0.125 M HEDTA in 0.2 M citrate (bottom)

The Am and the Ln distribution ratios increase with increasing HNO₃ concentration. Maintaining high Am distribution ratios at several buffer solution (right); HEDTA = *N*-(2-hydroxyethyl)ethylenediamine-*N,N,N'*-triacetic acid; SF (separation factor) = D_{Ln}/D_{Am} molar HNO₃ is a desirable feature of the T2EHDGA-based ALSEP solvent. The La distribution ratio is less than 1 over most of the HNO₃

Separations and Waste Forms
2013 Accomplishments Report

concentration range examined, which is the basis for separating La from the minor actinides in the extraction step. To separate the minor actinides from the remaining Ln, the minor actinides are selectively stripped into a citrate-buffered aqueous solution containing a polyaminocarboxylate ligand. The data on the bottom of Figure 41 represents one such possibility. In this case, a 0.125 M HEDTA solution in a 0.2 M citrate buffer is used as the stripping reagent. The data show that efficient minor actinide stripping can be achieved (Am D values < 1), while retaining the Ln elements in the organic phase (Ln D values > 1). These results demonstrate the potential of the ALSEP process for greatly simplifying the separation steps needed to fully close the nuclear fuel cycle.

Mixed-Donor Extractants

B. P. Hay, haybp@ornl.gov, A. M. Panagopoulos, and B. A. Moyer

By combining an amide oxygen donor with heterocyclic nitrogen donor, it is possible to obtain a neutral chelating extractant that exhibits selectivity for An(III) over Ln(III). For example, picolinamides formed by attaching ortho $-C(=O)NHR$ groups to pyridine exhibit selectivity for Am(III) over Eu(III) on extraction from nitric acid solution into *t*-butylbenzene [Nigond, 1995]. Although picolinamides exhibit low D values, it was thought that by preorganizing the ligand architecture to provide a complementary arrangement of binding sites, it should be possible to achieve a much more potent mixed-donor extractant [Lumetta, 2002]. Synthesis and testing have confirmed that a preorganized analog of picolinamide, 1, results in an unprecedented factor of 10^8 increase in trivalent f-block metal extraction efficiency over a conventional picolinamide, 2. In addition to the exceptional D value, the potent extractant 1 exhibits an Am/Eu separation factor near 10.

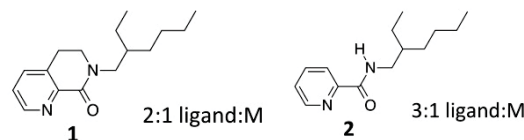
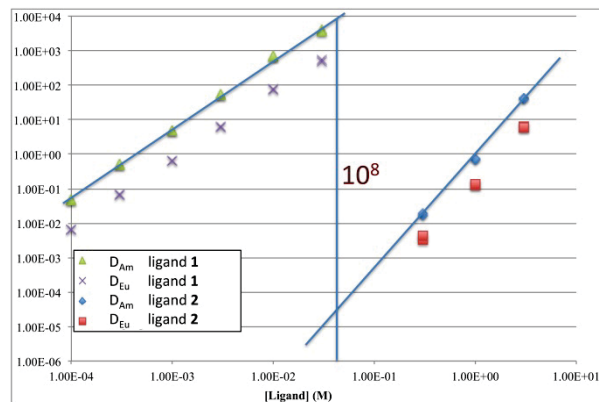


Figure 42. Preorganization of picolinamide extractant increases extraction efficiency by 8 orders of magnitude. Variation of the distribution ratios of Am(III) and Eu(III) as a function of the initial ligand concentration in 1,2 DCE. Aqueous phase: $[Eu(NO_3)_3] = 10^{-4}$ M, $[HNO_3] = 10^{-4}$ M, and $[LiNO_3] = 7.0$ M containing a spike of Am-241 and Eu-152/154. Slope analysis indicates a ligand:metal ratio of 2:1 for 1 and 3:1 for 2.

DPAH Flowsheet Concept for Minor Actinide Separations

D. R. Peterman, dean.peterman@inl.gov; and P. R. Zalupski

A flowsheet concept for the selective separation of the minor actinides from the lanthanides in acidic media has been developed. The flowsheet concept is based on the dithiophosphinic acid (DPAH) bis(trifluoromethyl)phenyldithiophosphinic acid, “0” extractant (developed at INL), and the neutral oxygen-containing synergist tri-*n*-octylphosphine oxide (TOPO). It is assumed that this process would follow a separation process, such as COEX™ or UREX, in which the uranium and plutonium are separated from the used fuel. In the case of UREX processing, the resulting feed composition would contain approximately 0.75M HNO_3 . For COEX™ processing, the raffinate would contain a much higher HNO_3 concentration, requiring a reduction in the HNO_3 concentration prior to processing. Reduction to a maximum of 1.0 M HNO_3 would be required to design an efficient

Separations and Waste Forms
2013 Accomplishments Report

process for the separation of actinides from lanthanide based on the proposed concept.

Experiments were performed in order to measure the extraction, scrub, strip, and wash distribution ratios, D_M , values needed for development of a flowsheet concept. Typical values of D_M for the extraction of americium and europium determined using 0.5 M “0” + 0.1 M TOPO dissolved in mesitylene as a function of aqueous phase acidity are shown in Figure 43.

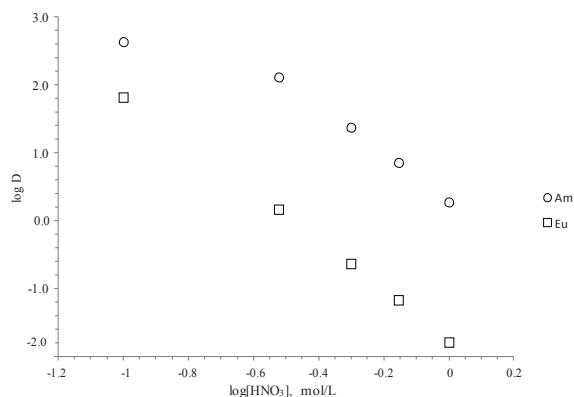


Figure 43. Distribution ratios for the extraction of americium (open circles) and europium (open squares) by 0.5 M “0” + 0.1 M TOPO dissolved in mesitylene as a function nitric acid concentration.

Based upon a goal of 99% separation of the actinides from lanthanides, the flowsheet was designed to achieve one order of magnitude greater separation (99.9%). In addition, less than 1% contamination of the actinide product with lanthanides was targeted. Assuming a UREX-like raffinate contains 0.75 M HNO₃, flowsheet calculations demonstrated that the targeted minor actinide separation is achievable using the INL DPAH solvent.

Separation of Americium from Curium and Trivalent Lanthanides Using Bis-triazinyl Pyridine Derivatives

L. H. Delmau (ORNL), K. N. Tevepaugh (ORNL/Tennessee Tech), D. D. Ensor (Tennessee Tech)

Neutral ligands are being investigated for the extraction of americium from curium and lanthanides at high acidity. Indeed, being able to extract americium from a feed that contains not only lanthanides, but also fission products and curium would be a great advantage over the numerous processes considered for potential

nuclear fuel reprocessing, processes that commonly address one type of separation (An/Ln, Am/Cm, etc.) at a time. While this is the ultimate goal, at the very least, selective actinide/lanthanide separation would lead to the replacement of TALSPEAK, with all the solution constraints associated with it. In either case, neutral ligands extract at high acidity and can be stripped at low acidity, in both cases thanks to a nitrate concentration swing. Therefore there is no need for complexing agents, unless a selective Am from Cm separation is required, which then could be envisioned using an aqueous ligand such as tetraethyl diglycolamide (TEDGA). As an alternative to aqueous complexants, a neutral ligand bearing two CMPO groups on a pyridine scaffold was tested and showed a decreased selectivity between americium and europium, but a definite enhancement of the americium/curium selectivity. Further investigations were conducted and showed that the combination of this neutral ligand (named NL157) and CA-BTP extracts in the following order: Cf > Cm > Am >> Eu, but this order seems to vary with the lanthanide loading.

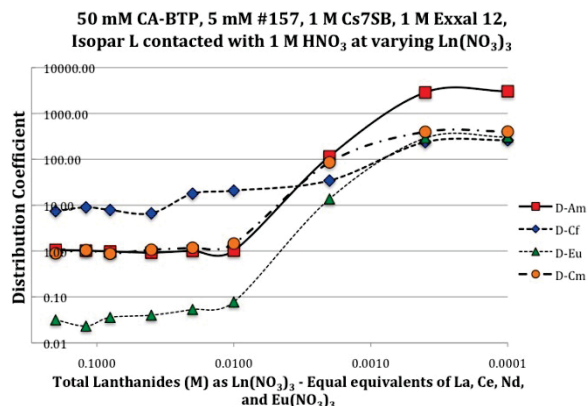


Figure 44. Results for Am, Cm, Cf, and Eu extraction from nitric acid.

Exploiting the Higher Oxidation States of Americium

B. J. Mincher, bruce.mincher@inl.gov

The 1 M diamylamylphosphonate (DAAP) distribution ratios for the Lns, Cm, and other constituents of dissolved fuel from a COEX™ raffinate simulant, under the conditions envisioned for the Am(VI) extraction were

Separations and Waste Forms
2013 Accomplishments Report

measured under both “natural” and bismuthate-oxidized conditions (Figure 45). With the exception of Ce, the Lns and Cm were not oxidized under the conditions that lead to the oxidation and extraction of Am. Separation factors ($\alpha_{Am/M(III)}$) ranged from ~800 for La to ~80 for Cm, to ~44 for Eu. These separation factors assume D_{Am} of 4, a value achieved in batch contact tests. However, the efficiency of Am extraction depends on the oxidation yield of Am(VI), and its persistence depends on the presence of trace reducing agents, the presence of residual Bi(V), and the contact time with the organic solvent. These data were used to revise the proposed bismuthate oxidation-process flowsheet. Based on that flowsheet, a cold test was performed to demonstrate the DAAP single-stage extraction and stripping of oxidized Ce. This Ce/bismuthate slurry was then easily filtered using a cross-flow filter and the bismuthate-free permeate was introduced into a 5-cm centrifugal contactor for the extraction. The overall Ce extracted was only 70% using 0.25 M DAAP, possibly due to cerium reduction on the high-surface area iron filter. The loaded solvent was next subjected to a strip designed to back-extract Am, and finally, a strip for cerium. The test successfully showed that bismuthate filtration is practical, that Ce is extracted and stripped as expected. However, a non-reducing filter medium will be required for a successful Am hot test.

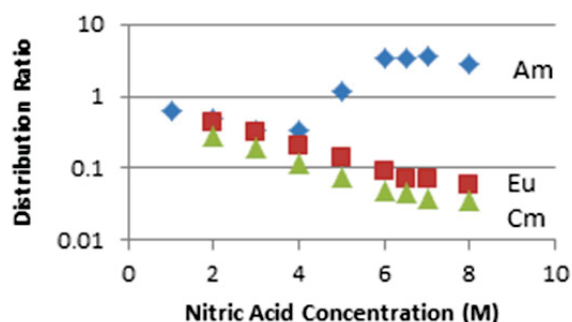


Figure 45. The solvent extraction of Am, Eu and Cm from bismuthate-treated COEX raffinate simulant using DAAP.

With an eye toward replacing chemical oxidants, electrochemical manganese studies are being performed at the University of North Carolina (UNC) at Chapel Hill. Manganese and

americium have similarities in their electrochemical behavior in that a one-electron transfer step must be bypassed to obtain higher valence states. Through the use of ruthenium-containing phosphonate complexes anchored to indium-tin oxide carbon electrodes, the UNC group has shown preliminary results in which bulk electrolysis has generated permanganate (Mn(VII)) from Mn(II).

Oxidation of Am(III) with Cu(III) Periodate

S. I. Sinkov and G. J. Lumetta

Separation of trivalent Am from other trivalent f-block elements, such as Cm and the lanthanides (Ln), is difficult to achieve because of the similarity in the chemistries of these species. One strategy for separating Am is to convert it from its common +3 oxidation state to a higher oxidation state, such as +5 or +6. The chemistries of Am(V) and Am(VI) are very different from that of Cm(III) and Ln(III), and this fact can be exploited to devise schemes for separating Am. The team has been investigating aqueous-soluble oxidizing agents for converting Am(III) to Am(VI) under acidic conditions relevant to reprocessing of irradiated fuels. One particularly interesting oxidant is copper(III) periodate, $KNa_4Cu(HIO_6)_2 \cdot xH_2O$ (Figure 46).



Figure 46. Photograph of $KNa_4Cu(HIO_6)_2 \cdot xH_2O$ compound.

In FY 2013, a systematic study was conducted on the oxidative action of the copper(III) periodate compound towards Am(III). The extent of Am(III) oxidation to

Separations and Waste Forms
2013 Accomplishments Report

Am(VI) was investigated using a constant initial Cu(III)-to-Am(III) molar ratio of 10:1 and varying nitric acid concentration from 0.25 to 3.5 M. In the acidity range from 0.25 to 3 mol/L, greater than 98% of Am(III) was oxidized to Am(VI); however, at 3.5 mol/L HNO₃, the conversion to Am(VI) was only 80%. The 10:1 molar excess of Cu(III) to Am(III) corresponded to 3.33:1 stoichiometric excess of Cu(III) to Am(III). The team tested the oxidative action of NaBiO₃ on Am(III) at the same acidity (3.5M HNO₃) and the same stoichiometric excess of Bi(V) oxidant to Am(III) of 3.33:1. With the Bi(V) compound, the extent of Am(III) conversion to Am(VI) was only 19%, while with Cu(III) compound this value was found to be about 4 times higher under otherwise identical conditions. The decrease in the extent of Am(III) oxidation to Am(VI) with Cu(III) periodate at 3.5 M HNO₃ can be compensated for by applying a higher molar excess of the Cu(III) compound. The team found that by going from 10:1 molar ratio [80% conversion to Am(VI)] to 20:1 molar ratio the yield of Am(VI) can be increased to 98%.

Until this study, NaBiO₃ was considered the most effective reagent for converting Am(III) to Am(VI) in acidic media. But this compound has a serious disadvantage for practical application in separations because the solution of oxidized Am must remain in contact with solid NaBiO₃ to maintain the higher Am oxidation state. The presence of solids is incompatible with liquid-liquid extraction, or ion-exchange operations. Our results show that the Cu(III) periodate compound is a superior oxidant to NaBiO₃, yielding rapid conversion to Am(VI) in homogeneous acidic solution, and thus is an excellent candidate for further development of Am separation systems.

Catalyzed Oxidation of Am(III) to Am(VI) Using Ozone

G. S. Goff, L. Seaman, G. D. Jarvinen, and W. Runde

One of the primary drawbacks of using sodium bismuthate as an oxidant is its low solubility in nitric acid, which requires it to be used as a slurry. Since ozone by itself is an insufficient oxidant, the team performed

preliminary studies to identify homogeneous catalysts to promote ozone oxidation of Am(III). Catalyst X is a homogeneous catalyst, which is soluble in nitric acid. Tests with Catalyst X have shown that quantitative oxidation of Am(III) to Am(VI) can be achieved in 0.01 to 1 M HNO₃ solutions, and at least partial oxidation can be achieved in 3 M HNO₃ solutions. Oxidation rates appear to be slower at higher acid concentrations, with 96% oxidation after 3 hours in 0.01 M HNO₃ and 86% and 25% oxidation after 24 hours in 1 M and 3 M HNO₃, respectively. The UV-vis-NIR absorbance spectra show no evidence of either Am(IV) or Am(V) during the oxidation experiments. Figure 47 shows typical results for the oxidation of Am(III) in 1 M HNO₃.

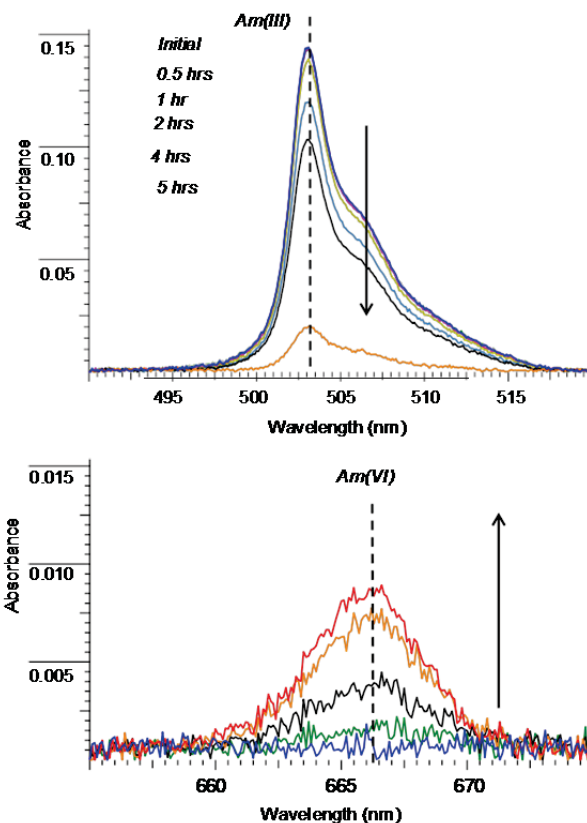


Figure 47. Ozone-catalyzed oxidation of Am(III) to Am(VI) in 1 M HNO₃ in the presence of Catalyst X.

Separations and Waste Forms
2013 Accomplishments Report

Minor Actinide and Lanthanide Separations by Ion Exchange

*D. T. Hobbs, david.hobbs@srnl.doe.gov; and
 A. Clearfield (Texas A&M)*

FY 2013 experimental work focused in the following areas: (1) investigating methods to oxidize americium in dilute nitric acid with subsequent ion-exchange performance measurements of ion exchangers with the oxidized americium and (2) synthesis, characterization and testing of ion-exchange materials. Americium oxidation testing sought to determine the influence that other redox active components may have on the oxidation of Am(III). Experimental findings indicated that Pu(IV) is oxidized to Pu(VI) by peroxydisulfate, but there are no indications that the presence of plutonium affects the rate or extent of americium oxidation at the concentrations of peroxydisulfate being used. Tests also explored the influence of nitrite on the oxidation of Am(III). Given the formation of Am(V) and Am(VI) in the presence of nitrite, it appears that nitrite is not a strong deterrent to the oxidation of Am(III), but may be limiting Am(VI) by quickly reducing Am(VI) to Am(V).

Three titanate ion exchangers were synthesized using a microwave-accelerated reaction system and determined to have high affinities for lanthanide ions in dilute nitric acid (see Table 10). The $\text{HK}_3\text{Ti}_4\text{O}_4(\text{SiO}_4)_3 \cdot 4\text{H}_2\text{O}$ (K-TSP) ion exchanger exhibited the highest affinity for lanthanides in dilute nitric acid solutions. The Ge-TSP ion exchanger also shows promise as a material with high affinity, but additional tests are needed to confirm the preliminary results. On the other hand, carbon nanotubes and nitrogen-doped carbon nanotubes exhibited low, but measureable affinities for lanthanide ions in dilute nitric acid solutions (pH 3 and 6). The multi-wall carbon nanotube (MWCNT) exhibited much lower affinities than the K-TSP in dilute nitric acid solutions. However, the MWCNT are much more chemically stable in concentrated nitric acid solutions and, therefore, may be candidates for chromatographic separations in more concentrated nitric acid solutions.

Table 10. Americium and Europium Distribution Values, K_d , (mL/g) for Potassium Titanosilicates (K-TSP) Prepared using a Microwave-Accelerated Reaction System and Commercially Available MWCNT Materials from pH 3 to pH 6.

pH	Average K_d for Am ³⁺ with K-TSP (mL/g)	Average K_d for Eu ³⁺ with K-TSP (mL/g)	K_d for Eu with Germanium Substituted K-TSP (mL/g)	Range of K_d Values for Eu ³⁺ with MWCNT (mL/g)
3	110	15	90	16-22
4	2300	280	--	--
5	4000	500	--	--
6	7500	300	--	15-33

Future Progress

In the coming two years, the Sigma Team will be moving toward a team milestone to demonstrate a laboratory-scale americium separation in 2015. While it remains to define the requirements of this milestone, it is anticipated that it will likely entail a demonstration flowsheet of Am separation with simulated feed using prototype small-scale engineering equipment. Based on the progress to date, three technology concepts are being considered as candidates for demonstration:

- *Advanced TALSPEAK*—Using a new combination of extractant and aqueous complexant(s), the emerging technology offers a flatter pH dependence and faster kinetics than the original TALSPEAK process. It will be developed further to formulate the solvent, investigate the extraction and stripping behavior of all metal species involved, and design an optimal flowsheet.
- *ALSEP*—By comparison to similar concepts promoted in other countries, ALSEP offers a flatter pH dependence, likely faster kinetics, and higher Am/Ln separation factors. Criteria for selecting the best combination of extractants will be established, followed by collection of the needed data, extractant selection, and flowsheet development. An option for a selective Am/Cm separation via a selective Am strip will be considered.

Separations and Waste Forms
2013 Accomplishments Report

- *Selective Am(VI) Extraction*—A suitable method of oxidation will be selected, and the appropriate flowsheet will be developed with an eye on the question of stability of Am(VI) under conditions of the extraction. A cross-flow filtration loop will be set up and tested to determine the feasibility of sodium bismuthate as a possible chemical oxidant.

While the maturation of the above technology concepts will require certain projects to incorporate an applied component to their work scope, the Sigma Team will maintain its science-based approach. Even as applied efforts proceed in the Sigma Team, projects will continue to seek understanding of the underlying chemical principles in hypothesis-driven inquiry: An understanding of the chemical and radiolytic stability of dithiophosphinic acid extractants will be sought, along with identifying conditions for extraction from molar nitric acid. Radiolytic stability of the higher oxidation states of Am will be characterized, and various chemical and electrochemical methods for Am oxidation will be investigated. Interactions between combined extractants in a single solvent system will be elucidated, and alternative combinations for ALSEP type separations will be pursued. The principles underlying selective Am(III) complexation vs Cm(III) remain to be fully revealed, and better complexants need to be developed. A dedicated effort to computationally design and test a new family of mixed-donor extractants for An/Ln separation will enter a phase of experimental testing of synthesized candidate compounds. Systems of interest overall will include mainly acidic media, especially nitric acid, and work on alkaline conditions will be phased out.

In summary, the Sigma Team will continue on its course of science-based inquiry according to its original aims to provide the scientific basis for An/Ln and Am/Cm separations. However, the needs of FCRD to begin to demonstrate emerging technology concepts has led to new priorities within the Sigma Team to mature its most promising candidate systems. This new orientation means addressing an additional set of questions related to developing working prototypes. While

pursuing such objectives, the Sigma Team will continue to consider altogether new ideas and alternative concepts.

References

1. Arm, S. T., C. Phillips, and A. Dobson (2008). "Industrial Application of GNEP Solvent-Extraction Processes." In *Solvent Extraction: Fundamentals to Industrial Applications. Proceedings of ISEC 2008 International Solvent Extraction Conference, Tucson, AZ, Sept. 15–19, 2008*. B. A. Moyer, , Ed. Montreal: The Canadian Institute of Mining, Metallurgy and Petroleum, Vol. 1, pp 709–714.
2. Boullis, B. (2008). "Future Nuclear Fuel Cycles: Prospects and Challenges. In *Solvent Extraction: Fundamentals to Industrial Applications.*" *Proceedings of ISEC 2008 International Solvent Extraction Conference; Tucson, AZ, Sept. 15–19, 2008*, B. A. Moyer, Ed. Montreal: The Canadian Institute of Mining, Metallurgy and Petroleum, Vol. 1, pp 29–41.
3. Carelli, M., F. Franceschini, E. Lahoda, and B. Petrovic (2011). "A Comprehensive Approach to Deal with the Nuclear Waste Problem." In *Proceedings of the WM2011 Conference*. Phoenix, AZ: American Nuclear Society, Paper 11452.
4. Gelis, A. V., G. F. Vandegrift, A. Bakel, D. L. Bowers, A. S. Hebden, C. Pereira, and M. Regalbuto (2009). "Extraction Behaviour of Actinides and Lanthanides in TALSPEAK, TRUEX and NPEX Processes of UREX+." *Radiochim. Acta* 97, 231–232.
5. Herbst, R. S., P. Baron, and M. Nilsson (2011). "Standard and Advanced Separation: PUREX Processes for Nuclear Fuel Reprocessing." In *Advanced Separation Techniques for Nuclear Fuel Reprocessing and Radioactive Waste Treatment*. K. L. Nash and G. J. Lumetta, Eds. Oxford: Woodhead Publishing, pp 141–175.
6. Hill, C. (2010). "Overview of Recent Advances in An(III)/Ln(III) Separation by Solvent Extraction." In *Ion Exchange and*

Separations and Waste Forms
2013 Accomplishments Report

- Solvent Extraction*, Vol. 19. B. A. Moyer, Ed. Philadelphia: Taylor and Francis Chap. 3.
7. Hill, C. (2011). "Development of Highly Selective Compounds for Solvent Extraction Processes: Partitioning and Transmutations of Long-Lived Radionuclides from Spent Nuclear Fuels." In *Advanced Separation Techniques for Nuclear Fuel Reprocessing and Radioactive Waste Treatment*. K. L. Nash and G. J. Lumetta, Eds. Oxford: Woodhead Publishing, pp 311–362.
 8. Laidler, J. J. (2008). "An Overview of Spent-Fuel Processing in the Global Nuclear-Energy Partnership." In *Solvent Extraction: Fundamentals to Industrial Applications. Proceedings of ISEC 2008 International Solvent Extraction Conference; Tucson, AZ, Sept. 15–19, 2008*. B. A. Moyer, Ed. Montreal: The Canadian Institute of Mining, Metallurgy and Petroleum; Vol. 1, pp. 695–701.
 9. Lumetta, G. J., B. M. Rapko, P. A. Garza, B. P. Hay, R. D. Gilbertson, T. J. R. Weakley, and J. E. Hutchison (2002). "Deliberate Design of Ligand Architecture Yields Dramatic Enhancement of Metal Ion Affinity." *J. Am. Chem. Soc., Comm. Ed.* 124, 5644–5645.
 10. Lumetta, G. J., J. C. Carter, A. V. Gelis, and G. F. Vandegrift (2010a). "Combining Octyl(Phenyl)-N,N-Diisobutyl-Carbamoyl methylphosphine Oxide and Bis-(2-Ethylhexyl)Phosphoric Acid Extractants for Recovering Transuranic Elements from Irradiated Nuclear Fuel." In *Nuclear Energy and the Environment Symposium*; ACS Symposium Series 1046, Washington, DC. Chap. 9, pp. 107–118.
 11. Lumetta, G. J., A. V. Gelis, and G. F. Vandegrift (2010b). "Review: Solvent Systems Combining Neutral and Acidic Extractants for Separating Trivalent Lanthanides from the Transuranic Elements." *Solvent Extr. Ion Exch.* 28(3), 287–312.
 12. Moyer, B. A. (2009). "Sigma Team for Minor Actinide Separation Annual Report." AFCl-SEPA-PMO-MI-DV-2009-000180, Oak Ridge National Laboratory, September 30.
 13. Moyer, B. A. (2010). "Sigma Team for Minor Actinide Separation FY2010 Annual Report." FCRD-SEPA-2010-000125, Oak Ridge National Laboratory, September 30.
 14. Nash, K. L., C. Madic, J. N. Mathur, and J. Lacquement (2006). "Actinide Separation Science and Technology." In *The Chemistry of the Actinide and Transactinide Elements*. 3rd ed. L. R. Morss, N. M. Edelstein, J. Fuger, and J. J. Katz, Eds.; Dordrecht: Springer. Vol. 4, Ch. 22, pp 2622–2798.
 15. Nigond, L., N. Condamines, P. Y. Cordie, J. Livet, C. Madic, C. Cuillerdier, C. Musikas, and M. J. Hudson (1995). "Recent Advances in the Treatment of Nuclear Wastes by the Use of Diamide and Picolinamide Extractants." *Sep. Sci. Tech.* 30, 2075–2099.
 16. OECD Nuclear Energy Agency (2010). "Actinide and Fission Product Partitioning and Transmutation, Tenth Information Exchange Meeting." Mito Japan, October 6–10, 2008. Paris, France: Organisation for Economic Cooperation and Development.
 17. OECD Nuclear Energy Agency (2012). "Actinide and Fission Product Partitioning and Transmutation, Eleventh Information Exchange Meeting." San Francisco, CA, USA, November 1–4, 2010. NEA No. 6996, ISBN 978-92-64-99174-3. Paris France: Organisation for Economic Cooperation and Development.
 18. Regalbuto, M. (2011). "Alternative Separation and Extraction: UREX+ Processes for Actinide and Targeted Fission Product Recovery." In *Advanced Separation Techniques for Nuclear Fuel Reprocessing and Radioactive Waste Treatment*; K. L. Nash and G. J. Lumetta, Eds. Oxford: Woodhead Publishing, pp 176–200.
 19. Runde, W. H., and B. J. Mincher (2011). "The Higher Oxidation States of Americium: Preparation, Characterization and Use for Separations." *Chem. Rev.* 111(9), 5723–5741; dx.doi.org/10.1021/cr100181f.

Separations and Waste Forms
2013 Accomplishments Report

20. Salvatores, M. and G. Palmiotti (2011). "Radioactive Waste Partitioning and Transmutation within Advanced Fuel Cycles: Achievements and Challenges." *Progr. Part. Nucl. Phys.* 66, 144–166.
21. Tachimori, S. and Y. Morita (2010). "Overview of Solvent Extraction Chemistry for Reprocessing." In *Ion Exchange and Solvent Extraction*, Vol. 19. B. A. Moyer, Ed. Philadelphia: Taylor and Francis, Chap. 1.
22. Todd, T. A., and R. A. Wigeland (2006). "Advanced Separation Technologies for Processing Spent Nuclear Fuel and the Potential Benefits to a Geologic Repository." In *Separations for the Nuclear Fuel Cycle in the 21st Century*. G. J. Lumetta, K. L. Nash, S. B. Clark, and J. I. Friese, Eds. Washington DC: American Chemical Society, Vol. 933, pp 41–55.
23. DOE (2010a). *Nuclear Energy Research and Development Roadmap, Report to Congress*. Washington, DC: U.S. Department of Energy, Office of Nuclear Energy, April.
24. DOE (2010b). "Research Objective 3 Implementation Plan: Developing Sustainable Fuel Cycle Options." FCRD-TIO-2011-000025, Washington DC: U.S. Department of Energy, Office of Nuclear Energy, December..
25. Wigeland, R. A., T. H. Bauer, T. H. Fanning, and E. E. Morris (2006). "Separations and Transmutation Criteria to Improve Utilization of a Geologic Repository." *Nucl. Technol.* 154, 95–106.
3. Braley, J. C., D. McAlister, E. P. Horwitz, and K. L. Nash (2013). "Explorations of TALSPEAK Chemistry in Extraction Chromatography: Comparisons of TTHA with DTPA and HDEHP with HEH[EHP]." *Solvent Extr. Ion Exch.* 31(2), 107–121.
4. Brigham, D. (2013). "Lanthanide-Polyaminopolycarboxylate Complexation Kinetics in High Lactate Media: Investigating the Aqueous Phase of TALSPEAK." Ph.D. Dissertation, Washington State University, May.
5. De Sahb, C., L. A. Watson, J. Nadas, and B. P. Hay, (2013). "Design Criteria for Polyazine Extractants to Separate An(III) from Ln(III)." *Inorg. Chem.*, submitted.
6. Delmau, L. H., K. N. Tevepaugh,, and M. E. Freiderich, (2013). "Trivalent Actinide-Lanthanide Separation Using Bis- Dithio Phosphinic Acids and Bis Triazinyl Pyridine Derivatives." FCRD-SWF-2013-000274. ak Ridge National Laboratory, August 30.
7. Freiderich, M. E., D. R. Peterman,, J. R. Klaehn, P. Marc, and L. H. Delmau (2013). "Chemical Degradation Studies on a Series of Dithiophosphinic Acids (DPAHs)." *Ind. Eng. Chem. Res.*, submitted.
8. Garn, T. G., J. D. Law, B. J. Mincher, M. Greenhalgh, and V. Rutledge (2013). "Ce oxidation, Filtration and Distribution in 0.25 M Diamylamylphosphonate." FCRD-SWF-2013-000365. Idaho National Laboratory.
9. Gelis A.V. (2013). "Actinide and Lanthanide Separation Process (ALSEP)." United States Patent 8354085, January 15.
10. Gelis, A. V. (2013). "Actinide-Lanthanide Separation—ALSEP—Process Zr Suppression." FCRD-SWF-2013-000091. Argonne National Laboratory, January 30.
11. Gelis, A. V. (2013). "ALSEP Annual Report." FCRD-SWF-2013-000364. Argonne National Laboratory, September.
12. Goff, G. S., L. Seaman, G. D. Jarvinen, and W. Runde (2013). "Sigma Team for Minor Actinide Separations: Determination of the Feasibility of Oxidation of Americium by

Publications

1. Alsobrook, A. N., and D. T. Hobbs (2013). "Ion Exchange Performance of Titanosilicates, Germanates and Carbon Nanotubes." FCRD-SWF-2013-000147 (SRNL-STI-2013-00234). Savannah River National Laboratory, April 24.
2. Braley, J. C., G. J. Lumetta, and J. C. Carter (2013). "Combining CMPO and HEH[EHP] for Separating Trivalent Lanthanides from the Transuranic Elements." *Solvent Extr. Ion Exch.*, published on-line March 25. DOI:10.1080/07366299.2013.785912.

Separations and Waste Forms
2013 Accomplishments Report

- Ozone in Nitric Acid.” FCRD-SWR-2013-000209, Los Alamos National Laboratory, June 28.
13. Goff, G. S., L. Seaman, G. D. Jarvinen, and W. Runde (2013). “Sigma Team for Minor Actinide Separations: LANL FY2013 Annual Report.” FCRD-SWR-2013-000367. Los Alamos National Laboratory, September 20.
 14. Grimes, T. S., and K. L. Nash (2013). “Acid Dissociation Constants and Rare Earth Stability Constants for DTPA.” *J. Solution Chem.*, submitted for publication, July.
 15. Guelis, A. V., and G. J. Lumetta (2013). “Recommendation Regarding the Reference ALSEP Solvent Formulation.” FCRD-SWF-2013-000097. Argonne National Laboratory and Pacific Northwest National Laboratory, March.
 16. Hay, B. P., L. H. Delmau, and B. A. Moyer (2013). “Sigma Team for Minor Actinide Separations: Data on Computation, Synthesis, and Testing.” FCRD-SWF-2013-000253. Oak Ridge National Laboratory, August 30.
 17. Heathman, C. (2013). “Functionalization Characterization and Evaluation of Dipicolinate Derivatives with f- Element Complexes.” Ph.D. Dissertation, Washington State University, September.
 18. Hobbs, D. T., T. C. Shehee, and A. Clearfield (2013). “Experimental Findings on Minor Actinide and Lanthanide Separations Using Ion Exchange.” FCRD-SWF-2013-000276 (SRNL-STI-2013-00524). Savannah River National Laboratory, September 19.
 19. Jensen, M. P., and R. Chiarizia (2013). “Constrained Complexes for Americium-Curium Separation.” FCRD-SWF-2013-000333. Argonne National Laboratory, September 13.
 20. Johnson, J., and K. L. Nash (2013). “A Combined Cyanex-923/HEH[EHP]/Dodecane Solvent for Recovery of Transuranic Elements from Used Nuclear Fuel.” Paper 8247, *Global 2013*, Salt Lake City, Utah, September 29–October 3.
 21. Leggett, C. J., and M. P. Jensen (2013). “Studies of Size-Based Selectivity in Aqueous Ternary Complexes of Americium(III) or Lanthanide(III) Cations.” *J. Solution Chem.*, in press.
 22. Lumetta, G. J., J. C. Carter, C. M. Niver, and A. V. Gelis (2013). “Recommendation Regarding Stripping Zirconium from ALSEP Solvents.” FCRD-SWF-2013-000038. Pacific Northwest National Laboratory, January.
 23. Lumetta, G. J., J. C. Carter, C. M. Niver, and M. R. Smoot (2013). “Actinide-Lanthanide Separation (ALSEP) Process Development: PNNL Results for FY 2013.” FCRD-SWF-2013-000210. Pacific Northwest National Laboratory, August.
 24. Lumetta, G. J., A. V. Gelis, J. C. Braley, J. C. Carter, J. W. Pittman, M. G. Warner, and G. F. Vandegrift (2013). “The TRUSPEAK Concept: Combining CMPO and HDEHP for Separating Trivalent Lanthanides from the Transuranic Elements.” *Solvent Extr. Ion Exch.*, 31(3), 223–236.
 25. Meyer, T. J., and C. Dares (2013). “Electrochemical Oxidation of Actinides.” Report to INL. Chapel Hill, NC: University of North Carolina, August 19.
 26. Mincher, B. J., N. C. Schmitt, and J. D. Law (2013). “A Refined Bismuthate Flowsheet Concept.” FCRD-SWF-2013-000361. Idaho National Laboratory, September 27.
 27. Mincher, B. J., N. C. Schmitt, R. D. Tillotson, G. Elias, B. M. White, and J. D. Law (2013). “Characterizing Diamylmethylphosphonate (DAAP) as an Americium Ligand for Nuclear Fuel Cycle Applications.” *Solvent Extr. Ion Exch.*, in press.
 28. Moyer, B. A. (2013). “Sigma Team for Minor Actinide Separations FY2013 Accomplishments and Directions.” FCRD-SWF-2013-000389. Oak Ridge National Laboratory, September 30.
 29. Nash, K. L. (2013). “Advancing the Scientific Basis of Trivalent Actinide-Lanthanide Separations.” Paper 8246. *Global 2013*, Salt Lake City, UT, September 29–October 3.

Separations and Waste Forms
2013 Accomplishments Report

30. Nash, K. L. (2013). "Fundamental Studies for Improving TALSPEAK-Type Separations." FCRD-SWF-2013-00323. Washington State University, September 18.
31. Nash, K. L., G. J. Lumetta, and J. D. Vienna (2013). "Irradiated Nuclear Fuel Management: Resource Versus Waste." In *Radioactive Waste Management and Contaminated Site Clean-Up*. W. E. Lee, M. I. Ojovan, and C. M. Jantzen, Eds. Oxford: Woodhead Publishing Ltd, in press; Chap. 5.
32. Peterman, D. R., P. R. Zalupski, C. L. Riddle, J. R. Klaehn, and J. D. Law (2013). "Flowsheet Concept for the Separation of Minor Actinides Using INL DPAH Extractants." FCRD-SWF-2013-000334. Idaho National Laboratory, September 20.
33. Shehee, T. C., A. N. Alsobrook, J. D. Burns, R. Silbernagel, A. Clearfield, and D. T. Hobbs (2013). "2013 Actinide Separation Conference Presentations on Minor Actinide Separations by SRNL Participants." FCRD-SWF-2013-000187 (SRNL-L3100-2013-000107). Savannah River National Laboratory, June 17.
34. Shehee, T. C., and D. T. Hobbs (2013). "Status of Testing at the Savannah River National Laboratory Investigating the Oxidation and Ion Exchange of Americium." FCRD-SWF-2013-00192 (SRNL-L3100-2013-00103). Savannah River National Laboratory, June 18.
35. Zalupski, P. R., D. E. Ensor, C. L. Riddle, and D. R. Peterman (2013). "Complete Recovery of Actinides from UREX-like Raffinates using a Combination of Hard and Soft Donor Ligands." *Solvent Extr. Ion Exch.*, 31, 430–441.

Separations and Waste Forms
2013 Accomplishments Report

This page intentionally left blank.

CHAPTER 6
OFF-GAS SIGMA TEAM

CHAPTER 6: OFF-GAS SIGMA TEAM

R. T. Jubin, jubinrt@ornl.gov

Effects of Sorbent Aging on Iodine Adsorption

S. H. Bruffey and R. T. Jubin, jubinrt@ornl.gov

In an off-gas system, any capture material will be exposed to a gas stream for months at a time. This gas stream may be at elevated temperature and could contain water, NO_x, and a variety of other constituents comprising the off-gas stream in a traditional nuclear fuel reprocessing plant. For this reason, it is important to evaluate the effects of long-term exposure, or aging, on proposed capture materials.

Humid Aging of Silver Functionalized Aerogel

One material under consideration is silver-functionalized silica aerogel. Aerogels are being produced at PNNL and distributed to other labs for testing. For aging studies conducted during FY 2013, a feed gas of moist air (dew point 15°C) was used. Both the samples and the feed gas were held at 150°C. After 6 months of aging, the material was loaded with iodine under conditions identical to previous studies in FY 2012. The material was first dried under 2-L/min N₂ for 16 to 24 hr at 150°C. No mass loss was observed in this step. After drying, iodine loading was initiated at 56 ppm under 0.172-m/s superficial velocity. The mass of the sample was monitored continuously, and when no further mass gain was observed (generally after >7 days) the loading was allowed to continue for an additional 18 to 24 h prior to the termination of iodine flow. The sample was then purged under 0.172-m/s dry air for 24 hours. Loading curves are shown in Figure 48. Final observed mass gains for each sample are seen in Table 11.

These studies indicated that aging of the silver functionalized aerogel under a moist air stream for up to 6 months can decrease its iodine capacity by 26%, i.e., from 31 mass% iodine capacity when fresh, to 23 mass% iodine capacity after aging (the average of 1 to 6 month results). This loss in

capacity is seen within the first month of aging and does not continue to decrease as aging continues.

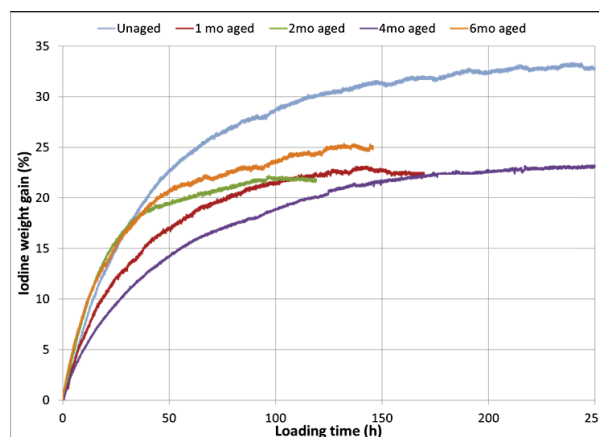


Figure 48. Iodine loading curves for humid-air aged aerogels

Table 11. Iodine loading for humid-air aged aerogels

Aging Time (months)	Iodine Sorbed (%)
0	30.7
1	22.4
2	21.7
4	22.8
6	23.9

NO_x Aging of Reduced Silver Mordenite

Silver mordenite obtained from Molecular Products in an engineered pelletized form was reduced in hydrogen at 230°C to increase the total iodine loading capacity. After reduction, the material was loaded with iodine in a TGA and determined to have an iodine loading capacity of 7.1 mass%.

Stainless steel test specimen holders were manufactured from 150-mm (6-inch) sections of 316 stainless steel tubing (wall thickness 2.1 mm (0.083 inches); internal diameter 21 mm (0.834 inches). An assembled specimen holder is shown in Figure 49. Valves on either end provide a

Separations and Waste Forms
2013 Accomplishments Report

means to seal the chamber after admitting gaseous reagents or after air purging. Ten grams of Ag⁰Z were placed in each holder and pressurized slightly above ambient with a mixture of 2% NO₂/balance CO₂-free air. The holders were kept in an oven maintained at 150°C for a period of 1 or 2 months.



Figure 49: Test specimen holder for NO₂ aging of Ag⁰Z

Iodine loading of the aged mordenite was conducted in two TGAs in a stream of dry air containing I₂ at 50 ppmV. Iodine loading curves were obtained for 0-, 1-, and 2-month aged material. Loading curves are shown in Figure 50. Observed iodine loading as determined with the TGA are reported in Table 12 along with I₂ loading as determined with NAA.

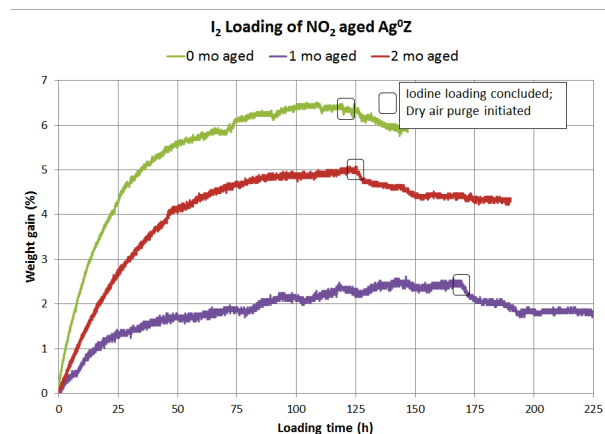


Figure 50: Iodine loading curves for 2% NO₂ aged Ag⁰Z

Table 12: Iodine loadings for 2% NO₂ aged Ag⁰Z

Aging Time (months)	Iodine loading (%) (TGA)	Iodine Loading (%) (NAA)
0	5.9	6.8
1	1.8	3.3
2	4.3	5.1

As shown in Figure 50, the iodine loading curves behaved in an unexpected manner as the aging progressed. 2 month aged Ag⁰Z

demonstrates a significantly higher iodine loading capacity than the 1 month aged Ag⁰Z. Previous aging studies with dry air and humid air have demonstrated progressively lower iodine capacities as aging time increases. At this point, this behavior is unexplained. Also an inconsistency is observed between iodine loadings determined thermo-gravimetrically and iodine loadings determined by NAA. For each sample, NAA indicates higher I₂ loadings than the TGA, a trend that has not been observed in previous iodine loading studies. However, the decrease in I₂ loading in both cases is about 25% relative at 2 months. To address this anomaly, second series of tests at the same test conditions is underway and extending to 6 months.

Silver-Functionalized Silica Aerogel for Iodine Adsorption and Immobilization

J. Matyas, josef.matyas@pnnl.gov, R. B. Engler, and R. A. Fouts

Summary Highlights

Several accomplishments have been made in FY 2013 in development of Ag⁰-functionalized silica aerogel for the removal and immobilization of iodine from gaseous products of nuclear fuel reprocessing. The synthesis of thiol-functionalized silica aerogel (an intermediate product in the synthesis of Ag⁰-functionalized silica aerogel) was optimized and scaled up. Also, maximum sorption test of thiol-aerogel for iodine revealed iodine loadings of more than 27 mass%, suggesting that silver may not be needed for an efficient capture of radioiodine. Good long-term stability and sorption performance of Ag⁰-functionalized silica aerogel was demonstrated under prototypic off-gas conditions. The humid-air aging, which simulated the impact of long-term exposure to process gases during process idling, resulted only in a 22 relative percent decrease of iodine sorption capacity.

The preliminary investigation of hot uniaxial pressing (HUP), hot isostatic pressing (HIP), and spark plasma sintering (SPS) showed that these sintering methods can be used to effectively consolidate powders of Ag⁰-functionalized silica aerogel into products of near-theoretical density (~2.9 × 10³ kg/m³). Also, removal of the organic

Separations and Waste Forms
2013 Accomplishments Report

moiety and adding 5.6 mass% of colloidal silica to Ag⁰-functionalized silica aerogel before processing resulted in denser products. Furthermore, the ram travel data for SPS indicated that rapid consolidation of powders with SPS can be performed at temperatures below 950°C.

Preparation and Sorption Performance of Functionalized Aerogels

A procedure developed in FY 2012 for preparing a thiol-functionalized silica aerogel has been further improved through optimization of mixing, temperature and time, and concentration of silane. These enhancements allow manufacturing of iodine sorbent with different concentration and coverage of the pore surfaces by silver nanoparticles. In addition, the rocking autoclave for supercritical thiolation of silica aerogel was constructed. This bench-scale apparatus enables synthesis of more than 800 mL of thiol-aerogel in one run while significantly decreasing the reaction time from hours to less than an hour.

For the efficient removal of iodine from process off-gases, elemental silver is found to provide selectivity and maximum sorption capacity. In making the Ag⁰-functionalized silica aerogels, thiol-terminated silanes are used to anchor silver ions from which silver nano-particles are made. Figure 51 shows an assembly for a maximum sorption test at 150°C of thiolated silica aerogel without silver. Results revealed a sorption capacity for iodine of more than 27 mass%. This suggests that under experimental conditions I₂ can react with the free thiol groups, forming an as yet unidentified iodine compound. Further tests are needed, however, to determine if thiol-aerogel is a viable sorbent and if other constituents in the off-gas do not compete for the sulfur site or alter this organic moiety.

Samples of Ag⁰-functionalized silica aerogel were “aged” in flowing humid air at 150°C for up to 6 months and then loaded with iodine. This long-term exposure to process gases, which simulates plant idling, resulted only in a decrease of iodine sorption capacity from 31 to 24 mass%; a decrease of 22% relative, suggesting good long-term stability of the sorbent.



Figure 51. Assembly to determine iodine loading capacity of thiolated silica aerogel; iodine vapors at 150°C for 24 hr.

Consolidation of Ag⁰-Functionalized Silica Aerogel into Dense Product

Hot pressing, cold pressing followed by sintering in a furnace, and regular melting in a furnace are the common methods to consolidate aerogels. In contrast, there are no studies reported in the literature on the sintering of aerogels with HIP and SPS. Consolidation experiments were therefore performed with Ag⁰-functionalized silica aerogel powders without iodine to investigate feasibility of these methods to produce a fully dense product [Matyáš and Engler, 2013]. Iodine-loaded aerogels were not tested in these initial experiments because the potential release of iodine during consolidation might corrode the vendor equipment. Preliminary tests indicated that the decomposition of organic moiety that is used to bind the silver nanoparticles to the solid substrate by providing Si- and Ag-active links could impede the sintering to near theoretical density. Furthermore, high silver loadings (>25 mass%) in silica aerogel might prevent fast and efficient consolidation to the waste form because the available silica might be insufficient for encapsulation of iodine in the form of AgI particles. The lack of silica resulted in accumulation of silver particles at the grain boundaries.

Figure 52 shows the change in the apparent density and open porosity of samples consolidated with the SPS technique with increased amounts of added colloidal silica. Silver-functionalized

Separations and Waste Forms
2013 Accomplishments Report

aerogel with the organic moiety was consolidated to density $\sim 2.6 \times 10^3 \text{ kg/m}^3$ and contained 2.9% open porosity (SPS-1). Removal of the organic moiety before sintering (SPS-2) resulted in the increased density $\sim 2.8 \times 10^3 \text{ kg/m}^3$ and decreased open porosity to 2.2%. An addition of 5.6 (SPS-3) and 10.5 (SPS-4) mass% of colloidal silica further increased density to $\sim 2.9 \times 10^3 \text{ kg/m}^3$, and decreased open porosity to 0.5 and 0.7%, respectively. The same trend was observed for HUP and HIP samples. Figure 53 shows images of densified SPS samples detailing fused silica grains and silver in the form of nanoparticles and μ -sized nodules. Adding of colloidal silica significantly restricted accumulation of silver at the grain boundaries and resulted in a more uniform distribution of particles throughout the samples.

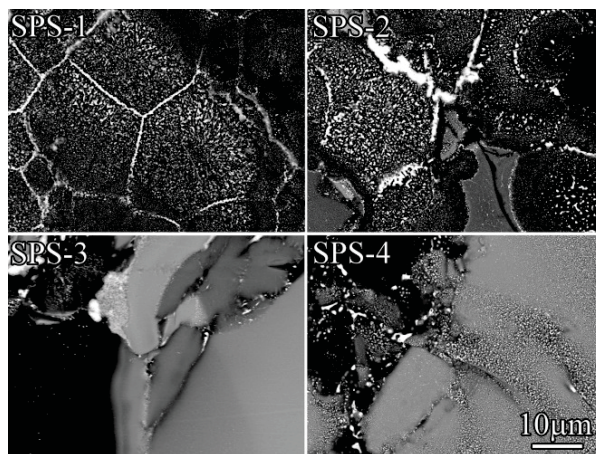


Figure 53. Backscattered electron images of fused silica grains for SPS samples; white spots are nanoparticles and μ -sized nodules of silver.

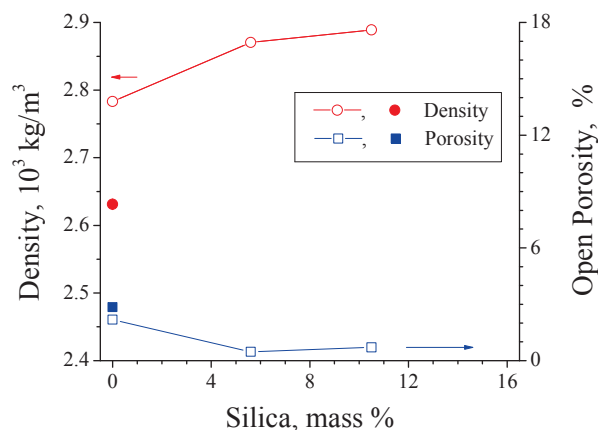


Figure 52. Apparent density and open porosity of SPS samples vs. increased concentration of added silica. Red-filled circle and blue-filled square represent sample SPS-1 (Ag^0 -functionalized aerogel with organic moiety).

Additional SPS data (not shown for brevity) indicate that Ag^0 -functionalized aerogel can be consolidated at temperatures well below 1200°C . For example, the addition of 5.6 mass% of silica to Ag^0 -functionalized aerogel powder can decrease the SPS sintering temperature to less than 950°C . This is important for future tests, especially those with iodine-loaded aerogels, considering that lower sintering temperatures may increase the retention of iodine.

Publication

1. J. Matyáš and R. K. Engler (2013). "Assessment of Methods to Consolidate Iodine-Loaded Silver-Functionalized Silica Aerogel." PNNL-22874. Pacific Northwest National Laboratory.

Deep Bed Iodine Adsorption Testing

N. Soelberg, nick.soelberg@inl.gov

Introduction

"Deep-Bed" adsorption tests are performed to measure sorbent efficiency and capacity for capturing a sorbate under conditions that represent actual operating conditions. The sorbed bed depth can be varied to maximize the ability to measure either sorption efficiency or capacity. Sorption efficiency is measured with a sorbent bed that is deeper than the sorbate mass transfer zone (MTZ). The MTZ is the zone of a certain depth in the bed in which the sorbate is being actively adsorbed; where mass transfer is occurring. The depth of the mass transfer zone depends on many operating and physical parameters.

The capacity of a sorbent can be measured in deep-bed tests as long as the test is operated for sufficient time that the sorbent in at least the leading edge of the MTZ approaches saturation. This is done in a sorbent bed that is shallow enough to speed the time duration needed for the entire mass of that sorbent to approach saturation. The thinner the bed, the faster a sorption capacity

Separations and Waste Forms
2013 Accomplishments Report

test can be performed, which leads to “Thin-bed” or even single particle testing. Results of thin-bed testing are reported elsewhere in this FY 2013 report.

If this first bed is shallow enough for practical determinations of sorbent capacity, it is typically too shallow to demonstrate sorption efficiency, because it is not as deep as the MTZ. The sorbate breaks through a shallow bed almost immediately, resulting in a low and invalid estimate of sorption efficiency.

FY 2013 Methyl Iodide Test Results

Both sorption efficiency and capacity can be measured with a deep-bed system that includes a shallow bed segment in front of deeper bed segments, as shown in Figure 54. Multiple segments of varying length can be used to enable gas sampling during a sorption test, and separate analyses of different sorbent masses from different bed depths after a test is completed. Tracking sorbate breakthrough and capacities over time from segment to segment also enables the depth of the MTZ to be estimated.

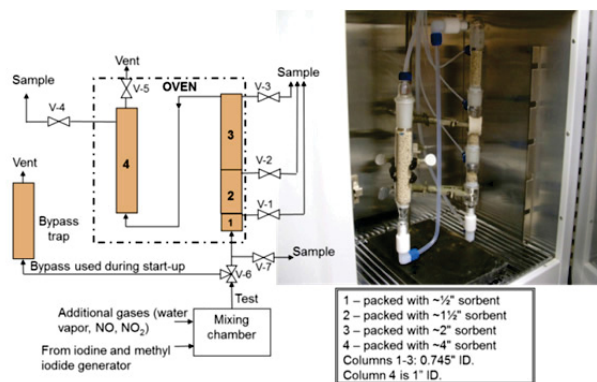


Figure 54. A schematic (left) and photo (right) of the Deep-bed Sorbent Test System used in these studies.

Two multi-laboratory test plans were prepared early in FY 2013 to provide a basis and guidance for the Off-gas Sigma Team iodine adsorption research and demonstration [Jubin and Soelberg, 2012; Jubin, et al. 2012]. Methyl iodide adsorption testing proceeded according to these test plans. Testing accomplishments are summarized in Table 13. A key finding was the replication of the results showing the conversion of the gaseous CH_3I to I_2 as the gas passes through the Ag^0Z column.

References

1. Jubin, R.T., and N. R. Soelberg (2012). “Joint Test Plan for the Thin Bed and Deep Bed Testing of Iodine Sorbents,” FCRD-SWF-2013-000031. November 15.
2. Jubin, R.T., B. B. Spencer, N. R. Soelberg, D. M. Strachan, and T. M. Nenoff (2012). “Joint Test Plan to Identify the Gaseous By-Products of CH_3I Loading on AgZ .” INL/EXT-12-27978, FCRD-SWF-2013-000070. December 26.

Publication

1. Soelberg, N. R., T. G. Garn, M. R. Greenhalgh, J. D. Law, R. Jubin, D. M. Strachan, and P. K. Thallapally (2013). “Radioactive Iodine and Krypton Control for Nuclear Fuel Reprocessing Facilities,” *Hindawi Publishing Corporation, Science and Technology of Nuclear Installations*. Article ID 702496, 12 pages, <http://dx.doi.org/10.1155/2013/702496>.

Separations and Waste Forms
2013 Accomplishments Report

Table 13. Testing accomplishments

Test	Objective	Sorbent	Inlet gas composition					Results
			CH ₃ I, ppm	I ₂ , ppm	H ₂ O, %	NO, ppm	NO ₂ , ppm	
CH3I 1	Blank. Measure blank levels of CH ₃ I and I ₂ @ sorbent bed inlet.	None	-	-	-	-	-	Detection limits at outlet of Bed 4: 0.01 ppm CH ₃ I using GC/FID and SPME), 0.0097 ppmv I ₂ using NaOH scrubbing and ICPMS analysis. Detection limits and blank levels are acceptable.
CH3I 2	Blank – CH ₃ I w/o H ₂ O or NO _x (Jubin 2012b 1.b.ii). Will gas-phase CH ₃ I reactions form I ₂ ?	None	18.8	-	-	-	-	Bed 4 outlet I ₂ measured at 0.29 ppmv, equals 1.5% of total iodine input in the CH ₃ I. Small amount if any gas-phase CH ₃ I reactions. Also confirmed gas temperature at bed inlet and outlet.
CH3I 3	Blank – CH ₃ I w/ H ₂ O and NO _x (Jubin 2012b 1.b.ii Test 1). Will gas-phase CH ₃ I reactions form I ₂ ?	None	33.1	-	1.8	833	833	Bed 4 outlet I ₂ measured at 1.28 ppmv, equals 3.4% of total iodine input in the CH ₃ I. Small amount if any gas-phase CH ₃ I reactions. Also tested different gas sample containers (glass tubes, Tedlar bags, and aluminized bags. Determined (a) regardless of bag, CH ₃ I can be light sensitive and is more stable in opaque or light-shielded containers, and (b) CH ₃ I levels tend to decrease to ~ 70% of initial levels after 3 days, and to ~10% of initial levels after 7 days, if not shielded from light.
CH3I 4	Replicate CH ₃ I adsorption and I ₂ generation (Jubin 2012b 1.b.iii.Test 1).	AgZ	36	-	1.8	833	833	<ul style="list-style-type: none"> - Initial CH₃I DF ≥ 3,000 (based on detection limit measurements). - Outlet I₂ or HI levels increased from non-detectable (0.01 ppm) to 20 ppm (~55% of input CH₃I) after breakthrough, indicating significant conversion to I₂ or HI. Analysis does not discriminate between I₂ and HI. - After Bed 1 breakthrough, input iodine was essentially 100% passing through Bed 1, but ~1/2 of the iodine was converted to from organic iodide to inorganic iodine, confirming prior results. - After test end, mass uptake by sorbent was 5.8 wt% sorbent. If this is all iodine, then iodine utilization was about 49%. Near the low end of uptake for I₂.
CH3I 5	Replicate CH ₃ I adsorption and I ₂ generation w/o H ₂ O or NO _x (Jubin 2012b 1.b.iii.Test 2).	AgZ	NA	-	0	0	0	Started in September 2013.
<p>Notes:</p> <ol style="list-style-type: none"> 1. All tests were performed with the sorbent beds at 150 °C, and with a gas superficial velocity in the beds of 0.072 m/s. 2. The balance gas in all tests was ultra-high purity (UHP) air supplied from gas cylinders. 3. GC/FID = gas chromatograph with flame ionization detector 4. SPME = solid phase micro-extraction. 5. ICPMS = inductively coupled plasma mass spectrometer. 6. NA = not available yet. 								

Chalcogels for Iodine Adsorption and Immobilization

B. J. Riley, brian.riley@pnnl.gov, J. Chun, D. Pierce, W. Lepry, and J. Matyas

Chalcogen-based aerogels, or *chalcogels*, are a unique type of high porosity iodine sorbent. One of the drawbacks of these materials is that they are friable. In previous years, PNNL developed methods to make the chalcogels in granular form for use in flow-through experiments and this process worked well. However, another idea for an engineered form was put forth by INL to imbed the chalcogels in a matrix of polyacrylonitrile (PAN) to significantly increase mechanical rigidity while minimizing the loss of open porosity. A scoping study was performed to evaluate the feasibility of this approach for Sn_2S_3 chalcogels. For this process, different mass ratios of Sn_2S_3 :PAN (0, 33, 50, and 70% Sn_2S_3) were added to dimethyl sulfoxide (DMSO), which dissolved the PAN, and then this mixture was added to deionized water. Upon adding, porous granules were formed. Scanning electron micrographs of these granules are presented in Figure 55. The porosity was very uniform in the pure PAN material and became much more irregular with increasing Sn_2S_3 loadings. At loadings > 50% Sn_2S_3 , the porosity collapsed.

Figure 56 shows the maximum iodine adsorption of the Sn_2S_3 chalcogels as well as the PAN, 33% Sn_2S_3 in PAN, and 50% Sn_2S_3 in PAN as a function of time where the graphs start at 0% iodine and the mass% uptake is normalized to the mass of starting material. These plots show the following: (1) the iodine adsorption by the PAN is negligible, but measureable, (2) the maximum iodine loading increases as the fraction of Sn_2S_3 increases, and (3) the highest iodine-loading was achieved with pure Sn_2S_3 chalcogels. In all sorbents containing Sn_2S_3 and iodine, SnI_4 was found as the primary I-containing phase confirming chemisorption of the iodine and a large fraction of the Sn_2S_3 was amorphous. The kinetics of iodine adsorption varied between the different sorbents where maximum adsorption was reached much faster for the Sn_2S_3 powder over the granular form although they were nearly identical in iodine loading and phase distribution. The iodine loading

in the PAN- Sn_2S_3 hybrid sorbents increased as the Sn_2S_3 :PAN ratio increased.

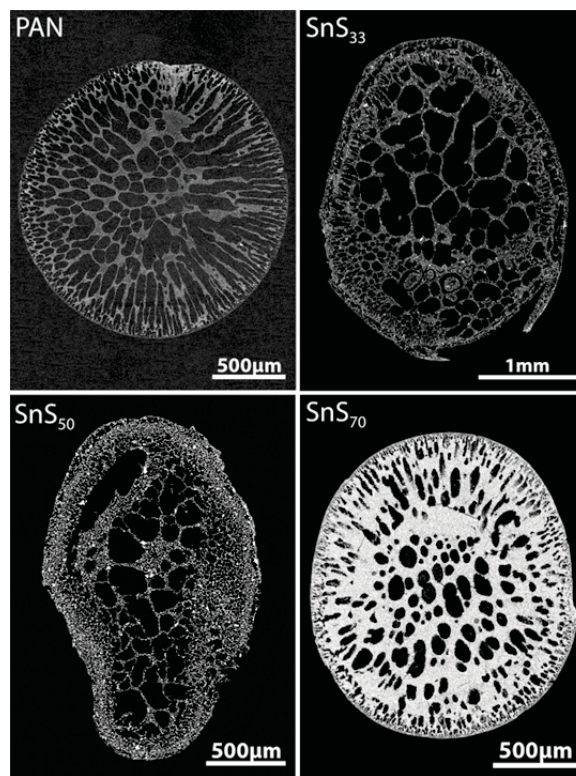


Figure 55. Cross-sectional SEM micrographs of the pure PAN (PAN) and various chalcogel-PAN sorbents, SnS_{33} , SnS_{50} , and SnS_{70} .

Consolidation experiments with chalcogels containing maximum iodine loading were performed by heating the material in sealed quartz ampoules with the addition of GeS_2 , a glass forming additive. Full collapse of the chalcogel was attained at $\sim 600^\circ\text{C}$ with an amorphous background and some residual peaks for SnI_4 because the solubility limit of SnI_4 in the glass phase was reached at this heat-treatment temperature. It is likely that a larger fraction of SnI_4 could be incorporated into the glass by increasing temperature. FY 2014 activities will include the evaluation of alternative sintering technologies such as SPS and hot isostatic pressing for the iodine-sorbed chalcogels because both are promising technologies for rapid consolidation of waste forms with components susceptible to volatilization.

Separations and Waste Forms
2013 Accomplishments Report

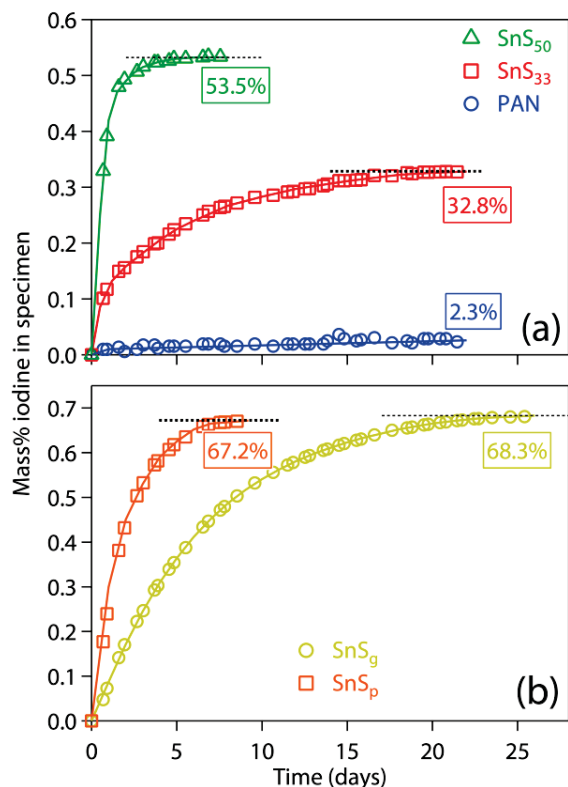


Figure 56. Iodine uptake in desiccator experiments for (a) PAN hybrid sorbents and (b) pure chalcogenides.

Iodine / Tritium Co-Adsorption

B. B. Spencer, spencerbb@ornl.gov, and S. H. Bruffey

The purpose of this study was to evaluate the co-adsorption of water and iodine onto type 3A molecular sieve (3AMS) and Ag⁰Z. Water adsorption was important because the water is likely to contain tritium. To address the concerns of co-adsorption, the extent of coadsorption of the non-targeted species (e.g., how much iodine is trapped on the water sorption column) and whether the adsorption of one component affects the sorption of the other component (e.g., changes in capacity) are needed to adequately design an operating reprocessing plant. Both thin and deep bed or column experiments were conducted to obtain a better understanding of the co-adsorption of water and iodine on 3AMS and Ag⁰Z.¹⁻³

Adsorption of water on 3AMS is accompanied by limited co-adsorption of iodine under conditions expected in the effluent streams from UNF processing operations (e.g., oxidative pretreatment or nitric acid dissolution). Pore sizes in the crystallite structure of the molecular sieve

are small enough to admit the small water molecule, hence sorption. Iodine in the gas stream containing no water associated is unlikely to be admitted into the crystallite structure of the 3AMS because the kinetic diameter of the iodine molecule is too large to enter the pores. The 3AMS sorbs about 20 wt% water (dry solids basis), while iodine collected on the media is only a few tenths of one weight percent. The amount of water sorbed seems unaffected by the presence of iodine, as shown in Figure 57.

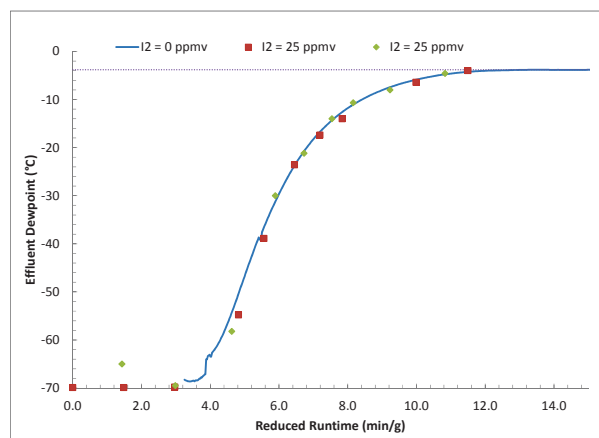


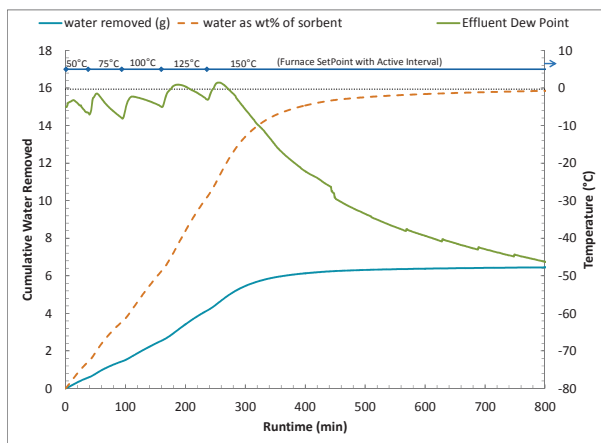
Figure 57. Coadsorption of water and iodine (feed gas water dewpoint 0 °C (solid line), iodine 0 (red square symbols) or 25 ppmV (green diamond symbols)).

Regeneration of the sorbent is accomplished by heating it to temperatures above 150°C, but less than 275°C, while passing dry carrier gas through the bed. These studies indicate that both water and iodine are desorbed together (see Figure 58) Although there is a tendency for the iodine to desorb more rapidly than the water, the process does not seem promising as a means to separate the iodine and water with high efficiency.

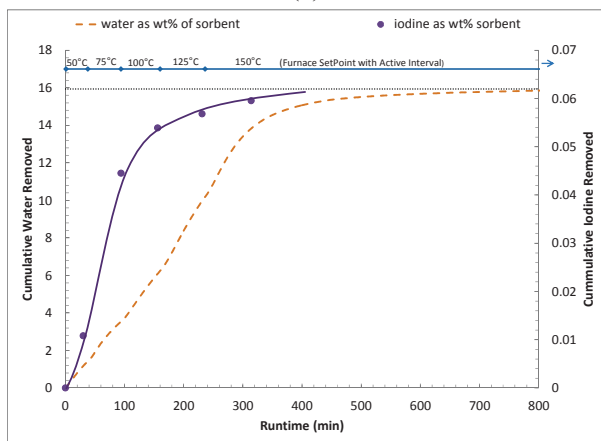
Silver exchanged mordenite (AgZ) may be used to remove iodine from off-gas streams. It is typically treated with hydrogen at a temperature of 230°C to ensure the silver is reduced to metal (called reduced silver mordenite, or Ag⁰Z) to improve the performance of the sorbent. The high temperature treatment drives excess water from the crystalline structure. During off-gas treatment operations, the Ag⁰Z is maintained at a temperature of 150°C to promote the reaction between the silver and iodine. It was shown that Ag⁰Z absorbs about 1 wt% moisture from humid gas streams at 150°C. Based on this study, water

Separations and Waste Forms 2013 Accomplishments Report

sorption is reversible. However, in typical applications where iodine and water are both present in the off-gas stream, the adsorption rate of iodine is lower than when water is present.



(a)



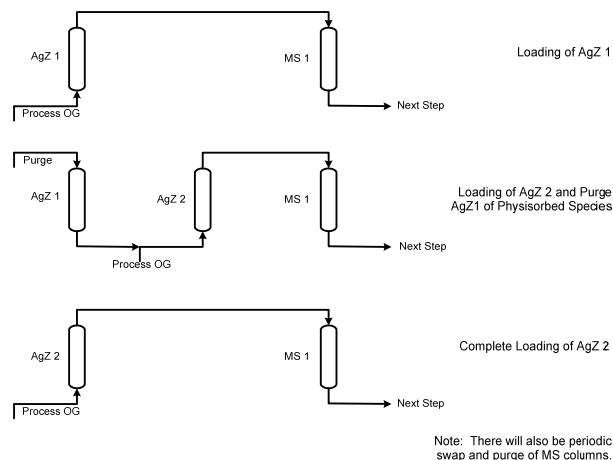
(b)

Figure 58. (a) Water and (b) iodine desorption from 3AMS during a slow approach to 150°C.

It was also shown that a portion of the iodine is removed when the feed stream is changed to dry air, indicating that iodine is physisorbed as well as chemisorbed. Heating the sorbent to 200°C causes additional iodine to be removed beyond that typically observed during the standard air purge at 150°C.

An off-gas processing sequence was proposed that could separate the iodine and water sequestered with these sorbents; refer to Figure 59. It involves placing the AgZ sorbent upstream of the 3AMS. When breakthrough of iodine from the AgZ column is imminent, a second column is placed on-line that accepts both the process off-

gas. A low flow rate purge stream is passed through the first column which is heated to remove physisorbed iodine from the first AgZ column. This purge stream merges with the process off-gas stream and is treated by the new (second) AgZ column. The cycle repeats with respect to the AgZ column. Essentially no iodine reaches the downstream 3AMS column, which would be regenerated for reuse while a companion 3AMS column goes on-line.



Note: There will also be periodic swap and purge of MS columns.

Figure 59. Concept for implementation of system to separately confine iodine and tritium.

Publications

1. Spencer, B. B., R. T. Jubin, S. H. Bruffey, K. K. Anderson, and J. F. Walker, Jr. (2012). "Preliminary Assessment of Tritium (Water) / Iodine Co-adsorption on 3A Molecular Sieve." FCRD-SWF-2013-000078 also ORNL/LTR-2012/623. Oak Ridge National Laboratory, December.
2. Spencer, B. B., S. H. Bruffey, J. F. Walker, Jr., and R. T. Jubin (2013). "Study of Iodine and Water Co-adsorption on Thin Beds of 3AMS and AgZ." FCRD-SWF-2013-000116 and ORNL/LTR-2013/103. Oak Ridge National Laboratory, March.
3. Spencer, B. B., S. H. Bruffey, J. F. Walker, Jr., K. K. Anderson, and R. T. Jubin (2013). "Iodine and Water Co-adsorption on Deep Beds of 3AMS and AgZ." FCRD-SWF-2013-000329 and ORNL/LTR-2013/439. Oak Ridge National Laboratory, September.

Determination of Baseline Iodine Waste Form Performance Characteristics

T. M. Nenoff, tmnenof@sandia.gov, P. V. Brady, C. Mowry, T. J. Garino, SNL

One thrust of this waste form research program is to develop effective iodine capture materials that can be readily converted into materials suitable for disposal or storage under a variety of conditions. Currently, I_2 sorption on Ag-mordenite which is currently a possible capture media for radiological iodine gas from a future reprocessing plant. Long-term storage requires a waste form that controls the release of iodine to levels commensurate with the required performance of the storage or repository site. A material of interest is a glass composite material (GCM) waste form has been developed for which a U.S. Patent was recently issued [Garino, et al., 2011; Nenoff, et al., 2012a]. It is an inhomogeneous composite assemblage of low temperature sintering Bi-Si-Glass and iodine capture material (e.g., AgZ and iodine loaded AgZ (AgI-Z), see Figure 60 and Figure 61.

In an effort to establish the chemical durability of this composite material, it is important to establish both the chemical durability of the Bi-Si-Glass and the iodine release from the inhomogeneous GCM of AgI-Z/Glass/Ag. Durability results from all these studies can be compared against other candidate waste form materials, including ceramics, cement, and other glass compositions.

The effect of variations in the GCM composition on results from the single pass flow through (SPFT) test were studied [Chou and Wollast, 1985], including: (1) temperature and pH of SPFT test on the dissolution of GCM components (e.g., AgI-Z, Bi-Si Glass), (2) presence of Ag flake in the GCM, (3) optimization of AgI-Z mass loadings, and (4) iodine loading in AgZ (from ORNL: 0.5, 1.4, 3.5, 5, and 7.8 wt% iodine loading into AgZ.) These ranges in iodine loading fall within anticipated loadings on zeolite sorbents from the off-gas streams in future nuclear fuel reprocessing plants.

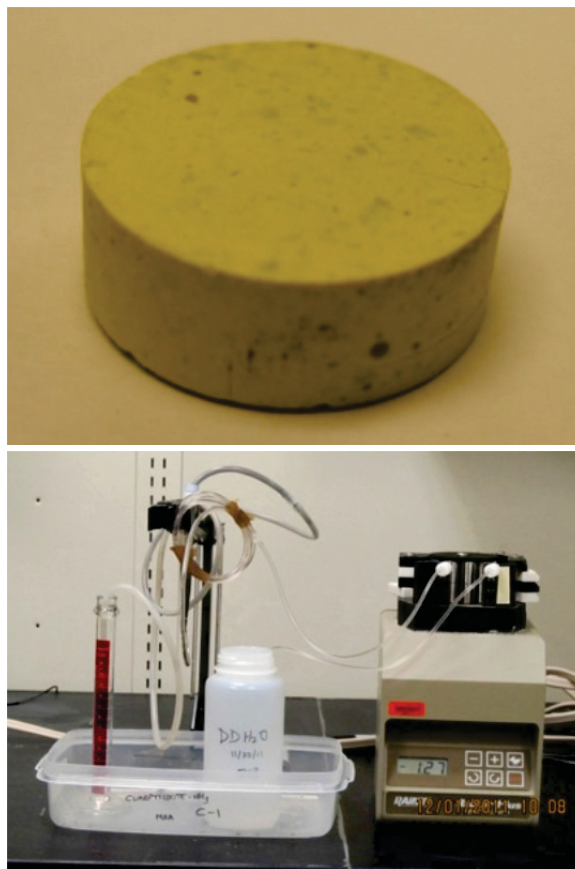


Figure 60. top, CGM of AgI-Z/Glass/Ag, 12 mm diameter; bottom, Single Pass Flow Through Test apparatus.

Dissolution studies included the SPFT test, product consistency test (PCT), and MCC-1 protocols [ASTM 1998, 2010a, 2010b]. The SPFT apparatus is shown in Figure 60. For the SPFT test, 2 grams of ground (to $\approx 1\mu\text{m}$; surface area = $3.06\text{ m}^2/\text{g}$) GCM was placed in 2 mL reactor. A peristaltic pump moved test solutions through the reactor bed at a flow rate of 7 mL/h. Rate measurements were made at 25°C. Feedwater solutions were 0.01M NaCl at pH ~ 7 and ~ 3 . The pH ~ 3 solutions were adjusted with HCl. Effluents were analyzed for pH, and for Ag, I, Zn, and Si with ICP-MS in semi-quantitative mode and each reported value represents the average of 12 determinations. In order to ensure that test results were directly comparable results from other glass waste forms, SPFT tests were performed on a low-activity reference material (LRM) glass. Consistency between the LRM rates measured at Sandia and measured previously at other laboratories gave confidence that the SPFT

Separations and Waste Forms
2013 Accomplishments Report

approach used at SNL would yield results consistent with those obtained at other laboratories [Nenoff, et al., 2013a].

The SPFT tests were performed on the individual GCM components (1) AgI-Z and (2) Bi-Si glass at 25°C and 60°C and pH = 3, have $q/S = 9 \times 10^{-6}$ to 9×10^{-7} m/s (glass) and 1×10^{-7} to 1×10^{-8} (AgI-Z); where q is the fluid flux (m^3/s) and S is mineral surface area (m^2). The 25°C glass degradation rates range from 5×10^{-4} g/(m^2d) at pH = 3.2 to 9×10^{-5} g/(m^2d) at pH(25°C) = 7.5; the 60°C glass degradation rates were 9×10^{-3} g/(m^2d) at pH = 4.2 and 7×10^{-4} g/(m^2d) at pH(25°C) = 7.6. The 25°C AgI-Z degradation rates increase from $\sim 1 \times 10^{-5}$ g/(m^2d) at pH = 5.5 to 2×10^{-5} g/(m^2d) at pH = 3.5.

In comparison, SPFT testing on the entire GCM waste form indicated that iodine release is less than that of the Si and Zn constituents that comprise the glass and is limited by the low solubility of AgI (see Figure 61.) The SPFT data suggest that the GCM degradation will maintain ambient Ag levels at less than 20–50 ppb. This will hinder iodine release from the GCM and keep I levels below ~ 12 ppb. The left side of Figure 61 shows the microstructure of a sintered GCM waste form containing AgI-Z (7.8% iodine loaded). The results from these PCT and MCC-1 studies conducted in these series do not indicate any obvious dependency of I or Ag release on I loading.

To summarize, all samples studied exhibited similarly low level releases of key waste form components, in particular Ag and I, over a range of pH and temperatures. The results indicate that the GCM behaves quantitatively similar to the standard nuclear glass waste forms with respect to durability and degradation rates [Nenoff, et al., 2012b]. Over the ranges evaluated, the SPFT, PCT, and MCC-1 results and analysis indicate that I release from the GCM waste form are insensitive to iodine loading. Further details are contained in the FY 2013 milestone reports [Nenoff, et al., 2013c, 2013d, 2013e].

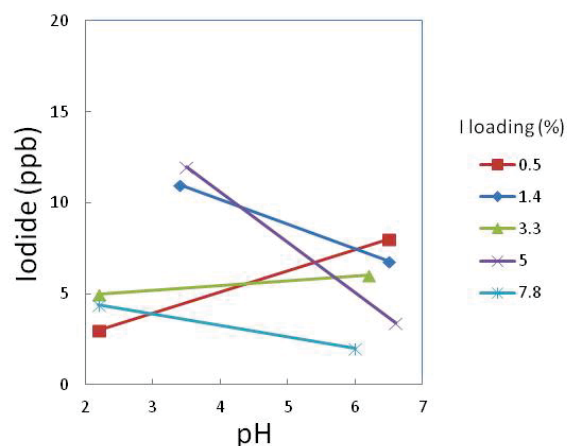
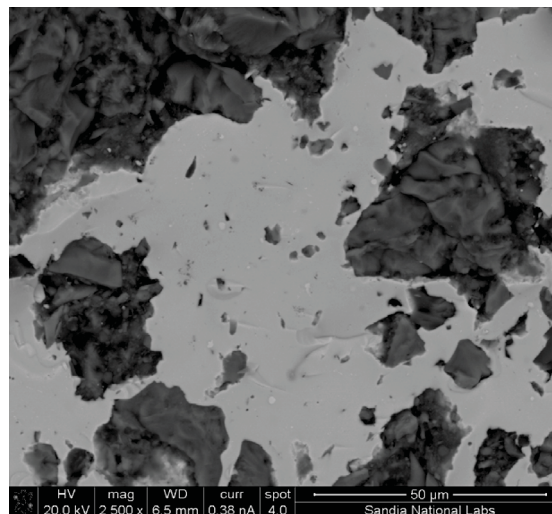


Figure 61. (top) An SEM photomicrograph of the sintered microstructure of a GCM containing AgI-Z (7.8% iodine). (bottom) Effluent iodine levels from SPFT tests of GCM containing various iodine loadings on AgI-Z at 25°C; data scatter is due to uncertainty in the leachant flow rate and the ICP-MS analyses.

References

- Garino, T. J., T. M. Nenoff, J. L. Krumhansl, and D. Rademacher (2011). “Low-Temperature Sintering Bi-Si-Zn Oxide Glasses for Use in Either Glass Composite Materials or Core/Shell ^{129}I Waste Forms”, *J. Amer. Ceram. Soc.* 94(8), 2412-2419.
- Nenoff, T. M., J. L. Krumhansl, T. J. Garino, and N. W. Ockwig (2012a). “Low Sintering Temperature Glass Waste Form for Sequestering Radioactive Iodine.” U.S. Patent 8,262,950, September 11.

Separations and Waste Forms
2013 Accomplishments Report

3. Chou, L., and R. Wollast (1985). “Steady-state Kinetics and Dissolution Mechanisms of Albite.” *Am. J. Science*, 285, 963-93.
4. ASTM (1998). “Standard Test Method for Static Leach Testing of Monolithic Waste Forms for Disposal of Radioactive Waste.” ASTM C1220-10. West Conshohocken, PA: American Society for Testing and Materials.
5. ASTM (2010a). Standard Practice for Measurement of the Glass Dissolution Rate Using the Single-Pass Flow-Through Test Method, American Society for Testing and Materials, West Conshohocken, PA.
6. ASTM (2010b). “Standard Practice for Measurement of the Glass Dissolution Rate Using the Single-Pass Flow-Through Test Method.” West Conshohocken, PA: American Society for Testing and Materials.
7. Nenoff, T. M., P. V. Brady, and C. D. Mowry (2013a). “Single Pass Flow Through Testing of LRM Glass.” DOE/NE-SWG milestone report M3FT-13SN0312043. FCRD-SWG-2013-000088, SNL-2013-0646P. January 29.
8. Nenoff, T. M., P. V. Brady, T. J. Garino, and C. D. Mowry (2012). “Determination of Baseline Iodine Waste Form Performance Characteristics.” FCRD-SWF-2012-000172, SAND 2012-6892C.
9. Nenoff, T. M., P. V. Brady, and C. D. Mowry (2013b). “Effect of pH and Temperature on AgI-Mordenite and Bi-Si Glass Dissolution.” DOE/NE-SWG milestone report M3FT-13SN0312044, FCRD-SWF-2013-000098, SAND 2013-1205P, February 13.
10. Nenoff, T. M., P. V. Brady, T. Garino, and C. D. Mowry (2013c). “SPFT Testing of Optimized Weight Loadings of AgI-Z in GCM.” DOE/NE-SWG milestone report M3FT-13SN0312045, FCRD-SWF-2013-000215, SAND 2013-5763P. July 16.
11. Nenoff, T. M., P. V. Brady, T. Garino, and C. D. Mowry (2013d). “Complete study including SPFT testing of variable I₂ loading in one AgI-Z.” DOE/NE-SWG milestone report M3FT-13SN0312046, FCRD-SWF-

2013-000232, SAND 2013-7437 P. September 15.

Related Publications

1. Hughes, J. T., D. F. Sava, T. M. Nenoff, and A. Navrotsky (2013). “Thermochemical Evidence for Strong Iodine Chemisorption by ZIF-8.” *J. Amer. Chem. Soc.*, Accepted: 10.1021/ja406081r.
2. Sava, D. F., K. W. Chapman, M. A. Rodriguez, J. A. Greathouse, P. S. Crozier, H. Zhao, P. J. Chupas, and T. M. Nenoff (2013). “Competitive I₂ Sorption in Cu-BTC from Humid Gas Streams.” *Chem. Mater.*, 25(13), 2591–2596.
3. Rodriguez, M., T. J. Garino, D. X. Rademacher, X. Zhang, and T. M. Nenoff (2013). “The Synthesis of Ba- and Fe-Substituted CsAlSi₂O₆ Pollucites.” *J. Amer. Ceram. Soc.*, 96(9), 2966-2972.
4. Garino, T. J., T. M. Nenoff, M. A. Rodriguez, C. D. Mowry, and D. X. Rademacher (2013). “Optimization of Sintered AgI-Mordenite Composites for ¹²⁹I Storage.” *Proceedings of American Nuclear Society: Global 2013*. Salt Lake City, UT, in press.

Patents

1. Krumhansl J. L., and T. M. Nenoff (2013). “Mixed-Layered Bismuth-Oxygen-Iodine Materials for Capture and Waste Disposal of Radioactive Iodine.” U.S. Patent 8,383,021, February.
2. Garino, T. J., D. F. Sava, and T. M. Nenoff (2013). “Pelletized Molecular Sieves and Method of Making Pelletized Molecular Sieves,” filed November 7..
3. Garino, T. J., and T. M. Nenoff (2013). “Metal Matrix Waste Forms for Fission Products,” filed August 15.

Investigation Hot Pressing of Iodine Loaded Silver Mordenite

R. T. Jubin, jubinrt@ornl.gov, and S. H. Bruffey

Extensive work has been initiated to evaluate AgZ as a capture media for the iodine released to the off-gas streams during the reprocessing of

Separations and Waste Forms
2013 Accomplishments Report

UNF. This effort was initiated to determine if HIP method could be effective for the direct conversion of iodine-loaded reduced silver-exchanged mordenite (I-Ag⁰Z) into a suitable waste form. The high temperatures and pressures exerted on a material with HIP have been demonstrated to successfully convert krypton- and chlorine-bearing materials into waste forms with high density. The minimal pretreatment required for HIP makes this a potentially attractive and economically desirable method for waste form production. Additionally, the HIP can serve as the primary container for the waste form.

In the late 1970's and early 1980's INL examined the technical feasibility of immobilizing ⁸⁵Kr in a zeolite structure that was hot isostatically pressed. The zeolite was sintered at 700 °C and 100 MPa for 2 to 4 hours [Christensen, et al., 1983]. The resulting product was amorphous. Work at ANL [Pereira, et al., 1997] and INL [Priebe and Bateman, 2008] to develop a waste form for the electrochemical process salt waste utilized a glass frit and zeolite loaded with chloride salt. This mixture was treated at 700 to 750°C and pressures from 41 MPa to 172 MPa in a HIP. The National Nuclear Lab in the United Kingdom has demonstrated that A and X zeolites could be successfully processed at 900°C in a HIP converting them to sodalite [Maddrell, 2005]. In Japan, work has been conducted on the sintering of AgS [Nishimura, et al., 2007]. The material was sintered at 700°C and 100 MPa for three hours in a HIP. Silver nitrate impregnated alumina (AgA) was also sintered at 850°C and 175 MPa for three hours in a HIP.

In the initial stages of this work, the use of a HUP to prepare samples of (Ag⁰Z) was assessed and the resulting product of the process was evaluated. The starting material was fresh Ag⁰Z with a bulk density of 770 kg/m³. The first pressed sample consisted of the engineered pelletized form produced by the manufacturer and the second sample consisted of the same material that had been crushed with a mortar and pestle. The pressing was conducted at ~27.5 MPa at 750°C for 1 h. Figure 62 shows the resulting compacts from intact Ag⁰Z pellets and from crushed Ag⁰Z. The mechanical strength of the pellet was too low to measure.

To evaluate the benefits of the higher pressure that could be achieved with HIP, a contract was placed with a commercial vendor, for a second phase of scoping tests. The test structure was designed to determine the effect of pressure and temperature variations on pellet size. Additionally, samples of I-Ag⁰Z were also pressed, providing insight into the effects of iodine presence on pressing and whether there is any migration of iodine as a result of different temperatures involved in the pressing process.

The sample containers were constructed of 304 stainless steel tubing and each contained approximately 5 g of Ag⁰Z or I-Ag⁰Z. The wall thickness was 0.51 mm (0.020") and the end-caps were 0.25 mm (0.010") thick. The capsules were sealed by electron beam welding in a vacuum chamber. During the electron beam welding Capsule #1 failed due to a failed electron beam weld on one end of the capsule during final closure and the sample leaked. Figure 63 shows a representative sample capsule prior to pressing. The seven remaining sample capsules were sintered in the vendor HIP and the capsules returned to ORNL for analysis. Figure 64 shows a representative post pressing sample.



Figure 62. Compacts from pellet form Ag⁰Z (left) and crushed Ag⁰Z (right) after sintering in a HUP.

Separations and Waste Forms
2013 Accomplishments Report



Figure 63. Side view of I-Ag⁰Z loaded capsule



Figure 64. A photograph of the HIP capsule containing Ag⁰Z

The results from the density measurements show a direct correlation between the HIP pressure and the HIP temperature. There was no obvious advantage in regards to density for the crushing of the sample prior to sintering. The calculated density of the AgZ that was sintered at 175 MPa was $2.6 - 2.65 \times 10^3 \text{ kg/m}^3$. This is an increase in density of $\sim 340\%$ over the bulk density of the starting material. After sintering at 100 MPa, the density increased by $\sim 275\%$ over that of the starting material with the one exception of the

sample that was pressed at 850°C , which also achieved a density of $\sim 2.6 \times 10^3 \text{ kg/m}^3$. This is a significant increase in density over those that were sintered in a HUP in which the density was increased by only 170% over the bulk density of the starting material.

The samples are now undergoing destructive analysis. This includes sectioning the sample (see Figure 65), scanning electron microscopy (SEM) of the cross sectioned surface, and XRD to determine the resulting phases present in the sintered sample. Analysis of the silver and iodine distributions within the resulting product are also being determined.



Figure 65. A photograph of the cross-sectioned HIP capsule containing iodine loaded Ag⁰Z

References

1. Christensen, A. B., J. A. Del Debbio, D. A. Knecht, J. E. Tanner, and S. C. Cossel (1983). "Immobilization of Krypton 85 in Zeolite5A." *Proceedings of the 17th DOE Nuclear Air Cleaning Conference*, CONF-820833, 183-197.
2. Pereira, C., M. Hash, M. Lewis, and M. Richmann (1997). "Ceramic-Composite Waste Forms from the Electrometallurgical Treatment of Spent Nuclear Fuel," *Journal of Materials*, 34-40. July.
3. Priebe, S., and K. Bateman (2008). "The Ceramic Waste Form Process at Idaho National Laboratory." *Nuclear Technology*, 199 207, (162). May.

Separations and Waste Forms
2013 Accomplishments Report

4. Maddrell, E. (2005). "Capture and Immobilization of Iodine." National Nuclear Laboratory, November 2.
5. Nishimura, T., T. Sakuragi, Y. Nasu, H. Asano, and H. Tanabe (2007). "Development of Immobilization Techniques of Radioactive Iodine for Geological Disposal." *Mobile Fission and Activation Products in Nuclear Waste Disposal*, January 16-19. <http://mofap07.in2p3.fr/17janvier/Mofap07%20OHP%20T.pdf>.

New Kr Adsorbents – Part 1 – INL Krypton Capture Accomplishments

T. G. Garn, troy.garn@inl.gov, M. R. Greenhalgh, and J. D. Law, INL; S. H. Bruffey and R. T. Jubin, ORNL; T. M. Nenoff and I. Ava, SNL; P. Thallapally and D. M. Strachan, PNNL

Introduction

Accomplishments by the INL Kr capture off-gas team members for FY 2013 can be divided into four separate sub-sections that include:

1. The preparation and delivery of a newly developed silver exchanged mordenite in an engineered form sorbent (AgZ-PAN) to ORNL for iodine capacity testing
2. Collaborative research efforts with PNNL and SNL involving the preparation and performance evaluations of engineered forms of Ni-DOBDC metal organic framework (MOF) for Kr and Xe uptake
3. Kr and Xe capacity measurements to provide data supporting modeling efforts
4. Pressure swing testing to compare with previously obtained Kr and Xe thermal swing capacity measurements.

The following provides a brief description of each completed accomplishment

Preparation and Delivery of AgZ-PAN

The AgZ-PAN exhibits a higher surface area than commercially available AgZ. 22 grams of AgZ-PAN were prepared with the INL patent pending process [Garn, et al., 2013] and characterized for surface area Ag content. The surface area was determined to be 280 m²/g with

Brunauer, Emmett, and Teller theory, and the Ag content was 8.95 wt%. A sample of the AgZ-PAN was provided to ORNL for thin-bed testing in December 2012. A test plan was prepared describing the activation and silver reduction procedures. Higher activation temperatures of 150°C prior to testing had no negative impact on measured physical properties of the material. Preliminary test results indicated the non-reduced material demonstrated capacity for iodine and further testing could be performed with reduced material. An additional 20 g were also prepared for future deep-bed iodine testing at INL

Engineered Form Ni-DOBDC MOF

A joint effort to prepare engineered forms of a Ni-DOBDC MOF was completed with contributions from PNNL, SNL and INL. Two independent methods were used, one at INL and one at SNL, to prepare engineered forms from Ni-DOBDC MOF powder developed and prepared at PNNL. Xenon and Kr in air capacity test evaluations were performed on both engineered forms at ambient temperature with the cryostat experimental setup at INL. Test results from the INL engineered form of MOF indicated a Xe capacity of 1.6 mmol/kg sorbent and no Kr capacity. A large loss of surface area occurred over a short test duration rendering the material unusable. Four capacity tests were completed with the SNL engineered form MOF at ambient temperature and resulted in Xe capacities of 1.4, 4.2, 5.0 and 3.8 mmol/kg sorbent with no Kr capacity observed. Two additional capacity tests were performed at 240 K to further evaluate SNL material. Xenon capacities of 50.7 and 49.3 mmol/kg of sorbent and Kr capacities of 0.77 and 0.69 mmol/kg of sorbent were obtained at 240 K. Following the adsorption evaluations, the SNL material had lost about 40% of the initial mass and 40% of the initial surface area. In general, the Xe capacities at ambient temperature for the INL and SNL engineered forms of Ni-DOBDC MOFs were lower than the 9.8 mmol/kg sorbent test results reported by INL in FY 2012 with the PNNL initial engineered form material. These results indicate that the methods used at INL and SNL to prepare an engineered form detrimentally affect the adsorption capacity of the material. The completion of this effort was documented in

Separations and Waste Forms
2013 Accomplishments Report

FCRD-SWF-2013-000227 [Garn and Greenhalbh, 2013].

AgZ-PAN Capacity Data for Modeling Support

Adsorption isotherms were obtained in the cryostat system for both Kr and Xe at a temperature of 220 K with the INL AgZ-PAN sorbent. These isotherms were created by varying the Kr and Xe gas concentrations in helium independently and acquiring sorbent capacities at each concentration. Xenon concentrations ranged from 100 to 1000 ppmV and Kr concentrations ranged from 150 to 2500 ppmV. These capacity data were linearly regressed with three separate techniques to obtain the Langmuir parameters Q_{\max} and K_{eq} . These data were then fit to the Langmuir equation. The resulting Xe isotherm can be seen in Figure 66.

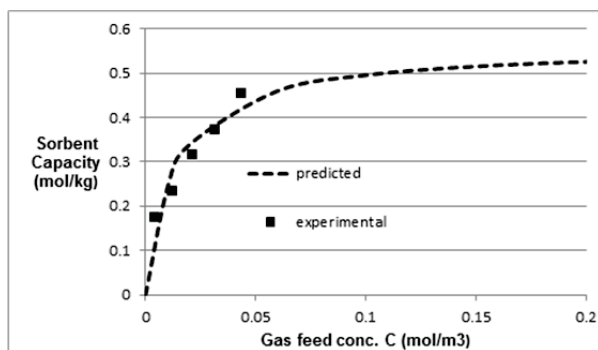


Figure 66. Xenon adsorption isotherm on AgZ-PAN at 220K

The equilibrium and maximum capacity values were over predicted for Kr due to the low capacities found during testing. These data were provided to INL modeling project in support of the development of the Off-gas SeParation and REcoverY (OSPReY) model. Additional isotherm testing is planned with either more sorbent or higher gas concentrations or a combination of both

Pressure Swing Testing

Pressure Swing Adsorption (PSA) tests were performed utilizing both the HZ-PAN and AgZ-PAN sorbents. The results were then compared with the previous Thermal Swing Adsorption (TSA) results for both Kr and Xe in air. The two engineered form sorbents were evaluated for Kr and Xe capacities at ambient temperature and 140 Pa (20 psig) in PSA operations. The AgZ-PAN showed an increase of more than three times

capacity for Xe when compared to TSA operations without pressure and a small Kr capacity increase was observed. The HZ-PAN sorbent had no capacity for either Kr or Xe in air at ambient temperature with TSA operations however; under 140 Pa PSA operations, it obtained capacities of 27 mmol/kg and 2.9 mmol/kg for Xe and Kr respectively. The selectivities of Xe relative to Kr were also calculated for the sorbents. The results of these tests indicate that PSA operations can be utilized to increase the capacities of both Kr and Xe under ambient conditions with the sorbents tested. Results for the pressure swing comparison testing were reported in FCRD-SWF-2013-000273 [Garn and Greenhalgh, 2013b].

References

1. Garn, T. G., J. D. Law, M. R. Greenhalgh, T. J. Tranter (2013). "A Composite Media For Fluid Stream Processing, A Method Of Forming The Composite Media, And A Related Method Of Processing A Fluid Stream" 2939-10703 BA-590 Patent Application.
2. Garn, T. G. and M. R. Greenhalgh (2013a). "Development and Test Evaluations for Ni-DOBDC Metal Organic Framework (MOF) Engineered Forms." FCRD-SWF-2013-000227. July.
3. Garn, T. G., and M. R. Greenhalgh (2013b). "Pressure Swing and Thermal Swing Adsorption Capacity Comparisons for Kr and Xe using AgZ-PAN and HZ-PAN Sorbents." FCRD-SWF-2013-000273. August.

Publications

1. Greenhalgh, M., T. G. Garn, and J. D. Law (2013). "Development of a Hydrogen mordenite sorbent for the capture of Krypton from used nuclear fuel reprocessing off-gas streams." Submitted to *Journal of Nuclear Science and Technology*, July.
2. Soelberg, N., T. Garn, M. Greenhalgh, J. Law, R. Jubin, D. Strachan and P. Thallapally (2013). "Radioactive Iodine and Krypton Control for Nuclear Fuel Reprocessing Facilities." *Science and Technology of Nuclear Installations*, Article ID 702496

Separations and Waste Forms
2013 Accomplishments Report

- Garn, T. G., M. R. Greenhalgh, and J. D. Law (2013). "Novel Sorbent Development and Evaluation for the Capture of Krypton and Xenon from Nuclear Fuel Reprocessing Off-Gas Streams." *Global 2013 Proceedings*, Paper 7523, September.

New Kr Adsorbents – Part 2 – Metal Organic Frameworks

*P. K. Thallapally, praveen.thallapally@pnnl.gov,
J. Liu, and D. M. Strachan*

Metal organic framework materials are hybrid organic and inorganic compounds that are being developed to remove Kr and Xe from process off-gases at near ambient conditions.

Kr Removal using Two Bed Approach

The current process to remove Xe and Kr from process off-gas is to cryogenically distill the air components, leaving behind a mixture of Xe and Kr. Installing a cryogenic process and its operation are expensive and energy intensive. Thus, a process to remove these gases at higher temperatures is expected to be advantageous and cost effective, especially if the process could operate at close to ambient conditions and be used to separate Kr from Xe. In addition to the possibility of removing Xe and Kr from air at elevated temperatures, ⁸⁵Kr is isolated in a MOF cage thereby also isolating the corrosive decay product Rb.

Among thousands of MOFs synthesized thus far, the team selected NiDOBDC and FMOFCu (Figure 67) for three reasons. First, both MOFs contain unsaturated metal centers that are polar and favorable for Xe and Kr adsorption. Second, the NiDOBDC is known to have high hydrothermal stability and higher Xe capacity (55 mass%) than activated carbon (45 mass%). Third, Ni/DOBDC has a uniform, 11-nm cylindrical pores that are larger than the kinetic diameters of Xe and Kr (0.396 nm and 0.360 nm, respectively). However, it was selected because the connecting windows have dimensions practically similar to the kinetic diameter of Kr and smaller than the kinetic diameter of Xe. Therefore, Xe diffusion into the cavities should be restricted, giving FMOFCu higher Kr selectivity than NiDOBDC, based on molecular sieving, where the connecting

windows are much larger than the kinetic diameters of Xe or Kr. Results from previous breakthrough experiments in which a single sorption bed containing either NiDOBDC or FMOFCu suggest both MOFs selectively remove Xe over other gases in the stream.

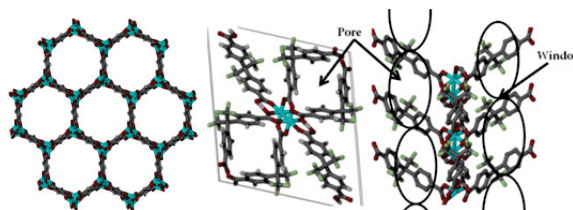


Figure 67. Crystal structures for MOFs after removing solvent molecules. Left: Ni/DOBDC; and right: FMOFCu.

To capitalize on the preference of these materials to remove Xe over Kr, experiments were carried out in which two sorption beds containing either the same or one bed each of NiDOBDC or FMOFCu to remove Xe in the first sorption bed at 233 K (-40°C). The resulting gas mixture (air plus the remaining Kr) was sent to bed 2 also at 233 K where Kr was selectively removed. The hypothesis was that by removing Xe in bed 1, the adsorption capacity of Kr would be higher in bed 2 because Xe was no longer present to compete for sorption sites. These experiments were performed at 233 K because the breakthrough for Xe and Kr would be too short for the experimental set-up used (amount of MOF, experimental apparatus, etc). Therefore, selection of 233 K as the test temperature allowed sufficient time for the switch between one adsorption bed and the other. Based on these encouraging results future tests will be planned to demonstrate the operability at higher temperatures.

Two separate experiments were conducted with the two stage adsorption modules. In the first experiment, both beds were loaded with 0.92 g of NiDOBDC. In the second experiment, bed 1 was loaded with 0.92 g of NiDOBDC and bed 2 was loaded with 1.15 g FMOFCu. The Xe and Kr mixture in air (400 ppm Xe and 40 ppm Kr in dry air) with a flow rate of 330 mm³/s (20 sccm) was passed through the bed 1 until the outlet concentration of Kr equaled the inlet concentration. At this point, the outlet gas mixture (40 ppm Kr in dry air with less-than-detectable Xe) from bed 1 was passed through bed 2

Separations and Waste Forms
2013 Accomplishments Report

containing NiDOBDC. The breakthrough time of Kr from the bed 2 was recorded to determine the Kr capacity. In Figure 68, the breakthrough time of Kr from bed 1 loaded with the Ni/DOBDC was 366 s while the breakthrough time of Kr from bed 2 was 960 s (without Xe in the gas mixture). In the second experiment, the Kr breakthrough time from bed 1 loaded with the NiDOBDC was 372 s (Kr and Xe competing for the same sites) while the Kr breakthrough time from bed 2 loaded with the FMOFCu was 2016 s (no competition with Xe). See the discussion below for the Kr capacity of FMOFCu with Xe and Kr present. These results clearly demonstrated that the retention time for Kr in bed 2 after removing Xe on bed 1 increased significantly enhancing Kr adsorption capacity and selectivity.

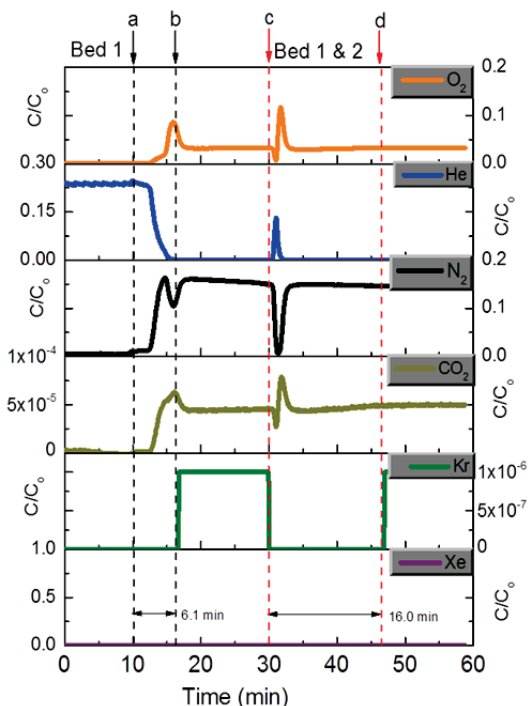


Figure 68. Breakthrough curves for gas mixtures using two bed adsorption modules at 233K. Adsorbents in bed 1 and 2 are NiDOBDC. a) Gas mixture [Xe (400 ppm), Kr (40 ppm) in air] into bed-1, b) gas mixture breakthrough from bed 1, c) Gas mixture from bed 1 (Xe removed) introduced to bed 2 d) breakthrough of Kr from bed-1.

The Kr capacities for NiDOBDC and FMOFCu in bed 1 and 2 at 233 K are summarized in Table 14. Both MOF materials can adsorb ppm levels of Kr from the gas mixture in the absence of Xe. The outlet gas stream leaving bed 2 contains only N₂, O₂, and CO₂ demonstrating the removal

of Xe and Kr at ppm levels with excellent capacities and selectivities at near room temperature. The Kr capacity of NiDOBDC from air containing 40 ppm Kr and 233 K increased from 0.24 mmol/kg (with Xe) to 0.61 mmol/kg (no Xe); an increase in capacity by a factor of 2.5. Similarly, Kr capacity of the FMOFCu increased from 0.28 mmol/kg to 1.03 mmol/kg; an increase by a factor of 3.7. Moreover, the results indicate if FMOFCu is used to capture Kr after removal of Xe, it can adsorb about 0.86 mass%. This is highest reported Kr adsorption capacity at 233 K from gas mixture containing 40 ppm Kr in air. The increase in Kr capacity is due to the reduction of competitive adsorption of Xe. The larger enhancement factor of FMOFCu is caused by the special pore size and geometry. As mentioned earlier, the FMOFCu has bottleneck windows with a diameter close to the kinetic diameter of Kr (0.360 nm) and are smaller than the corresponding Xe diameter (0.396 nm). Therefore, Kr can diffuse into pores of the FMOFCu easier when no Xe is present to block the pathway. This can explain the significant enhancement of Kr capacity for the FMOFCu. As for the Ni/DOBDC, no such size restriction exists and removing Xe molecules in advance just provides extra adsorption sites for Kr molecules. Therefore, the enhancement factor for Kr on Ni/DOBDC is smaller than that for FMOFCu.

Table 14. Kr capacities of two MOF materials at 233K from 40 ppm Kr in Air with and without Xe.

MOF	n_{Kr} (mmol/kg): Bed 1 of 2*	n_{Kr} (mmol/kg): Bed 2 of 2*	Enhance factor
Ni/DOBDC	0.24	0.61	2.5
FMOF-Cu	0.28	1.03	3.7

* 400 ppm Xe and 40 ppm Kr mixed in air was passed through bed 1 at 233K. The outlet gas stream with 40 ppm Kr but no Xe was passed through bed 2.

Radiation Stability of NiDOBDC

In a repository, a MOF containing ⁸⁵Kr would experience a substantial amount of radiation exposure as the ⁸⁵Kr decays to the stable isotope ⁸⁵Rb through beta decay with a half-life of 10.8 y. Over the repository lifetime of a MOF loaded to 50 mass% (much higher than the measured capacity of about 1 mass%) with ⁸⁵Kr, the total radiation exposure would be on the order of 10¹³ R. This is, of course, a very conservative case. For

Separations and Waste Forms 2013 Accomplishments Report

the work reported here, self-irradiation, i.e. incorporation of ^{85}Kr or another short-lived isotope was not possible. It was also not possible to irradiate a MOF sample for sufficient time to accumulate 10^{13} R exposure with the ^{60}Co source at PNNL. Four specimens of NiDOBDC MOF were irradiated in the High Exposure Facility (HEF) at PNNL with a ^{60}Co source that gave an exposure rate of 40 kR/h.

Four separate containers, each containing a NiDOBDC test specimen, were placed in the HEF. Exposure times of 1, 2, 4, and 7 days were used to attain exposures of 0.96×10^6 , 1.92×10^6 , 3.84×10^6 , and 6.72×10^6 R, respectively. After exposure to radiation, the surface area of Sample #1 was $800 \text{ m}^2/\text{g}$, Sample #2 $786 \text{ m}^2/\text{g}$, Sample #3 $889 \text{ m}^2/\text{g}$, and Sample #4 $878 \text{ m}^2/\text{g}$ compared to NiDOBDC before radiation exposure ($933 \text{ m}^2/\text{g}$). Within the experimental error, the surface areas were unchanged by irradiation.

As shown in Figure 69, the uptake of Xe and Kr by NiDOBDC after radiation was 20% and 36% less than the capacity before irradiation. This reduction is, in part, caused by the presence of a small amount of impurity found in the specimens exposed to radiation, but not in the specimen to which these sorption data were compared. This impurity was identified as nickel formate in the X-ray diffraction pattern (not shown). Another possibility for the reduction in Xe and Kr capacities is the improper activation of samples used in the radiation experiments. To prove this, sorption experiments with NiDOBDC specimens that have no impurities are needed.

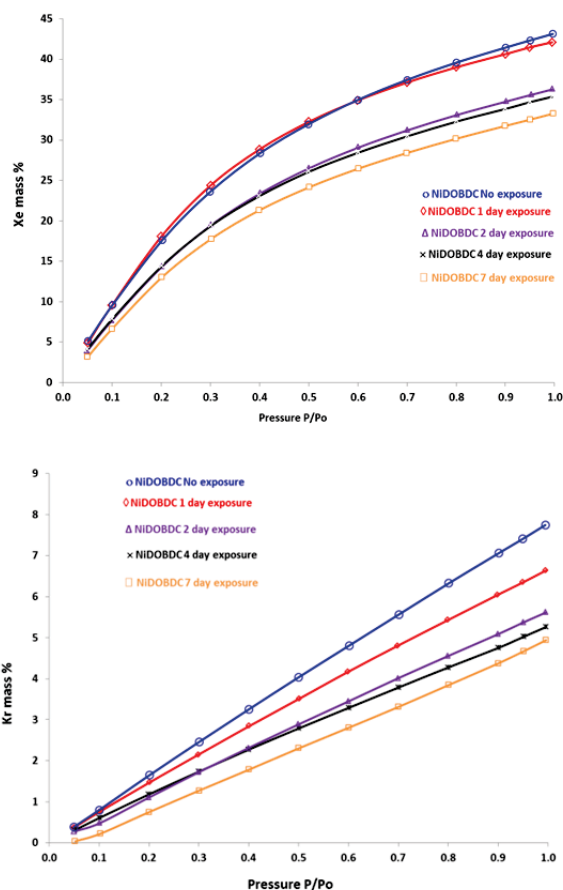


Figure 69. Xenon (top) and Kr (bottom) adsorption measurements after exposed to radiation.

Scale-up

The team was able to scale up the amount of NiDOBDC MOF from about 100 mg per run to 10 to 15 g per run. While this may seem like a very small amount of material, in the world of MOFs this is a large increase in the amount of material per batch. This increase was accomplished in the PNNL “Milligrams to Kilograms” facility, a facility developed specifically because MOFs and other materials for carbon sequestration were only available in mg quantities. Being able to scale production to 10grams is a major step forward. For this particular MOF, this is the first time that this scale has been accomplished. A few MOFs have been manufactured at 25-g scale at BASF, but the NiDOBDC was not one of them.

Over the past few months, the team has been working on producing 60 grams of NiDOBDC MOF for testing at INL for separation of Kr and Xe at room temperature. The NiDOBDC was

Separations and Waste Forms
2013 Accomplishments Report

produced by us and others in a small scale (100 mg) with the procedure described in previous reports. One of the initial batches contained a nickel formate impurity and the source of the impurity is under investigation.

Publications

1. Liu, J., D. Strachan, and P. Thallapally (2014). "Enhanced Noble Gas Adsorption in Ag@MOF-74Ni Article" *Chemical Communications* 2014, DOI: 10.1039/C3CC47777K
2. Thallapally, P., and D. Strachan (2013). "Initial proof-of-principle for Radiation Stability of NiDOBDC MOF." PNNL-22518. Pacific Northwest National Laboratory.
3. Thallapally, P., J. Liu, and D. M. Strachan (2013). "Demonstrate the Removal Efficiency and Capacity of MOF Materials for Krypton Recovery." PNNL-22693. Pacific Northwest National Laboratory.
4. Soelberg, N., T. Garn, M. Greenhalgh, J. Law, R. Jubin, D. Strachan, and P. Thallapally (2013). "Radioactive Iodine and Krypton Control for Nuclear Fuel Reprocessing Facilities." *Science and Technology of Nuclear Installations*, Article ID 702496
5. Fernandez, C., J. Liu, P. Thallapally, and D. M. Strachan (2012). "Switching Kr/Xe Selectivity with Temperature in a Metal-Organic Framework." *Journal of the American Chemical Society* 134, 9046-9049.
6. Liu, J., P. Thallapally, and D. Strachan (2012). "Metal-Organic Frameworks for Removal of Xe and Kr from Nuclear Fuel Reprocessing Plants, *Langmuir*, 28, 11584-11589.

Off-Gas Adsorption Modeling

V. J. Rutledge and J. D. Law, jack.law@inl.gov

The absence of industrial scale nuclear fuel reprocessing in the United States has limited the drivers for developing the advanced simulation capability focused on reprocessing plant operations. A capability of accurately simulating the dynamic behavior of advanced fuel cycle separation processes will provide substantial cost savings and many technical benefits.

During the processing of UNF, volatile radionuclides controls are needed to reduce the release of volatile radionuclides to regulatory limits [Jubin, et al., 2012]. The volatile radionuclides of concern are ^3H , ^{14}C , ^{85}Kr , and ^{129}I . Methods are being developed to capture these radionuclides. Dynamic models are under development to simulate adsorption / absorption of these radionuclides in the off-gas systems.

Currently, a general dynamic adsorption model has been developed and incorporated in the Multi-physics Object Oriented Simulation Environment (MOOSE) code that is being developed at the INL. Within the MOOSE code is a set of OSPREY models with which the behavior of the volatile radionuclides is calculated. These models handle the behavior of the volatile radionuclides once they enter the off-gas streams. Inputs to the models include gas composition, sorbent and column properties, equilibrium and kinetic data, and inlet conditions. Each model in the code has as an output the component concentrations along the length of the column as a function of time, ultimately leading to the time at which breakthrough occurs. The breakthrough calculations can be used to determine bed capacity, which, in turn, can be used to size columns. The model also can be used to calculate the temperature and the pressure drop along the column length as a function of time.

The OSPREY code contains a general adsorption model in which the user can change parameters and species in order to simulate specific systems. Submodels for simulating the behavior of specific gaseous species are being developed within OSPREY. Experimental data collected at the INL and system parameters were used for the development of a model specific for krypton adsorption.

A collaboration between FCRD Off-gas Sigma Team members and a Nuclear Energy University Programs (NEUP) grant including ORNL, Syracuse University, and Georgia Institute of Technology (GIT) has been formed to develop off gas models and support off-gas research. Through this collaboration an initial tritium specific model has been developed. The OSPREY code has been integrated with the Generalized Statistical Thermodynamic Adsorption (GSTA)

Separations and Waste Forms
2013 Accomplishments Report

Isotherm model that was created at GIT. Since GSTA is a generalized isotherm model, it should work for a wide variety of isotherms, including the Langmuir Isotherm for which the OSPREY code was initially developed. The integration of OSPREY with the GSTA isotherm model broadens the use of the OSPREY code beyond the Langmuir-type adsorption case.

References

1. Jubin, R. T., N. R. Soelberg, D. M. Strachan, and G. Ilas (2012). "Fuel Age Impacts on Gaseous Fission Product Capture During Separations.." FCRD-SWF-2012-000089. Oak Ridge National Laboratory.

Publications

1. Rutledge, V. J. (2013). "Osprey Model." INL/EXT-13-28150. Idaho National Laboratory, January.
2. Rutledge, V. J., L. Tavlarides, L. Ronghong, A. Ladshaw (2013). "Tritium Specific Adsorption Simulation Utilizing the OSPREY Model." FCRD-SWF-2013-000384, Idaho National Laboratory, September.
3. Rutledge, V. J. (2013). "Off-gas Adsorption Model and Simulation." *Proceedings from GLOBAL 2013*, Salt Lake City, UT, September.

Assessment of the Iodine Pathways and Off-Gas Stream Characteristics

R. T. Jubin, jubinrt@ornl.gov, D. M. Strachan, and N. Soelberg

UNF is currently being reprocessed in only a few countries, notably France, England, Japan, and Russia. In a previous document, the requirements for treating off-gas streams from the reprocessing of UNF and the implications of current United States regulations that set the limits for releases from such a facility were addressed at the plant level [Jubin, et al., 2012]. These regulations ultimately dictate the decontamination factor (DF) that must be met in the facility. That report focuses on the four primary volatile radionuclides: ^3H , ^{14}C , ^{85}Kr , and ^{129}I . Some flexibility in the approaches to addressing the requirements exists, however. For the cases

described in the "fuel age report" [Jubin, et al., 2012], several options for meeting regulations are discussed, including fuel "aging" to allow short-lived radionuclides to decay prior to reprocessing, apportioning environmental releases to different radionuclides, siting of the reprocessing facility, designing equipment to mitigate effects of releases (such as stack height and other parameters that affect air dispersion). The discussion in that report is limited to the overall plant DF that would be needed to meet the regulatory requirements, but does not address the complexity of the distribution of the volatile species within the plant as depicted in Figure 70.

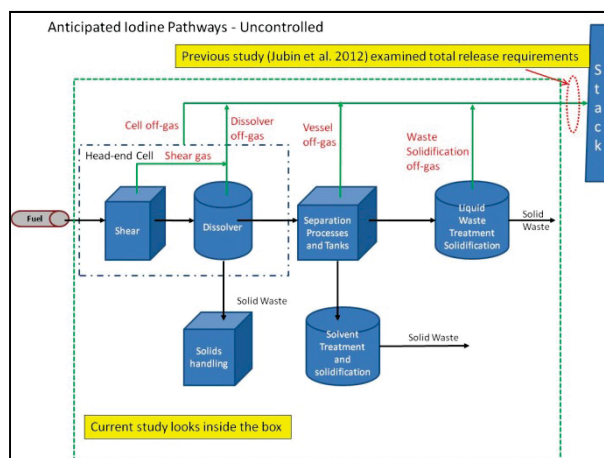


Figure 70. Schematic of typical unit operations for an aqueous-process-based UNF reprocessing plant.

Since the gaseous radionuclides can partition to different off-gas streams associated with the various unit operations within the reprocessing plant (aqueous), for example, from the head-end, dissolver, vessel, cell, and melter, an understanding of each of these streams is critical. Each of these off-gas streams has a range of flow rates and compositions and could have different gaseous radionuclide control requirements, depending on how the gaseous radionuclides partition. In the current report [Jubin, et al., 2013], the available literature is reviewed to summarize specific engineering data on the flow rates, forms of the volatile radionuclides in off-gas streams, distributions of these radionuclides in these streams, and temperatures of these streams. This document contains an extensive bibliography of the information contained in the open literature, but there is no discussion of volatile radionuclide

Separations and Waste Forms
2013 Accomplishments Report

behavior during electrochemical or other non-aqueous UNF separations processes.

Iodine removal has always been primarily focused on the head-end off-gas operations. But, in light of the estimated iodine emissions control efficiencies of up to 99.9% or higher needed to meet U.S. regulatory requirements, the control of iodine in just the dissolver off-gas is insufficient. This is borne out with actual operating experience and tests with actual nuclear fuel that show iodine evolution from the dissolver solution into the dissolver off-gas ranges between 95 and 99% of the iodine inventory for any batch of fuel dissolved. Iodine evolution from the dissolver solution can be improved to >95% with NO₂ sparging and the addition of KIO₃ to the dissolver solution. Several studies have shown that much of the residual iodine in the dissolver solution is in the form of colloidal iodine (AgI and PdI₂); organic iodides formed in the dissolver also factor into the iodine retention. Colloidal iodine is slow to react, being surface kinetics dominated, hence results vary depending on the length of sparging time. These forms of iodine result in 1-5% of the iodine in a fuel batch being retained in the dissolver solution. This iodine, along with the organic iodides that form from the organics in the new or recycled nitric acid, is carried with the dissolver solution and undissolved solids into other parts of the plant, where it evolves into other off-gas streams. Even if the iodine in the dissolver off-gas is efficiently controlled, the iodine in other reprocessing facility off-gas streams may also need to be controlled to achieve a total iodine emissions control consistent with regulatory requirements.

The flow of the vessel off-gas stream may be on the order of 10 times greater than that of the dissolver off-gas stream. This stream typically contains 40–50% of the iodine that remained in the dissolver solution. Hence, the iodine concentrations in this stream may be lower than the dissolver off-gas concentrations by as much as a factor of 10⁵ because of the higher gas flow rates and lower, but not insignificant, quantities of iodine present. A significant fraction of the iodine in the vessel off-gas is organic iodides.

Results reported in the literature suggest that 40 to 50% of the iodine in the dissolver solutions

transfers to the organic solvent. Some of these organic iodides are volatile and report to the vessel off-gas, while other iodides are less volatile and accumulate in the used solvent. Caustic washing of the used solvent during solvent recovery does not remove significant quantities of this iodine.

A limited amount of information was found on the release of iodine during waste solidification operations. The quantities of release were found to be process specific. The range of release was estimated to be between 0.1 and 1% of the iodine inventory in the plant; still sufficiently high to be of regulatory concern and, therefore, require removal. Limited information was found on the solubility of iodine in typical waste borosilicate glasses.

Figure 71 summarizes graphically the major iodine pathways and iodine distribution within an aqueous reprocessing facility. Based on this study [Jubin, et al., 2013], four major iodine release pathways have been identified as potentially needing treatment to prevent the release of iodine to the stack:

- Dissolver off-gas, including the off-gas from the fuel shearing operation;
- Vessel off-gas, including the vents from the process operations and tanks within the facility;
- Off-gas from liquid waste solidification, including the production of waste forms from the primary off-gas system traps. Vents from the waste storage tanks in this section of the plant must also be connected to iodine-trap system;
- Treatment activities on used solvent and on the solidification of discarded used solvent.

The head-end cell gas may or may not need treatment for iodine removal, as it is not expected to contain more than about 0.2% of the iodine processed in the plant. Results from the literature also suggest that iodine removal is needed even during plant idling, because sufficient iodine accumulates in the vent lines to result in a slow but significant release.

Separations and Waste Forms
2013 Accomplishments Report

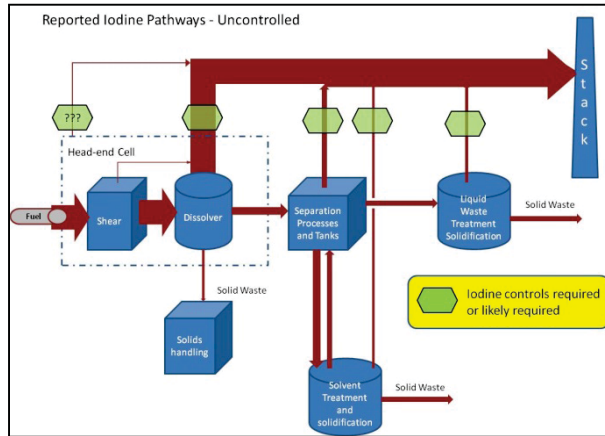


Figure 71. Summary iodine pathways and distribution throughout an aqueous reprocessing facility.

References

1. Jubin, R. T., N. R. Soelberg, D. M. Strachan, and G. Ilas (2012). "Fuel Age Impacts on Gaseous Fission Product Capture During Separations." FCRD-SWF-2012-000089. Oak Ridge National Laboratory.
2. Jubin, R. T., D. M. Strachan, and N. R. Soelberg (2013). "Iodine Pathways and Off-Gas Stream Characteristics for Aqueous Reprocessing Plants – A Literature Survey and Assessment." FCRD-SWF-2013-000308. Oak Ridge National Laboratory.

CHAPTER 7
FUNDAMENTAL SCIENCE, MODELING AND
SIMULATION

CHAPTER 7: FUNDAMENTAL SCIENCE, MODELING AND SIMULATION

Leigh Martin, leigh.martin@inl.gov

Metal Corrosion Mechanisms

Deterministic Modeling of Metal Alloy Passivation and Corrosion Properties

X. Y. Liu, xyliu@lanl.gov, and C. D. Taylor, cdtaylor@lanl.gov

The development of advanced waste forms for disposition of fission products, particularly technetium, requires a science-based approach to the prediction of their resistance to environmental degradation. In the case of metallic alloy waste forms, as proposed as part of the Waste Forms and Separations Campaign, the fundamental degradation mechanism is via corrosion. Although the corrosion properties of technetium alloy waste forms can be simulated by electrochemical testing, a fundamental understanding, pertinent to performance over geological timeframes, can be obtained using deterministic, *ab initio* models. The objectives of this project are currently focused on obtaining a detailed model of the passivation properties, by simulating the oxide films that form on candidate alloy waste forms comprised primarily of Fe, Mo, Cr and Tc.

R&D Overview

In FY 2013, R&D activities focused on determining the optimal density functional theory models for accurate prediction of technetium dioxide properties using quantum mechanical, electronic structure-based codes (see Figure 72). Once this objective had been achieved, the optimal models were then applied to simulate the growth of oxide films on close-packed surfaces of technetium metal. The first-principles database was then applied to develop an interatomic potential following the Reactive Force Field method that will enable the simulation of larger scale features of the alloy waste forms relevant to corrosion, such as intermetallic phases and grain-boundaries.

Electrochemical testing at LANL was also conducted to provide a means for validating the predictions made by these methods. A kinetic Monte Carlo scheme developed in a previous year of the project was applied to simulate the active dissolution of the alloy systems, Fe-Tc, Mo-Tc and Ni-Tc, in order to find optimal alloy combinations that limit the corrosion rate of the material in a worst-case corrosion scenario. First-principles modeling was also applied to simulate the reactions of water, hydrogen and oxygen on alloy metal surfaces.

Results

The work completed in FY 2013 provides the foundation for FY 2014 and FY 2015 efforts to model oxide stability and corrosion properties of candidate alloy waste form materials. Researchers considered the mechanism of technetium oxidation, beginning with computing the properties of the oxide using a number of first-principles approaches, and then moving to oxygen chemisorption and multilayer oxide growth. Researchers examined a number of surface terminations for the TcO₂ oxide phase and found that the “striped” non-polar surface termination was preferred (see Figure 72). The multilayer models developed in this work can be used as templates to study the kinetics of oxide growth and to develop first-principles derived interatomic potentials for metallic systems containing Tc that undergo oxidation.

Separations and Waste Forms
2013 Accomplishments Report

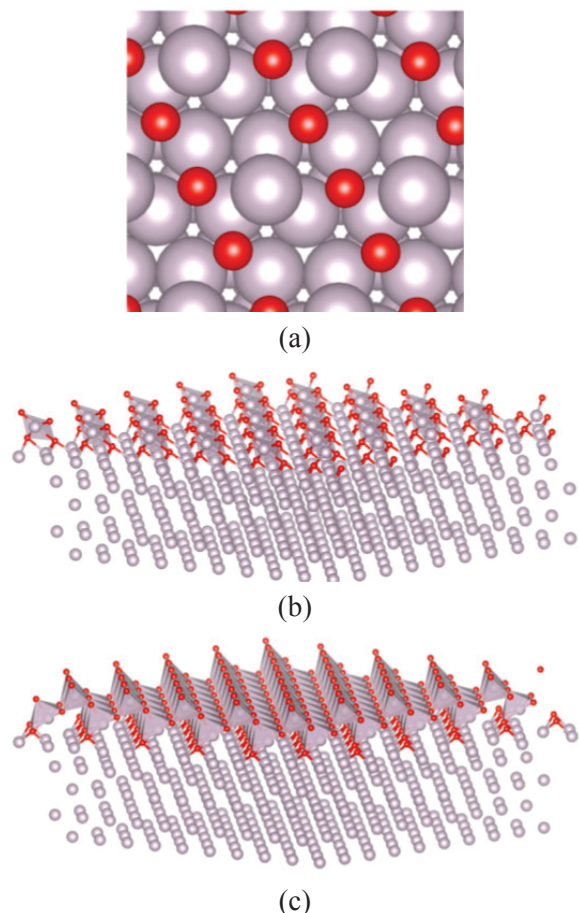


Figure 72. First-principles models for the initial growth of oxides on technetium metal (a) half-monolayer, (b) full mono-layer and (c) a bilayer.

Corrosion is a natural process facilitated by electrochemical processes occurring in aqueous conditions due to the interaction between the metal and the solvent. The equilibrium potential between Tc and its various oxidized species as a function of pH, so called a Pourbaix diagram, can be used to map out the lines of equilibrium between different reactions as potential and acidity are varied. The Eh-pH diagram of the Tc-O-H system has been constructed by solving the Nernst equations for possible reactions between Tc and its oxidizing products and compared to available experimental data (see Figure 73). The available experimental data taken for Tc, TcO₂ and TcO₄⁻ fall nicely into the estimated stability region at pH= 4. Future electrochemical analysis will yield additional data for the alloy systems, as well as the theoretical construction of surface phase diagrams for these alloy materials.

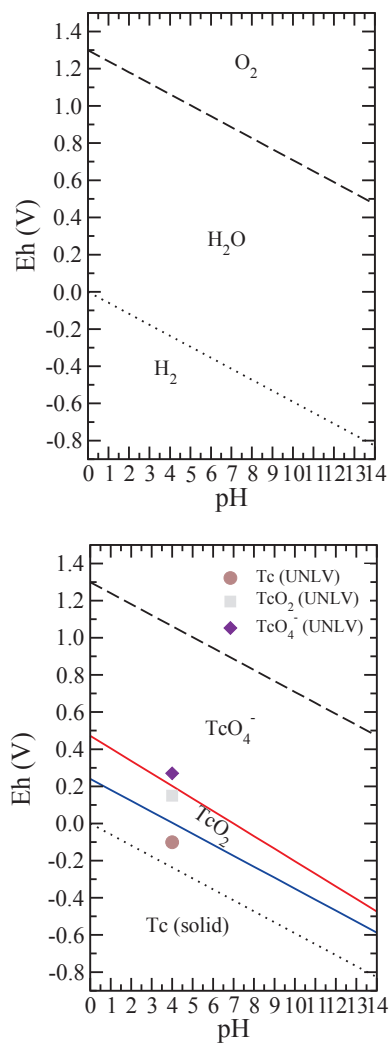


Figure 73. Pourbaix diagrams plotting the equilibrium potential (E) as a function of pH in pure water (top) and the system Tc-O-H (bottom) at 1.0 M, 298.15K, and 1.0 atm. In pure water, two possible cathodic reactions are $O_2 + 4H^+ + 4e^- = 2H_2O$ (long dashed line) and $2H^+ + 2e^- = H_2$ (short dotted line). In the system Tc-O-H, two possible reactions, in equilibrium with solid Tc, are $TcO_2 + 4H^+ + 4e^- = Tc + 2H_2O$ (blue) and $TcO_4^- + 8H^+ + 7e^- = Tc + 4H_2O$ (red). The potential plotted on the y-axis is in units of volts relative to the standard hydrogen electrode. Solid circle, square, and diamond are from experimental data, representing for Tc, TcO₂, and TcO₄⁻, respectively.

Publications

1. Taylor, C. D., and X. Y. Liu (2013). "Investigation of Structure and Composition Control Over Active Dissolution of Fe-Tc Binary Metallic Waste Forms by Off-Lattice Kinetic Monte-Carlo Simulation." *Journal of Nuclear Materials*, 434 382-388.

Separations and Waste Forms
2013 Accomplishments Report

Technetium Incorporation into Iron Oxides

F. N. Smith, frances.smith@pnnl.gov

During the reprocessing of commercial nuclear fuels or the vitrification of high-level defense waste, technetium is an element of concern due to its volatility and tendency to partition among different waste streams. One solution is to capture Tc in metallic waste forms (e.g., Fe-Tc alloys) as part of the separations and/or vitrification process. Since corrosion is a concern during the long-term storage of metallic waste forms, an atomic-scale understanding of Tc incorporation mechanisms into iron oxide corrosion products is necessary. Here, quantum-mechanical calculations are being used to evaluate the energy of different Tc incorporation scenarios into bulk goethite (α -FeOOH), a common corrosion product and potential waste form itself. Technetium speciation in near-surface environments will ultimately be evaluated.

The two main questions being addressed in this study are: (1) how is Tc incorporated into the bulk goethite (α -FeOOH) structure; and (2) how stable is Tc in near-surface (i.e., slab) environments. The latter will be investigated both in the absence and presence of adsorbates, such as water (H_2O), oxygen (O_2), hydrogen (H_2) and peroxide (H_2O_2), which contribute to the understanding of the long-term behavior of these iron oxides under potential waste-storage environments, including radiolysis scenarios.

The purpose of the first year of this study is to investigate incorporation mechanisms for Tc in goethite (α -FeOOH) as a first step in understanding the long-term stability of iron oxide corrosion products in minimizing radionuclide transport in the environment. The favorability of different Tc incorporation mechanisms in bulk goethite are being evaluated, as well as the effect of increasing Tc concentrations on incorporation energies. Comparisons are being made with previous modeling efforts on Tc incorporation into hematite (α -Fe $_2$ O $_3$), where charge-balanced Tc(IV) substituting for structural Fe(III) was found to be more stable than Tc(VII) incorporated into an interstitial site as the pertechnetate anion (TcO $_4^-$; Skomurski et al., 2010a). Recent experimental work indicates that Tc(IV) likely substitutes directly for Fe(III) in goethite, and once in the

structure, Tc is hard to oxidize and leach [Um, et al., 2011]; however, the exact exchange mechanism of that incorporation remains unknown.

By exploring the stability of Tc in the bulk goethite structure, the ground work is laid for evaluating the stability of Tc in surface slab environments, both in the presence and absence of adsorbates such as H_2O and O_2 , as well as radiolytic species such as H_2 and H_2O_2 . While this study begins with goethite, similar methodology can also be extended to include magnetite (Fe(II)Fe(III) $_2$ O $_4$), a common corrosion product of steel under appropriately anoxic or reducing conditions (Dodge et al., 2002), and a potential host for Tc(IV) based on recent experimental work involving titanomagnetite nanoparticles [Liu, et al., 2012]. Due to the single oxidation state of iron in goethite, however, it serves as a more straightforward starting point for evaluation of possible Tc-incorporation mechanisms and stability in this, and other, iron oxide phases.

This modeling effort is part of a larger body of modeling and experimental studies being performed on Fe-Tc metallic systems at University of Nevada, Las Vegas and LANL. The properties of alloyed and unalloyed Fe, Mo and Tc surfaces of various phase/composition and orientation were previously computed by Density Functional Theory (DFT) [Taylor, 2011a,b], and both water and oxygen were found to react with the unalloyed and alloyed materials, forming passive oxides.

Methodology

Charge localized, ab initio methods are being used to explore possible Tc incorporation scenarios in bulk goethite. Specifically, the modeling software CRYSTAL09 [Dovesi, et al., 2005; Dovesi, et al., 2009] is being used to optimize bulk goethite models. From these models, charge-balanced, coupled substitution mechanisms will be evaluated to calculate Tc incorporation energies. The unrestricted Hartree Fock level of theory, which allows for unpaired electronic spin, will be used based on previously successful modeling efforts involving the Tc-hematite system where discrete Fe(II)/Fe(III)/Tc(IV)/Tc(VII) charge distributions were maintained during structure and energy

Separations and Waste Forms
2013 Accomplishments Report

optimizations [Skomurski, et al., 2010a]. Combined HF-DFT methods may also be tested in order to better account for the exchange and correlation contributions to the ground-state energy of the system. Basis sets used for iron and technetium in previous studies [Skomurski, et al., 2010a, 2010b] will also be used here to provide a basis of comparison to other Tc-iron oxide systems.

Bulk Incorporation Energies

Strong spectroscopic evidence is presented by Um, et al. [2011] pointing towards the incorporation of Tc into goethite as Tc(IV) rather than Tc(VII). Based on the similarity in atomic radii between Tc(IV) and Fe(III), substitution into the octahedral Fe site is likely feasible. This type of mechanism is supported by previous modeling efforts where Tc(IV) was found to favorably substitute for Fe(III) in the hematite structure, along with the transformation of two Fe(III) to Fe(II) for charge balance [Skomurski, et al., 2010a]. Although goethite and hematite have different chemistries and structural arrangements of atoms, the Fe(III) coordination environment between them is similar and they are part of a temperature-based transformational series favoring hematite over goethite as temperature increases [Gualtieri and Venturelli, 1999]. As such, it is possible that similar Tc(IV) substitution mechanisms could be favored in both.

The following schematic is used to describe the method for calculating incorporation energy (E_{inc}) using atomic-scale models:

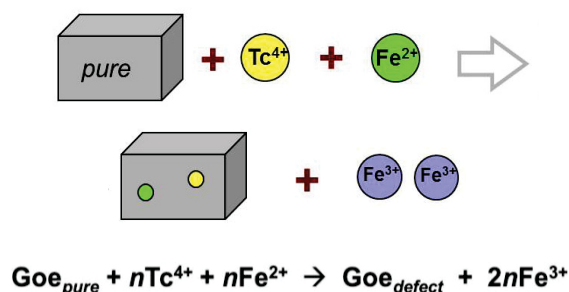


Figure 74. Schematic illustrating one possible charge-compensated substitution scheme where Tc^{4+} and Fe^{2+} replace two lattice Fe^{3+} in bulk goethite.

Here, the gray box on the left represents the pure (un-doped) iron oxide phase, and the

Tc(IV)/Fe(II)-doped or “defect” iron oxide phase on the right. In this case, two Fe(III) cations are removed to accommodate a charge-balanced substitution of Tc(IV) and Fe(II) into the bulk. The incorporation energy is the sum of the optimized energy for the doped iron oxide case and excised Fe(III) cations on the right, minus the sum of the energy of the optimized pure iron oxide plus the Tc(IV) and Fe(II) cations on the left. A negative incorporation energy would indicate favorable incorporation of the Tc(IV)/Fe(II) pair, while a positive energy would indicate unfavorable incorporation of the impurities. The cations being added or removed can be treated as gas phase species (as illustrated here) by calculating the energy of an atom in a box and accounting for its ionization energy. Alternatively, solid-phase references can be used, such as $\text{TcO}_2 \cdot x\text{H}_2\text{O}$ for Tc(IV), following the method described by Shuller, et al. [2013]. Solvation energies could also be applied substituting cations as well to simulate a more aqueous-based incorporation scenario.

The substitution scenario described above is not the only possibility, and a study by Kerisit, et al. [2011] illustrates a number of different incorporation scenarios for uranium of different oxidation states in goethite, magnetite, and hematite, evaluated using a molecular dynamics approach. In that study, charge compensated, vacancy compensated, as well as protonation/deprotonation schemes were used for incorporating various uranium (VI, V, and IV) moieties into those iron oxides. While not all of those incorporation schemes would be appropriate for accommodating Tc(IV) in the goethite structure based on charge differences, they suggest a number of reasonable alternatives to test in order to determine the most energetically-favorable Tc-incorporation method in bulk goethite.

Once an energetically favorable Tc incorporation scheme is identified, goethite super cells will be generated, into which increasing amounts of Tc can be added in the same fashion (see Figure 75). In this way, the effect of Tc loading on E_{inc} can be evaluated to determine if there is an incorporation limit for Tc in the goethite structure, or at least if a limit is approaching. Ultimately, surface slabs will be

Separations and Waste Forms
2013 Accomplishments Report

generated using the most stable incorporation mechanism to investigate the effect of free surfaces and adsorbates on Tc stability in iron oxide corrosion products of metallic Fe-Tc waste forms.

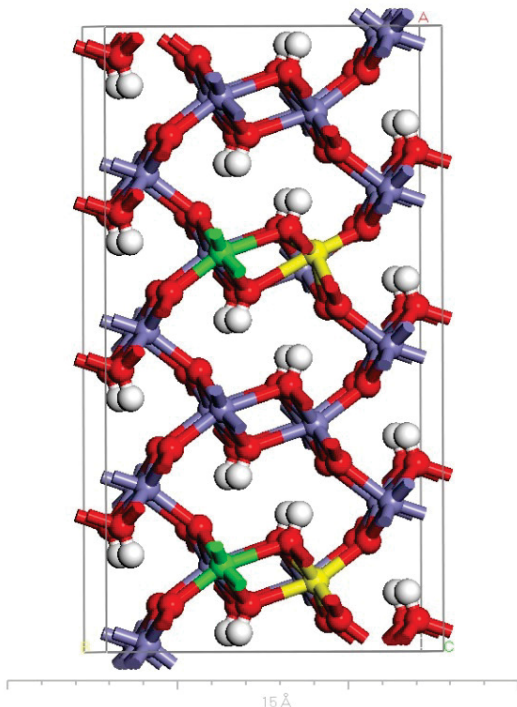


Figure 75. Goethite super cell illustrating a charge-compensated substitution of two Fe(II) (green) and Tc(IV) (yellow) pairs for four Fe(III) lattice atoms (purple). Red and white spheres are oxygen and hydrogen, respectively.

References

1. Dodge, C. J., A. J. Francis, J. B. Gillow, G. P. Halada, C. Eng, and C. R. Clayton (2002). "Association of Uranium With Iron Oxides Typically Formed on Corroding Steel Surfaces." *Environmental Science and Technology*, 36, 3504-3511.
2. Dovesi, R., R. Orlando, B. Civalleri, C. Roetti, V. R. Saunders, and C. M. Zicovich-Wilson (2005). "CRYSTAL: A Computational Tool for the Ab Initio Study of the Electronic Properties of Crystals." *Z. Kristallogr.*, 220, 571-573.
3. Dovesi, R., V. R. Saunders, C. Roetti, R. Orlando, C. M. Zicovich-Wilson, F. Pascale, B. Civalleri, K. Doll, N. M. Harrison, I. J. Bush, P. D'Arco, and M. Llunell, (2009)

CRYSTAL09 User's Manual. University of Torino.

4. Gualtieri, A. F., and P. Venturelli (1999). "In Situ Study of the Goethite-Hematite Phase Transformation by Real Time Synchrotron Powder Diffraction." *American Mineralogist* 84, 895-904.
5. Kerisit, S., A. R. Felmy, and E. S. Ilton (2011). "Atomistic Simulations of Uranium Incorporation into Iron (Hydr)oxides." *Environmental Science and Technology*, 45, 2770-2776.
6. Liu, J., C. I. Pearce, O. Qafoku, E. Arenholz, S. M. Heald, and K. M. Rosso (2012). "Tc(VII) Reduction Kinetics by Titanomagnetite (Fe_{3-x}Ti_xO₄) Nanoparticles." *Geochimica et Cosmochimica Acta* 92, 67-81.
7. Skomurski, F. N., K. M. Rosso, K. M. Krupka, and B. P. McGrail (2010a). "Technetium Incorporation into Hematite (α -Fe₂O₃)." *Environmental Science and Technology*, 44, 5855-5861.
8. Skomurski, F. N., S. Kerisit, K. M. and Rosso (2010b). "Structure, Charge Distribution, and Electron Hopping Dynamics in Magnetite (Fe₃O₄) (100) Surfaces from First Principles." *Geochimica et Cosmochimica Acta* 74, 4234-4248.
9. Taylor, C. D. (2011a). "Cohesive Relations for Surface Atoms in the Iron-Technetium Binary System." *Journal of Metallurgy* 2011, pp. 8.
10. Taylor, C. D. (2011b). "Surface Segregation and Adsorption Effects of Iron-Technetium Alloys from First-Principles." *Journal of Nuclear Materials* 408, 183-187.
11. Shuller, L. C., R. C. Ewing, U. and Becker (2013). "Np-Incorporation into Uranyl Phases: A Quantum-Mechanical Evaluation." *Journal of Nuclear Materials* 434, 440-450.
12. Um, W., H.- S. Chang, J. P. Icenhower, W. W. Lukens, R. J. Serne, N. P. Qafoku, J. H. Westick, Jr., E. C. Buck, and S. C. Smith (2011). "Immobilization of 99-Technetium(VII) by Fe(II)-goethite and

Separations and Waste Forms
2013 Accomplishments Report

Limited Reoxidation.” *Environmental Science and Technology* 4904-4913.

Thermodynamics and Kinetics

Thermodynamics and Kinetics of Advanced Separations Systems

L. Martin, leigh.martin@inl.gov

The overarching goals of the multi-national laboratory research on Thermodynamics and Kinetics of Advanced Separations systems is to study the behavior of the actinides and lanthanides in solvent extraction systems through fundamental chemical measurements. Through the combination of theory and experimental measurements, the research team of: Lawrence Berkeley National Laboratory (LBNL), Savannah River National Laboratory (SRNL) and ANL lead by INL are gaining a deeper understanding of the behavior of these metals in advanced separations systems.

In prior years the research at the INL has mainly focused on developing the techniques to further understand the thermodynamic and kinetic driving forces of the TALSPEAK separation. In FY 2013 a small portion of this research has been continued however the program is beginning to expand its horizons to encompass research into the building blocks of other potential separations systems.

One of the initial research activities performed in FY 2012 investigated the effects of metal extraction when changing the lactate counter ion in TALSPEAK separations to NH_4^+ , K^+ or Na^+ . A “standard” TALSPEAK extraction configuration of 0.17 M HDEHP in n-dodecane as the organic phase, 1M total lactate: 0.05M DTPA at pH3.6 in the aqueous phase was used for this investigation. The primary metals of interest were Ce^{3+} , Eu^{3+} , Am^{3+} and Cm^{3+} .

The distribution ratios for the metal ions studied show by changing the counter ion to potassium appeared to increase the distribution of all the metal ions under study whereas, when the counter ion was changed to the ammonium ion all metal ion extraction was seen to be suppressed (Table 15). Interestingly in the potassium system, there is a significant increase in the Cm extraction

that leads to an observed decrease in the Ce/Cm and Eu/Cm separation factors (Table 16).

Table 15. Distribution coefficients and separation factors for Ce^{3+} , Eu^{3+} , Am^{3+} and Cm^{3+} from different lactate buffer systems into 0.17 M HDEHP in n-dodecane. [lactate buffer] = 1.0 M, pH 3.6, 50 mM DTPA, all metal ions at tracer quantities.

Aqueous phase buffer	D_{Ce}	D_{Eu}	D_{Am}	D_{Cm}
Sodium Lactate	4.65 ± 0.20	3.84 ± 0.08	0.053 ± 0.001	0.041 ± 0.001
Potassium Lactate	7.50 ± 1.20	6.36 ± 0.20	0.082 ± 0.007	0.073 ± 0.001
Ammonium Lactate	2.83 ± 0.12	1.41 ± 0.11	0.033 ± 0.006	0.031 ± 0.001

Table 16. Summary of the separation factors for Ln / An as a function lactate buffer systems into 0.17 M HDEHP in n-dodecane. [lactate buffer] = 1.0 M, pH 3.6, 50 mM DTPA, all metal ions at tracer quantities.

Aqueous phase buffer	$\text{SF}_{\text{Ce/Am}}$	$\text{SF}_{\text{Ce/Cm}}$	$\text{SF}_{\text{Eu/Am}}$	$\text{SF}_{\text{Eu/Cm}}$
Sodium Lactate	87.1	113.1	72.0	93.5
Potassium Lactate	91.9	102.1	77.9	86.6
Ammonium Lactate	84.6	90.3	42.2	45.1

When these experiments were performed in the presence of macro amounts of metal ion (10 mmol), representative of more realistic operational conditions, both the sodium and potassium lactate system showed depressed metal distribution values. However, this trend was not universally observed in the ammonium ion system.

The extraction data for all metal ions under study, compare reasonably well with that previously measured from sodium lactate media (classic TALSPEAK aqueous phase). However, it can be seen from the results shown here that the lactate counter ion does have an effect on the individual metal ion distribution ratio. When the counter ion is changed to potassium the distribution values are seen to significantly increase but when the lactate counter ions are changed to the ammonium ion, the distribution values are somewhat depressed.

Separations and Waste Forms
2013 Accomplishments Report

In addition to the work detailed above, the DTPA complexation kinetics studies from FY 2012 were expanded to cover the lanthanide series. Rate constants for the reaction of DTPA with the lanthanide ions have been determined using lanthanide-Xylenol Orange dye complexes in aqueous solution range of temperatures at pH 3.6. These reactions were found to occur by two separate mechanisms, resulting in double-exponential decay kinetics. The faster decay of this study was DTPA-dependent. The forward complexation rate constants became slower for the higher lanthanides, ranging from $\sim 55,000 \text{ M}^{-1} \text{ s}^{-1}$ for Eu(III) to $3,500 \text{ M}^{-1} \text{ s}^{-1}$ for Lu(III) at room temperature. However, the measured Arrhenius and thermodynamic parameters for these two lanthanide ion complexations were effectively equivalent within experimental error; $\sim 80 \text{ kJ mol}^{-1}$ for E_a and DH^\ddagger and $\sim 100 \text{ J mol}^{-1} \text{ K}^{-1}$ for DS^\ddagger . From the intercept values determined in the pseudo-first-order kinetic runs, lanthanide-DTPA decomplexation rate constants were also calculated. The behavior of these rate constants was similar to that of the complexation data; showing a decrease in value from $\sim 150 \text{ s}^{-1}$ for Eu(III) to $\sim 10 \text{ s}^{-1}$ for Lu(III) and having very similar temperature-dependence; with E_a and $DH^\ddagger \sim 50 \text{ kJ mol}^{-1}$ and $DS^\ddagger \sim -50 \text{ J mol}^{-1} \text{ K}^{-1}$.

Experiments were continued in FY 2013 to measure the enthalpy of extraction using two-phase calorimetry for the solvating extraction system TOPO in toluene. The heat of extraction for the whole lanthanide series has been determined and can be seen in Figure 76.

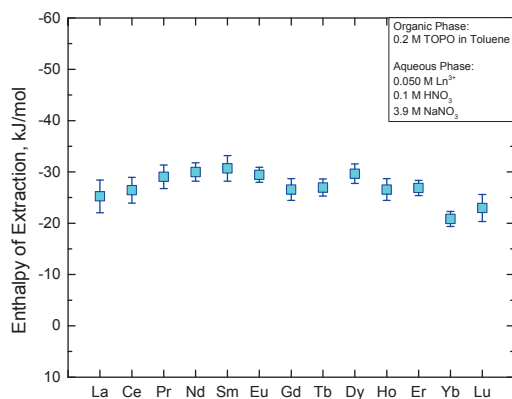


Figure 76. Measured heat of extraction for the lanthanide series. Aqueous phase = $0.05 \text{ M Ln}(\text{NO}_3)_3$, 0.1 M HNO_3 and 3.9 M NaNO_3 . Organic phase = 0.2 M TOPO in toluene.

The values determined across the series vary very little with the change in size of the metal ion in solution with the largest heat being that of Sm at $-30.69 \text{ kJ mol}^{-1}$ and the smallest being that of Yb at $-20.85 \text{ kJ mol}^{-1}$.

Publications

1. Nishihama, S., R. P. Witty, L. R. Martin, and K. L. Nash (2013). "Thermodynamic Features of Benzene-1,2-Diphosphonic Acid Complexes with Several Metal Ions." *Solvent Extraction and Ion Exchange* 31, 370-383.
2. Griffiths, T. L., L. R. Martin, P. R. Zalupski, J. Rawcliffe, M. J. Sarsfield, N. D. M. Evans and C. A. Sharrad (2013). "Understanding the Solution Behaviour of Minor Actinides in the Presence of EDTA, Carbonate and Hydroxide Ligands." *Inorganic Chemistry* 52, 3728-3737.

Thermodynamics for Actinides and Lanthanides Separation

L. Rao, lrao@lbl.gov

Objectives

To achieve accurate prediction and precise control of the behavior of actinides and lanthanides in the TALSPEAK process, Complexation of Cm(III) with two major components, lactate and DTPA, were systematically studied to determine the thermodynamic parameters of the reactions at different operating temperatures. These data, in comparison with the previous data on Ln(III), provide thermodynamic base to help interpret the separation behavior of Ln(III)/An(III).

Complexation of Cm with DTPA (10-70°C)

The experimental details and raw data at different temperatures were summarized in the FY 2012 report, but only the constants at 25°C were calculated and included in the FY 2012 report. In FY 2013, data at all other temperatures were processed and summarized in Table 17.

Separations and Waste Forms
2013 Accomplishments Report

Table 17. Thermodynamic data on the formation of $\text{Cm}(\text{dtpa})^{2-}$ ($I = 1.0 \text{ M NaClO}_4$). ^aValues of ΔH obtained by Van't Hoff equation. Method: sp – spectrophotometry, cal – calorimetry).

$t / ^\circ\text{C}$	Method	$\log\beta_1$	ΔH , $\text{kJ}\cdot\text{mol}^{-1}$	ΔS , $\text{J}\cdot\text{K}^{-1}\cdot\text{mol}^{-1}$
10	Sp	22.19 ± 0.11		
25	sp, cal	21.67 ± 0.09	-40.7 ± 2.1	277 ± 9
			-41.2 ± 2.2^a	278 ± 10^a
40	Sp	21.39 ± 0.14		
55	Sp	21.07 ± 0.15		
70	Sp	20.85 ± 0.18		

For the lanthanide/DTPA systems studied previously under this project, Nd(III) and Eu(III) form two complexes with DTPA: $\text{Ln}(\text{dtpa})^{2-}$ and $\text{Ln}(\text{Hdtpa})^{-3}$. Differing from the lanthanides, thermodynamic data from this study show that, in the temperature range from 10°C to 70°C , the trivalent actinides (Am^{III} and Cm^{III}) form only one complex with DTPA, $\text{An}(\text{dtpa})^{2-}$. This was demonstrated by the experimental spectrophotometric data and theoretical calculations.

DFT calculations were carried out to optimize the structures and compare the energies of HCmL^- and CmL^{2-} . The optimized structures are shown in Figure 77.

First, DFT calculations show that the structure with the proton on the carboxylate oxygen atom, as shown in Figure 77(a), is more stable by 0.5 eV than the structure with the proton on the amine nitrogen atom. Secondly, DFT calculations indicate that the EuL^{2-} species has a stronger affinity toward proton than the CmL^{2-} species (with a difference of $\Delta\Delta E(\text{H}^+) \sim 2.76 \text{ kcal/mol}$), which explains the reason that EuHL^- was observed, but CmHL^- was not under the same conditions.

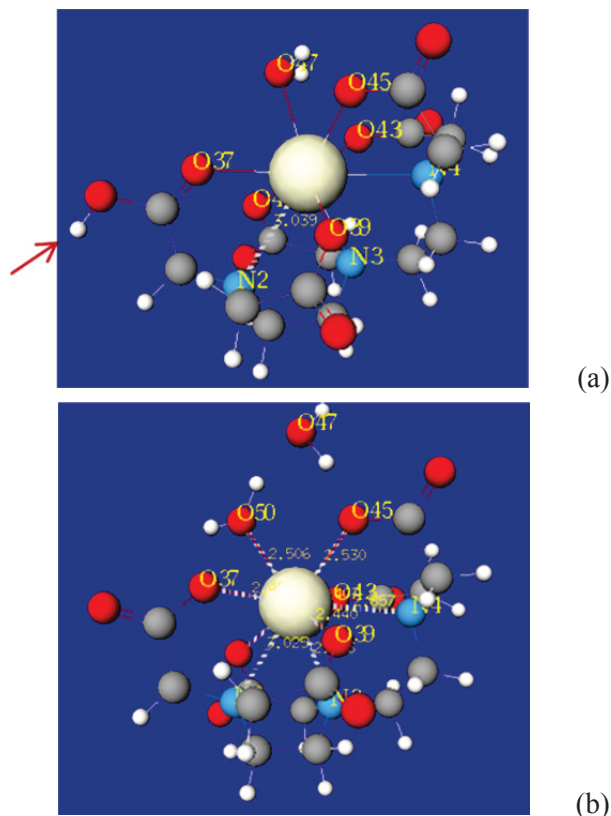


Figure 77. Optimized structures of DTPA complexes with $\text{An}(\text{III})$ and $\text{Ln}(\text{III})$. (a) HML^- with proton on the carboxylate O that is not bonded to the metal center. The position of the proton is indicated with a red arrow. (b) ML^{2-} with second water in the second solvation shell.

The complexation of $\text{Cm}(\text{III})$ with DTPA is more exothermic than that of $\text{Ln}(\text{III})$, which could be assumed to result from a stronger interaction of $\text{An}(\text{III})$ with the N donors in DTPA than that of $\text{Ln}(\text{III})$. Structural information from the DFT calculation supports such assumption.

Comparisons of the thermodynamic parameters between $\text{An}(\text{III})/\text{DTPA}$ and $\text{Ln}(\text{III})/\text{DTPA}$ are shown in Table 18 and Table 19.

Table 18. Formation constants of the DTPA complexes

t	$\log\beta$				
	CmL^{2-}	NdL^{2-}	HNdL^-	EuL^{2-}	HEuL^{2-}
10°C	22.19	20.48	22.8	21.31	23.58
25°C	21.67	19.97	22.2	21.00	23.27
40°C	21.39	19.85	21.99	20.8	23.08
55°C	21.07	19.8	21.81	20.5	22.6
70°C	20.85	19.49	21.68	20.33	22.43

Separations and Waste Forms
2013 Accomplishments Report

Table 19. Thermodynamic data on Cm(III)/lactate complexation at different temperatures ($I = 1.0\text{ M NaClO}_4$).

Reaction	$t\text{ }^\circ\text{C}$	$\log\beta_M$	ΔH $\text{kJ}\cdot\text{mol}^{-1}$	ΔS $\text{J}\cdot\text{K}^{-1}\cdot\text{mol}^{-1}$
$\text{H}^+ + \text{L}^- = \text{HL}(\text{aq})$	10	3.46 ± 0.04		
	25	3.67 ± 0.03	-0.55 ± 0.22	68 ± 1
	40	3.68 ± 0.04		
	55	3.70 ± 0.04		
	70	3.72 ± 0.04		
$\text{Cm}^{3+} + \text{L}^- = \text{CmL}^{2+}$	10	2.85 ± 0.24		
	25	2.80 ± 0.16	-0.4 ± 2.0	
	40	2.76 ± 0.22		
	55	2.78 ± 0.21		
	70	2.74 ± 0.31		
$\text{Cm}^{3+} + 2\text{L}^- = \text{CmL}_2^+$	10	4.97 ± 0.13		
	25	4.81 ± 0.05	-5.6 ± 1.2	
	40	4.60 ± 0.20		
	55	4.33 ± 0.31		
	70	4.18 ± 0.11		
$\text{Cm}^{3+} + 3\text{L}^- = \text{CmL}_3$	10	6.43 ± 0.25		
	25	6.32 ± 0.26	-11.9 ± 2.0	
	40	6.06 ± 0.21		
	55	5.78 ± 0.31		
	70	5.69 ± 0.30		

Complexation of Cm with Lactate (10–85°C)

The fluorescence emission spectra of Cm(III)-lactate titrations at 25°C are shown in Figure 78. As the ligand concentration increases, the intensity increases, and the peaks shift slightly to longer wavelengths. Similar variations in the spectra were observed at other temperatures. The formation constants for the 1:1, 1:2, and 1:3 Cm(III)-Lact complexes at 10–85°C were

calculated by analyzing the spectra, and are summarized in Table 19. The enthalpies of complexation determined by calorimetry agree with the values by van't Hoff extrapolation.

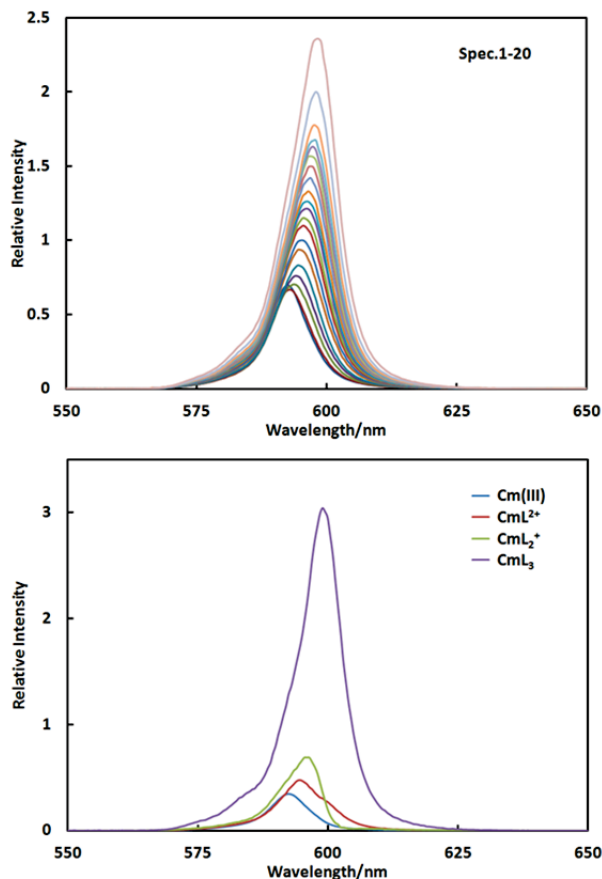


Figure 78. Fluorescence emission spectra of Cm(III)/Lactate solutions at 25°C. Initial solution: $V = 1\text{ mL}$, $[\text{Cm(III)}] = 0.0192\text{ mM}$, $[\text{H}^+] = 1.0\text{ mM}$. Titrant: 0.2/0.8 M NaL/NaClO₄, L = lactate, total addition of 0.21 mL.

The fluorescence lifetime, in conjunction with the speciation calculated from the thermodynamic parameters, indicates that lactate coordinates with Cm(III) through the “end-on” mode (Figure 79a), each replacing two water molecules.

Separations and Waste Forms
2013 Accomplishments Report

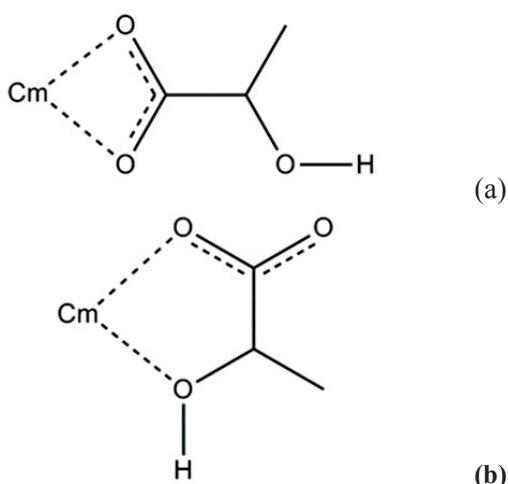


Figure 79. Possible coordination modes in Cm(III)/lactate complexes. (a) "End-on" mode; (b) "side-on" mode.

Computational and Spectroscopic Investigations of DTPA Complexes

L. Roy, lindsay.roy@srl.doe.gov

In FY 2013, work focused on two different tasks addressing how DTPA ligand interacts with *f*-elements by integrating experiment and computation programs to study DTPA speciation within the pH window of TALSPEAK using Raman spectroscopy. Initial studies focused on the DTPA ligand by analyzing the relevant ligand spectral peaks so as to identify the structural characteristics that differentiate the protonated species. TALSPEAK has been demonstrated to operate effectively over a very small pH range, and in the pH range, there are three possible DTPA species present. On paper, this seems like it would cause a significant effect in the chemistry of the extraction. Through the computational modeling, the effects are minute. The goal of this project is to understand ligand arrangement in solution and how it affects complexation within the pH window of TALSPEAK. The second task focused on Raman spectroscopy experiments on the coordination of the Metal-DTPA. In the pH window of TALSPEAK, there was almost no change in the spectra. This indicates that the coordination of the metal is independent of the pH of the system, as the majority of the protons are located on the amines, hence leaving the carboxylic acid groups available for coordination. Protonation of the amine moieties leads to strong

intramolecular interactions that help to orient the DTPA molecule to allow for a cage-like coordination with the metal center. The goal of this project is to understand metal-ligand complexation within the pH window of TALSPEAK.

Protonation studies began by looking at the first protonation sequence of the QM/MM optimized DTPA⁵⁻ structure. There are eight possible sites for coordination; five on the carboxylate groups and three on the nitrogen backbone. The three lowest energy structures are protonation on the nitrogen backbone, shown in Figure 80 with interatomic distance information. Labels 1 and 3 refer to protonation of the terminal nitrogen atoms, and label 2 is the protonation of the center nitrogen of DTPA. First, the energy difference between 1 and 3 is ~0.21 eV; solutions for these two calculations for all intents and purposes should be the same.

In species 1, the weak hydrogen bonding to the neighboring carboxylate groups is much weaker than in 3, based on bond distance. A weak hydrogen bond is characterized by having mainly electrostatic or dispersion interactions of hydrogen with the corresponding acceptor atom. The H---A bond lengths are generally between 2.2 and 3.3 Å and have a bond energy ~4 kcal·mol⁻¹.¹ Also, 3 has formed two five-membered rings with the carboxylate groups leading to the formation of a bifurcated hydrogen bond. Clearly, the weak bifurcated hydrogen bonding effect with the neighboring carboxylate groups causes an added stabilization effect. To quantify this effect, further NBO analyses probing the extent of hydrogen bonding will be continued and reported in the next fiscal year.

Separations and Waste Forms
2013 Accomplishments Report

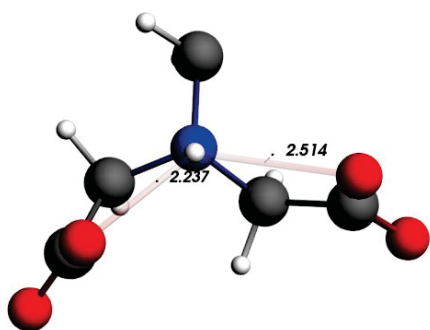
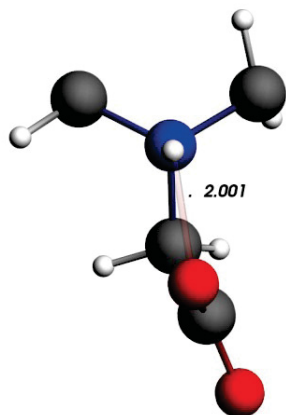
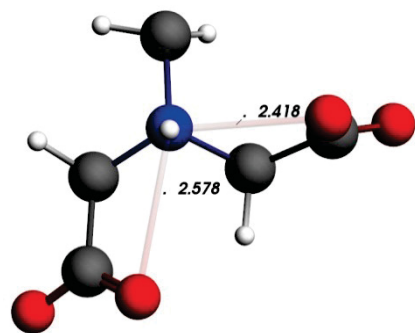


Figure 80. Structural information of the nitrogen fragments for the three lowest energy species in HDTPA^{4-} . The other atoms were removed for clarity. The bond distances are shown in Angstroms. The ADFView program generated the bond distances to 0.001 Å but accuracy is only to 0.01 Å.

When comparing 2 and 3, a similar five-membered ring is formed with the carboxylate groups and at a shorter distance than seen in 3. Energetically, solution 2 is only 0.004 eV higher in energy than 3; that energy difference is not within the computational error limit given the method. However, the results do lend some credence to the previous NMR results. Based on these calculations, both species are statistically possible in solution, especially at room

temperature. Protonation of the terminal nitrogen atom may be preferred because of the ability to form a bifurcated hydrogen bond with the two adjacent carboxylate groups, rather than just one hydrogen-bonded five-membered ring with the central nitrogen. The preliminary transition state geometry between 2 and 3 is shown in Figure 81. The structure is currently being verified to show that it is a saddle point on the potential energy surface. The barrier of transition is ~ 1.56 eV ($36 \text{ kcal}\cdot\text{mol}^{-1}$). The pathway appears to go through a five-membered ring structure formed from the terminal and central nitrogen atoms (the same conclusion to explain the first protonation species by Manning and Gravley).² It is possible that this type of exchange occurs continuously in the molecule.

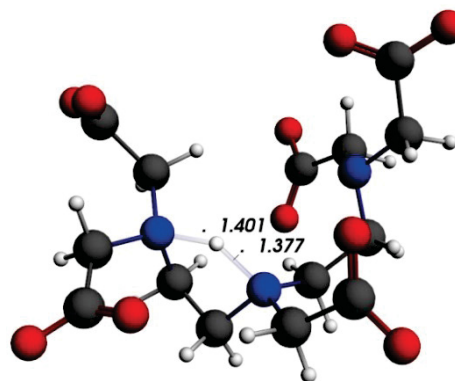


Figure 81. Structural information about the transition geometry between 2 and 3. The bond distances are shown in Angstroms. The ADFView program generated the bond distances to 0.001 Å but accuracy is only to 0.01 Å.

When doubly protonating DTPA^{5-} , there are 28 possible protonation structures. As expected, protonation of the terminal nitrogen atoms is the lowest energy structure; Both hydrogen atoms participate in bifurcated hydrogen bonding to the terminal carboxylate groups. There are 56 possible structure combinations when adding three protons to DTPA^{5-} . Interestingly, calculations predict protonation will occur on the two terminal nitrogen atoms and the carboxylate group coordinated to the central nitrogen atom. Then, ~ 0.05 eV above that structure is the all protonated nitrogen structure. In other words, the structure is stabilized by forming a 5-membered ring with the central nitrogen atom. It is important to point out that $\text{H}_3\text{DTPA}^{2-}$ is expected to be the primary

structure within the pH range of TALSPEAK. Although the calculations have not been performed yet, the transition barrier between the two structures is expected to be very small (on the order of 5-6 kcal·mol⁻¹). Analysis is still ongoing to verify these two structures and to describe the chemistry in acid/base terms. One theory could be that the basicity of the central nitrogen is lowered upon adding two equivalents of acid, thereby allowing for protonation to occur at the carboxylate group instead.

Preliminary studies investigating the metal complex studies were performed using lanthanum nitrate (La(NO₃)₃). Lanthanum was selected as an actinide equivalent because of its *f*⁰ electronic state as a 3+ cation and it will not fluoresce when interrogated by the laser. (Americium was shown to fluoresce with a 785 nm laser, preventing the direct evaluation of Am-DTPA complexes.) The model of [La^{III}(DTPA)(H₂O•2OMe₂)]²⁻ was built from the Nd^{III} and Am^{III} analogues. Figure 82 shows the structure of the La-DTPA model complex.

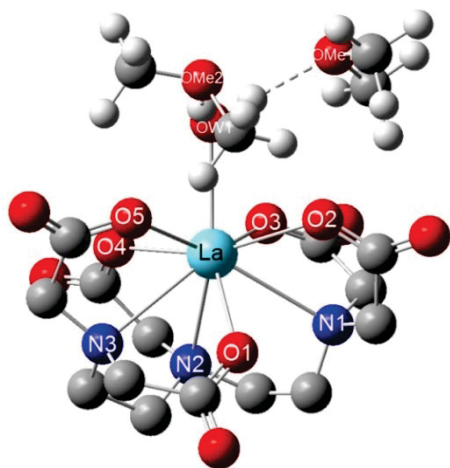


Figure 82. View of the optimized structure of [La^{III}(DTPA)(H₂O•2OMe₂)]²⁻. Hydrogen atoms on the DTPA⁵⁻ ligand are removed for clarity.

Comparison of the Raman spectra of [La^{III}(DTPA)(H₂O•2OMe₂)]²⁻ and [Am^{III}(DTPA)(H₂O•2OMe₂)]²⁻ show that there is good agreement between the two structures. The Raman spectrum of DTPA⁵⁻ is also included in the figure to show that structural differences will occur when a metal complex is formed. Therefore, the lanthanum analogue should provide useful

structural information on the protonation of the Am-DTPA. Like the previous experiments, the current results are preliminary, and additional Raman experiments are currently being performed on La-DTPA. Because the nitrate anion is problematic in these systems (nitrate shows a Raman response of ~1000 cm⁻¹), synthesis will use La(OH)₃ as the starting material. In Figure 83, the preliminary results of the DTPA @ pH=3 and La-DTPA indicate that there are significant changes among the spectra. As mentioned previously, this is expected as the chelation of a metal will significantly change the structure/electronics of the DTPA backbone. Notably, there is no change in the Raman spectra between pH 3 and 7 in the La-DTPA complex. This lack of change is to be expected since the chelation mechanisms of DTPA will have very small effect on the structure of the complex (since the change is only a proton).

Upon complexation, both experiment and theory show a pronounced doublet forms around 400 cm⁻¹ and the peak of DTPA @ pH=3 of about ~850 cm⁻¹. These librational modes are attributed to a rocking motion of the N-C backbone and the CO(O) modes, respectively. All of the other modes directly correlate to either free DTPA @ pH=3 or La(NO₃)₃.

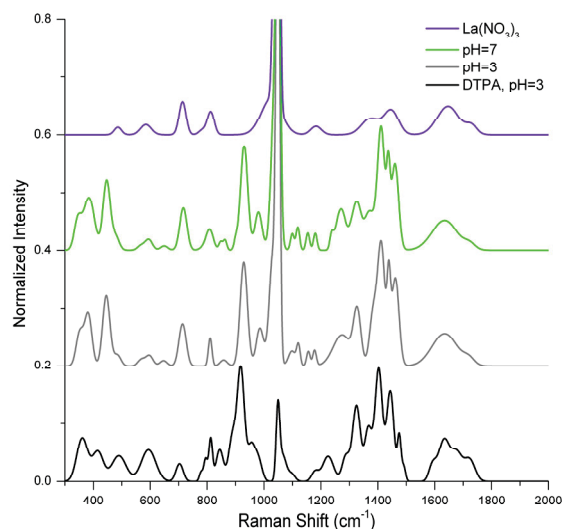


Figure 83. Preliminary Raman spectra of La-DTPA complexes at various pHs.

Through computational modeling, each of the three species can be investigated individually and their individual contributions can be weighed based on their concentration in the system. The

Separations and Waste Forms
2013 Accomplishments Report

models were verified through Raman spectroscopy for the uncomplexed DTPA, and were in agreement of the computationally calculated spectra. Preliminary experimental measurements of La-DTPA complex indicate that there is no change in the coordination environment. Computational models are currently running to confirm these experimentally observed spectra. Across the TALSPEAK process pH range, there are three different species that are present, but the chemical/electronically difference of these species is not significant enough to be the cause of the TALSPEAK pH profile.

References

1. Desiraju, G. R., and T. Steiner (2001). *The Weak Hydrogen Bond: In Structural Chemistry and Biology (International Union of Crystallography Monographs on Crystallography)*; Oxford University Press, USA.
2. Manning, T. J., and E. D. Gravley (1995). "PRotation Sequence Study of the Solutiokn Structure of DTOA by 1H NMR." *Spectrosc. Lett.* 28(3), 291-300.

Publications

1. Bridges, N. J., and L. Roy (2013). "Computational and Spectroscopic Investigation of the DTPA Complexes." SRNL-TR-2011-00185, Rev 0, Savannah River National Laboratory, August 30

Solvent Extraction Studies Using a Microfluidic Chip

A. Gelis, gelis@anl.gov, C. Launieri and J. Clemens (Texas A&M).

A system is proposed for probing metal-ligand coordination complexes during solvent extraction in a high throughput droplet microfluidics format. The modular system will be capable of simultaneously quantifying solvent extraction kinetics, monitoring metal concentrations and determining coordination environments of fluorescent metal ions in both the organic and aqueous phases. A microfluidic organic/aqueous droplet-based flow will enable rapid mixing and provide known interfacial areas between the immiscible phases to perform solvent extraction. Such a system is ideal for the study of complex

solvent extraction schemes including those used for actinide/lanthanide separation in nuclear fuel reprocessing. These schemes have complex extraction mechanisms involving extractants, buffering agents, and complexing agents which make kinetic modeling and chemical speciation studies very challenging. For this reason, the structures of extraction complexes are unknown and the fundamental chemistry underlying these systems is not yet understood. Researchers propose to overcome the challenges with a droplet microfluidic system that utilizes time resolved laser induced fluorescence spectroscopy (TRLIFS), accomplished with chip-integrated lenses and fiber optics, to probe the speciation of fluorescent lanthanides and actinides in real time. Measurements will be taken in the bulk phases and at the aqueous-organic interface as the droplets pass through a focal point, allowing the investigation of the intermediate metal-ligand species that form near the phase boundary. The coordination environments will be probed by measuring the change fluorescence decay lifetimes – which is known to change as inner-sphere coordination changes – with respect to reaction completion and distance from the phase interface. The extraction completion will be monitored using TRLIFS by correlating the emission intensity to offline concentration measurements using Atomic Emission Spectroscopy (AES). The fluorescence-emitting outer electron transitions in lanthanide and actinide ions are extremely sensitive to changes in the chemical environment due to interaction of the excited d-orbital electrons with the molecular orbitals of the ligands. This will be used to estimate the hydration number of the metal ion complexes in the organic phase, the aqueous phase, and at the interface.

To probe the metal ion's coordination environment and measure its interfacial mass transfer rate constants, the new system will build on previous iterations of droplet devices by incorporating on-chip optics for in-line spectroscopic analysis via TRLIFS. The concentrations of Eu(III) and Cm(III) can be measured by comparing the fluorescence emission intensity of the 5D0-7F0 and 8S7/2-6D7/2 transitions, respectively, with a series of calibration curves [Choppin and Wang, 1997]. Calibration curves will be developed by running

Separations and Waste Forms
2013 Accomplishments Report

pre-equilibrated solutions through the system, and correlating the emission intensity to the concentration measured by an inductively coupled plasma-atomic emission spectrometer. The lifetimes of the Eu(III) and Cm(III) fluorescent transitions, measured with respect to distance from the phase interface, will be used to probe the complex's coordination environment. The lifetime of the transition will depend on the inner coordination sphere of the metal in solution. The presence of high frequency oscillators (such as -OH groups) in the inner coordination sphere will decrease the fluorescence lifetimes through quenching [Supkowski and Horrocks, 2002; Kimura and Choppin, 1994]. When the metal chelates with buffers, complexing agents, and extractants, the fluorescence lifetimes in aqueous solutions will increase because the quenching -OH groups of water are displaced from the inner coordination sphere. This concept can be used to examine the structure of metal complexes.

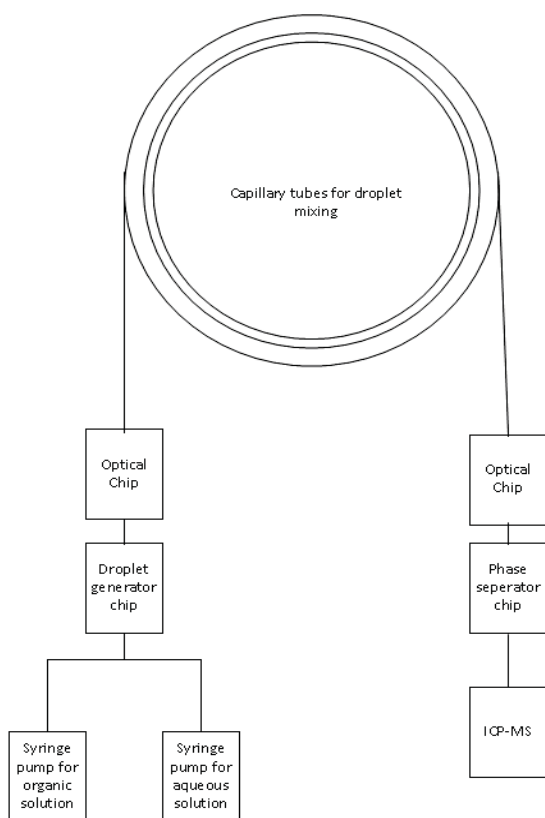


Figure 84. Lanthanide extraction system monitored by fluorescence spectroscopy. The pressure-driven droplet microfluidic system will include a droplet generator chip, an initial optical chip, capillary extraction tubing, a second optical chip, and a phase separator chip.

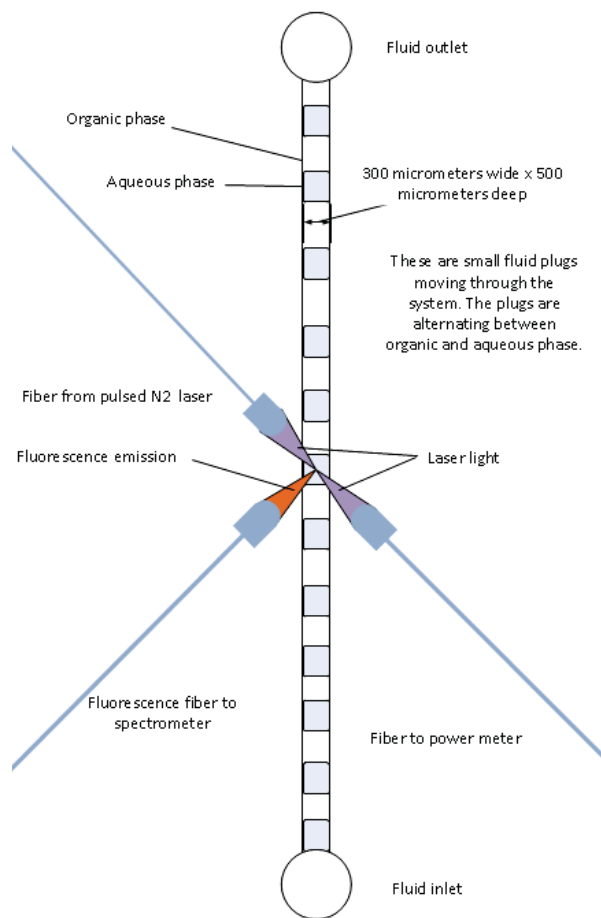


Figure 85. The optical chips have lenses that are focused to a common focal point in the middle of the microfluidic channel making it possible to examine the concentrations and fluorescent emission lifetimes of metal ion species at specific points in the two phase flow.

References:

1. Choppin, G. R., and Z. M. Wang (1997). "Correlation between Ligand Coordination Number and the Shift of the 7F0-5D0 Transition Frequency in Europium(III) Complexes." *Inorganic Chemistry* 36 (2), 249-252.
2. Supkowski, R. M. and W. D. Horrocks Jr, (2002). "On the Determination of the Number of Water Molecules, q, Coordinated to Europium(III) Ions in Solution from Luminescence Decay Lifetimes." *Inorganica Chimica Acta*, 340 (0), 44-48
3. Kimura, T., and G. R. Choppin (1994). , "Luminescence Study on Determination of the

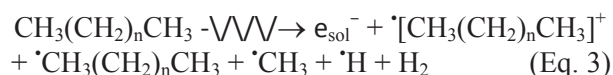
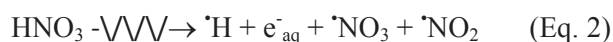
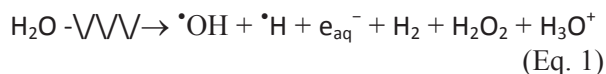
Separations and Waste Forms
2013 Accomplishments Report

Hydration Number of Cm(III).” *Journal of Alloys and Compounds* 213–214 (0), 313-317.

Fundamental Radiation Chemistry

B. J. Mincher, bruce.mincher@inl.gov

The irradiation of any solvent extraction ligand in an organic diluent in contact with a radioactive aqueous phase exposes that ligand to numerous radiolytically-produced reactive species created by the decomposition of water, nitric acid and the organic phase diluent. The reactive species produced in the biphasic system arise from the direct radiolysis of these diluents, as shown in equations 1-3. Ligands that have kinetically fast reactions with these produced reactive species will quickly degrade, adversely impacting solvent extraction selectivity and efficiency. Therefore, to mitigate ligand degradation under these harsh conditions, methods have been developed at INL to understand the mechanisms of the radiolytic degradation of candidate fuel cycle ligands. The techniques employed have included steady state gamma-ray irradiations coupled with state-of-the-art mass spectrometry to measure the loss in ligand concentration with absorbed dose and to identify radiolysis products; pulsed linear accelerator irradiations for kinetic analyses of the very fast reactions of the produced radical species with ligands; and alpha-irradiation using a number of techniques. The alpha-radiolysis work is novel and significant in that very few such studies have been performed due to the difficulty in handling alpha-radiation sources. Yet, the very high LET of alpha radiation ensures that its effects on ligands will be different than that of beta/gamma radiation.



Significant Work Accomplished

A comprehensive investigation of the radiation chemistry of CMPO was performed. This included the use of gamma-irradiation in aerated and de-aerated solution, and in the

presence of aqueous phases of varying acidity. The main conclusions were that the presence of an aqueous phase containing molar amounts of nitric acid protects CMPO from radiolytic degradation. Increasing nitric acid concentration provided increasing protection. The presence of dissolved oxygen also protects CMPO. The effect of nitric acid concentration on CMPO degradation is shown in Figure 86. The products of CMPO radiolysis were identified, and reconciled with the effect of irradiation on solvent extraction distribution ratios. In general, distribution ratios decreased with absorbed dose, while stripping distribution ratios increased. This work resulted in publication of a journal paper, in fulfillment of milestone M4FT-13IN0304093 [Mincher, et al., 2013]. It may be concluded based on this work that under realistic process conditions, CMPO is fairly stable, but that acidic radiolysis products do build up to interfere with stripping at high absorbed doses.

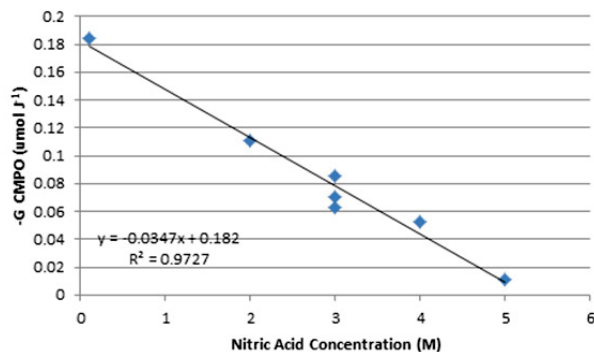


Figure 86. The decrease in the radiolytic degradation (*G*-value in $\mu\text{mol J}^{-1}$) of CMPO, when gamma-irradiated as 0.1 M CMPO/dodecane in contact with aqueous solutions of increasing nitric acid concentration.

Four high LET alpha sources were used to irradiate CMPO solutions. Of these, 211At (Chalmers, Sweden) and the He ion beam (University of Notre Dame, IN) delivered absorbed doses of a factor of 10 lower than did 244Cm (INL) and alpha from the B(n,a)Li reaction using a Training, Research, Isotopes, General Atomics (TRIGA) reactor (UC Irvine, CA). The effects on CMPO concentration, solvent extraction and the amounts of radiolysis products produced were much lower than for gamma-irradiation. The lack of change in solvent extraction distribution ratios for Cm-irradiated CMPO solution is shown in Figure 87. This work

Separations and Waste Forms
2013 Accomplishments Report

was summarized in a journal manuscript in fulfillment of milestone M3FT-13IN0304094, [Mincher, et al., 2014] and an additional journal manuscript [Mezyk, et al., 2013]. It may be concluded based on this work that alpha radiolysis effects on CMPO are not severe.

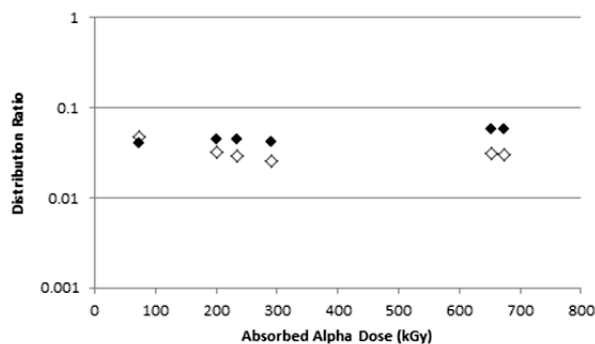


Figure 87. The solvent extraction (solid symbols) and strip distribution ratios (open symbols) of Am from 2 M HNO₃, for initially 0.1 M CMPO/dodecane irradiated using ²⁴⁴Cm in 0.1 M HNO₃. The CMPO concentration was diluted to 0.16 M prior to the extraction contacts.

The gamma-CMPO findings above suggested that CMPO degradation was largely due to electron transfer reactions with radiolytically-produced dodecane radical cations. Linear accelerator experiments were performed in collaboration with the University of Notre Dame and Brookhaven National Laboratory in an attempt to observe these elusive radical cations in pulse irradiated solution. The results are so-far inconclusive, although the method has been refined for the next irradiation campaign. These results were documented in a report in fulfillment of milestone M4FT-13IN030495.[4]

Methods were successfully developed to measure the kinetics of the very fast reactions of the •NO₃ radical with lanthanide•CMPO complexes dissolved in the organic phase. Since Nd is observable by UV/Vis spectroscopy, the spectral shift of the Nd absorbance that accompanied CMPO complexation was used to determine the metal:ligand ratio that ensured there would be no free CMPO in the pulse irradiated solution. This spectra shift is shown in Figure 88. It was concluded that CMPO reacts about 3x faster in organic solution than in aqueous solution, and that the reactions of its metal complexes were about an order of magnitude faster than for free CMPO. These values are important to the accurate

kinetic modeling of CMPO radiation chemistry. The results were summarized in a report in fulfillment of milestones M4FT-13IN0304092 and M3FT-13IN0304091.[5]

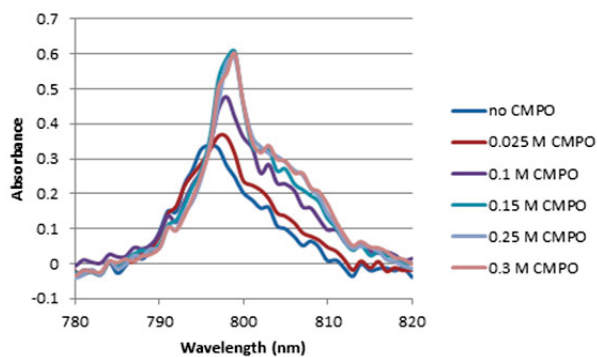


Figure 88. The wavelength and intensity shift of Nd absorbance at initially 796 nm in t-butanol upon addition of CMPO.

Publications

1. Mincher, B. J.; S. P. Mezyk, G. Elias, G. S. Groenewold, and L. G. Olson (2013). "The Radiation Chemistry of CMPO: Part 1. Gamma Radiolysis." *Solvent Extr. Ion Exch.* 31:715-730.
2. Mincher, B. J., S. P. Mezyk, G. Elias, G. S. Groenewold, J. A. Laverene, M. Nilsson, and J. Pearson (2014). "The Radiation Chemistry of CMPO: Part 2. Alpha Radiolysis." *Solvent Extr. Ion Exch.*, In press.
3. Mezyk, S. P., B. J. Mincher, C. Ekberg, and G. Skarnemark (2013). "Alpha and Gamma Radiolysis of Nuclear Solvent Extraction Ligands Used for An(III) and Ln(III) Separations." *J. Radioanal. Nucl. Chem.* 296:711-715.
4. "Solvent Radical Cations Milestone Report." FCRD-SWF-2013-000296.
5. Mincher, B. J., and S. P. Mezyk (2013). "Development of a Method to Measure the Rate Constant for the Reaction of •NO₃ with Metal-Complexed CMPO in the Organic Phase." FCRD-SWF-2013-000231. July 25.

Separations and Waste Forms
2013 Accomplishments Report

Contactors Modeling and Validation Data

K. E. Wardle, kwardle@anl.gov

Solvent extraction (SX) process simulation tools are critical for advanced process design, evaluation, and optimization and, in turn, provide the quantitative basis for system-level evaluation of process options. Process-level simulations depend both on accurate chemical data and engineering understanding of unit operations performance over the range of process conditions. This effort seeks to deliver computational tools for simulation of SX contactor unit operations providing a pathway for prediction of key operational performance measures (e.g. stage efficiency, extent of separation) for any conditions using multiphase Computational Fluid Dynamics (CFD). In addition, a companion experimental effort is being conducted to provide the necessary data for validation of these advanced modeling tools.

Of the available SX equipment types, annular centrifugal contactors have the largest relative knowledge gap and at the same time the greatest opportunity for significant benefits due to their compact size and efficiency. While the tools developed here are generally applicable to all SX equipment types, the present focus has been on prediction of the complex flow in ACCs. CFD simulations of these devices can provide insight into improvements in design, enable operational optimization over a wider range of conditions than is currently available, and provide tools to support the confident deployment of this technology in various areas of chemical processing.

R&D Overview

Multiphase CFD methods tend to be regime-dependent, and consequently, the turbulent multiphase flows in ACCs and other SX devices present a unique challenge as they inherently span multiple flow regimes from fully phase-segregated and, free-surface flow to fully dispersed multiphase flow. Successful simulation of such flows requires a computational framework capable of combining sharp interface capturing methods with multi-fluid dispersed flow modeling. In addition, droplet breakup/coalescence models are needed to capture the evolution of the droplet size

distribution to predict liquid-liquid interfacial area. Experimental validation of these advanced models with detailed multiphase data from actual contactors is essential. The experimental facility used for this work consists of two different size ACCs (2-inch and 5-in rotor sizes) each customized for a variety of interrogation methods including flow monitoring and mass balancing, high-speed imaging, and for the larger contactor, electrical resistance tomography.

Accomplishments

Simulation

During FY 2013, the hybrid multiphase solver that was developed in the previous fiscal year was further extended for prediction of mean local droplet size and liquid-liquid interfacial area. A number of droplet breakup and coalescence models from the literature were implemented in a flexible framework to enable runtime selection and model evaluation. Using limited available literature data for drop size in the centrifugal contactor being studied [Wyatt, et al., 2013], a preliminary investigation was conducted in which a selected pair of breakup/coalescence models were calibrated using simulations in a simplified annular mixer geometry. The resulting models were then applied to relative evaluation of the predicted droplet sizes in mixing zone CFD simulations for two different contactor mixing vane configurations: four straight vanes (4V) and eight curved vanes (CV). Figure 89 shows a comparison of the relative droplet sizes for the two cases with a somewhat smaller drop size found in the 4V case. However, it was apparent from observations of transient variation in the droplet size that coalescence was being overpredicted, resulting in larger droplet sizes in both cases and a more dramatic degradation of mixing performance given the lower annular liquid height observed in the CV case. This highlights significant uncertainty in the underlying models for breakup and coalescence, the potential challenges with sub-model calibration, and the need for development of more fundamental and transferrable models for these critical phenomena.

Separations and Waste Forms
2013 Accomplishments Report

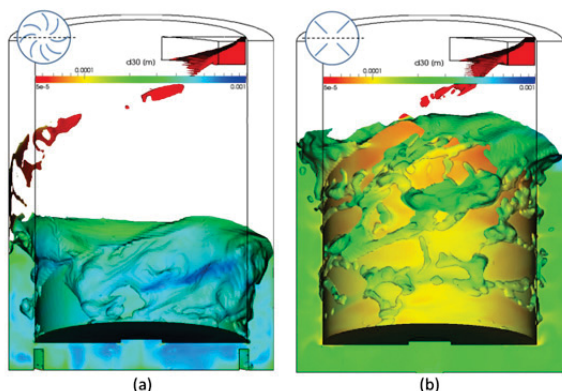


Figure 89. Comparison of liquid holdup and drop size for prediction for simulations in the annular mixing zone of a centrifugal contactor with (a) eight curved vanes and (b) four straight vanes.

In addition, separate simulations were conducted to investigate the flow of liquids exiting the rotor and in the ‘collector ring’ of the centrifugal contactor. Liquids separated by the centrifugal force experienced in the contactor’s rotor, are spun out of rotor exit ports (typically four or more) and collected in a trough called the collector ring. The high speed at which these liquid streams exit the rotor causes breakup and splashing of droplets on the collector ring wall. It has been postulated that this could be a potential pathway for phase contamination should droplets be able to travel from one collector ring to the other. Two-phase CFD simulations for flow in the light phase (lower) collector ring were conducted and indeed identified this as a plausible phenomena (Figure 90).

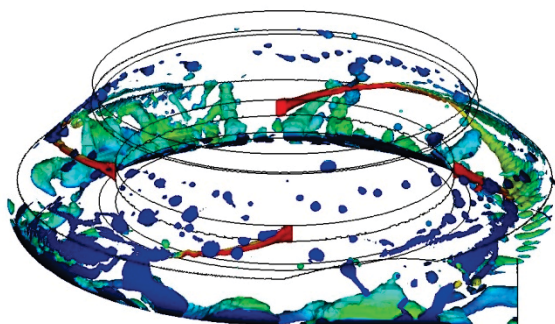


Figure 90. Snapshot of simulated organic phase flow in the lower collector ring of a centrifugal contactor. The liquid surface is colored by velocity magnitude.

Experiment

In situ optical measurements of the liquid-liquid droplet size distribution in a centrifugal

contactor were accomplished using the unique combination of a high-resolution digital camera and high-magnification precision lens system with a short-pulse (500 nanoseconds), high-power strobe light for illumination. Measurements of droplet size at multiple locations in the vane region at the bottom of the housing were done to provide a first ever direct comparison of droplet size for the 4V and CV configurations. Sample images, measurement locations, and drop size results are shown in Figure 91.

It was determined that the drop size is comparable between the two systems—confirmation that there is not an abundance of very small drops in the 4V case that could lead to separation issues (and none have been observed to date). In FY 2014, additional measurements will be conducted near the rotor axis location to give a better value for overall comparison which avoids local variations due to vane proximity. Moreover, as manual image processing for droplet identification is a bottleneck, future work should focus on development of automated methods. This is very challenging due to the high density of droplets, low index of refraction between the liquids (contrast), presence of air bubbles, and general difficulty of *in situ* imaging of moving droplets of this scale in an actual device. A scoping effort was conducted to evaluate the effectiveness of available techniques and a promising method was identified which is based on image pre-processing for contrast enhancement followed by pattern matching to identify droplets.

Separations and Waste Forms
2013 Accomplishments Report

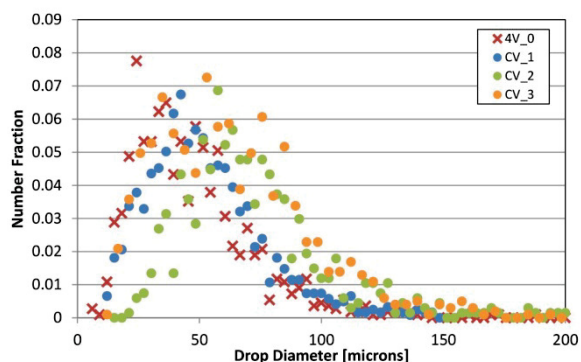
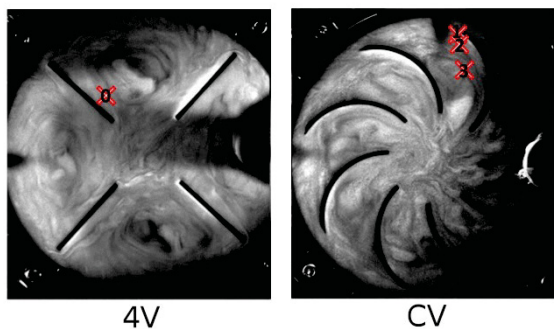
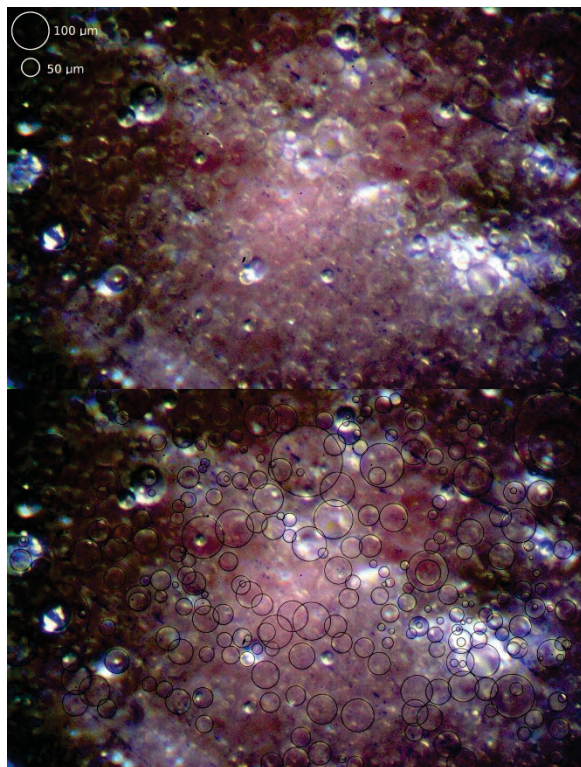


Figure 91. Sample image set (lower shows identified droplets) and droplet size distributions for locations in the 4V and CV contactor geometries. Measurements are in a CINC V05 at 10 L/min and an O/A of 1/3.

References

- Wyatt, N. B., T. J. O’Hern, and B. Shelden (2013). “Drop-size Distribution and Spatio-temporal Distribution in an Annular Centrifugal Contactor.” *AICHE J.* 59, 2219. April 16.

Publications

- Wardle, K. E. (2013). “Hybrid Multiphase CFD Simulation for Liquid-Liquid Interfacial Area Prediction in Annular Centrifugal Contactors.” In *Proceedings of Global 2013*. Salt Lake City, UT, .September 29–October 3.
- Wardle, K. E., and H. Weller (2013). “Hybrid Multiphase CFD Solver for Coupled Dispersed/Segregated Flows in Liquid-Liquid Extraction.” *Int. J. of Chem. Eng.* 2013, 128936.
- Vedantam, S., K. E. Wardle, T. V. Tamhane, V. V. Ranade, and J. B. Joshi (2012). “CFD Simulation of Annular Centrifugal Extractors.” (invited review article) *Int. J. Chem. Eng.* 2012, 759397.

1st Principles Modeling of Hydrolysis Reactions

P. Zapol, zapol@anl.gov

The objective of this project is to develop models based on first-principles calculations to provide constitutive relations that can be used to predict the long term behavior of glass waste forms. ANL modeling effort is focused on mechanisms of chemical reactivity of the glasses in aqueous solutions. First-principles calculations of hydrolysis reactions on alkali-borosilicate glass surfaces are used to determine energies and barriers for hydrolysis reactions on the surface. The network connectivity of glass is described by coordination number of network-forming atoms Q^n to n bridging oxygen atoms. The set of reaction barriers for elementary reactions with all network-former pairs Q^n-O-Q^n and site distribution in the glass provides information for kinetic modeling of the overall dissolution rate as a function of composition, temperature and pH.

In FY 2011 and FY 2012, researchers performed validation of this modeling approach using a first-principles based model to calculate

Separations and Waste Forms
2013 Accomplishments Report

dissolution rates for orthoclase mineral at acidic conditions. In this modeling, calculated reaction barriers were used to compare x-ray reflectivity data on dissolution of (001) surface at five pH values (0, 1.1, 2, 3 and 3.4) and five temperature values from 36°C to 76°C. The agreement of these data with the overall rate results based on kinetic modeling and calculated barriers demonstrated applicability of the approach to model dissolution of multicomponent oxides. In FY 2013, calculations of reaction barriers were performed on a sodium borosilicate glass with composition SiO₂ (68%), B₂O₃ (18%) and Na₂O (14%). Glass structures were provided by the collaborators at SNL (L. Criscenti) using classical molecular dynamics simulations with composition-dependent force fields. At ANL, models of glass structures in bulk and slab geometries were optimized using density functional theory within generalized gradient approximation, Figure 92(a,b). The climbing-image nudged elastic band method was used to calculate the reaction barriers given in Figure 92(c).

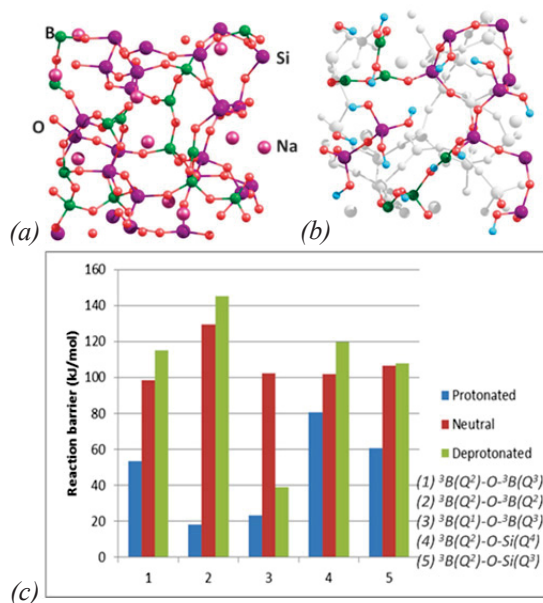


Figure 92. Structures of (a) bulk and (b) surface of sodium borosilicate glass and (c) hydrolysis reaction barriers calculated with first-principles methods.

Calculated reaction barriers for B-O-B hydrolysis reactions in a sodium borosilicate glass indicate that the reaction barriers in the presence of protons (acidic conditions) (18-60 kJ/mol) are considerably lower than the reaction barriers in neutral conditions (98-102 kJ/mol). In contrast,

the presence of extra OH groups (basic conditions) does not result in barriers for B-O bonds that are lower than those in neutral conditions, with exception of the B(Q¹) site (configuration 3 in Figure 92(c)). Similar trends are obtained for hydrolysis of B-O-Si bonds.

Our previous calculations in FY 2011 and FY 2012 for Si-O-Si bonds in orthoclase indicated that Si-O bonds have lower barriers for hydrolysis reactions at both acidic and basic conditions relative to neutral conditions. Nuclear waste glasses are observed to undergo a change in dissolution mechanism with increase in pH. These first-principles results provide a possible explanation for the change of mechanism from incongruent to congruent dissolution at higher pH. Namely, the calculated reaction barrier difference between Si and B bonds is smaller under basic conditions than under neutral or acidic conditions. These calculated reaction barriers can be used for kinetic modeling of glass dissolution.

Publication

- Zapol, P., H. He, K. D. Kwon, and L. J. Criscenti (2013). "First-Principles Study of Hydrolysis Reaction Barriers in a Sodium Borosilicate Glass." *International Journal of Applied Glass Science* 4 395–407.

**Non-Ideality in Solvent
Extraction Systems**

Experimental / Theoretical Inquiry into Non-Ideal Chemistry of Solvent Extraction

P. Zalupski, peter.zalupski@inl.gov, L. Delmau (ORNL), T. Levitskaia (PNNL), M. Milsson (ECI), and S. Clegg (UEA)

The overarching objective of the collaborative efforts of the FCRD "Non-Ideality in Solvent Extraction Systems" project is to advance the ability of theoretical representation of solute partitioning in two-phase systems. Our efforts entail surveys of the existing theory, which, together with the established new means of experimental inquiry into basic physical chemistry of liquid mixtures, allow us to progressively represent chemistry using equations. Such mathematical description is fundamental to the goal of computational prediction of aqueous

Separations and Waste Forms
2013 Accomplishments Report

separations using models that accurately describe non-ideal behavior in the liquid phases. Non-ideal behavior in solutions always complicates accurate representation of mixtures when modeling a chemical system. A theoretical representation, i.e., model, is particularly challenging when modeling chemical systems as complex as those encountered in aqueous partitioning processes for actinide recycling from dissolved UNF. This research effort illustrates how non-idealities obstruct accurate modeling of separations based on liquid-liquid distribution of the metal between two immiscible phases, i.e. solvent extraction. The overarching objective of the project seeks to build experimental capabilities to enable studying fundamental physical properties of solutions. Such inquiry builds thermodynamic knowledge of complex mixtures, allowing better numerical representation, and, as a result, greater accuracy of computational prediction.

Modeling of Simplified TALSPEAK Delivers More Details on Experiment/Model Discrepancy

Liquid-liquid distribution of europium and americium has been monitored for a Talspeak-like 2-phase system, where the compositions of aqueous and organic mixtures were modified to reduce complications of non-ideal solution behavior. Europium and americium partitioning was monitored as the acidity of aqueous mixtures varied across a wide range ($2 < \text{pH} < 5$). The compositions of aqueous mixtures were predicted based on the developed thermodynamic model of an electrolyte mixture containing europium, sodium nitrate, malonate buffer and an aqueous complexant – diethylenetriaminepentaacetic acid, DTPA. The model, contained in a FORTRAN routine called PitzINL, was developed using thermodynamic data describing the interactions of ions present in the mixture. The overall model predicts aqueous speciation based on Pitzer ion-interaction theory. The model estimates the effects of non-ideal behavior of ions on the overall chemical speciation. The Pitzer model is used to calculate activity coefficients, and the Pitzer interaction parameters can be changed by the program user. The DTPA protonation and complexation equilibria can be calculated either with activity coefficients from the model, or using

concentrations of the species present in electrolyte mixtures.

Figure 93a shows the collected Eu^{3+} and Am^{3+} distribution ratios for the pH dependence study where aqueous environments were based on $\text{M}^{3+} / \text{Na}^+ / \text{NO}_3^- / \text{H}_2\text{Mal} / \text{Hmal}^- / \text{Mal}^{2-} / \text{DTPA} / \text{H}_2\text{O}$ system, the ionic strength was sequentially fixed at 0.25, 0.5, 0.75, 1.00 and 1.25 mol kg^{-1} and the organic environment consisted of 0.04 M HDEHP in *n*-dodecane. Typically, the liquid-liquid distribution of trivalent *f*-elements in Talspeak system consistently decreases, followed by a drastic drop when the pH of an aqueous solution reaches 4, as illustrated by Figure 93b. This trend has been an enigma to the efforts of fundamental studies on the Talspeak chemistry as it does not match the predicted behavior of liquid-liquid distribution of trivalent metals based on the thermodynamic model developed by Nilsson and Nash [2009]. The increasing discrepancy between the experimentally-observed partitioning behavior and the prediction has been mainly attributed to various solute-partitioning equilibria unaccounted for in the model. The results of the study demonstrate this very clearly. When the concentrations of all components of the investigated liquid-liquid system have been reduced the partitioning behavior follows the prediction until pH of 3.5 (Eu) and pH of 4 (Am). An important aspect of this study is the overlapping ionic strength dependence throughout the large part of the study. The observed independence on the concentration of sodium during the initial (more acidic) stages of the solute partitioning experiment is followed by an obvious very unpredictable distribution behavior in the $4 < \text{pH} < 5$ region. Neuman, et. al. [1996] argued that sodium salt of HDEHP forms large cylindrical aggregates when in contact with high pH environment. If this was indeed the case the availability of HDEHP dimer required for the coordination of the metal ion could impact the partitioning behavior. This is clearly indicated in the study as the partitioning of europium, which predominantly reports to the organic phase, is affected more, relative to americium, at the high pH conditions.

Most importantly to the objectives of the research efforts, the program PitzINL calculated

Separations and Waste Forms
2013 Accomplishments Report

the formulations for all aqueous environments in this study. It appears that when non-ideal chemistry of Talspeak-like aqueous electrolyte systems is considered in speciation calculations the resulting partitioning data is more coherent, and further indicates that structural transformations in the organic phase of the Talspeak system may explain the observed discrepancy between an experiment and a model.

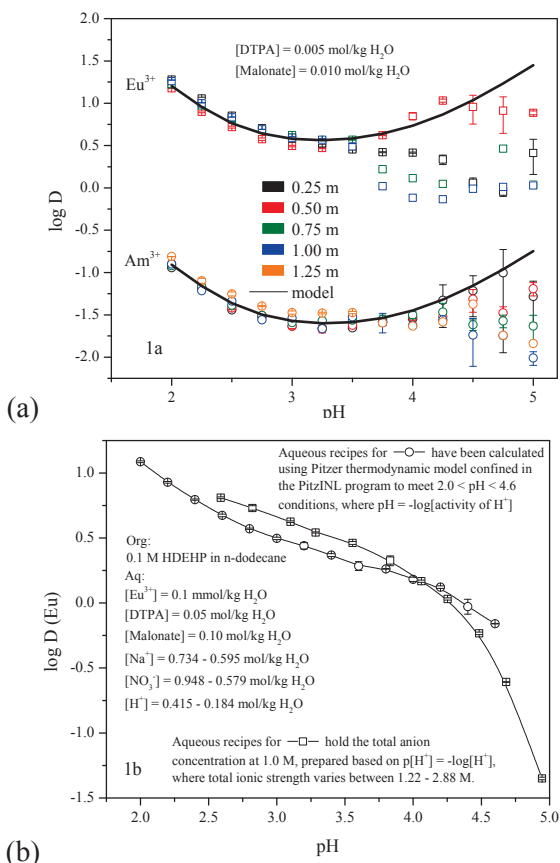


Figure 93. Solvent extraction studies on the pH dependence for europium and americium distribution, where (a) aqueous solution consists of 5 mmol kg⁻¹ DTPA, 10 mmol kg⁻¹ malonate, 10 μmol kg⁻¹ M³⁺ traced with ¹⁵⁴Eu and ²⁴³Am, and ionic strength is fixed at 0.25, 0.5, 0.75, 1.00 and 1.25 mol / kg using NaNO₃ and the organic solution is 0.04 M HDEHP in n-dodecane system, (b) aqueous and organic solutions are representative of typical Talspeak-type liquid-liquid distribution system.

Potentiometric Studies for the DTPA Protonation and Eu³⁺ Complexation in Sodium Nitrate Background Electrolyte Pave Way to Pitzer Parameterization

Acid dissociation constants and europium complexation constants by DTPA have been

collected at 10 different ionic strengths controlled by sodium nitrate. The collected thermodynamic data compares well with that reported in the literature for different aqueous electrolyte media. Ionic strength dependencies for all investigated equilibria are well-defined. The Eu³⁺ complexation will be complemented by the collection of analogous ionic strength study for Eu³⁺ complexation by nitrate anion. Thermodynamic data will be represented by the Pitzer ion interaction theory.

Isopiestic Equilibration Study for a Ternary Mixture of Eu(NO₃)₃ and NaNO₃ has been Completed

Isopiestic equilibration studies for the mixtures of Eu(NO₃)₃ and NaNO₃ in various proportions were performed to assign the unavailable Pitzer parameters for ternary electrolyte interactions: “+ +, θ(Eu, Na)”, “+ + -, ψ(Eu, Na, NO₃)”. The assembled thermodynamic data was added to the thermodynamic model for Eu³⁺ / Na⁺ / NO₃⁻ / H₂Mal / HMal / DTPA / H₂O aqueous electrolyte mixture.

Non-Ideal Behavior of HDEHP Dimer is Not Impacted by Aqueous Phase Equilibration

Vapor pressure measurements revealed that aqueous equilibration of the “dry” organic environment of HDEHP in n-octane does not influence the behavior of this liquid cation exchanger in solution. As such, activity coefficients for HDEHP in aliphatic diluent present in a two-phase system must match those obtained for a “dry” binary mixture.

References

1. Nilsson, M., and K. L. Nash (2009). “Trans-Lanthanide Extraction Studies in the TALSPEAK System: Investigating the Effect of Acidity and Temperature.” *Solvent Extr. Ion Exch.* 27, 354-377.
2. Neuman, R. D., Z.-J. Yu, and T. Ibrahim (1996). “Role of Reversed Micelles of Acidic Organophosphorus Extractants in Cobalt/Nickel Separation – A Position Paper.” In *Proc. International Solvent Extraction Conference, ISEC'96*, Vol. 1, D. C. Shallcross, R. Paimin, and L. M. Prvcic, Eds. Melbourne, Australia, University of Melbourne, pp. 135-140.

Separations and Waste Forms
2013 Accomplishments Report

Publications

1. Gray, M. F., P. R. Zalupski, and M. Nilsson (2013). "Determination of Activity Coefficients Of Di-(2-Ethylhexyl)phosphoric Acid Dimer in Select Organic Solvents Using Vapor Phase Osmometry." *Solvent Extr. Ion Exch.*, 31, 5.

Thermodynamics of Trivalent Lanthanides in Concentrated Aqueous Solutions

T. G. Levitskaia, S. Chatterjee, T. A. Robinson, and E. L. Campbell

The overall project objective is to develop predictive modeling capabilities based on solution thermodynamics to support nuclear fuel R&D needs. Successful design of new separation processes for advanced fuel cycle concepts largely relies on the availability of such predictive capability. Design of a liquid-liquid extraction separation process that achieves an accurately controlled selective transport of the species of interest is of paramount importance. Aqueous matrices containing actinides and lanthanides encountered during nuclear fuel reprocessing have high ionic strength and do not behave as ideal solutions. Activity coefficients must be determined to take into account the deviation from ideality and to predict the behavior of the various solution components in nuclear fuel separation systems. To date, thermodynamic characteristics of the multicomponent electrolyte solution containing lanthanide and actinide ions have been insufficiently studied.

It is apparent that the activity effects of the relevant metal species change as the aqueous and/or organic media are changed. Consequently the deviation from the thermodynamic ideality has to be taken into account to calculate the thermodynamic properties of solutions and predict their behavior. For instance, the activity coefficients are needed to predict the thermodynamic driving force for transport across liquid-liquid interface, complex formation, precipitation processes, third phase formation and other processes involving actinide/lanthanide solutions.

To address these needs, the main focus of this project is to develop and validate the experimental methodology for determining the activity effects

in the aqueous solutions based upon Pitzer, Bromley, or alternative electrolyte treatments and generating the thermodynamic database for the lanthanide and actinide ions in the complex electrolyte solutions. If developed, this method can be universally applied for the determination and quantification of the non-ideality effects in any aqueous electrolyte solution applicable to fuel cycle separations.

Work conducted at PNNL in Fiscal Year 2013 mainly was focused on determination of activity effects in aqueous 3:1 binary lanthanide nitrate solutions at 25°C. Our previous experiments have demonstrated that water activity and osmotic coefficients of the electrolyte solutions can be accurately measured by the combination of two techniques, a variable-impedance hygrometer referred to as a Water Activity Meter, and Vapor Pressure Osmometry (VPO). This method overcomes limitations of the traditional isopiestic technique, which is not suitable for the measurements of in presence of volatile compounds in solution, such as nitric acid. The water activity measurements have been completed for binary lanthanide nitrate $\text{Ln}(\text{NO}_3)_3$ solutions in wide concentration range for the entire trivalent lanthanide series (La-Lu with the exception of Pm). The osmotic coefficients and Pitzer parameters for each binary system were obtained by the least squares fitting of the water activity data and compared with the corresponding literature values. These experiments lead to a new and extended set of experimental data with which the values generated by the isopiestic method can be compared. Thermodynamic data collected using the water activity meter and VPO agree with the literature data assembled using the isopiestic method. The agreement between the technique used in this work and isopiestic method affords confidence when building a thermodynamic model for a studied electrolyte system, yielding accurate Pitzer parameters. This finding validates this new experimental capability to support parameterization when constructing numerical representations of solutions. The non-ideality parameters obtained for the binary $\text{Ln}(\text{NO}_3)_3$ solutions were correlated with the thermochemical radii of the trivalent lanthanide ions revealing systematic trends useful for the prediction of the

Separations and Waste Forms
2013 Accomplishments Report

short- and long-range interactions in the binary 3:1 electrolyte solutions.

The water activity results obtained for the binary $\text{La}(\text{NO}_3)_3$ system is shown in Figure 94. This plot is representative for all other binary $\text{Ln}(\text{NO}_3)_3$ system. The experimental measurements collected in this work are compared with the literature data obtained by the classical isopiestic technique [Rard, et al., 1979; Rard, et al., 1977].

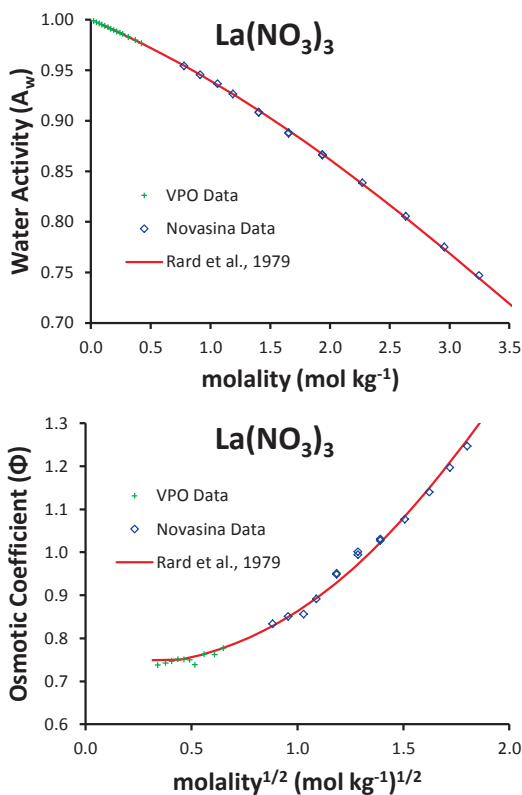


Figure 94. Water activity (left panes) and osmotic coefficient (right panes) data for the binary lanthanide nitrate systems at 25°C. Green and blue symbols correspond to the data collected using VPO and water activity meter, respectively. The solid red line is literature values obtained using isopiestic technique [Rard, et al., 1979].

As can be seen from Figure 94, excellent agreement between the literature data collected using isopiestic method and experimental data obtained by water activity and VPO methods in this work is observed. The water activity instrument supplies accurate measurements at the high end of the molal concentrations starting with water activity of 0.95 and below. The vapor pressure osmometer is able to provide reliable

results for the dilute solutions as water activity approaches unity.

Pitzer parameters for the binary $\text{Ln}(\text{NO}_3)_3$ systems were obtained by fitting osmotic coefficient data calculated using VPO and the water activity measurements (Table 20). Excellent agreement between Pitzer parameters obtained in this work by the combination of the water activity and VPO techniques and literature data collected using isopiestic method [Pitzer, 1991] is observed. In the fitting, three Pitzer parameters were refined simultaneously. In the concert with the water activity, it was observed that $\beta^{(0)}$ parameter, which depends on the spatial interaction between two charged species in a solvating medium, was nearly constant for the early (La–Eu) lanthanide nitrates and steeply increased from $\text{Eu}(\text{NO}_3)_3$ to $\text{Ln}(\text{NO}_3)_3$.

Table 20. Tabulation of Pitzer parameters of binary lanthanide nitrate solutions at 25°C obtained in this work.

Analyte	$(3/2) \beta^{(0)}$	$(3/2) \beta^{(1)}$	$(3^{3/2}/2) C^\phi$
$\text{La}(\text{NO}_3)_3$	0.67 ± 0.01	7.2 ± 0.3	-0.131 ± 0.005
$\text{Ce}(\text{NO}_3)_3$	0.65 ± 0.01	8.6 ± 0.1	-0.112 ± 0.006
$\text{Pr}(\text{NO}_3)_3$	0.70 ± 0.03	7.3 ± 0.3	-0.14 ± 0.01
$\text{Nd}(\text{NO}_3)_3$	0.64 ± 0.01	8.7 ± 0.4	-0.10 ± 0.01
$\text{Sm}(\text{NO}_3)_3$	0.66 ± 0.02	7.7 ± 0.3	-0.10 ± 0.01
$\text{Eu}(\text{NO}_3)_3$	0.66 ± 0.02	8.0 ± 0.3	-0.09 ± 0.01
$\text{Gd}(\text{NO}_3)_3$	0.75 ± 0.01	7.9 ± 0.2	-0.14 ± 0.01
$\text{Tb}(\text{NO}_3)_3$	0.77 ± 0.01	8.4 ± 0.2	-0.14 ± 0.01
$\text{Dy}(\text{NO}_3)_3$	0.73 ± 0.01	8.3 ± 0.3	-0.10 ± 0.02
$\text{Ho}(\text{NO}_3)_3$	0.77 ± 0.03	8.3 ± 0.5	-0.12 ± 0.01
$\text{Er}(\text{NO}_3)_3$	0.84 ± 0.01	8.6 ± 0.3	-0.15 ± 0.01
$\text{Tm}(\text{NO}_3)_3$	0.87 ± 0.01	9.0 ± 0.2	-0.16 ± 0.01
$\text{Yb}(\text{NO}_3)_3$	0.94 ± 0.04	8.4 ± 0.3	-0.17 ± 0.01
$\text{Lu}(\text{NO}_3)_3$	0.86 ± 0.01	9.3 ± 0.3	-0.13 ± 0.01

The nature of the Ln^{3+} ion has pronounced effect on the water activity and therefore on the osmotic coefficient of the binary $\text{Ln}(\text{NO}_3)_3$ solution (Figure 95). This effect is amplified as the salt concentration increases. To illustrate this dependence, the water activity of the representative isomolal $\text{Ln}(\text{NO}_3)_3$ solutions was plotted versus the Ln^{3+} radius (Figure 96).

Separations and Waste Forms
2013 Accomplishments Report

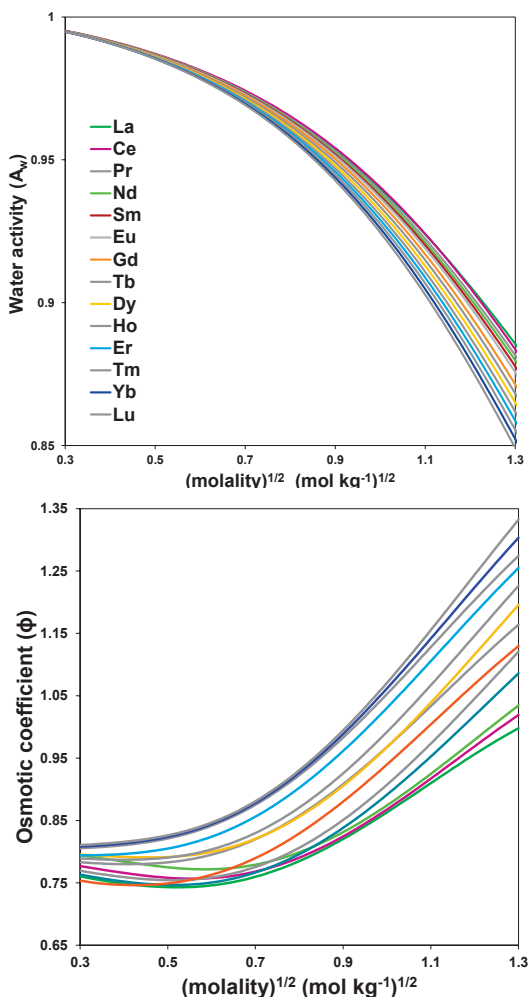


Figure 95. Dependence of the water activity (left pane) and osmotic coefficient (right pane) on the $\text{Ln}(\text{NO}_3)_3$ molality in the aqueous binary systems.

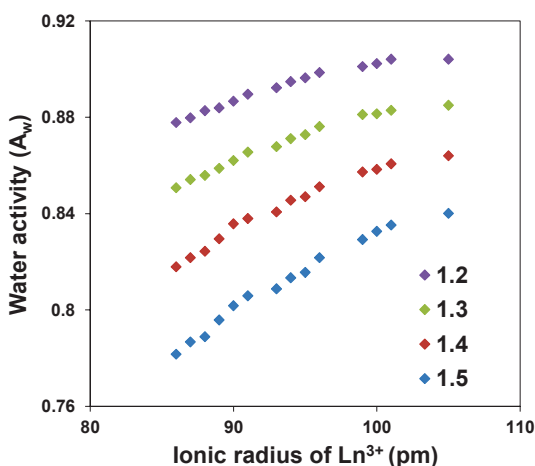


Figure 96. Dependence of the water activity on the Ln^{3+} ionic radii in the isomolal $\text{Ln}(\text{NO}_3)_3$ binary systems. The $m^{1/2}$ for each system is specified in the plot legend. Lanthanide ion radius data taken from Marcus [1997].

The water activity systematically increases with the Ln^{3+} radius, this increase is greater for the more concentrated solutions. This trend can be attributed to the structure of the lanthanide aqua ions and their effect on the hydrogen bond network of water. In dilute aqueous solutions, the 1st coordination sphere the Ln^{3+} exhibits the hydration number changing from nine for the light ions (La^{3+} - Sm^{3+}) to eight for the heavy ions (Dy^{3+} - Lu^{3+}) in accord with the contraction of the lanthanide ionic radii in the same order. For the middle Eu^{3+} - Tb^{3+} region of the lanthanide (III) series the intermediate (between 9 and 8) hydration numbers are proposed [Cotton, 2005]. Monte Carlo simulations of $\text{Ln}^{3+}(\text{aq})$ ions proposed a dissociative substitution mechanism and very fast exchange between the bulk and hydrated water during the change in coordination number from 9 to 8 in mid lanthanide series [Galera, et al., 1993]. The second coordination sphere of Ln^{3+} contains as many as 17–18 water molecules. As the aqueous concentration of the lanthanide salt increases, the average number of the water molecules in the 2nd coordination sphere decreases as they are preferentially exchanged by anions. This process is more pronounced for the late Ln^{3+} with the small ionic radii and responsible for the gradual reduction of the water activity and increase of the osmotic coefficient from the early to the late lanthanides.

The observed systematic trends lead to the conclusion that the non-ideality effects in the lanthanide electrolyte systems vary with the nature on the Ln^{3+} in part leading to the dissimilar thermodynamic and kinetic behavior in the aqueous separation systems. Similar trends can be expected for the trivalent actinide ions.

References

1. Cotton, S. A. (2005). "Establishing Coordination Numbers for the Lanthanides in Simple Complexes." *C. R. Chimie* 8, 129–145.
2. Galera, S., J. M. Lluch, A. Oliva, J. Bertrán, F. Foglia, L. Helm, and A. E. Merbach (1993). "Monte-Carlo Simulations of the Tripositive Lanthanide Ions in Aqueous-Solution." *New J. Chem.* 17:773-779.
3. Marcus, Y. (1997). *Ion Properties*. New York: Marcel Dekker.

Separations and Waste Forms
2013 Accomplishments Report

- Pitzer, K. S. (1991). "Ion Interaction Approach: Theory and Data Correlation in Activity Coefficients in Electrolyte Solutions." K. S. Pitzer, Ed., Boca Raton, Florida: CRC Press, p. 75.
- Rard, J. A., G. D. Miller, and F. H. Spedding (1979). "Isopiestic Determination of the Activity-Coefficients of Some Aqueous Rare-Earth Electrolyte-Solutions at 25°C. $\text{La}(\text{NO}_3)_3$, $\text{Pr}(\text{NO}_3)_3$, and $\text{Nd}(\text{NO}_3)_3$." *J. Chem. Eng. Data* 24:348-354.
- Rard, J. A., L. E. Shiers, D. J. Heiser, and F. H. Spedding (1977). "Isopiestic Determination of the Activity Coefficients of Some Aqueous Rare Earth Electrolyte Solutions at 25°C. 3. The Rare Earth Nitrates." *J. Chem. Eng. Data* 22:337-347.

Extractant Design by Covalency

A. J. Gaunt, gaunt@lanl.gov, E. R. Batista, K. S. Boland, G. Jarvinen, J. M. Keith, S. A. Kozimor, A. Olson, B. L. Scott (all LANL); J. R. Klaehn and D. R. Peterman (both INL)

Importance of Work and Context to DOE-NE Mission

This project aims to provide an electronic structure-to-function understanding of extractants for actinide selective separation processes. The expectation is that unraveling the chemical bonding basis that underpins actinide selectivity will aid in the proposition of new tailored extractant designs based upon a bottom up rational approach. The research entails a multi-disciplinary approach that integrates chemical syntheses, structural determination, K-edge X-ray Absorption Spectroscopy (XAS), and DFT calculations. The work also bridges across the gap with DOE Office of Science (SC) programs by taking concepts that originated in curiosity driven research and attempting to develop them for DOE-NE into a tool-set that is useful for 'use-inspired' more applied systems.

Summary of Research Accomplishments and FY 2013 Results

Our results in FY 2013 included the on-time completion of the first Level 2 milestone for this project, establishing the capability to extend sulfur

K-edge XAS measurements on dithiophosphinates into the solution phase in order to provide measurement conditions that more closely model those encountered in separation processes. Additional key achievements centered on analysis of f-metal complexes with dithiophosphinates and synthetic progress towards a new ligand design that researchers anticipate will exhibit actinide selectivity that is 'tuned-in' by electronic structure design.

Developing Solution XAS Capability

Previous work on this project has shown great progress in uncovering correlation between electronic structure differences (as analyzed by ligand sulfur K-edge XAS) and An/Ln separation factors of different dithiophosphate extractant ligands. These results enabled us to identify "special" electronic structure properties that appear to correlate with the Am/Eu separation factors (Figure 97).

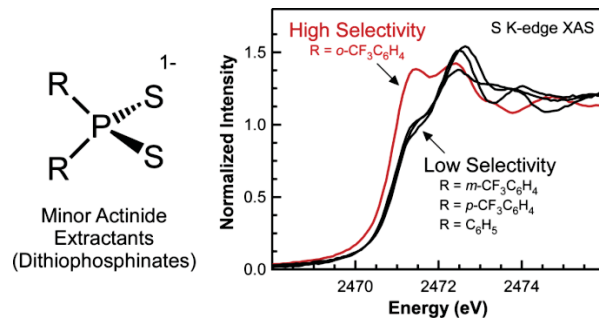


Figure 97. Solid-state sulfur K-edge XAS spectra of a range of dithiophosphate extractant ligands, showing that the ligand with the largest An/Ln separation factor has a very distinct electronic structure profile compared to ligands with lower separation factors.

Researchers found that the *ortho*- CF_3 substitution in $\text{S}_2\text{P}(\text{o}-\text{CF}_3\text{C}_6\text{H}_4)_2^{1-}$ inhibits rotation of the aryl groups, thereby holding the $\text{S}_2\text{P}(\text{o}-\text{CF}_3\text{C}_6\text{H}_4)_2^{1-}$ in a geometric configuration that appears electronically poised for selective actinide binding by increased charge delocalization - effectively causing the extractant to become a 'softer' donor. This notion fits nicely with the hypothesis that the 'softer' the donor then the greater the potential for enhanced covalency in the An-S bonding, which can be reflected in increased An(III) versus Ln(III) selectivity. The next step in the evolution of the K-edge XAS studies was to provide the crucial scientific basis to allow us to

Separations and Waste Forms
2013 Accomplishments Report

conclude that bonding information from the solid state is relevant for extractant designs that will be utilized in the solution phase. Moving into the solution regime required significant spectroscopic technique development and upgrades of the experimental capabilities at the Stanford Synchrotron Radiation Laboratory (SSRL). In particular, the complexity of handling fluids (with a view to future measurements on radioactive actinide containing solutions) required the design and construction of solution flow cell to contain the samples (Figure 98).

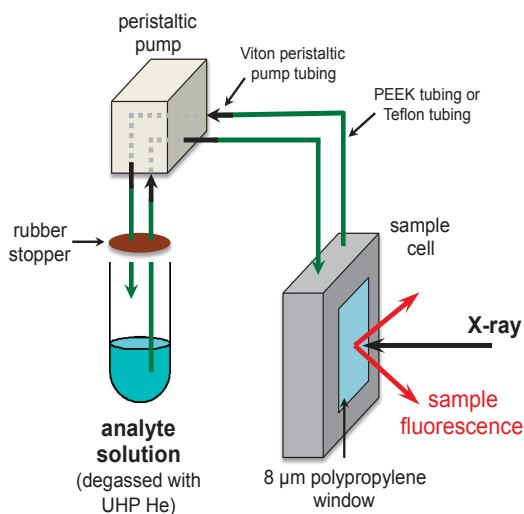


Figure 98. Diagram of circulation system that was implemented for solution-phase S K-edge XAS experiments at SSRL.

The solution data acquired using the flow cell experimental configuration was consistent with measurements acquired in the solid state to explain why *ortho*-substituted $S_2P(o-CF_3C_6H_4)_2^{1-}$ is an exceptional extractant. Upon direct comparison of $S_2P(o-CF_3C_6H_4)_2^{1-}$ solid- and solution-state S K-edge XAS data (Figure 99), researchers observe similar features in the pre-edge region of the spectrum, albeit subtle differences in peak intensities are evident. This suggests that the aryl ‘ring-twist’ (enforced by the steric requirements of the *ortho*-CF₃ group) observed in the solid state also prevails in solution and remains an important influence upon the electronic structure of the extractant. Moving on to a solution phase comparison within a carefully selected family of extractants, with performances spanning the range of high to low An/Ln separation factors, the S K-edge XAS spectra

confirm the unique electronic structure of $S_2P(o-CF_3C_6H_4)_2^{1-}$ (CH_2Cl_2 was employed as the solution/solvent medium; see Figure 99).

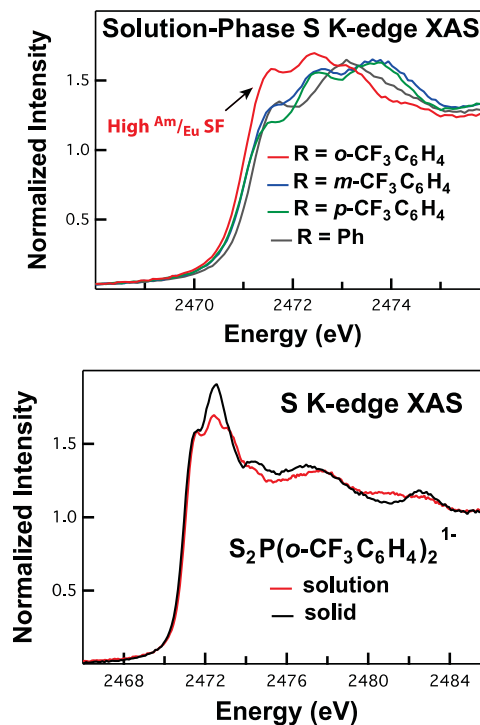


Figure 99. Direct comparison of solution phase versus solid-state data for the $[S_2P(o-CF_3C_6H_4)_2]^{1-}$ extractant (top), which is reported to exhibit the largest An/Ln separation factors; comparison of the solution phase (in dichloromethane) sulfur K-edge XAS spectra of dithiophosphinate extractant molecules bearing different substituents on the aryl ring (bottom).

Similar to conclusions derived from solid-state measurements, the position of the *ortho*-CF₃ substituent in $S_2P(o-CF_3C_6H_4)_2^{1-}$ is believed to inhibit rotation of the aryl groups, thereby holding the $S_2P(o-CF_3C_6H_4)_2^{1-}$ in a geometric configuration that appears electronically poised for selective actinide binding, while the other ligands do not exhibit this behavior.

Analysis of F-Metal Complexes

Data that was acquired on unbound extractant molecules was very promising, in the sense that an electronic structure correlation to actinide selectivity was identified. The ultimate goal is to unravel the electronic structure/covalency differences in the bonding between lanthanide and actinide compounds, in order to determine if the differences identified in the extractants themselves

Separations and Waste Forms
2013 Accomplishments Report

translate into measurable differences in the f-metal complexes. To this end, a series of lanthanide compounds have been characterized and some results recently published. Initial direct experimental data on actinide-extractant complexes has shown just how exceptionally complicated this problem is, with both experimental and computational approaches pushing the boundaries of existing capabilities in actinide science. As a consequence, an alternative strategy was needed that will allow future interpretation of the K-edge XAS spectra of extractant complexes by first of all robustly characterizing a model actinide compound, namely $\text{Np}^{\text{IV}}(\text{S}_2\text{PPh}_2)_4$. This compound is prepared in good yield, in very high purity, the molecular structure determined by single-crystal X-ray and Extended X-Ray Absorption Fine Structure (EXAFS) analysis, and its robustness renders this compound ideal for development of technically/logistically challenging XAS measurements on samples containing high specific-activity transuranic radioisotopes.

The results show that EXAFS can be used to effectively model the structural data (Figure 100), and therefore be a valuable tool to decipher structures of other actinide-extractant complexes. Analysis of sulfur K-edge XAS data on $\text{Np}(\text{S}_2\text{PPh}_2)_4$ compared to Nd and U compounds (Figure 100) suggested increased d-orbital participation in M-S bonding for the actinides relative to the lanthanides. For $\text{Np}(\text{S}_2\text{PPh}_2)_4$, a small pre-edge feature near 2470 eV was partially resolved from the rising edge. Based on previously established d- and f-orbital energy trends, this lower-energy feature is likely associated with f-orbital mixing, providing the first experimental evidence for covalent bonding between actinide 5f and S 3p orbitals. Given the potential impact of this key finding, it will be essential to verify with repeat measurements, different compounds, and calculations to provide confidence to definitive assignments.

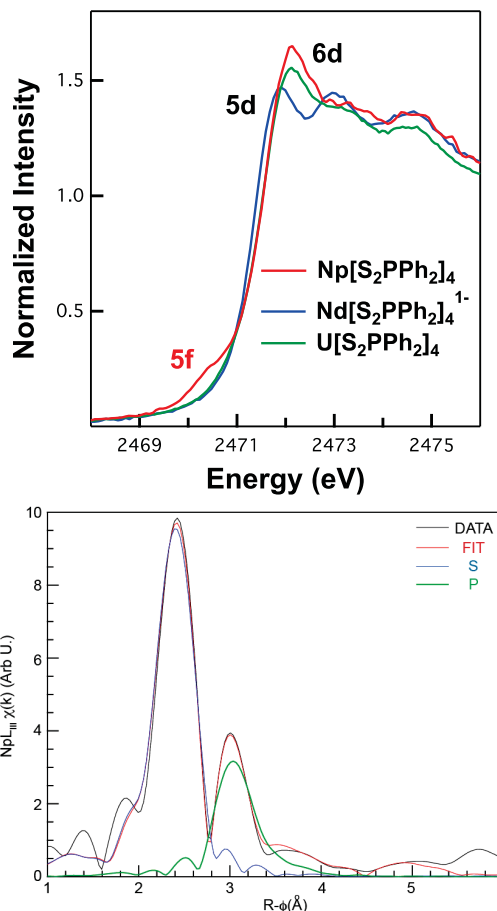


Figure 100. EXAFS spectrum of $\text{Np}(\text{S}_2\text{PPh}_2)_4$ (left), and sulfur K-edge XAS comparison of $\text{Np}(\text{S}_2\text{PPh}_2)_4$ with Nd and U analogues (right).

New Ligand Design

Based upon the K-edge XAS data pertaining to the 'free' uncoordinated extractant molecules, it was possible to make predictions for a new ligand design that should be actinide selective. The hypothesis is that the ring twist in $\text{S}_2\text{P}(\text{o-CF}_3\text{C}_6\text{H}_4)_2^{1-}$ is responsible for the unique electronic structure that results in preferential actinide binding. Therefore, a new ligand design that 'locks-in' the ring twist by preventing aryl ring rotation is predicted to optimize the actinide selectivity. A multi-step synthesis towards a first new ligand design has been implemented (Figure 101). Near future plans intend to explore the selectivity of this new ligand through solvent extraction studies to confirm if the prediction is correct or not.

Separations and Waste Forms
2013 Accomplishments Report

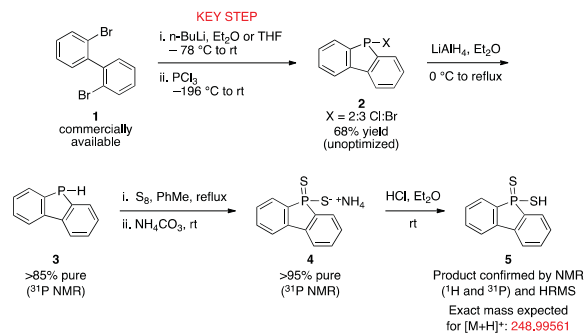


Figure 101. Reactivity scheme depicting the synthetic steps en route to successful synthesis of product 5, in which the phenyl rings are ‘tethered’ to confer favorable orbital mixing for actinide binding.

Publications

1. Boland, K. S., D. E. Hobart, S. A. Kozimor, M. M. MacInnes, and B. L. Scott (2013)., “The Coordination Chemistry of Trivalent Lanthanides with Diphenyldithiophosphinate Anions.” *Polyhedron*, in press. DOI: <http://dx.doi.org/10.1016/j.poly.2103.09.019>.

Decay Impacts in Waste Forms

Transmutation of Radionuclides to Chemically Distinct Daughter Products on Crystalline Waste Form Stability

C. Stanek, stanek@lanl.gov

The effect of transmutation of radionuclides to chemically distinct daughter products (e.g. ^{90}Sr decay to ^{90}Zr and ^{137}Cs to ^{137}Ba) on crystalline waste form stability is an important problem that has received limited attention during the past 30 years of waste form development due to the technical challenges associated with study of this problem. However, improvements in computational materials science methodologies and availability of very short-lived radioisotopes due to nuclear medicine have enabled this topic to be reconsidered. Ultimately, researchers posit that improved understanding of waste form behavior during chemical evolution will not only allow for improved predictability of waste form performance, but also enable improvements in the design of chemically durable waste forms [Mascarelli, 2013; Jiang, et al., 2010]. This section summarizes recent accomplishments related to study of this topic, including: completion of a Roadmap for Understanding β -Decay Effects of Fission

Products in Waste Forms and development of an accelerated chemical aging experimental approach for the validation of theory.

Roadmap for Understanding β -Decay Effects of Fission Products in Waste Forms

A roadmap document titled “Understanding β -Decay Effects of Fission Products in Waste Forms” was jointly prepared by PNNL and LANL staff. This report defines scientific challenges that current prevent systematic understanding of decay-induced effects on crystal structure and phase stability. A corresponding research plan, consisting of integrated experiments and theory, was proposed to address these research challenges in order to ultimately enable design of advanced waste forms. The primary research challenge identified is the effect of evolving chemistry on the phase stability of crystalline waste forms. That is, the important question is: what happens to a crystalline waste form upon the formation of a chemically disparate daughter product? In order to systematically address this question, there are a number of features of the problem to be tackled. Apart from the obvious consideration of phase stability of a range of candidate waste forms as a function of daughter product concentration, it is also important to fundamentally understand the nature of the daughter products residing upon formation in an undesirable coordination. That is, it is tempting to treat daughter products from transmutation as conventional dopants that are e.g. charge compensating by conventional means. Rather, a rather simple defect chemistry analysis [3] suggests that transmutation leads to a different type of defect that requires separate treatment. The role of transmutation on phase stability and defect chemistry requires improved understanding of thermodynamic behavior. It is also necessary to understand kinetic behavior to fully understand waste form evolution, which includes: radiolysis associated with β decay, direct nuclear displacement associated with both the β particles but also the recoil of the daughter nucleus, and the thermal diffusion of defects either present thermally or created via these damage processes. Related to these issues is the consideration of defects that may influence the thermodynamic and kinetic behavior. For example, due to conservation of energy and momentum, the daughter nucleus

Separations and Waste Forms
2013 Accomplishments Report

will recoil following beta decay. The shape and magnitude of the energy spectrum of the recoiling daughter nucleus is difficult to quantify and there are very few measurements of the beta-recoil spectrum in solids due to the problem of scattering.

To address these issues, researchers have proposed a combined experimental-theoretical approach. The experiments proposed (and already begun) rely on samples that introduce daughter products either by ion implantation or by transmutation of very short-lived isotopes. The ion implantation approach is discussed in the other report in this section, and the very short-lived isotope approach will be discussed in the next subsection here. For the theory, DFT is the only viable approach to consider the effects of chemical evolution on crystalline solids. Although in some cases classical pair potentials can be used to adequately describe the starting waste form compound, *e.g.* CsCl, these types of models will not capture radioparagenetic phase formation where the bonding nature deviates from purely ionic in a way that is difficult to predict *a priori*.

Accelerated Chemical Aging of Crystalline Waste Forms

Since “short-lived” fission products (*e.g.* ^{90}Sr and ^{137}Cs) have half-lives too long for efficient direct experimental examination, researchers devised an “accelerated chemical aging” approach to determine the effect of daughter product formation on waste form stability [Stanek, et al., 2012]. This approach involves the study of samples comprised of very short-lived isotopes. This approach allows us to experimentally examine the behaviors observed in DFT calculations, such as the formation of non-intuitive phases. An example of this shown in Figure 102, where figure (a) describes a DFT prediction of rocksalt BaCl formation from the decay of $^{137}\text{CsCl}$ [Jiang, et al., 2009]. An experiment to validate this prediction would require several hundred years. A similar result is shown in Figure 102(b), which predicts the formation of a bixbyite-like Hf_2O_3 structure from the decay of $^{177}\text{Lu}_2\text{O}_3$. For this example, it is important to note that ^{177}Lu is not a fission product of interest from a waste disposal perspective. However, it does mimic the chemical behavior of ^{137}Cs and ^{90}Sr , but does so very

rapidly. Specifically, the chemical effects of transmutation that require experiments of more than 200 years for ^{137}Cs or ^{90}Sr , can be performed in less than 2 months. Indeed, $^{177}\text{Lu}_2\text{O}_3$ transmission electron microscopy samples have been fabricated and corresponding experiments were recently performed, see Figure 103. Further analysis is required to fully explain the data, but initial structure refinement suggests the formation of ~ 5 discrete phases during the transmutation of $^{177}\text{Lu}_{2-x}\text{Hf}_x\text{O}_3$ from $x = 0$ to $x = 1$. These phases do not correspond to the relevant equilibrium phase diagram, which indicates that the chemical evolution of crystalline waste forms requires special consideration.

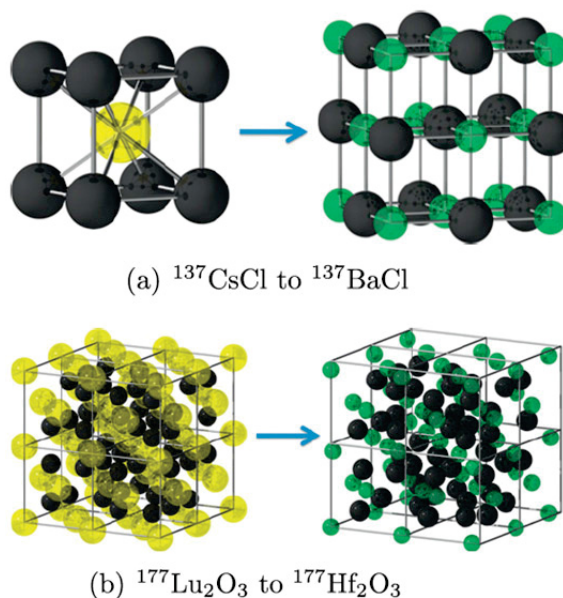


Figure 102. Two examples of DFT predictions, where (a) describes the formation of rocksalt BaCl from the decay of ^{137}Cs in CsCl, and (b) describes the formation of bixbyite Hf_2O_3 from the decay of ^{177}Lu in Lu_2O_3 . In both examples, the yellow atoms refer to the parent atom, green to the daughter, and black to stable lattice anions.

Separations and Waste Forms
2013 Accomplishments Report

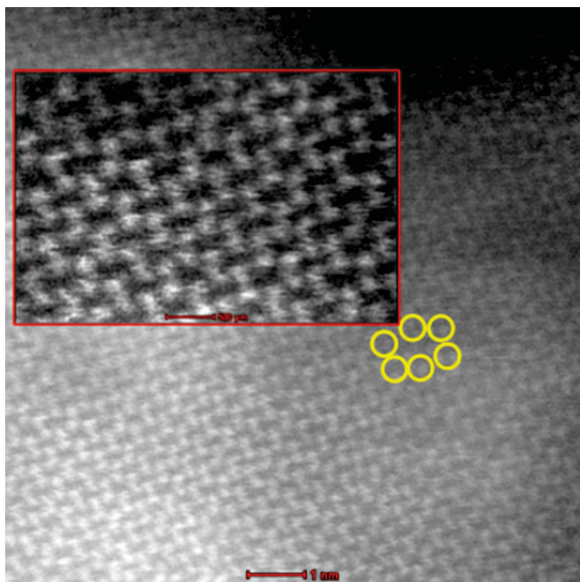


Figure 103. Preliminary TEM results for $^{177}\text{Lu}_2\text{O}_3$, which suggest the formation of non-intuitive phases.

References

1. Mascarelli, A., (2013). "Eternal Challenge." *New Scientist*, 220: 2941. November 2.
2. Jiang C., et al., (2010). "Using 'Radioparagenesis' to Design Robust Nuclear Waste Forms." *Energy and Environmental Science* 3: 130.
3. Uberuaga, B. P., C. Jiang, C. R Stanek, K. E. Sickafus, N. A. Marks, D. J Carter, A. L. Rohl (2010). "Implications of Transmutation on the Defect Chemistry in Crystalline Waste Forms." *Nucl. Inst. Meth. B* 268: 19, 3261.
4. Stanek C.R., et al., (2012). "Accelerated Chemical Aging of Crystalline Nuclear Waste Forms." *Current Opinion of Solid State and Materials Science* 16: 126.
5. Jiang C. et al., (2009). "Predicting from First Principles the Chemical Evolution of Crystalline Compounds Due to Radioactive Decay: The Case of the Transformation from CsCl to BaC.", *Phys. Rev. B* 79: 132110.

Chemical and Charge Imbalance Induced by Radionuclide Decay: Effects on Waste Form Structure

W. Jiang, weilin.jiang@pnnl.gov; L. Kovarik (PNNL), and T. M. Nenoff (SNL)

Introduction

Our previous report on the irradiation study of aluminosilicate pollucite ($\text{CsAlSi}_2\text{O}_6$) [Jiang and Van Ginhoven, 2013] indicates that the material is readily amorphizable under ion or electron irradiation. Complete amorphization in pollucite occurs under F^+ ion irradiation at 673 K. This behavior is attributed to the accumulation of lattice disorder and eventual collapse of the crystal structure at a critical dose. The production of lattice disorder is a result of elastic collisions in the damage cascade process that is initiated by the energetic projectiles. Amorphization in pollucite was also observed upon 300 keV electron irradiation. Each electron can only impart a small amount of energy to the target atom through elastic collision, which is well below the threshold displacement energy for any of the sublattices in pollucite. Radiolysis is responsible for the material amorphization. Our report [1] also indicates that once $\text{CsAlSi}_2\text{O}_6$ pollucite is amorphized, cesium becomes mobile at moderately high temperatures (673 K). It tends to diffuse to the surface and escape from the solid. This would be the worst scenario for the potential waste form, as it needs to confine ^{137}Cs radionuclides from release to the environment. Researchers have also reported [1] that Cs is immobile in polycrystalline pollucite even under He^+ ion irradiation. Therefore, it is crucial to maintain pollucite in the crystalline form to prevent from possible Cs release. Due to self electron irradiation and heat generation in addition to chemical effects associated with β^- decays, a fundamental study is needed to understand and predict structural evolution in pollucite. This technical report summarizes some of the recent results on critical temperature for amorphization, threshold electronic energy density for amorphization, and identification of Ba-containing precipitates in Ba-doped pollucite.

Experimental Procedures

Ba-doped pollucite of $\text{Cs}_{0.9}\text{Ba}_{0.05}\text{AlSi}_2\text{O}_6$ and $\text{Cs}_{0.9}\text{Ba}_{0.1}\text{AlSi}_2\text{O}_6$ used in this study was obtained

Separations and Waste Forms
2013 Accomplishments Report

from Sandia National Laboratories. Both samples were implanted with 1.2 MeV F^+ ions up to a fluence of $1.36 \times 10^{17} F^+/cm^2$, corresponding to an atomic concentration of 5 at.% at the profile peak maximum. The implantation was performed at temperatures of 673 and 873 K; the implanted samples were subsequently annealed in flowing Ar at 1073 K for 4 and 2 hours, respectively. Cross sectional thin specimens of the implanted and post-annealed samples were prepared using a FEI Helios 600 Nanolab system of focused ion beam (FIB) and were examined using a FEI aberration-corrected Titan 80-300 scanning transmission electron microscope (STEM). The Stopping and Range of Ions in Matter (SRIM) simulations [Ziegler, et al., 1985] were performed under the assumption that the threshold displacement energy for each sublattice in $CsAlSi_2O_6$ is 50 eV, which can be corrected once the accurate values are determined.

Results and Discussion

Figure 104(a) shows a low-resolution high-angle annular dark-field (HAADF) STEM micrograph of $Cs_{0.9}Ba_{0.1}AlSi_2O_6$ pollucite implanted with 1.2 MeV F^+ ions to $1.36 \times 10^{17} F^+/cm^2$ at 673 K and annealed at 1073 K for 4 hours. Selected area electron diffraction (data not shown) inside the implantation band indicates that the surface layer is completely amorphized. The crystalline-amorphized interface is shown in the inset of the figure. Beyond the amorphization layer is the unaffected area showing crystalline grains with precipitates (brighter areas) at the grain boundaries of the Ba-doped pollucite. EDXS analysis (data not shown) indicates that the precipitate consists of mainly Ba, Si and O, while the darker area is pure $CsAlSi_2O_6$ pollucite. Further analysis to identify the crystal phase of the precipitate is reported below. The white area surrounding the sample is due to larger thickness where more electrons are scattered into the high-angle detector.

Under the irradiation conditions, the material is fully amorphized from the surface to the depth of 1.7 μm , as shown in Figure 104(a). SRIM simulation was performed and the result is shown in Figure 104(b). The damage peak maximum is predicted to be at 1.55 μm . Clearly, the amorphization at the damage peak is produced due

to damage accumulation and structural collapse at a critical dose for amorphization through elastic collision-induced damage cascades. In contrast, the precipitates within the amorphization band are found to be not amorphized, exhibiting more resistance to ion-beam irradiation induced amorphization at the elevated temperature.

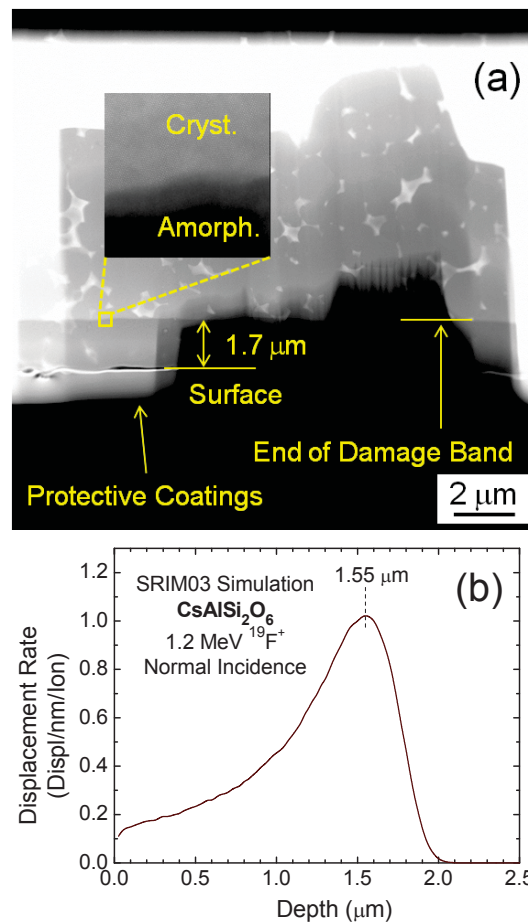


Figure 104. (a) Low-resolution HAADF STEM for $Cs_{0.9}Ba_{0.1}AlSi_2O_6$ pollucite implanted with 1.2 MeV F^+ ions to $1.36 \times 10^{17} F^+/cm^2$ at 673 K and annealed at 1073 K. The pollucite is amorphized from surface to the depth of 1.7 μm . (b) SRIM simulation of depth profiles of lattice displacement rates.

In order to avoid full amorphization in pollucite due to damage accumulation, sample temperature must be raised to increase the simultaneous recovery rate. When a total balance between the rate of defect production and that of defect recovery is reached, amorphization through the damage accumulation will not occur. Figure 105(a) shows the near-surface region of $Cs_{0.9}Ba_{0.1}AlSi_2O_6$ implanted with 1.2 MeV F^+ ions

Separations and Waste Forms
2013 Accomplishments Report

to $2.73 \times 10^{16} \text{ F}^+/\text{cm}^2$ at 873 K. The corresponding dose [~ 5 dpa (displacements per atom)] at the damage peak ($\sim 1.55 \mu\text{m}$ deep) is relatively high and the material is still not amorphized, suggesting that the irradiation temperature (873 K) is close to the critical temperature for amorphization in pollucite. However, a continuous amorphization band from the surface to the depth of 460 nm is observed in the material, as shown in Figure 105(a). The result suggests that the amorphization in pollucite is a direct result of radiolysis through ionization in the near-surface region, where the electronic energy deposition by the incident F^+ ions exceeds the critical density for amorphization. This result is consistent with electron irradiation of pollucite. It was evident that the pollucite material was readily amorphized under 300 keV electron irradiation during STEM for alignment of the crystal zone axis to the electron beam. Since the maximum energy imparted to the lattice atoms by 300 keV electrons through elastic collisions is well below the threshold displacement energy (on the order of 10 – 100 eV) for the sublattices in $\text{CsAlSi}_2\text{O}_6$, accumulation of atomic displacements is not responsible for the amorphization. Instead, the amorphization is attributed to ionization-induced radiolysis due to electronic energy deposition from the electron beam. It should be noted that similar to what has been observed in the nuclear collision processes, the precipitate within the amorphized pollucite band is not amorphized, showing a greater resistance to radiolysis. Figure 105(b) shows the same sample after post annealing at 1073 K for 2 hours. As a result, the amorphized layer was thinned slightly from 460 to 430 nm, suggesting that there is only a moderate epitaxial recrystallization at the interface. A magnified view of the crystalline-amorphized interface for the annealed sample is shown in Figure 105(c).

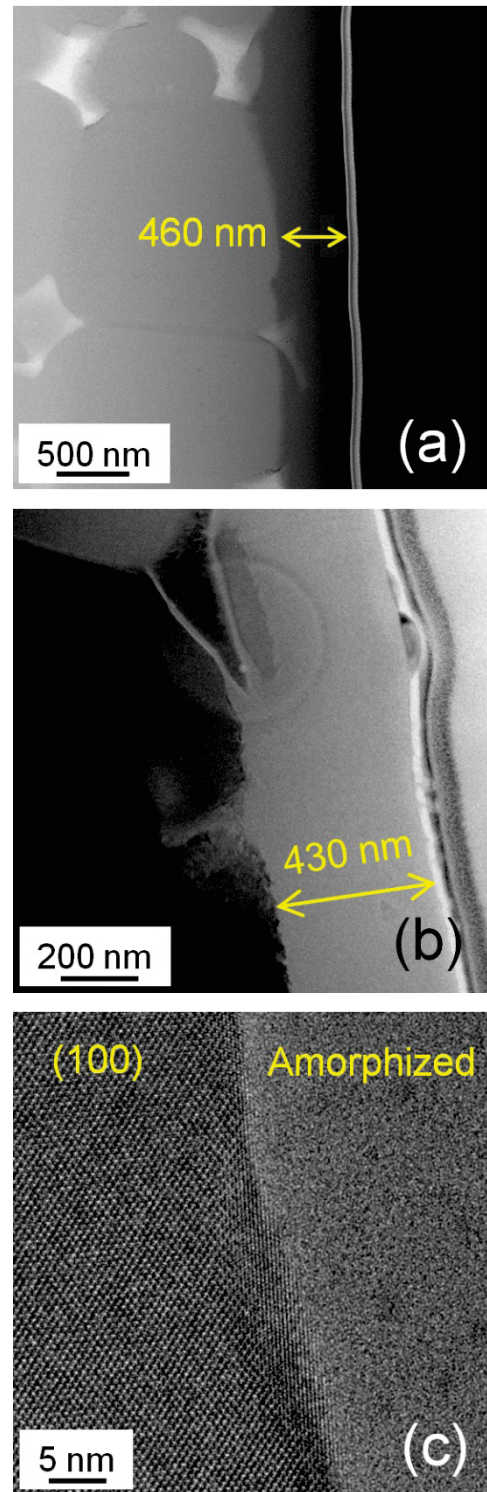


Figure 105. (a) Low-resolution HAADF STEM for $\text{Cs}_{0.9}\text{Ba}_{0.1}\text{AlSi}_2\text{O}_6$ pollucite implanted with 1.2 MeV F^+ ions to $2.73 \times 10^{16} \text{ F}^+/\text{cm}^2$ at 873 K. (b) Bright-field TEM image of the implanted sample in (a) after annealing at 1073 K. (c) High-resolution HAADF STEM image of the annealed sample showing the crystalline-amorphized interface.

Separations and Waste Forms
2013 Accomplishments Report

Similar behavior of ionization-induced material decomposition and amorphization in as-implanted $\text{Cs}_{0.9}\text{Ba}_{0.05}\text{AlSi}_2\text{O}_6$ is also observed, as shown in Figure 106. The thickness (460 nm) of the amorphization band in the Ba-doped pollucite under the identical irradiation conditions is the same as the data for the as-implanted $\text{Cs}_{0.9}\text{Ba}_{0.1}\text{AlSi}_2\text{O}_6$ [Figure 105(a)]. In addition, Cs accumulation at the sample surface is observed by EDXS (data not shown) for the amorphized pollucite at 873 K, as shown in Figure 106(b).

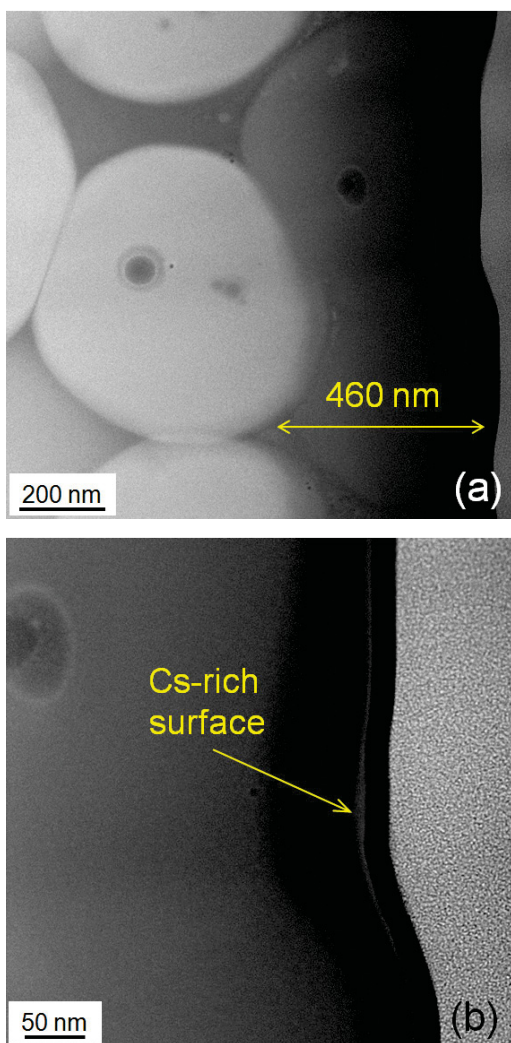


Figure 106. (a) HAADF STEM image showing a 460 nm thick amorphized layer from the surface of $\text{Cs}_{0.9}\text{Ba}_{0.05}\text{AlSi}_2\text{O}_6$ implanted with 1.2 MeV F^+ ions to $2.73 \times 10^{16} \text{ F}^+/\text{cm}^2$ at 873 K. (b) A magnified view showing a thin Cs-rich layer on the surface.

This result is consistent with the previous report [1] that Cs is mobile in amorphized pollucite and

tends to diffuse to the surface. The observed holes in the grains are not yet completely understood, but might be associated with Cs aggregation and evaporation during the sintering process. It is not related to ion irradiation. A separate study is required for clarification and understanding.

According to SRIM simulation with the results shown in Figure 107, the observed thickness (460 nm) of the amorphized surface layer at ion fluence of $2.73 \times 10^{16} \text{ F}^+/\text{cm}^2$ corresponds to an electronic energy deposition rate of 860 eV/nm/ion. Thus, the threshold density of electronic energy deposition for amorphization in $\text{CsAlSi}_2\text{O}_6$ is estimated to be $235 \text{ keV}/\text{nm}^3$. Because this value is much larger than that from self electron irradiation in $^{137}\text{CsAlSi}_2\text{O}_6$, pollucite crystal is not expected to be fully amorphized due to ionization by the electron irradiation from the β^- decay process. After hundreds of years, a significant fraction of ^{137}Cs (half life = 30.2 years) decays to ^{137}Ba , resulting in a dramatic change in the composition. New crystalline phases, e.g., the observed precipitate phase (see below) with more resistance to radiolysis, can form in the structure.

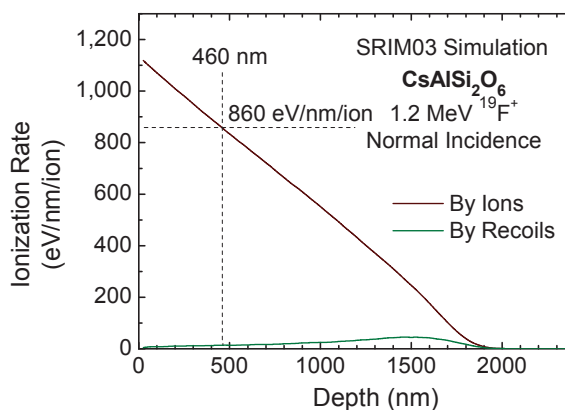


Figure 107. SRIM simulation of ionization rates as a function of depth in $\text{CsAlSi}_2\text{O}_6$ pollucite irradiated with 1.2 MeV F^+ ions.

A detailed STEM study of the Ba-containing precipitate has also been performed to identify its composition and crystal phase. For a chosen precipitate, three zone axes were aligned with the electron beam and atomic-level resolution HAADF STEM images were recorded for lattice patterns, as shown in Figure 108. Based on EDXS analysis (data not shown) that suggests the precipitate consists of mainly Ba, Si and O, a

Separations and Waste Forms
2013 Accomplishments Report

search of current database for barium silicates was conducted. Simulations of lattice patterns and comparisons to the STEM data were performed based on commercial software “Crystal Maker”. The best match of the lattice patterns between the experiment and simulation is shown in Figure 108, which suggests that the precipitate is a monoclinic $Ba_2Si_3O_8$ crystal with space group P21/c, lattice parameters $a = 1.2477$ nm, $b = 0.4685$ nm, and $c = 1.3944$ nm, and interplanar angles $\alpha = 90^\circ$, $\beta = 93.54^\circ$, and $\gamma = 90^\circ$. The zone axes were identified to be $[-2,0,1]$, $[-4,8,1]$ and $[-1,2,0]$, respectively, as indicated in Figure 108.

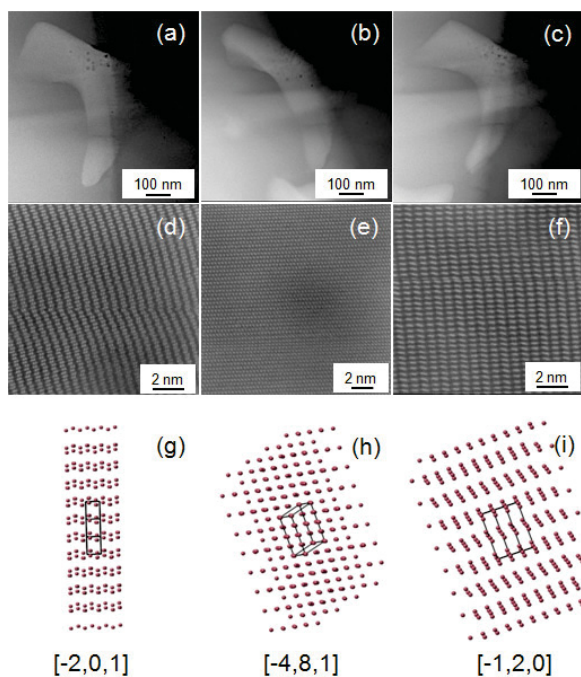


Figure 108. (a), (b) and (c) Low-resolution HAADF STEM images of a Ba-containing precipitate in Ba-doped pollucite $Cs_{0.9}Ba_{0.1}AlSi_2O_6$ observed along three zone axes. (d), (e) and (f) The corresponding high-resolution HAADF STEM images of the precipitate. (g), (h) and (i) Lattice simulations of monoclinic $Ba_2Si_3O_8$ projected along the $[-2,0,1]$, $[-4,8,1]$ and $[-1,2,0]$ axes, which matches the observed lattice patterns, respectively.

In order to confirm the crystal structure of the precipitate, electron diffractions along the three zone axes were also performed. The results are shown in Figure 109(a) through (c). The lattice spacing parameters d_1 and d_2 have been measured and are indicated in the figures. Simulation of the diffraction patterns was conducted using software “JEMS” and the corresponding lattice spacing

results for the $Ba_2Si_3O_8$ are obtained and indicated in Figure 109(d) through (f) for zone axes $[-2,0,1]$, $[-4,8,1]$ and $[-1,2,0]$, respectively. There is an excellent agreement between the simulation and experiment, confirming that the precipitate is the monoclinic $Ba_2Si_3O_8$. Note that the exact origin of the small bright diffraction dots in Figure 109(b) is not clear at this time. It might be associated with a possible superlattice structure of Al substitution for Si or Cs substitution for Ba.

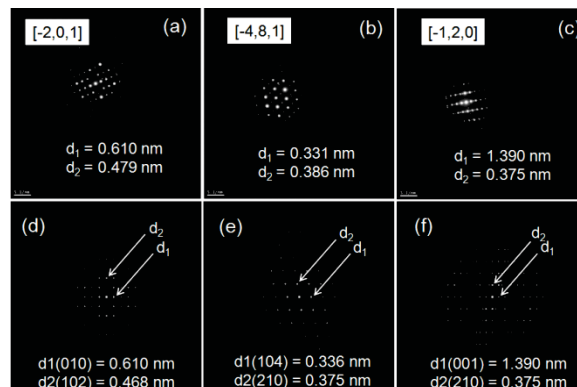


Figure 109. (a), (b) and (c) The corresponding electron diffraction patterns from the Ba-containing precipitate shown in Figs. 5 (a), (b) and (c). (d), (e) and (f) show simulated diffraction patterns of $Ba_2Si_3O_8$ projected along the $[-2,0,1]$, $[-4,8,1]$ and $[-1,2,0]$ axes, which match the observed diffraction patterns, respectively.

Conclusions

F^+ ion implantation at 673 K leads to amorphization of $CsAlSi_2O_6$ pollucite crystals. The critical temperature for amorphization is close to 873 K. The pollucite is also susceptible to electron irradiation induced amorphization due to ionization-induced material decomposition (radiolysis). Complete amorphization through radiolysis can be avoided below the threshold density of electronic energy deposition, which has been determined to be 235 keV/nm³ in this study. Cesium is mobile and diffuses to the surface in amorphized pollucite at elevated temperatures. Ba-containing precipitates in $Cs_{0.9}Ba_{0.1}AlSi_2O_6$ are identified as monoclinic $Ba_2Si_3O_8$, which is more irradiation resistant to ion- and electron-irradiation induced amorphization.

References

- Jiang, W., and M. Van Ginhoven (2013). “Chemical and Charge Imbalance Induced by

Separations and Waste Forms
2013 Accomplishments Report

Radionuclide Decay: Effects on Waste Form Structure.” FCRD-UFD-2012-000377, PNNL-20312-3. Pacific Northwest National Laboratory. Also in “Separations and Waste Forms Research and Development FY2012 Accomplishment Report.” FCRD-SWF-2013-000073; INL/EXT-12-27936. Idaho National Laboratory, February 2013, p. 97 – 100.

2. Ziegler, J. F., J. P. Biersack, and U. Littmark (1985). *The Stopping and Range of Ions in Solids*. New York: Pergamon. Available at <http://www.srim.org>.

Publications

1. Van Ginhoven, R. M., W. Jiang, and C. Stanek (2013). “DRAFT Roadmap for Understanding β Decay Effects of Fission Products in Waste Forms.” PNNL-22363. Pacific Northwest National Laboratory.
2. Jiang, W., M. E. Bowden, Z. Zhu, P. A. Jozwik, J. Jagielski, and A. Stonert (2012). “Defects and Minor Phases in O^+ and Zr^+ Ion Co-implanted $SrTiO_3$.” *Industrial and Engineering Chemistry Research* 51, 621-628.
3. Jiang, W., R. M. Van Ginhoven, L. Kovarik, J. E. Jaffe, and B. W. Arey (2012). “Superlattice Structure and Precipitates in O^+ and Zr^+ Ion Co-implanted $SrTiO_3$: a Model Waste Form for ^{90}Sr .” *Journal of Physical Chemistry C* 116, 16709-16715.
4. Jaffe, J. E., R. M. Van Ginhoven, and W. Jiang (2012). “Interstitial and Substitutional Zirconium in $SrTiO_3$.” *Computational Materials Science* 53, 153-157.
5. Jiang, W., and R. M. Van Ginhoven (2012). “Chemical and Charge Imbalance Induced by Radionuclide Decay: Effects on Waste Form Structure.” PNNL-20312-3. Pacific Northwest National Laboratory.
6. Jiang, W., R. M. Van Ginhoven, and D. M. Strachen (2012). “Chemical and Charge Imbalance Induced by Radionuclide Decay: Effects on Waste Form Structure.” PNNL-20312. Pacific Northwest National Laboratory.
7. Jiang, W., R. M. Van Ginhoven, and D. M. Strachen (2010). “Chemical and Charge

Imbalance Induced by Radionuclide Decay: Effects on Waste Form Structure.” PNNL-20049. Pacific Northwest National Laboratory.

Nano-Continuum Modeling of Nuclear Waste Glass Corrosion

C. Steefel, cisteefel@lbl.gov

The focus of the nano-continuum scale modeling of nuclear waste glass corrosion is an experiment involving a French glass SON68 specimen leached for 25 years in a granitic environment [Guittonneau, et al., 2011; Gin, et al., 2011; Gin, et al., 2013]. The 25 year experiment carried out by French scientists offers a unique opportunity to examine the controls on the rate of nuclear glass corrosion under controlled experimental conditions using a borosilicate glass of the kind typically considered for nuclear waste storage. The long term experiment makes it possible to move beyond the initial rate stage, with direct measurements of the longer term, residual rates of corrosion. Important in this regard is whether the rate of corrosion shows a parabolic dependence on time, as would be expected from a conventional diffusion model in which the reaction products (amorphous silica-rich gel) create a diffusion barrier that grows in width over time, or whether the time dependence is linear [Guittonneau, et al., 2011]. A linear dependence on time would call into question the model of a PRI presented by Cailleteau et al, 2008, although it does not entirely preclude such a model if the interface maintains a constant width over time. The leachate concentration measurements every 56 days over 25 years by Guittonneau, et al. [2011] provide data to constrain the long term corrosion rate and its time dependence. Equally important, and in the end critical for understanding the actual mechanisms involved, was the use of high spatial resolution chemical profiling of the nuclear glass leach layer. In this regard, the width of the reaction zone constrains to some extent the mechanisms involved, since a sharp boundary is not compatible with models presented earlier in which leaching occurs by interdiffusion over a significant width of the gel corrosion layer. In addition, the spatial ordering of concentration profiles (coincident or non-coincident) may offer

Separations and Waste Forms
2013 Accomplishments Report

constraint on the mechanisms involved [Gin, et al, 2013].

This section focuses on capturing the nano-scale concentration profiles reported in Gin, et al. [2013]. Carrying out the numerical analysis all the way to 25 years would require a larger grid, albeit in one dimension, so this will be reported on in subsequent reports. The research uses a high resolution continuum model with a constant grid spacing of 1 nanometer to investigate the glass corrosion mechanisms. While the continuum assumption is a severe approximation given the fact that the pores themselves are close to this size, this is currently the only way researchers have to consider the longer spatial and time scales for this problem. In addition, it allows us to include full multicomponent chemistry (including precipitation and dissolution), something which is not possible with molecular modeling approaches [Bourg and Steefel, 2012].

Summary of 25 Year French Glass SON68 Leaching Experiment

A Guittonneau, et al [2011] report on a 25.75-year leaching experiment designed to improve understanding of the mechanisms controlling glass dissolution in geological disposal conditions. A SON68 glass block was leached in slowly renewed synthetic groundwater (at 90°C, 100 bars) in contact with sand, granite and Ni–Cr–Mo alloy specimens. One hundred and sixty-three samples were collected over the duration of the experiment and were used to calculate the mean thickness of the altered glass (28 (\pm 9) μ m) and the glass dissolution rate. After several months, the corrosion rate remained constant at $6 \times 10^{-3} \text{ g m}^{-2} \text{ d}^{-1}$ over the 25 years of the experiment, which is about 20 times higher than the residual rate measured in a batch reactor at the same temperature. The glass alteration layers investigated by SEM at the end of the experiment showed neither a homogeneous thickness nor a homogeneous morphology.

The location of the sampling valve (at half the height of the glass block) seems to divide the glass block into two parts. In the upper half (above the sampling valve), the general morphology of the alteration layer consists in a relatively simple and uniform gel and some secondary phases which are

rare earth phosphates. The mean measured thickness of this alteration layer is 6.7 (\pm 0.3) μ m. However, in the lower half of the glass block, the gel layer is thicker, with a mean measured thickness of 81.3 (\pm 1.1) μ m. These results indicate that the chemistry of the leachate solution was not homogeneous, presumably due to the effects of local transport. This led the authors to conclude that rate of glass corrosion is very sensitive to the composition of the leachate solution close to the glass surface, and thus to the rate of water renewal (flow). The study clearly shows that the overall rate of corrosion (aside from the variations in corrosion rate presumably due to local transport effects) was constant (linear) over nearly 25 years.

While the Guittonneau, et al. [2011] study presented important information on the bulk leaching rate of the nuclear glass specimen over 25 years, the ground-breaking study by Gin et al (2013) on the SON68 glass specimen presented extremely high spatial resolution post-mortem chemical profiles using atom probe tomography (APT) and energy-filtered transmission electron microscopy. The APT technique allows the 3D reconstruction of the elemental distribution at the reactive interphase with sub-nanometer precision. The results show that (1) Li from the glass and hydrogen from the solution exhibit anti-correlated 15 nm wide gradients located between the pristine glass and the hydrated glass layer, and (2) boron exhibits an unexpectedly sharp profile (\sim 3 nm width) located just outside (on the solution side) of the Li/H interdiffusion layer. The authors interpreted the sharp profile as being consistent with a dissolution front rather than a diffusion-controlled release of boron. As a result, the accessibility of water to the pristine glass could be the rate-limiting step under these conditions. More generally, these findings strongly support the importance of interdiffusion coupled with hydrolysis of the pristine glass silicate network as the primary controls on the long-term dissolution rate. The primary objective of the nano-continuum approach presented here is to determine whether this conceptual model is supported by quantitative numerical modeling.

Separations and Waste Forms
2013 Accomplishments Report

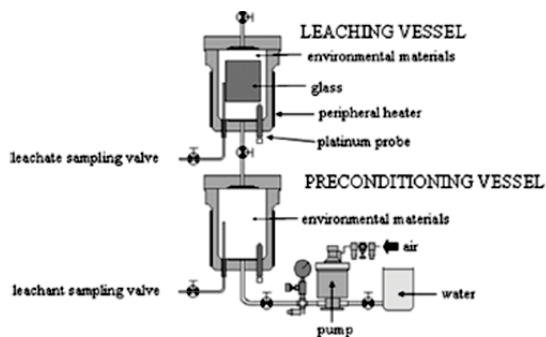


Figure 110. Experimental setup for the 25 year SON68 glass leaching experiment [Guittonneau, et al, 2011]

Kinetic-Microscopic-Continuum Model (K μ C)

A new Kinetic Micro-Continuum (K μ C) model for glass corrosion has been developed that avoids *a priori* assumptions about rate-limiting steps in the overall corrosion process. The K μ C model provides a flexible approach in which individual parameters and processes are tunable, but in every case coupled within an overall dynamic framework. The K μ C model may currently be run with either a single glass composition, which requires initially congruent dissolution, or it may be run with one or more glass end-member compositions that show differing thermodynamic and kinetic behavior. Since the single glass composition can be used to model overall incongruent reaction by incorporating rapid re-precipitation and/or ripening reactions, it is the preferred approach. The model currently includes the following processes

- Diffusion of water through the pristine glass and its alteration products;
- Ion exchange between water and the cations in the glass;
- Kinetically controlled hydrolysis reactions resulting in breaking of glass network bonds (Si, B, Al,...). The rate may be described by either a linear or a nonlinear Test of Significant Toxicity (TST) law with an affinity control supplied by a specific phase (e.g., amorphous silica), or with an irreversible rate law with no affinity control. In either case, far from equilibrium dependencies of the rate on other dissolved

(e.g., pH, Al, silica) or sorbed species can be included;

- Multicomponent diffusion of ions through the glass corrosion products;
- Precipitation reactions for amorphous and/or crystalline phases of variable composition that are kinetically and thermodynamically controlled;
- Kinetically controlled ripening and/or densification reactions that can reduce the porosity and/or pore connectivity (and thus the diffusivity) of the corrosion products;
- Kinetically and thermodynamically controlled formation of new crystalline phases (e.g., smectite, zeolite), with possible consequences for the transport properties of the corrosion layer;
- Flow and diffusion in the aqueous phase adjacent to the glass surface.

The K μ C model incorporates the possibility of diffusion-limited glass corrosion by considering explicitly the kinetically-controlled densification of either (1) a residual silica-rich glass network in which other important components (e.g., the cations and network former boron) have been leached, or (2) of a newly precipitated silica-rich gel layer. However, in contrast to the GRAAL model [Frugier, et al., 2008; Cailleteau, et al., 2008], a diffusion-limited corrosion rate is not assumed *a priori* in the K μ C model. Whether a passivating layer (i.e., defined as the PRI by Frugier et al., 2008) forms in the K μ C model depends on the relative rates of (1) silica recrystallization and densification, (2) leaching of the glass constituents, and (3) dissolution and/or recrystallization of the corrosion products.

The dissolution rate of the glass in the K μ C model is not artificially limited by the approach to amorphous silica saturation (e.g., Grambow, 2006), although this formulation can be used if needed. Thus, non-zero corrosion rates are allowed under conditions of silica saturation. Since the K μ C model is formulated with an explicit treatment of multicomponent diffusion, kinetically-controlled mineral dissolution and precipitation, and glass corrosion, it can take into

Separations and Waste Forms
2013 Accomplishments Report

account the possibility that local chemical conditions within the nano- and micropores in the reaction products (i.e., the silica gel layer) may differ from conditions in the bulk solution adjacent to the corroding glass. In the absence of a reaction layer that limits diffusive transport to the pristine glass surface, silica saturation may not occur and the long-term rate of glass corrosion may remain high. In this case, the reduction in rate due to silica will be largely due to the ambient silica concentrations in the groundwater.

Model Setup for 25 Year French Glass Experiment

Ideally, the treatment of the corrosion of the SON68 glass over 25.75 years would involve a 3D analysis so as to capture the strong variations in the width of the corrosion zone on the glass surface within the experimental reactor. Clearly, there is some form of combined transport control at work here, potentially reflecting the role of both flow (the solution is renewed completely about once every five years, or at a rate of 22% of the total reactor porosity per year) and molecular diffusion. In addition to the 3D geometry, however, there is also the challenge representing adequately the multiple scales involved here, with the experimental reactor involving scales of 10s of centimeters, while the corrosion layers on the glass require discretization on the order of nanometers. Since the preliminary focus is on capturing the width of the various reaction zones close to the pristine glass surface and their relative positions, the research assumes a pure diffusion-controlled regime and a constant grid spacing of 1 nanometer. The assumption that a continuum model applies at this spatial scale is a severe approximation, given that pore sizes are close to this value, but the approach allows us to compare results with elemental profiles and avoids the additional requirement of a full atomistic treatment.

As a boundary condition at one of the reactor-glass specimen system, the research considers a Dirichlet condition corresponding to the Volvic mineral water used to replenish periodically the experimental reactor [Guittonneau, et al, 2011]. The fixed concentration (Dirichlet) boundary condition is probably the best approximation to a flow through system. At the other end of the 1D

system, the research assumes a no-flux condition, which is reasonable as long as the corrosion front does not fully penetrate the glass specimen. Within the first 25 nanometers of the reaction, the system is characterized by a porosity of 0.41 (as in the experimental system reported by Guittonneau, et al., 2011) and a mixture of quartz sand and granite. A diffusivity of 10^{-11} m²/s for all ions was assumed for the sand-granite mixture. The alloy specimens included in the experiments were not considered in the modeling. From 25 nanometers out to 225 nanometers, the system was assumed to consist of a SON68 borosilicate glass with a porosity of 1%. The diffusivity of the borosilicate glass was assumed to follow a threshold type of model [Navarre-Sitchler, et al., 2009], with a value of 10^{-23} m²/s (in approximate agreement with the value proposed by Gin, et al., 2013) for values of the porosity below 30% and a value of 10^{-11} m²/s for porosity values above 30%. Modeling carried out earlier (results not shown here) indicate that a simple porosity dependence, as in an unmodified Archie's Law formulation, cannot replicate the observed concentration profiles, since the reaction front continuously widens due to the porosity and diffusivity enhancement using this model. Some form of a threshold model, based on the idea that dissolution and porosity enhancement increase the rate of diffusivity by increasing connectivity [Navarre-Sitchler, et al., 2009], appears to be required.

The dissolution of the glass is assumed to follow an affinity rate law [Grambow, 2006], but with a cubic dependence on the saturation state (departure from equilibrium) with respect to amorphous silica. A linear TST dependence does not capture the sharp B front and places the B (and Na) dissolution front closer to the Li-H interdiffusion front. The rate of glass corrosion, in addition to following a cubic dependence on the departure from equilibrium, also depends on the hydration state of the glass. In other words, if the H₂O diffusion front has not yet penetrated the pristine glass, the rate is effectively zero. So the rate law used is given by

$$R_{corr} = ka_{H-hydrated}^5 \left(1 - \frac{Q_{am-silica}}{K_{am-silica}} \right)^3 \quad [\text{Eq. 1}]$$

Separations and Waste Forms
2013 Accomplishments Report

where k is the rate constant and $a_{H\text{-hydrated}}$ is the concentration of hydrated sites in the glass, and $Q_{am\text{-silica}}$ and $K_{am\text{-silica}}$ are the ion activity products and equilibrium constants with respect to amorphous silica. A higher order dependence on the concentration of hydrated sites in the borosilicate glass is also required so as to place the boron release front further from the Li-H interdiffusion front. This formulation could be reconciled with a model in which the number of hydrated sites needs to reach some threshold value before the dissolution of the glass accelerates appreciably.

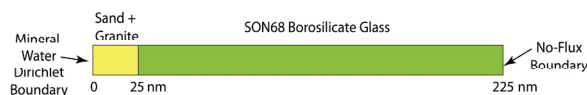


Figure 111. Schematic of modeling setup showing nanometer-scale reaction and diffusion zones

Simulation Results

The simulations described here present a semi-quantitative comparison of the modeling results and the data. In the modeling, concentration in the pore solution, rather than in the glass, is presented, so a quantitative comparison is not possible. The focus is on the relative position of the fronts, and in general, the width of the fronts as they evolve over time. Schematically, the geometry that researchers wish to capture in the modeling is given in Figure 112 taken from Gin, et al. [2013]. Most important is the relatively constant width of the reaction zones and the position of the sharp boron profile further from the pristine glass interface than is the Li-H interdiffusion zone. A more detailed APT profile from Gin, et al. [2013] is given in Figure 113.

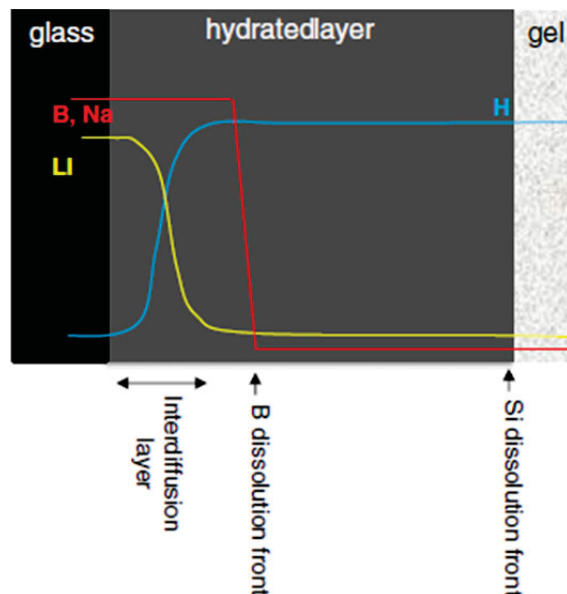


Figure 112. Schematic of the disposition of elemental leaching zones based on atom probe tomography (from Gin et al, 2013)

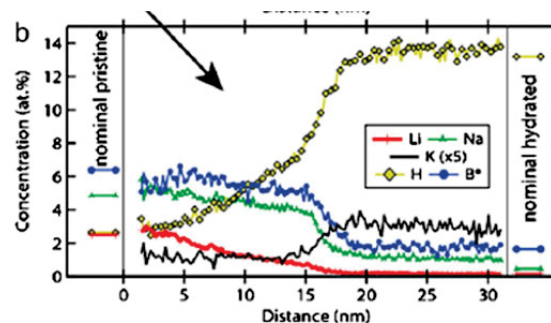


Figure 113. High resolution histogram of elemental abundance across the pristine glass-hydrated glass interface (from Gin et al, 2013)

The model results for the 1D run are shown in Figure 114 over a period of 4 years. Larger times than these require extending the grid (and the borosilicate glass) to larger distances, which will be presented in subsequent reports. The modeling results show that both the Li-H interdiffusion front and the B release (dissolution) front are relatively sharp, and remain so over the course of the 4 year simulation. In addition, the B release front is located further from the pristine glass interface than is the Li-H interdiffusion front, which makes sense insofar as the dissolution of the glass is promoted by its hydration.

Separations and Waste Forms
2013 Accomplishments Report

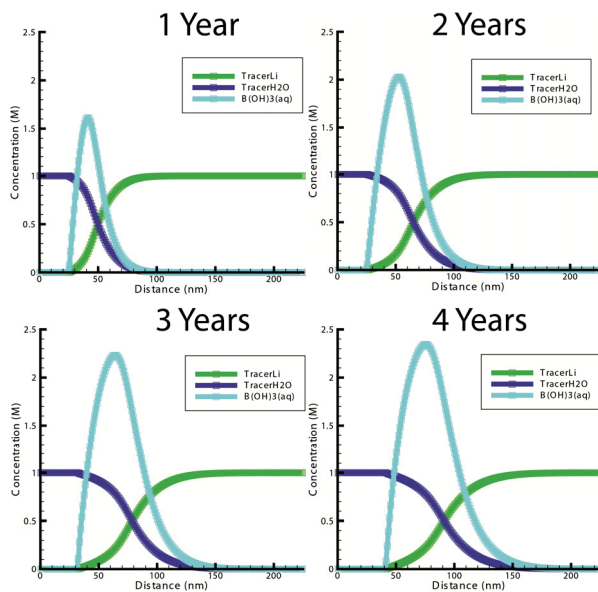


Figure 114. Simulation results using the $K\mu C$ model. Note the position of the B release front further from the pristine glass than the Li-H interdiffusion front, in qualitative agreement with the observations

In addition, the simulations predict a linear rate of front propagation over time once the initial period (less than 1 year) is passed. This can be explained by the maintenance of a constant width zone over which diffusion is limited (in agreement with the results of Navarre-Sitchler, et al, 2011). Again, if the silica-rich gel layer were limiting, the dependence on time would be parabolic since this zone grows with time.

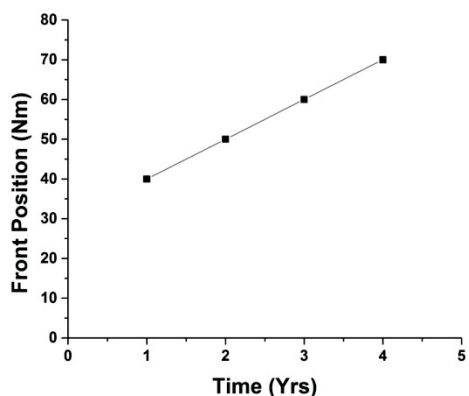


Figure 115. Simulated corrosion front position versus time. Note the linear (constant) rate of front propagation.

Discussion

To the extent that the simulations agrees with the observations in terms of the sharpness of the

reaction fronts, the non-coincidence of the B and Li-H fronts, and the constant (linear) rate of corrosion, they support the conceptual model proposed by Gin, et al. [2013]. The rate limiting step for corrosion appears to be the rate of diffusion of H (via water) into the pristine glass. The slow rate of diffusion, which is approximately 10^{-23} m²/s, controls the overall rate of glass corrosion. An explicit PRI zone is not really required here. Moreover, the linear rate follows from the fact that the amorphous silica gel corrosion layer that forms on the glass is not itself a diffusion barrier. If it were, one would observe a parabolic dependence on time for the corrosion rate in the simulations and experiments. Still, the conceptual model needs to involve one in which H diffusion into the glass is coupled with glass dissolution. Once the glass is hydrated, the rate of dissolution is relatively fast, as indicated by the relatively large rate constants required, as well as the sharpness of the dissolution front. Before hydration, however, the borosilicate glass corrosion is effectively zero.

References

1. Bourg I. C., and C.I. Steefel (2012), "Molecular Dynamics Simulations of Water Structure and Diffusion in Silica Nanopores." *J. Phys. Chem. C* 116: 11556-11564.
2. Cailleteau C., F. Angeli, F. Devreux, S. Gin, J. Jestin, P. Jollivet, and O. Spalla (2008). "Insight into Silicate-Glass Corrosion Mechanisms." *Nature Materials* 7, 978-983.
3. Frizon F, S. Gin, C. Jegou (2009) Mass transfer phenomena in nuclear waste packages. *Advances in Transport Phenomena* 1, 31-133.
4. Frugier P., S. Gin, Y. Minet, T. Chave, B. Bonin, N. Godon, J-E. Lartigue, P. Jollivet, A. Ayrat, L. De Windt, and G. Santarini (2008). "SON68 Nuclear Glass Dissolution Kinetics: Current State of Knowledge and Basis of the New GRAAL Model." *Journal of Nuclear Materials* 380, 8-21.
5. Grambow, B. (2006), "Nuclear Waste Glasses – How Durable?" *Elements* 2, 357-364.
6. Gin, S., J. Y. Ryan, D. K. Schreiber, J. Neeway, and D. Cabie (2013). "Contribution

Separations and Waste Forms
2013 Accomplishments Report

- of Atom-Probe Tomography to a Better Understanding of Glass Alteration Mechanisms: Application to a Nuclear Glass Specimen Altered 25 Years in a Granitic Environment.” *Chemical Geology* 349-350: 99-109.
7. Gin, S., C. Guittonneau, N. Godon, D. Neff, D. Rebiscoul, M. Cabie, and S. Mostefaoui (2011). “Nuclear Glass Durability: New Insight in Alteration Layer Properties.” *Journal of Physical Chemistry C* 115: 18696-19706.
 8. Guittonneau, C., S. Gin, N. Godon, J. P. Mestre, O. Dugne, and P. Allegri (2011). “A 25-year Laboratory Experiment on French SON68 Nuclear Glass Leached in a Granitic Environment—First Investigations.” *Journal of Nuclear Materials* 408: 73-89.
 9. Navarre-Sitchler, A., C. I. Steefel, L. Yang, L. Tomutsa, and S. A. Brantley (2009). “Evolution of Porosity and Diffusivity Associated with Chemical Weathering of a Basalt Clast.” *Journal of Geophysical Research* 114, doi:10.1029/2008JF001060.
 10. Navarre-Sitchler, A., C. I. Steefel, P. B. Sak, and S.aL. Brantley (2011). “A Reactive Transport Model for Weathering Rind Formation on Basalt.” *Geochimica Cosmochimica Acta* 75: 7644-7667.

Plant-Scale Model Development for Fuel Recycling

*V. F. de Almeida, and D. Dapaoli,
depaolidw@ornl.gov*

The overall goal of this plant-scale model development is to produce a computational model of a used fuel reprocessing plant. Since there is interest in modeling various reprocessing technologies, a computational model needs to be flexible to account for corresponding variations of a plant layout and flowsheet. This can be accomplished by building the model by composition of modules, i.e., a computer software realization of models representing significant processes. To that end, an integrated reprocessing plant is envisioned as a collection of all physicochemical processes needed to transform

spent nuclear fuel into new fuel and waste forms. The long-term vision for this work is the development of a fully integrated, dynamic, plant-level simulator able to design and optimize, a reprocessing plant based on a toolkit concept. This requires the development of modules following a given architecture and the integration of these modules into an environment.

The work in FY 2013 entailed three tasks – module development for common architecture; module integration into a plant-level environment; and roadmapping future development of modules for separations.

The first task continued the development of plant-level modules for an integrated recycling plant simulator. The modules are realizations of mathematical models into computer software for three processes, namely, tritium pretreatment, dissolution, and solvent extraction. These are in development following a commonality approach to enable the design of future integrated process modules with a common architecture; as such, they are prototypes for development of modules for other processes. During FY 2013, progress was made in modeling and development of computational modules for two unit operations – dissolver (Figure 116) [de Almeida, 2013] and tritium pretreatment (Figure 117) [de Almeida, 2012b]. Time integration coupling between a module and an external host code or environment has been described/proposed previously [de Almeida, 2012a]. Recently, the dissolver module has been fully integrated into an application [de Almeida, et al., 2013]. Time coupling was achieved by making the whole history of the state variables available to the application; this worked well for the testing intended. Additional development is needed in this topic for future larger integration.

Separations and Waste Forms 2013 Accomplishments Report

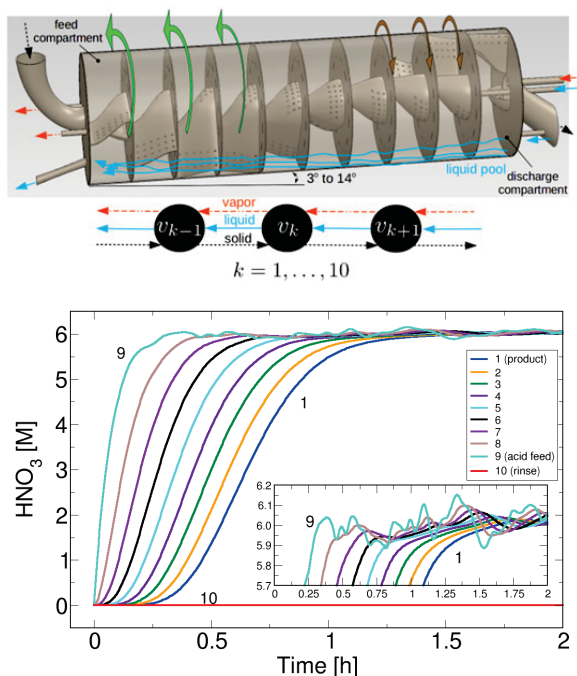


Figure 116. Rotary dissolver module Nitron [2].

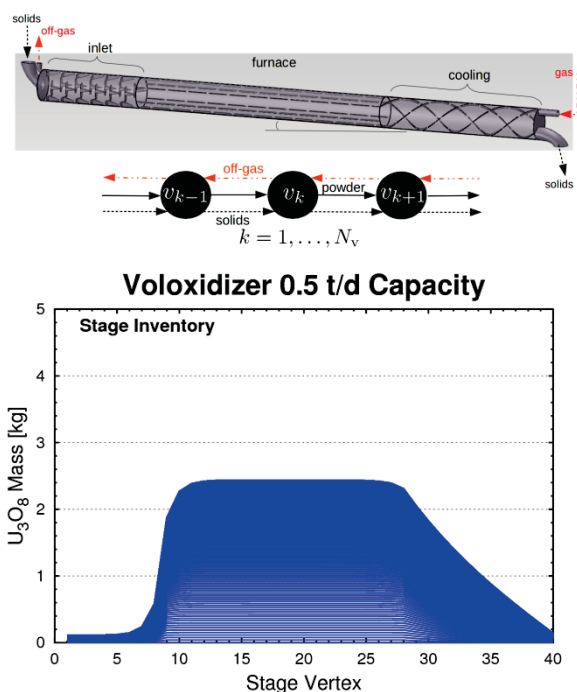


Figure 117. Rotary pretreater module Pulvox [3].

The second task continues the integration of one of these modules, dissolution, into the Separations and Safeguards Performance Model (SSPM) developed at Sandia National Laboratories (Figure 118) [4]. This effort, conducted by collaboration of ORNL with SNL, is

aimed at providing improved rigor to the modeling and simulation capabilities of SSPM and to test and analyze the integration of modules into a third-party environment. This experience helps refine the architecture of the modules developed in the first task. In FY 2013, the dissolver module, Nitron, was integrated into the SSPM successfully. A MATLAB open source version of Nitron was used for this purpose.

The third task involves roadmapping the development of additional separation process modules related to the work performed by the S&WF campaign. Topics involving solvent extraction (e.g., integration of SXFIT with SSPM to enable evaluation of candidate processes for minor actinide separations), off-gas management (development of adsorption bed modules for integration with SSPM), and continued development of additional plant-level modules are candidates.

Publications

1. de Almeida, V. F. (2012a). "Progress on Plant-Level Components for Nuclear Fuel Recycling: Commonality." Letter Report ORNL/LTR-2011-176. Oak Ridge National Laboratory, September. Also available by request to dealmeidav@ornl.gov.
2. de Almeida, V. F. (2013). "Progress on Plant-Level Modeling and Simulation of Used Nuclear Fuel Dissolution: Startup Condition with Quasi-Developed Flow and Varying Acid Concentration." ORNL/LTR-2013/437. Oak Ridge National Laboratory, September. Also available by request to dealmeidav@ornl.gov.
3. de Almeida, V. F. (2012b). "Progress on Plant-Level Components for Nuclear Fuel Recycling: Voloxidizer." Letter Report ORNL/LTR-2012-26. Oak Ridge National Laboratory, September. Also available by request to dealmeidav@ornl.gov.
4. de Almeida, V. F., B. B. Cipiti, M. D. McDaniel, and D. W. DePaoli (2013). "Milestone Letter Report – Plant-Scale Model Development." ORNL/LTR-2013-438. Oak Ridge National Laboratory, September.

Separations and Waste Forms
2013 Accomplishments Report

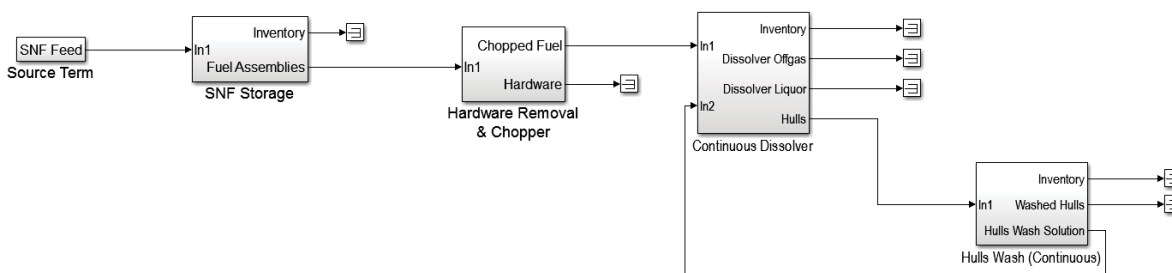


Figure 118. Simplified SSPM (Sandia) front end for Nitron integration testing.

Plant-Scale Model Integration

B. Cipiti, bbcipit@sandia.gov, and M. McDaniel

The objective of this work was to integrate a more detailed unit operation model for a reprocessing plant with a higher level plant model. This work demonstrates how various models can be integrated together to develop more detailed plant models, which provides value in future design of reprocessing plant concepts as well as safeguards and security system design. The Nitron continuous dissolver code was developed and modified in order to be integrated with a safeguards model, namely, SSPM.

The Nitron code simulates a continuous dissolver at the front end of a reprocessing plant. This code was written as an m-file in order to be consistent with the SSPM. The SSPM tracks elemental and bulk material flow through a reprocessing facility, but does not include detailed unit operation models.

It was necessary to generate a MATLAB S-Function to encapsulate the call to Nitron and to pass input and output signals between the SSPM and Nitron. In this case the S-Function served as the interface between the SSPM and the Nitron code, manipulating and mapping the inputs from the SSPM, calling and passing parameters to the Nitron code, and manipulating and mapping the outputs of Nitron back into the SSPM. The conversion of units and resolution of the time scales and scaling were important considerations for this work.

This work was able to successfully integrate Nitron with the SSPM and provided useful experience in integrating codes in the future. Figure 119 shows a comparison of the Nitron

output when run stand-alone. Figure 120 shows the results after integration with the SSPM. These results show that the integration worked as expected.

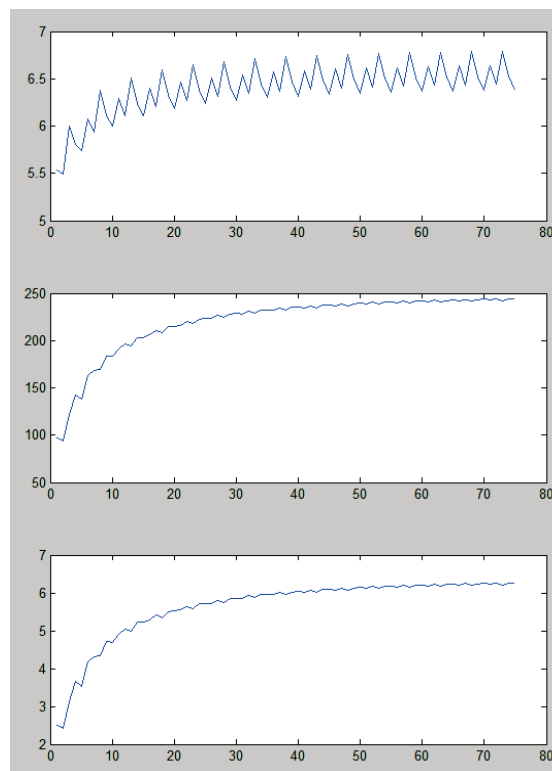


Figure 119. Nitron stand-alone output for 12 hours of dissolution. Top-Liquid volume flow rate (L/min); Middle-Uranium nitrate concentration (g/L); Bottom-Plutonium nitrate concentration (g/L)

Separations and Waste Forms
2013 Accomplishments Report

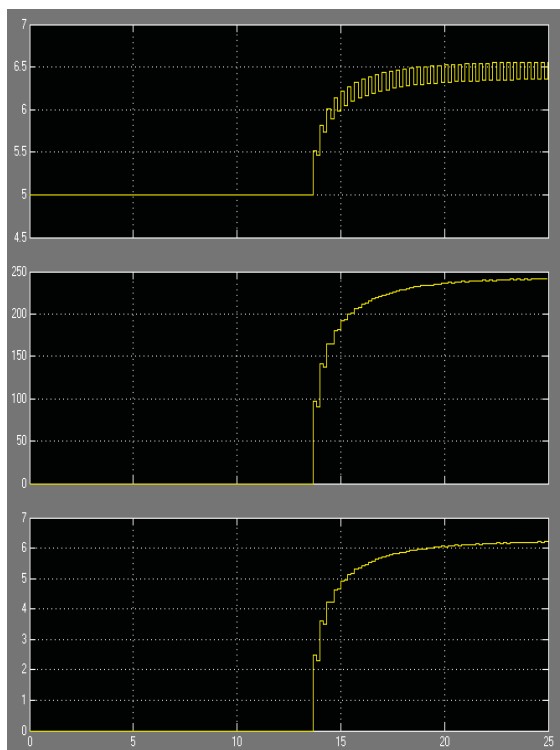


Figure 120. Results after integration with the SSPM; Top-Liquid volume flow rate (L/min); Middle-Uranium nitrate concentration (g/L); Bottom-Plutonium nitrate concentration (g/L).

Comprehensive Corrosion Model

P. Rieke, peter.rieke@pnnl.gov, and J. Ryan

The objective of the Comprehensive Corrosion Model project is to develop a glass corrosion modeling tool (GCMT) that will enable users to evaluate the goodness of a glass dissolution model by fitting the model to selected experimental databases. The GCMT is comprised of modular packages or programs that interact to (a) import databases, (b) evaluate specific models and (c) optimize model parameters. With access to five different databases and five models of glass corrosion, researchers can quantitatively evaluate existing, and test new, corrosion mechanisms. In engineering applications, the tool can be used to quantitatively validate the choice of model used to calculate the stability and performance of engineered waste forms. Currently the focus is on glass corrosion databases and models but the tool can be extended to almost any physical process.

The GCMT consists of four modules:

1. A database import and extraction module that allows selection of all or some of the glass dissolution data in a database. Advanced glass dissolution data, such as the depth profiles provided by atomic probe tomography, may also be analyzed.
2. A model selection module that allows the user to select amongst well-documented models of glass dissolution.
3. A parameter optimization module based upon the PEST.
4. A reactive transport module comprised of the COMSOL multiphysics package used for transport modeling and the PhreeqC thermodynamic and kinetic chemical reaction package. MatLab is used to control the flow of operations.

The GCMT integrates existing codes which are commercially available for reasonable cost, maintained by professional developers with regular upgrades, are compatible with the computational tools used in the nuclear industry and utilize the best aspects of each product.

Summary of GCMT Accomplishments for FY 2013

Over the course of this project in FY 2013, the number of databases which can be accessed by the GCMT and the number of dissolution models that can be fitted to the databases has been significantly expanded. In addition the code was reorganized and simplified in preparation of creating an initial graphical user interface (GUI).

Database Import and Selection

Currently the GCMT can import and select subsets of data from 5 databases, 4 of which were added in the past year. These include the SON68 data published by Frugier, et al. [2009], the SPFT, Pressurized Unsaturated Flow and PCT databases published by Pierce, et al. [2004] and the SPFT data published by Pierce, et al. [2010]. In addition, a protocol for adding new databases was developed which will streamline this process.

Separations and Waste Forms 2013 Accomplishments Report

Addition of Four Glass Corrosion Models

The GCMT now has access to 5 different models, 4 of which were added in FY 2013. The GRAAL model [Frugier, 2009] partial differential equations (PDEs) are solved using the COMSOL PDE solver as well as PhreeqC to calculate solution speciation. Both the Aagaard-Helgeson and Grambow-Muller models [Aagaard and Helgeson, 1982; Grambow and Müller, 2001] are implemented as linear equations in MatLab and use PhreeqC to calculate solution speciation and mineral supersaturation. A rudimentary continuum model of glass reactions uses COMSOL for transport and PhreeqC for kinetics. Most recently a MC model of dissolution [Kerisit and Pierce, 2011] has been added.

Evaluation of the GRAAL Model

To demonstrate that complex models can be efficiently fitted to large and varied data sets, the GRAAL model was fitted to the experimental SON68 corrosion data. Representative results are shown in Figure 121. The GRAAL model adequately reproduces SON68 data trends at zero or low solution flows but fails at longer times under high flows.

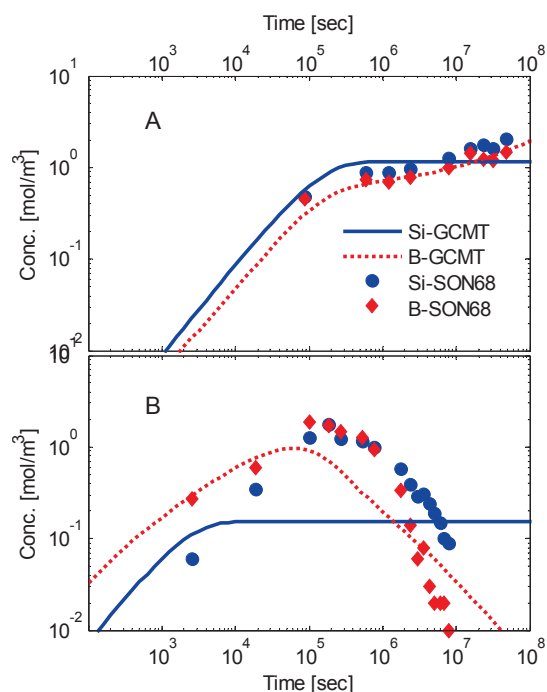


Figure 121. Representative fits of GRAAL model to SON68 data at a) no solution flow and b) at high solution flow.

Integration of a Monte Carlo Model

A Monte Carlo (MC) model of glass dissolution, used by Kerisit and Pierce to model aluminoborosilicate glasses [Kerisit and Pierce, 2011], was integrated into the GCMT. The MC program was compiled and run on a laptop computer and, while this limited the computational speed, it allowed optimization of the GCMT operational variables. Figure 122 shows the MC output and the linear fit to these data which represents the calculated dissolution rate. Because of the small size of the lattice that could be handled, the total dissolved material plateaus after about 800 seconds as the lattice becomes totally dissolved. Faster simulation will be required to overcome this limitation. In addition, logarithmically weighting the data was required to give equal emphasis to slowly dissolving glass composition.

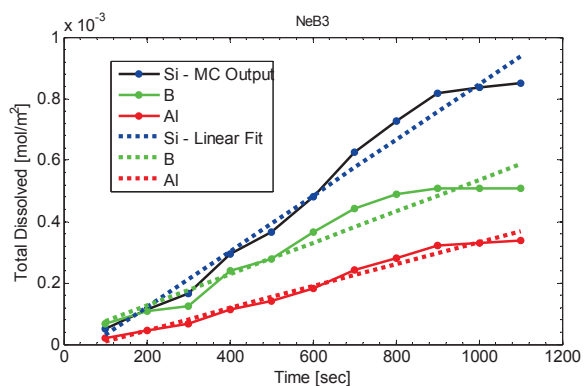


Figure 122. Total dissolved Al, B and Si (solid lines) and linear fits of the data (dashed lines) for the NeB3 glass on a 8x8x128 lattice

References

1. Frugier, P., et al. (2009). "Application of the GRAAL Model to Leaching Experiments with SON68 Nuclear Glass in Initially Pure Water." *Journal of Nuclear Materials* 392(3): p. 552-567.
2. Pierce, E. M., et al. (2004). "Waste Form Release Data Package for the 2005 Integrated Disposal Facility Performance Assessment." Pacific Northwest National Laboratory.
3. Pierce, E. M., et al. (2010). "Experimental Determination of the Effect of the Ratio of B/Al on Glass Dissolution Along The

Separations and Waste Forms
2013 Accomplishments Report

Nepheline (NaAlSiO₄)-malinkoite (NaBSiO₄) Join." *Geochimica et Cosmochimica Acta* 74: p. 2634-2654.

4. Åagaard, P., and H. C. Helgeson (1982). "Thermodynamic and Kinetic Constraints on Reaction Rates among Minerals and Aqueous Solutions. I. Theoretical Considerations." *American Journal of Science* 282: p. 237-285.
5. Grambow, B., and R. Müller (2001). "First-Order Dissolution Rate Law and the Role of Surface Layers in Glass Performance Assessment." *Journal of Nuclear Materials* 298(1-2): p. 112-124.
6. Kerisit, S., and E. M. Pierce (2011). "Monte Carlo Simulations of the Dissolution of Borosilicate and Aluminoborosilicate Glasses

in Dilute Aqueous Solutions." *Geochimica et Cosmochimica Acta* 75(18): p. 5296-5309.

Publications

1. Rieke, P. C., and J. Ryan, "Integration of Software Packages into Model Testing Tool." Milestone Report M4FT-13PN0304211.
2. Rieke, P. C., and J. Ryan, "Evaluation of Selected Models with Model Testing Tool." Milestone Report M4FT-13PN0304215.
3. Rieke, P. C., and J. Ryan, "Adaptation/Integration of Molecular Dynamic and/or Monte Carlo Techniques." Milestone Report M3FT-13PN0304216.

CHAPTER 8
ADVANCED SEPARATION PROCESS
ALTERNATIVES

CHAPTER 8: ADVANCED SEPARATION PROCESS ALTERNATIVES

R. T. Jubin, jubinrt@ornl.gov

Define and Document Case Study Flowsheet

J. D. Law, jack.law@inl.gov

Over the past 5 years significant work in the area of advanced separations has been accomplished by the FCRD S&WF Campaign. Using these advances, it is now possible to perform a case study to develop a full recycle flowsheet and a near-term target flowsheet that will meet the goals for a full recycle fuel cycle. This case study flowsheet will allow for objective comparison of technologies currently being developed by the SWF Campaign as well as future technology developments, to assess their benefits and potential improvements relative to this full recycle flowsheet. Ultimately, this effort will provide benefits in terms of understanding the interfaces between specific processes both upstream and downstream, will aid in identifying knowledge gaps and areas for process improvements, will serve as a tool for comparison of new technologies, and will identify potential regulatory issues for UNF recycling.

A team of experts from ANL, INL, ORNL, PNNL, SRNL, DOE-NE, AREVA and EnergySolutions was assembled to select technologies for both the processing of LWR UNF as well as fast reactor fuel in the full recycle option. This effort included identification of the case study processes and the preparation of material balance flowsheets. In identifying the case study flowsheets, it was decided that two cases would be developed: one which identifies the flowsheet as currently developed and another near-term target flowsheet which identifies the flowsheet as envisioned within two years, pending the results of ongoing research.

Scope

The scope of this activity includes the identification of case study technologies that comprise the flowsheet for a full recycle option for

both oxide fuel (LWR) and metal fuel cases. Fuel cooling times shorter than 5 years for LWR fuel and one year for fast reactor fuel are not included. This effort does not require that the technologies be fully developed but should be well beyond concept, i.e., have a fundamental understanding of the process performance and operating parameters. Industrial support provided through IDIQ A&ACs with AREVA and EnergySolutions aided in ensuring scale-up and operational concerns were considered. Constraints relative to this case study include:

- The case study flowsheet will be an evolving flowsheet to incorporate technology changes as they become sufficiently developed and demonstrated to allow for an objective assessment.
- The initial case study flowsheet will be prepared assuming an initial fuel cycle and will be integrated with the Fuel Cycle Options Study so that the two are consistent.
- The case study flowsheet does not reflect any decisions or down-selection; it is a basis for objective comparison of future technology developments.

This evaluation includes identification of the case study flowsheet, which reflects what the team believes would be the flowsheet were a full recycle facility pursued at this time. A second flowsheet has also been developed which incorporates technologies that are believed to be implementable within two years, pending the outcome of ongoing research activities. For both flowsheets, this effort includes identification of the individual unit operations that comprise the flowsheet, development of block flow diagrams, creation of a mass balance for the processes, and development of a detailed written description of the processes. This also includes documentation of the basis and assumptions used to support the mass balance, unknowns, and a description of ongoing research.

Separations and Waste Forms
2013 Accomplishments Report

Team Members

A team of experts from various DOE national laboratories, DOE-NE, and industry were chosen to participate in developing the full recycle case study flowsheets and mass balances. Team members, their affiliation, and areas of expertise are summarized below.

Full Recycle Case Study Team Lead

- Jack Law, INL

National Laboratory Team Members

- Tracy Rudisill, SRNL: Headend
- Candido Pereira, ANL: U/Pu separation
- Mark Williamson, ANL: Electrochemical separations
- Bruce Moyer, ORNL: Actinide/lanthanide separations
- Gregg Lumetta, PNNL: Actinide/lanthanide separations
- Bob Jubin, ORNL: Offgas separations
- John Vienna, PNNL: Waste forms
- Terry Todd, INL: fuel cycle

DOE Team Members

- Jim Bresee, DOE-NE; fuel cycle

Industry Team Members

- Sven Bader, Paul Murray, AREVA
- Bill Willis, Robert Carter, Chris Phillips, EnergySolutions

Other Support

- Nick Soelberg, INL: mass balances
- Julie Tripp, INL: Support
- Bill Ebert, ANL: waste forms, Electrochemical separations

Flowsheet Development

A report entitled “Separation and Waste form Campaign Full Recycle Case Study,” FCRD-SWF-2013-000380, was issued describing the flowsheets developed. This is an Applied

Technology Document as a result of the detailed flowsheet information presented. These details have, therefore, been left out of this Accomplishments Report.

Mass Balance Development

Mass balances have been identified and developed for the Case Study and near-term target flowsheets, for the aqueous reprocessing of used LWR fuel. Mass balance templates have also been identified for use in mass balances for the electrochemical reprocessing of the used fast reactor fuel, for the Case Study and near-term target flowsheets. These mass balances are all performed using Excel spreadsheets that contain multiple worksheet tabs. All calculations needed for a specific reprocessing case are performed within the spreadsheet for that reprocessing case. No separate spreadsheets are linked by sharing calculations or data.

Both the aqueous and electrochemical reprocessing mass balances are modeled after the aqueous and electrochemical reprocessing waste spreadsheet models developed for the Used Fuel Disposition Campaign. These mass balances were initially developed primarily to estimate reprocessing wastes, and are being adapted to also enable the inclusion of the specific Case Study and near-term target reprocessing features described in the final report.

These mass balances incorporate the input used fuel compositions and process rates and subsystems for the headend, off-gas, aqueous separation, electrochemical separation, and waste treatment sections of the overall flowsheet presented in the final report. Four separate mass balances have been created: (1) Case Study flowsheet for treatment used LWR fuel, (2) Near-term development flowsheet for treatment of used LWR fuel, (3) Case Study flowsheet for treatment of used fast reactor fuel, and (4) Near-term development flowsheet for treatment of used fast reactor fuel. The goal with the flowsheets is to have a quantitative representation of the separation and waste form processes being developed by the S&WF Campaign that will allow for comparison of technologies and flowsheet changes as new technologies are developed.

Separations and Waste Forms

2013 Accomplishments Report

Stream numbers were assigned to each of the major process stream entering and exiting a unit operation and the mass balance for each stream. The flowrate is represented based upon mass (Kg/day) for a 1,000 MT/yr facility operating 200 days/yr. In addition to the dissolved fuel components, co-flows, such as solvents and process chemicals, are included.

An Excel spreadsheet was adapted to enable the focus on the process streams in the Case Study and near-term target subsystems. Tabs in the template for different reprocessing options COEX™, New Extraction, UREX, and electrochemical reprocessing were replaced with tabs for (1) the fuel composition, (2) elemental distribution factors between different process streams, and (3) different aqueous reprocessing subsystems. The basic format of the tabs, with different streams in columns, and different element and isotope masses in rows, was maintained the same as in the template. This architecture of the spreadsheet model is shown in Figure 123.

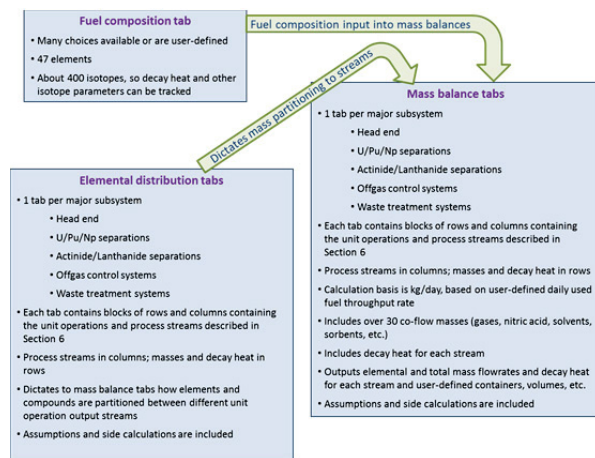


Figure 123. Architecture of the aqueous separations mass balance

Adaptation of an existing electrochemical reprocessing mass balance model to model the Case Study and near-term target flowsheets is still in progress. Like the mass balance model for the aqueous separations processes, it has columns for each numbered and tracked process stream. The masses and decay heat are organized in rows. These rows include both the masses of elements from the used fuel, and also masses of co-flows.

Conclusions

Case study flowsheets for the homogeneous recycle of the U/TRU resulting from the processing of LWR fuel, followed by electrochemical processing and recycle of metal fuel from a sodium fast reactor have been developed. These flowsheets include the identification of the technologies for the separation and waste form processes as well as identification of near-term target technologies which represent what the SWF Campaign believes will be the case study technologies within two years if the ongoing research is successful.

In conjunction with this case study evaluation, mass balances have been created for the LWR recycle case study flowsheet and near-term target flowsheet. These flowsheets detail the flow of material through the individual unit operations that comprise the headend, separation, product processing and waste treatment portions of the flowsheets based upon the assumptions documented in this report. Creation of the mass balances for the electrochemical processing portion of the case study and near-term target case is underway and additional assumptions/descriptions will be included in future revisions of this document.

Development of the case study flowsheet allows for objective comparison of technologies currently being developed by the S&WF Campaign as well as future technology developments, to assess their benefits and potential improvements relative to this full recycle flowsheet. Ultimately, this effort will provide benefits in terms of understanding the interfaces between specific processes both upstream and downstream, will aid in identifying knowledge gaps and areas for process improvements, will serve as a tool for comparison of new technologies, and will identify potential regulatory issues for UNF recycling. As such, this is envisioned as a “living” document which will undergo revision and updates as the research progresses.

Publications

1. Law, J. D., et.al. (2013). “Separation and Waste form Campaign Full Recycle Case

2013 Accomplishments Report

Study.” FCRD-SWF-2013-000380. Idaho National Laboratory, September 30.

Tritium Pretreatment

G. D. DelCul, delculgd@ornl.gov

Processing of UNF to recycle the usable components for additional energy production [Del Cul, et al., 2013a; Del Cul, et al., 2010], requires the fuel to be put into a form conducive to chemical separations (e.g., in aqueous-based processing systems, this usually means dissolution of the solid fuel into nitric acid). Removal of the several radioactive volatiles before the fuel is dissolved avoids releases in the multiple downstream separations processes and simplifies the off-gas sequestration processes. Disintegration of the solid fuel matrix by dry processing is an effective way for removing volatile species like tritium, iodine, xenon and krypton, and carbon-14.

An advanced form of dry processing that proceeds at relatively low temperatures under 350°C using NO₂ as an oxidant is being developed as an alternative to more conventional high temperature technologies using air or oxygen. An additional advantage is the complete removal of iodine and that the product can be selectively chosen to be U₃O₈, UO₃, or a nitrate by adjusting the processing conditions. Moreover, reacted NO₂ that becomes NO can be easily regenerated in a closed loop system by the addition of oxygen and it can be condensed and recovered as liquid or solid N₂O₄. (melting point -11.2°C, boiling point 21.2°C). The closed loop system also results in a large reduction in total off-gas volume requiring treatment to capture the volatilized fission products.

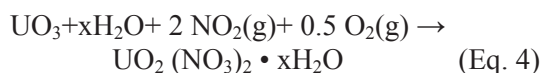
Conversion of the fuel to a powdered form improves the performance of downstream processes (e.g., rapid fumeless dissolution starting at very low nitric acid concentration) and is required for other proposed processes (e.g., fluoride volatility). In addition, conversion of the fuel to a powder enables dry separation of the fuel from the cladding, which benefits cladding recycling. The process is well suited for oxide-based fuels used in LWRs and heavy water reactor systems, and it may also have application to

oxide-based and sodium-bonded metallic fuel for fast reactors [Del Cul, et al., 2010].

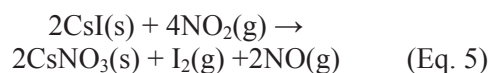
The oxidation of UO₂ UNF in the proposed process proceeds by the formation of U₃O₈ followed by continued oxidation to ε-UO₃ upon cooling, as shown in equations (1) and (2). Upon further cooling, a different reaction becomes favorable that produces the yellow/green compound, uranyl nitrosyl nitrate, as indicated in equation (3), which decomposes to a uranyl nitrate which is readily hydrated.



Recently completed limited parametric studies on the nitration of the UO₃ products produced according to the above step UO₃ can also be readily converted to uranyl nitrate hydrate salt UO₂(NO₃)₂ • xH₂O using a mixture of NO₂ and O₂ on wetted oxide as in equation (4). These results were obtained using natural uranium pellets as the starting material and confirmed using actual UNF from the Dresden reactor.



An additional reaction of particular interest is the reaction of NO₂ with embedded fission product halides such as iodine. Iodine is believed to be found in used fuel primarily as CsI which has been observed to react with NO₂ to produce CsNO₃ liberating iodine as shown by equation (5). The release of iodine in a dry head-end process is advantageous as it would eliminate the need for subsequent trapping of iodine from a number of off-gas streams present in a reprocessing facility.



Separations and Waste Forms
2013 Accomplishments Report

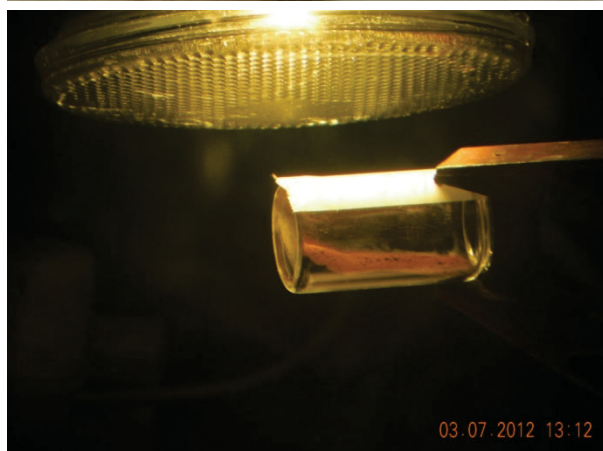
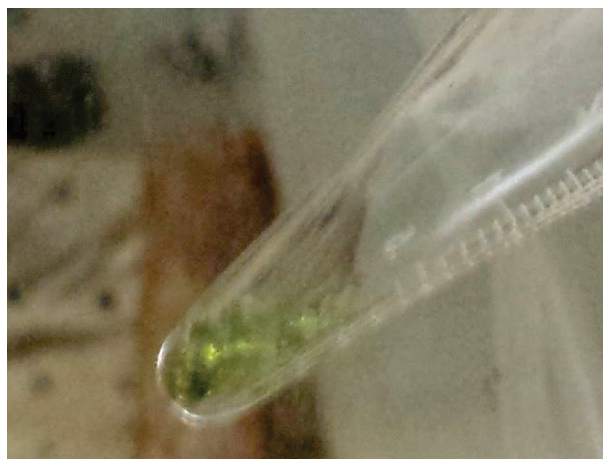


Figure 124. Treated UNF from the Dresden reactor. Uranyl nitrate hydrate on the top and UO_3 on the bottom

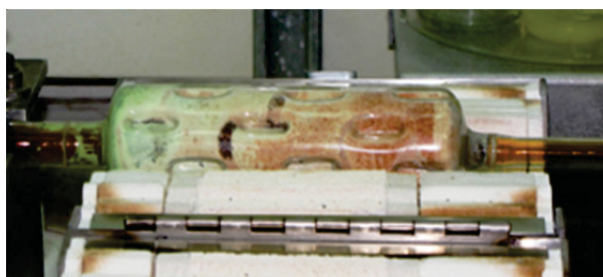


Figure 125. Closed loop treatment of natural uranium pellets at 1 Kg scale, mix oxide (red) and nitrate (green) product

The kinetics of the oxidation of U_3O_8 by NO_2 to triclinic $\epsilon-UO_3$ was examined by in-situ XRD and modeled; the results of which were previously reported in detail this year. The results demonstrated increased oxidation with temperature over the range tested with >90% conversion within 1 hr.

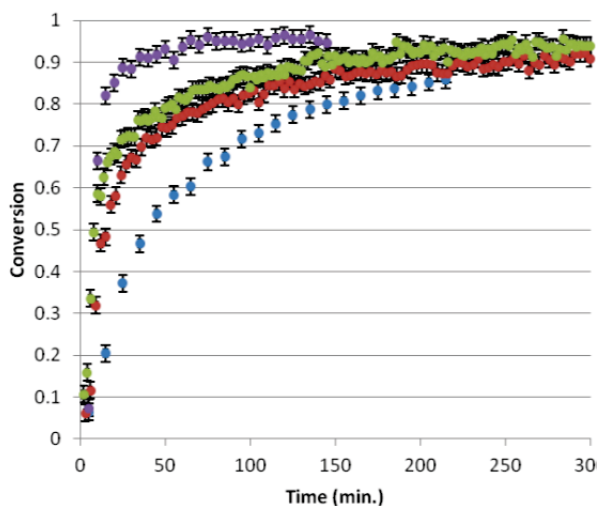


Figure 126. UO_3 phase fractions

The complete release of iodine was tested using surrogate materials and confirmed using used fuel from the Dresden reactor.

In addition to potential release of fission products, such as iodine, that are not released in standard air or O_2 oxidation, there are numerous potentially more impactful advantages to a NO_2 oxidation and nitration processes.

For the oxidation reaction, the $\epsilon-UO_3$ formed by reaction of U_3O_8 with NO_2 readily dissolves in dilute nitric acid with little to no fumes which could result in a simplified off-gas treatment process and a smaller required dissolver. This characteristic allows ready preparation of solutions with high heavy-metal concentrations and low free-acid concentrations that easily interface with advanced separation processes such as UREX and reduces the volume of raffinate waste produced.

For the nitration reaction, the uranyl nitrate compounds formed readily dissolve in water or can be directly dissolved in an organic extractant such as TBP, thus eliminating an initial aqueous phase and potentially reducing aqueous raffinate volume. In addition, the dissolution into organic or water could allow for a selective dissolution leaving behind such species as Tc, which is not thought to form a soluble nitrate.

Furthermore, it provides the opportunity for the development of other processes such as the

Separations and Waste Forms
2013 Accomplishments Report

purification of uranyl nitrate from the fission products by re-crystallization, electrochemistry in molten nitrates, purification via precipitation of uranium as ammonium diuranate (ADU) used widely to concentrate and purify uranium ores, and alkaline-side separation schemes (e.g. dissolution in carbonate or acetate solutions).

Another application of the NO₂ reactions with uranium oxides is in a combined process that includes chemical decladding by chlorination as an initial step followed by NO₂ reaction. The chlorination process may leave behind some chlorinated residues that could pose a problem during and after dissolution by introducing corrosive chlorides in the nitric acid evaporator systems. The NO₂ has potential to remove residual chlorine from the system making Zr removal by chlorination a more feasible process and is being investigated as part of the Zr recovery research being conducted at ORNL [Collins, et al., 2012].

Status

All the fundamental tenants of the process have been successfully demonstrated as a proof of principle, and many aspects have been corroborated multiple times at laboratory scale with surrogate material at kg scale and with UNF at tens of grams scale. The goal is to develop the process to a technology-readiness level sufficient to evaluate and estimate the cost of an engineering-scale implementation. The expediency of the additional process development activities will be highly dependent on the level of funding available. It is proposed that the most desirable approach would be based on lab- and bench-scale tests (100 g to 1–2 kg scale) using real fuel in parallel with bench- and prototype-scale tests using surrogate material [Del Cul, et al., 2013b].

Future Work

Under the appropriate conditions complete removal of iodine by NO₂ pretreatment is readily achievable. Current data indicates that the removal proceeds more effectively in the lower range of temperatures tested. A well designed parametric study coupled with the timely and accurate determinations of iodine provided by the methodology developed will allow for the

determination of the best conditions for the fast, reliable, and complete removal of iodine.

The fast and simple conversion of the UNF to a hydrated nitrate salt form appears to be the most promising for the complete removal of volatile fission products. The limited parametric studies showed complete conversion in 3 hours. However, a more detail analysis is needed to understand the reaction mechanisms, kinetics, and for the optimization of the process. These studies could be started using unirradiated UO₂ pellets. However the study of the actual release of volatile fission products (e.g., ³H, I, ¹⁴C, Kr, Xe) will require UNF. Similarly, purification and separation schemes (TBP, TRUEX, carbonates, acetates, electrochemical, re-crystallization, etc.) could be initially studied using surrogates, but could only be advanced and validated using authentic UNF.

Publicationss

1. Del Cul, G. D., E. D. Collins, B. B. Spencer, and R. T. Jubin (20130a). "A Practical Path Forward for U.S. Used Nuclear Fuel." *2013 International High-Level Radioactive Waste Management*. Albuquerque, New Mexico, May 1.
2. Del Cul, G. D., E. D. Collins, R. T. Jubin, and J. E. Rushton (2010). "Comprehensive Recycling of Used Nuclear Fuel – A Practical Alternative." *2010 American Nuclear Society Annual Meeting*. San Diego, California, June 13–17.
3. Collins, E. D., G. D. Del Cul, B. B. Spencer, R. R. Brunson, J. A. Johnson, D. S. Terekhov, and N. V. Emmanuel (2012). "Process Development Studies for Zirconium Recovery/Recycle, from Used Nuclear Fuel Cladding," *ATALANTE 2012 International Conference on Nuclear Chemistry for Sustainable Fuel Cycles, Elsevier Procedia Chemistry* Vol. 7, pp. 72–76.
4. Del Cul, G. D., J. A. Johnson, B. B. Spencer, and E. D. Collins (2013b). "Roadmap for Development of an Advanced Head-End Process." *Global 2013*. Salt Lake City, September 29–October 3.

Separations and Waste Forms
2013 Accomplishments Report

Planning for H-Canyon Testing

T. Severynse, thomas.severynse@srs.gov

A plan has been developed to provide for engineering-scale testing of two promising technologies being investigated by the NE FCRD S&WF campaign. One technology applies optical and gamma spectroscopic methods to measure actinides in feed, product and waste solutions in a chemical separations process. A second technology provides for characterization and capture of volatile radioisotopes that are generated during fuel irradiation, and released during pretreatment or dissolution of the fuel when it is processed.

Both of these technologies have been successfully demonstrated at the laboratory scale. Operational testing at the plant scale is the next phase required to advance the technology. Using the H Canyon facility at the Savannah River Site, operational testing can be performed that will: demonstrate equipment performance at an actual plant scale, assess technology robustness in a high-rad environment, and establish operational requirements and impacts associated with technology deployment.

The test plan (FCRD-SWF-2013-000146) describes equipment modifications that can be made in the H Canyon facility at the Savannah River Site to allow phased implementation of technology demonstrations, each phase building on the experience gained from previous phases. The technologies will be demonstrated during processing of aluminum-clad, highly enriched uranium fuel. The fuel will be dissolved chemically, and then processed through solvent extraction for purification and recovery of uranium and neptunium; aluminum, fission products, and plutonium are rejected to the waste stream. The test equipment will be integrated with the H Canyon operations; when possible, fuels selected for processing will have attributes that will benefit the testing of the technology. The technology demonstrations can be completed within five years, and will provide operating procedures, training, and analytical support required to complete the testing activities.

Process Monitoring

The process monitoring technology will be implemented in phases, to successively test the technology and its application for material balance. The initial phases of the process monitoring test require modifications to shielded samplers to provide access for instrumentation. Initially, spectrometric measurements will be made on solutions, collected in process vessels, circulated through the samplers. The final phase will provide new in-cell piping that will allow direct measurement of solutions during transfer to provide “real-time” monitoring. The test scope will complete the necessary modifications, and provide spectrometer equipment, including related computer hardware and software. The total cost of the process monitoring test is estimated to be approximately \$9M.

The process monitoring test uses spectroscopy to measure U, Pu, and Np in feed, product, and waste streams from dissolution of aluminum clad UNF. Initial testing will be at-line, through remotely operated sampling of solutions accumulated in dedicated receipt vessels. Subsequent tests will provide for in-line monitoring of solutions as they are generated to allow real-time mass balance and accountability of these materials.

The technologies to be tested include both absorption (UV-vis-NIR) and Raman spectroscopies for actinide measurement, and gamma spectroscopy via the multi-isotope process monitor to track process conditions (acidity, temperature) through measurement of isotopic distribution of radionuclides present. The test program will be implemented in three phases:

In phases 1 and 2, solution in the vessels will be circulated via airlift to an existing remotely operated sampler. The test preparations for these initial two phases will modify the piping in the sampler enclosure (Figure 127) to allow installation of flow cells and fiber optic cables for transmission of signals to remote instruments.

Separations and Waste Forms
2013 Accomplishments Report

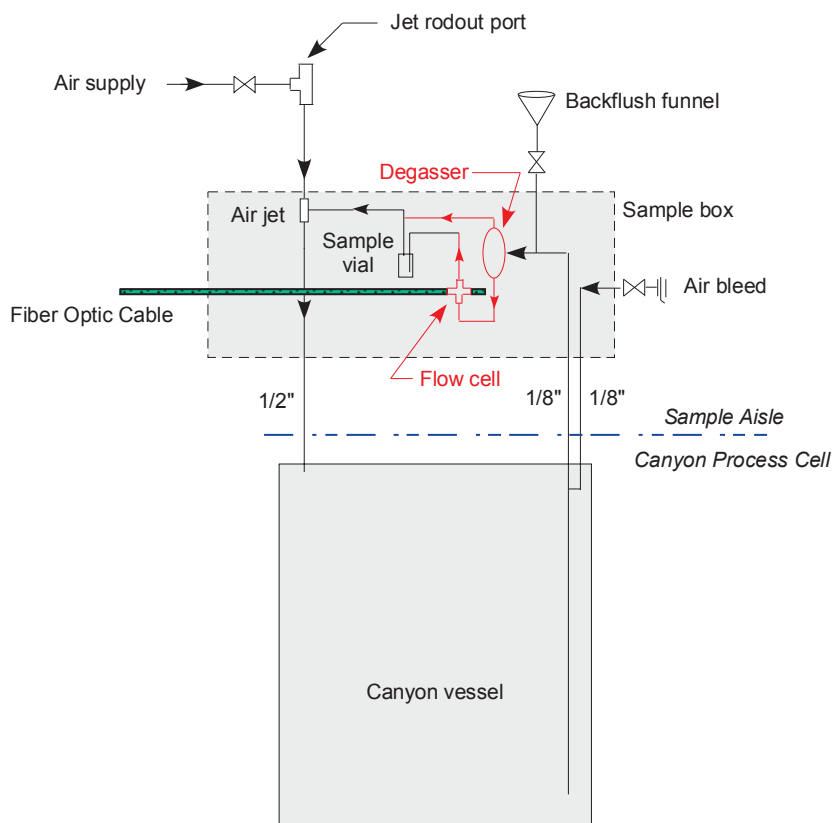


Figure 127. Modified H Canyon Sampler Piping

Phase 3 preparations will provide a flow cell and fiber optic cable directly to the solution transfer piping in the canyon cell. This installation will require fabrication of a new “jumper” (remotely installed cell piping), and routing of the cable from the canyon through a wall nozzle to the instrument corridor.

Off-Gas Treatment

As a result of UNF processing, volatile radionuclides may be released to the environment if there are no engineered controls in place for their removal. The principle species of concern include tritium (^3H), carbon-14 (^{14}C), krypton-85 (^{85}Kr), and iodine-129 (^{129}I). Regulatory requirements prescribe maximum acceptable releases of these materials based on potential exposure to offsite individuals. Studies performed for a variety of fuels with several burn-up values and time out of reactor cooling periods indicate that the main contributors to dose were ^3H and ^{129}I , and that required DFs for these isotopes could be as high as 720 and 8,000, respectively. Acceptable

DFs for ^{85}Kr and ^{14}C are expected to be closer to 60 and 30, respectively.

Various capture and treatment technologies are under evaluation in the FCRD program. The potential candidate treatment technologies that initially could be demonstrated for volatile species capture are under investigation by the Separations & Waste Forms Campaign Off Gas Sigma Team.

The off-gas technology demonstration provides for characterization and capture of volatiles in dissolver and process vessel off-gas streams. Three options have been identified for demonstration, each requiring incrementally more modifications in H Canyon. The first option includes development activities using surrogate solutions to establish analytical methods for measurement of volatile radionuclides, and to evaluate the effects of mercury, nitric acid, and temperature on their liquid-vapor distribution. A liquid sampling program will also be implemented at identified points where volatile radionuclide concentrations are significant or would be

Separations and Waste Forms
2013 Accomplishments Report

expected to change. Modifications will also provide for measurement and capture of krypton from the dissolver off-gas.

The second option will provide piping and equipment for sampling, characterization, and capture of off-gas from dissolvers (Figure 128),

individual vessels at key process points, and the combined process vessel vent exhaust (Figure 129). The total cost of off-gas characterization testing in these two options is estimated to be approximately \$10M.

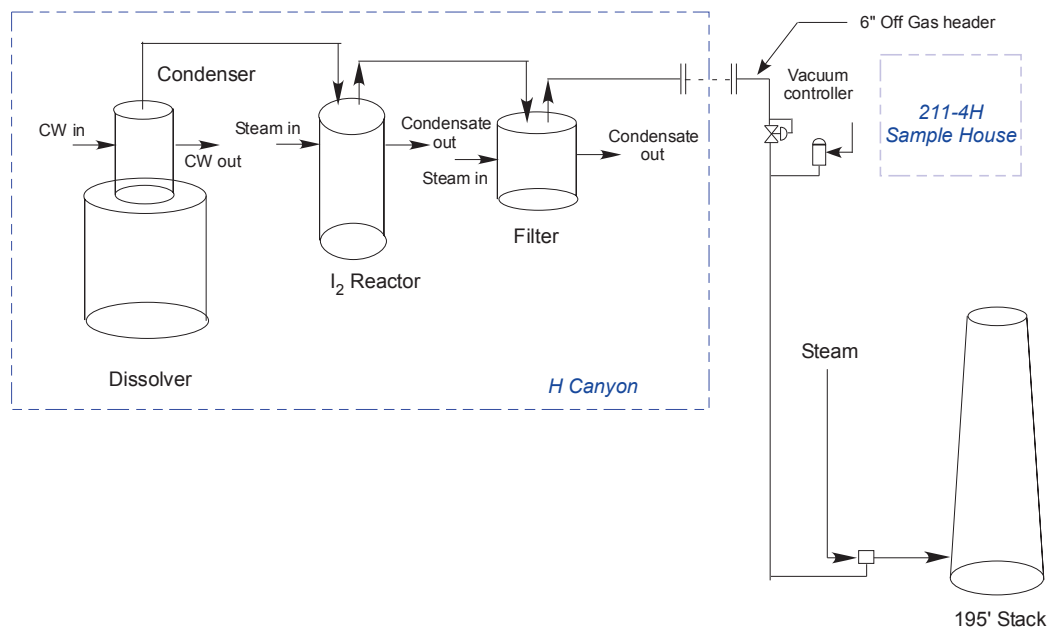


Figure 128. Dissolver Off Gas Flow Schematic

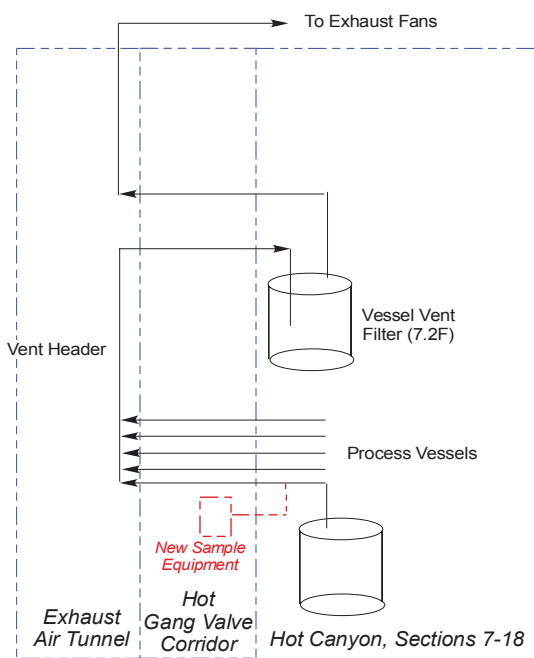


Figure 129. Hot Canyon Process Vessel Vent System

Publication

1. Severynse, T. F. (2013). "Plan for Potential Off-Gas Treatment and Process Monitoring Demonstration in H Canyon." FCRD-SWF-2013-000146. Savannah River National Laboratory, May.

CHAPTER 9
ADVANCED WASTE FORMS
AND PROCESSES

CHAPTER 9: ADVANCED WASTE FORMS AND PROCESSES

J. D. Vienna, john.vienna@pnnl.gov

Ceramic Waste Forms

K. Brinkman, kyle.brinkman@srnl.doe.gov, M.
 Tang, mtang@lanl.gov

Ceramics for High Level Waste Raffinate

K. S. Brinkman, kyle.brinkman@srnl.doe.gov

The research conducted in this work package is aimed at taking advantage of the thermodynamic stability of crystalline ceramics to create more durable waste forms (as compared to high level waste [HLW] glass) in order to reduce the reliance on engineered and natural barrier systems and enable a broader range of disposal options. Durable ceramic waste forms that incorporate a wide range of radionuclides have the potential to broaden the available disposal options and to lower the storage and disposal costs associated with advanced fuel cycles. Assemblages of several titanate phases have been successfully demonstrated to incorporate radioactive waste elements, and the multiphase nature of these materials allows them to accommodate variation in the waste composition. Recent work has shown that they can be produced from a melting and crystallization process. The objective of FY 2013 activities was to explore the phase formation and microstructural differences between lab scale melt processing in varying gas environments with alternative densification processes such as hot pressing (HP) and SPS. Crystalline ceramics have traditionally been processed by solid state sintering methods such as hot pressing, while melt and crystallization routes for waste streams of interest to the FCRD program have not been explored to a large extent [Brinkman, et al., 2013]. A premise of this work is that if the targeted crystalline phases are formed by a melt and crystallization method, the resulting durability will be comparable to SYNROC performance in the literature.

In this task, SRNL has focused on developing compositions and processing routes for crystalline ceramic waste forms to incorporate the combined

HLW raffinate stream containing cesium, strontium, lanthanide, and transition metals. Single phase hollandite compositions Cr-Hol, and Cr/Al/Fe-Hol containing corrosion products Cr and Fe demonstrated the best phase formation under reducing conditions that were targeted to minimize Cs-Mo phase formation in multi-phase compositions. The Cr-Hol and Cr/Al/Fe-Hol were incorporated into multiphase ceramics targeting hollandite, perovskite/pyrochlore and zirconolite phase assemblages from combined HLW raffinate waste streams (including Mo) resulting in two different multiphase compositions that were prepared as described in table x with ~25 weight % waste loading and varying concentrations of CaO, Al₂O₃, BaO, Cr₂O₃, Fe₂O₃ and TiO₂ additives. A combination of gas phase environment and solid state reducing agents were used to vary the redox conditions using different processing techniques: (1) melt processing of compositions *with* and *without* Ti/TiO₂ buffer in air and 1%H₂ /balance Argon gas environments, (2) SPS with a Ti/TiO₂ buffer in N₂ gas at varying temperatures, and (3) hot press *with* and *without* Ti/TiO₂ buffer in N₂ gas at varying temperatures.

Table 21. Ceramic Waste Form Compositions for SRNL Multiphase Melt Samples compared to SYNROC-C [2]; weight percent of oxide component ^a SYNROC-C cited was material prepared by melting of an oxide-nitrate mixture. Crystalline oxides of Ca, Ba, Fe, Ni, Al, Mo, Ti and Zr and nitrates of Cs, Sr, Nd, Gd and Ce were mixed and melt processed. SYNROC-C samples also contained oxide additions of Si, Mg, Co, Ni, Na, and K.

Composition	Cr-MP	CAF-MP	SYNROC-C ^a
Waste	24.58	24.66	19.81
Al ₂ O ₃	0	1.27	4.63
TiO ₂	49.01	49.16	61.4
CaO	1.38	1.39	9.59
BaO	10.52	10.56	4.57
Fe ₂ O ₃	0	6.65	0.894
Cr ₂ O ₃	14.50	6.33	-

Figure 130 displays the microstructure and Table 22 tabulates the phases observed in

Separations and Waste Forms
2013 Accomplishments Report

Multiphase Waste Form Cr/Al/Fe Hollandite with a Ti/TiO₂ buffer fabricated (1) melt processing in air at 1500°C, (2) melt processing in 1%H₂ balance Argon at 1500°C, (3) HP at 1200°C, and (4) SPS at 1230°C. Several differences between samples were observed with regards to phase formation, grain size and microstructure and elemental partitioning.

Table 22. Multiphase Waste Form Cr/Al/Fe Hollandite with Ti/TiO₂ Processing Comparison -Summary of Elements and Crystalline Phases (*Crystalline phases determined from XRD measurements and EDAX elemental analysis)

Spot	Elements (Major, Minor)	Crystalline Phases*
1	O,Al	Al ₂ O ₃
2	O,Ti	TiO ₂
3	O,Ti,Ca,Ba,Fe,Cr, (Nd,Zr,Cs,Al)	Hollandite
4	O,Ti,Y, (Fe)	(A ⁺³ _x B ⁺² _{1-x})TiO ₃ ?
5	O,Ti,Zr,Ca, (Fe,Nd)	CaZrTi ₂ O ₇
6	O,Ti,Ce,Nd,Pr,La,Y, (Ba,Fe,Al,Cr)	(A ⁺³ _x B ⁺² _{1-x})TiO ₃ ?
7	Mo	Metallic

Melting of the sample was enhanced when processed under reducing gas and a metallic alloy containing Mo was observed in the bottom of the alumina crucible. Enhanced melting resulted in larger grain size for the samples processed under hydrogen gas as compared to those melted in air. Samples melt processed in air exhibited the targeted phase with the exception of zirconolite. Samples melt processed in hydrogen exhibited the targeted phases of hollandite, perovskite/pyrochlore, zirconolite with residual TiO₂ and Al₂O₃.

The solid state sintering routes SPS and HP also demonstrated formation of the targeted phases. Hollandite, perovskite/pyrochlore, zirconolite, metallic alloy and TiO₂ and Al₂O₃ were observed distributed in a network of fine grains with small residual pores.

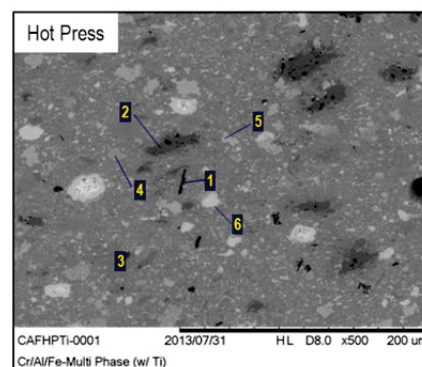
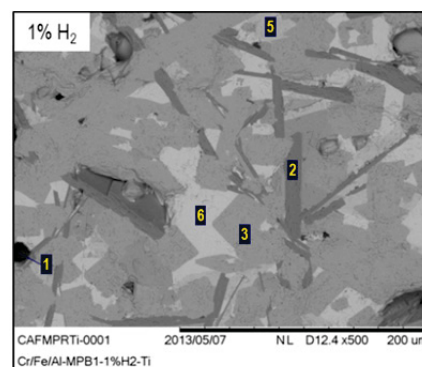
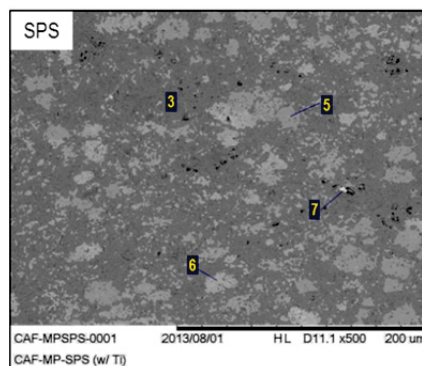
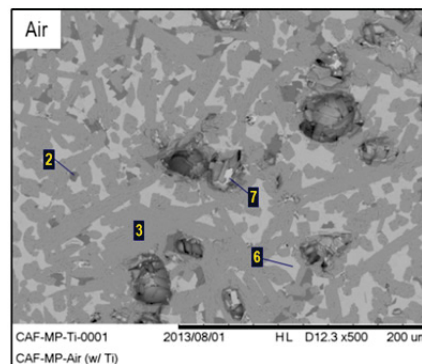


Figure 130. Multiphase Waste Form Cr/Al/Fe Hollandite with Ti/TiO₂ Processing Comparison-Backscattered Electron Micrograph

2013 Accomplishments Report

The titanate phases that incorporate M^{+3} rare earth elements were observed to be distinct titanate phases ($Nd_2Ti_2O_7$) with less degree of substitution as compared to the more homogeneous melt processed samples where a high degree of substitution and variation of composition within grains was observed. In general, the observations corroborate similar reports of melt processed versus solid state sintered waste forms in the literature showing that melt processed samples formed similar phases, however had larger grain sized along with large voids associated with the melt process; SPS and HP samples exhibited finer grain size with smaller voids. Metallic alloys were observed in the bulk of the sample for SPS and HP samples, but were found at the bottom of the crucible in melt processed trials. These results indicate that for a first melter trial, the targeted phases can be formed in air by utilizing Ti/TiO₂ additives which aid phase formation and improve the electrical conductivity. FY 2013 work has demonstrated that melting and crystallization is a promising processing method for fully crystalline ceramic waste forms. The targeted crystalline phases were achieved and further work is planned to evaluate waste form performance including radiation stability and durability of melt derived ceramics.

The principal goal of FY 2014 activities remains to provide a data package and support a successful Cold Crucible Induction Melter demonstration run to be conducted at INL. This work is part of collaborative activities with Alfred University as part of a DOE-NEUP program on advanced waste forms and the Australian Nuclear Science and Technology Organization.

References

1. Ringwood, A. E., et al. (1979). "Immobilization of High-Level Nuclear-Reactor Wastes in Synroc." *Nature* 278(5701): p. 219-223.
2. Sobolev, I. A., et al. (1997). "Comparative Study of Synroc-C Ceramics Produced by Hot-Pressing and Inductive Melting." *Mater. Res. Soc. Symp. Proc.* 465: p. 371.

Publications

1. Brinkman, K., J. Amoroso, J. Marra, and M. Tang (2013). "Crystalline Ceramic Waste Forms: Comparison of Reference Process for Ceramic Waste Form Fabrication." Technical Report: SRNL-STI-2013-00442, FCRD-SWF-2013-000229. Savannah River National Laboratory.
2. Amoroso, J., J. Marra, S. Conradson, M. Tang, and K. Brinkman (2013). "Melt Processed Single Phase Hollandite Waste Forms for Nuclear Waste Immobilization: $Ba_{1.0}Cs_{0.3}A_{2.3}Ti_{5.7}O_{16}$; A = Cr, Fe, Al." *Journal of Alloys and Compounds* 584: 590-599.

Characterization and Stability Test of Ceramic Waste Forms

M. Tang, mtang@lanl.gov, and K. Brinkman

LANL is focusing on characterization and testing procedures on the reference crystalline ceramics to develop the crystalline ceramic waste form to incorporate combined HLW raffinate stream and/or TRU stream from fuels fabrication processes. FY 2013 activities include: characterization of ceramic waste forms from SRNL and testing on their radiation stability. High-spatial resolution characterization with transmission electron microscopy (TEM), SEM with EDXS elemental mapping, X-ray photoelectron spectroscopy (XPS), EXAFS, X-ray absorption near edge structure (XANES), and XRD will be performed to analyze crystal structure, composition, structural and chemical homogeneity; electron and ion irradiation experiments are used to simulate self-radiation and test the stability of ceramic waste form.

Characterization and Radiation Stability Testing of Ceramics from SRNL

XANES, EXAFS, and XPS were used to measure the relative valence of Cr, Fe, and Ti elements on four Cr/Al/Fe single phase hollandites. These results will provide useful information for the development of crystalline ceramic waste forms. Normalized XANES spectra are shown for Fe and Cr in Figure 131. The Cr XANES and $\nu(R)$ EXAFS are identical within the

2013 Accomplishments Report

experimental uncertainty, showing that Cr speciation is unaffected by the processing. The spectra are clearly those of Cr(III), not exhibiting the intense pre-edge peak characteristic of Cr(VI) that originates in the non-centrosymmetric environment of these species. The EXAFS display a high degree of order extending out through the fourth or fifth near neighbor shell. The Fe XANES clearly show a change in the samples processed with H₂. The shift of the absorption edge to lower energy is consistent with the reduced species that would be expected to form under these conditions, with the extent of the shift within the range for the reduction of Fe(III) to (II).

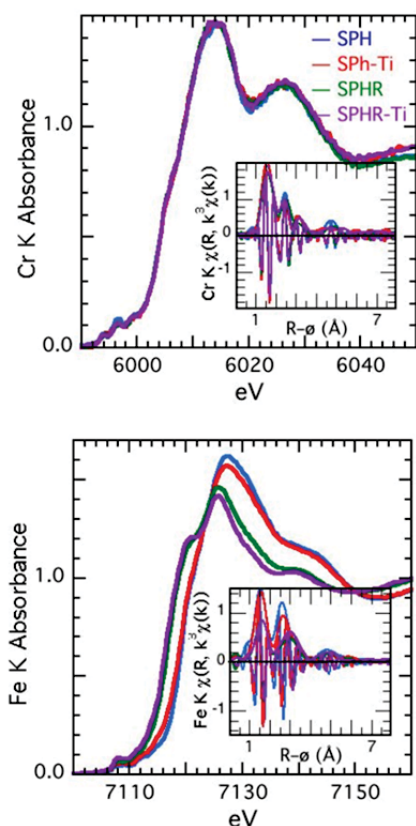


Figure 131. Cr and Fe XANES and EXAFS spectra of CAF-Hol: $Ba_{1.0}Cs_{0.3}Cr_{1.0}Al_{0.3}Fe_{1.0}Ti_{5.7}O_{16}$ processed in air (SPH); processed in air with Ti/TiO₂ (SPH-Ti); processed in 1% H₂ (SPHR); processed in 1% H₂ with Ti/TiO₂ (SPHR-Ti), according to the guide. The insets show the moduli and real components of the EXAFS in the (R) representation.

This change in speciation is also obvious in the EXAFS. The nearest neighbor peaks that represent the O shell are not only lower in

amplitude but also shifted to higher R, with the second near neighbor peaks showing an even greater expansion in distance.

LANL performed a series of ion irradiations to test the radiation stability of selected multiphase ceramic waste forms, which were used to simulate self-radiations in HLW from beta particle, gamma emissions, and alpha-decay process. Heavy ion (Kr) irradiations are used to produce the displacement damage in HLW which is generated by heavy recoil nuclei emitted from alpha-decay, while light ion (He/alpha) or in-situ electron radiations are used to simulate the ionization processes induced by beta and gamma particles. Ion beam irradiations were performed using Tandem accelerator or Danfysik implanter; and electron irradiations were using 300-keV electrons generated in a Tecnai F30 TEM.

Radiation stability on two multiphase ceramic waste form materials from SRNL were studied in FY 2013, one labeled as CSLNTM-2, which incorporates CS+LN+TM high Mo (13.88 mass%) waste streams with a waste loading of 60 mass%, another composition CWAHZCa100 which more closely resembles the reference ceramic composition with BaO and Fe₂O₃ additions targeting the hollandite phase in addition to perovskite, pyrochlore and zirconolite phases. Both samples were subjected to a 5 MeV alpha (He) beam with a fluence of 1×10^{17} ions/cm² (~ a dose of 7 GGy) and 600 keV Kr with a fluence of 2.5×10^{15} ions/cm² (~ a dose of 4 dpa) sequentially at room temperature to provide preliminary insight into the radiation damage tolerance of the ceramic waste form. Figure 132 shows the irradiation induced microstructural evolution of CSLNTM-2. Under 5 MeV alpha irradiation, there are some differences in relative intensities among the peaks in the spectra but no changes in the phases present are apparent, indicating good radiation damage tolerance. The changes in relative intensity could be due to texturing since the spectra were collected from the polished surface of the sample, rather than crushed powders. After sequential dual beam ion irradiations (5 MeV alpha and 600 keV krypton), XRD measurement shows an apparent broad diffraction feature in the scattering angle $2\theta = 25\text{--}35^\circ$, attributable to an amorphous structure.

2013 Accomplishments Report

It indicates that a phase transformation from crystalline to amorphous occurs upon heavy ion. The preliminary results indicate that these materials are radiation tolerant to the ionization damage, but susceptible to amorphization under recoil nuclei effects. EDXS under STEM mode and electron diffraction analysis were used to identify the phase compositions and crystalline structures. Figure 132 (top) shows TEM observation of dual beam irradiated zirconolite phase, and it suggests zirconolite exhibits very strong amorphization resistance under radiations. These identified crystalline phases in multiphase waste forms show the similar radiation response to the corresponding single phases under the similar radiation condition.

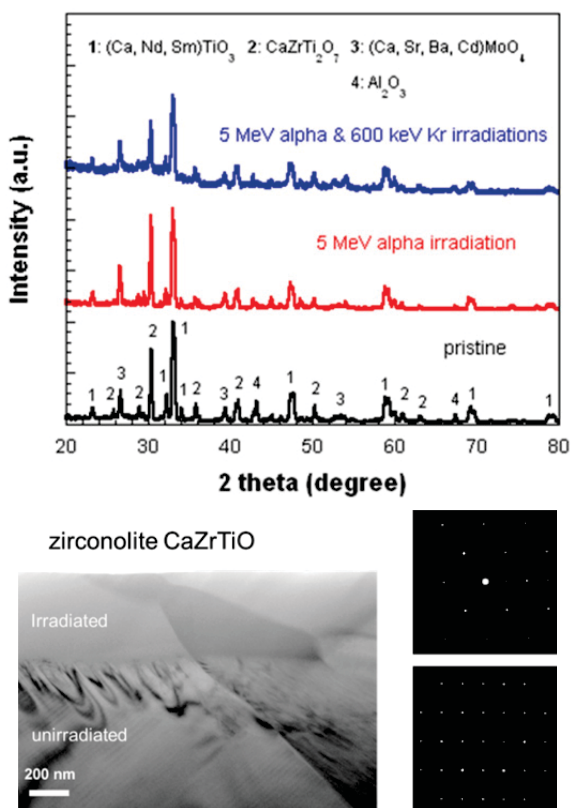


Figure 132. XRD results (top) of CSLNTM-2 before and after irradiations, Cross-sectional TEM micrograph (bottom) of irradiated zirconolite phase with corresponding selected area diffraction patterns.

Radiation Stability Testing on Double-Perovskite Phase Materials Incorporating Several Fission Products

The incorporation of radioactive elements in FPs into complex oxides, where the elements are constrained in the structure and enhanced durability and radioactive stability can be achieved, is an important research area in the nuclear fuel cycle. Perovskite structured $\text{Sr}_2\text{Fe}_{1.5}\text{Mo}_{0.5}\text{O}_{6-\delta}$ (SFM) has the capability of incorporating several FPs (such as Sr and Mo) into the crystalline network simultaneously while maintaining a stabilized structure. The radiation damage effects on the structure changes of this polycrystalline SFM sample was conducted under various ion irradiations including 200 keV He ions to a fluence of 5×10^{20} ions/ m^2 , 100 keV H to a fluence of 3×10^{21} ions/ cm^2 , and 600 keV Kr ions to a fluence of 2.5×10^{19} ions/ m^2 at room temperature. It was found in Figure 133 that the irradiated SFM sample decomposed into a layered $\text{Sr}_4\text{FeMoO}_{8-\delta}$ based phase and a metallic Fe based phase under light ion (He and H) irradiations. Nano-crystallized secondary phase was observed with particle sizes around 7 nm.

These results suggest that irradiation-induced reducing atmospheres may affect the stability of crystalline structure in complex oxides. Experiment results also reveal an amorphization in the heavy ion Kr irradiated sample, while no amorphization is observed in He/H irradiated SFM. These results also suggest that a potential criterion applied for radiation tolerance of nuclear wastes is the structural stability of the materials in locally reducing atmospheres arising from fission product decay in the crystalline matrix.

Separations and Waste Forms
2013 Accomplishments Report

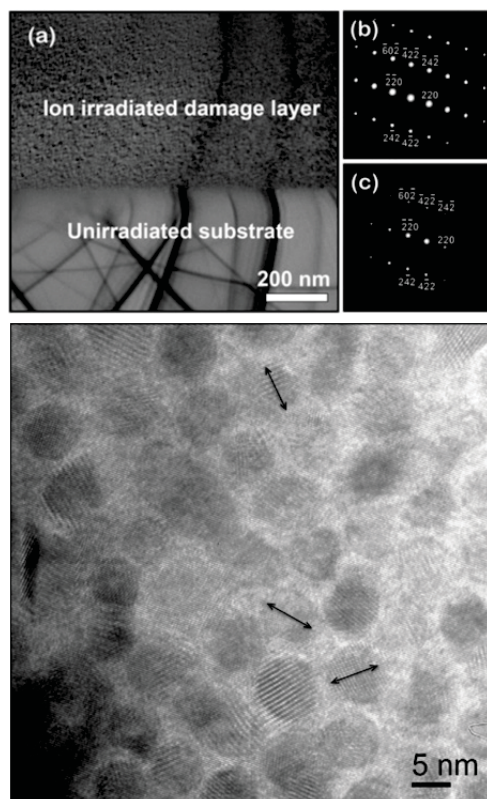


Figure 133. TEM image (left) of the He ion irradiated SFM sample with corresponding selected area diffraction patterns; high resolution TEM image (right) shows nano-crystallized secondary phase in the irradiated area.

Publications

1. Tang, M., P. Fuierer, P. Dickens, and E. Fu (2013a). "Irradiation Study on $\text{Sr}_{n+1}\text{Ti}_n\text{O}_{3n+1}$ Ruddlesden-Popper Phases Synthesized by Hot-Forging." *Phys. Status Solidi C* 10, No. 2, 216–220. DOI: 10.1002/pssc.201200523
2. Wang, S., M. Tang, L. Zhang, G. Xiao, K. S. Brinkman, and F. Chen (2013a). "Irradiation Effect on the Structure Change for $\text{Sr}_2\text{Fe}_{1.5}\text{Mo}_{0.5}\text{O}_{6-\delta}$ Perovskite Ceramic." *Journal of Alloys and Compounds*. 578: 170-175. <http://dx.doi.org/10.1016/j.jallcom.2013.04.166>
3. Wang, S., M. Tang, K. S. Brinkman, and F. Chen (2013b). *Nuclear Instruments and Methods in Physics Research Section B*, accepted

4. Tang, M., A. Kosoy, G. Jarvinen, J. Crum, L. Turo, B. Riley, K. Brinkman, K. Fox, J. Amoroso, and J. Marra (2013b). *Nuclear Instruments and Methods in Physics Research Section B*, accepted.

Glass Ceramics Waste Forms

Glass Ceramic Waste Form Development

J. Crum, jarrod.crum@pnnl.gov, J. Vienna, G. Piepel, C. Rodriguez, and C. Bonham

A borosilicate glass ceramic is currently being studied as an advanced waste form for immobilization of fission products in secondary waste streams generated during separation of UNF [[Crum, et al., 2011; Crum, et al., 2010]. A glass ceramic has the potential to at least double the waste loading compared to a single phase borosilicate glass (reference case), because insoluble fission products are intentionally crystallized into chemically durable and radiation-tolerant phases. To mature glass ceramics from a concept to a viable waste form, targeted processing properties and phase assemblages must be accurately predicted and achieved. This requires the collection of data and development of accurate models as a function of the projected waste composition space. In addition, the targeted phase assemblage must be demonstrated to be radiation tolerant and chemically durable over geologic time scales.

To begin accomplishing these objectives, phase one of the glass ceramic matrix was started this year. The matrix was statistically designed to vary key components like Al_2O_3 , B_2O_3 , CaO , Li_2O , Na_2O , SiO_2 , and waste loading (WL) by making multi-component-at-a-time changes. A multi-layered design was selected to better cover composition space. First, the composition space was defined by both an inner and outer set of extreme vertices. Second, two multi-component constraints ($\text{B}_2\text{O}_3/\text{Alkali}$ and $\text{Al}_2\text{O}_3+\text{CaO}+\text{WL}$) were utilized to minimize selection of composition space that is assumed to be unmeltable. The final matrix design consisted of 20 compositions, including replicates.

All of the compositions were successfully melted and all but one were characterized in terms

Separations and Waste Forms
2013 Accomplishments Report

of viscosity, electrical conductivity, and phase assemblage upon slow cooling according to the centerline cooling profile of 0.61 m \varnothing canister. One composition and its replicate, separated into two liquids (vertically stratified in the crucible) at temperatures below the melting temperature and were not further characterized.

Targeted crystalline phases of oxyapatite, Ln-borosilicate, powellite, and cerianite were obtained upon slow cooling and quantified by XRD. The amount of crystal phase data generated in phase 1 of the matrix is insufficient to model crystallinity of the individual phases as a function of composition.

Viscosity (η) and electrical conductivity (σ) were measured in the melt state as a function of temperature. Data were fit to the Arrhenius function: $\ln(\eta, \sigma) = A + B/T$, where A and B are fitted coefficients and T is in Kelvin. While the R^2 for these fits are quite good ($R^2 \geq 0.91$), some compositions appear to deviate (show curvature) somewhat from the Arrhenius relationship, likely because of crystallization and/or phase separation. For now, data that deviate from the Arrhenius function were removed and the data were refit to the Arrhenius function. The lower temperature data limit is given as crystallization temperature (T_c) and is the temperature when crystallization impacts viscosity behavior. However, in the future, accurate measurements of liquidus temperature and/or phase separation will be made to more accurately determine the temperature region where crystallization impacts η and σ .

Preliminary first-order mixture models were fit to measured slope (A), intercept (B), η , and σ with the coefficients given in Evaluation of the σ model coefficients reveals that adding alkali increases conductivity as was expected. Surprisingly, Al_2O_3 also appears to influence conductivity significantly. It has a significantly lower intercept than all other components and a very steep positive slope (increases with T). The literature points out that adding Al_2O_3 initially reduces conductivity, but further addition of Al_2O_3 can result in increased conductivity [Eldin and El Alaily, 1998]. This is because initially Al_2O_3 acts as a network former until all alkali are charge-compensated in the network. After which, it acts

as a network modifier. Additions of all other components reduce conductivity as expected.

Table 23. Because of the limited data collected to generate these models, they are considered helpful for designing the second phase of the matrix, but should not be considered a final model. That said, the model fits to the data show reasonable relationships between property measurements and composition.

Evaluation of the σ model coefficients reveals that adding alkali increases conductivity as was expected. Surprisingly, Al_2O_3 also appears to influence conductivity significantly. It has a significantly lower intercept than all other components and a very steep positive slope (increases with T). The literature points out that adding Al_2O_3 initially reduces conductivity, but further addition of Al_2O_3 can result in increased conductivity [Eldin and El Alaily, 1998]. This is because initially Al_2O_3 acts as a network former until all alkali are charge-compensated in the network. After which, it acts as a network modifier. Additions of all other components reduce conductivity as expected.

Table 23. First-order mixture model coefficients fitted separately to A and B Arrhenius coefficients.

	ln(σ) intercept	ln(σ) slope	ln(η) intercept	ln(η) slope
	<i>A</i>	<i>B</i>	<i>A</i>	<i>B</i>
WL	6.7	-5,127	-32.1	51,406
Al_2O_3	-18.5	30,785	-90.3	164,323
B_2O_3	12.7	-12,885	28.8	-62,945
CaO	25.8	-36,779	-21.0	27,555
Li_2O	16.3	8,905	-23.8	13,441
Na_2O	2.1	19,275	-27.4	38,498
SiO_2	12.5	-21,817	-7.5	18,663
R^2	0.83	0.90	0.71	0.81
*Overall R^2	0.94		0.91	

* Overall R^2 is for measured versus predicted $\ln(\sigma)$ and $\ln(\eta)$ as a function of temperature and composition.

In addition to the matrix study, a journal article was published this year that documents the results of first glass ceramic CCIM melter test in the Journal of Nuclear Materials [Crum, et al., 2014]. The article highlights the glass ceramic

2013 Accomplishments Report

formulation, successful melter test, and post melter test analysis of the waste form.

References

1. Crum, J. V., B. J. Riley, L. R. Turo, M. Tang, and A. Kossoy (2011). "Summary Report: Glass-Ceramic Waste Forms for Combined Fission Products." FCRD-WAST-2011-000358. Pacific Northwest National Laboratory.
2. Crum, J. V., L. R. Turo, B. J. Riley, M. Tang, A. Kossoy, and K. E. Sickafus (2010). "Glass Ceramic Waste Forms for Combined CS+LN+TM Fission Products Waste Streams." FCRD-WAST-2010-000181." Pacific Northwest National Laboratory.
3. Eldin, F. M. E., and N. A. El Alaily (1998). "Electrical Conductivity of Some Alkali Silicate Glasses." *Materials Chemistry and Physics* 52 [2]: 175-17.
4. Crum, J., V. Maio, J. McCloy, C. Scott, B. Riley, B. Benefiel, J. Vienna, K. Archibald, C. Rodriguez, V. Rutledge, Z. Zhu, J. Ryan, and M. Olszta (2014). "Cold Crucible Induction Melter Studies for Making Glass Ceramic Waste Forms: A Feasibility Assessment." *Journal of Nuclear Materials* 444 [1-3]: 481-492.

Publication

1. Crum, J., V. Maio, J. McCloy, C. Scott, B. Riley, B. Benefiel, J. Vienna, K. Archibald, C. Rodriguez, V. Rutledge, Z. Zhu, J. Ryan, and M. Olszta(2014). "Cold Crucible Induction Melter Studies for Making Glass Ceramic Waste Forms: A Feasibility Assessment." *Journal of Nuclear Materials* 444 [1-3] 481-492.

Glass Ceramic Process Engineering Studies and Product Testing Support

R. Jones, robert05.jones@sms.doe.gov, and J. Marra

Preliminary Engineering Study

Although vitrification is a mature technology that is used worldwide for the immobilization of HLW, shortcomings in existing vitrification technologies and the reference borosilicate waste

glass have prompted the investigation of a glass ceramic waste form as a waste form option for waste raffinates from future fuel recycling flow sheets. A preliminary Technology Readiness Assessment (TRA) was conducted for immobilization of HLW raffinate in a glass ceramic waste form using a CCIM. Relatively low Technology Readiness Levels (TRL) were found for five critical technology elements:

- Mixing, sampling, and analysis of waste slurry and melter feed
- Feeding, melting, and pouring
- Glass ceramic formulation
- Canister cooling and crystallization
- Canister decontamination.

A technology maturation plan (TMP) was developed by the S&WF Campaign in response to the TRA. Although the TRL's are low for most of these critical technology elements (TRL-1) primarily because the specific waste stream is not known or tested, the effort required to advance them to higher values is relatively low. A TRL of 2 would be obtained by completing an initial waste composition/property estimate, a preliminary engineering study, some additional laboratory scale tests of the glass-ceramic, and a mixing and sampling test. One of the elements to advance the technology to a TRL of 6 would be to perform a preliminary engineering study.

A report was prepared by SRNL to address the need "perform a preliminary engineering study". The preliminary engineering study consisted of three tasks:

- Glass Ceramic Waste Form Material Balance
- Glass Ceramic Waste Form Thermal Calculations
- Glass Ceramic Waste Form Pre-Conceptual Cost Study.

The report, entitled "Glass Ceramic Waste Form Material Balance," FCRD-SWF-2013-000120, documented the development of the material balance for the glass ceramic waste form.

Separations and Waste Forms
2013 Accomplishments Report

The material balance was based upon the technologies defined in the TMP for:

- Feed and sampling
- Feed adjustment
- Melting and pouring
- Heat treatment
- Canister configuration
- Canister handling
- Melter offgas cooling and deposit prevention
- Particulate and semi-volatile removal
- Gas heat
- Organic removal
- Nitrate mitigation
- Iodine capture.

A second report, entitled “Glass Ceramic Waste Form Thermal Calculations,” FCRD-SWF-2013-000193, examined the impact of thermal constraints on waste loading as a function of waste package size. The following four canisters were selected for study:

- 24” diameter, 15 ft tall canister proposed for borosilicate glass use at the Hanford Waste Treatment and Immobilization Plant Project,
- 16.9” (430mm) diameter, 4.4 ft (1330mm) tall universal canister for vitrified waste. This canister is the internationally accepted standard for borosilicate glass from reprocessing of LWR uranium oxide fuel (UOX).
- 12” diameter, 10 ft tall canister. This canister was selected to provide an intermediate canister diameter for this study, the study assumes a maximum length to diameter ratio (L/D) of 10.
- 9” diameter, 7.5 ft tall canister. This canister was selected as the minimum diameter for this study, the study assumes a maximum L/D of 10.

Waste forms are subjected to thermal stability limits. For example, the alkali/alkaline earth elements are very soluble in glass; it is possible to add so much radioactive Cs/Sr to glass that it causes it to exceed the glass transition (tolerance) temperature, allowing it to crystallize, thereby altering the waste form. Other radionuclides also contribute significant decay heat. Container size must therefore be limited based on waste loading, total thermal output rate (power), and the acceptable maximum allowable temperature to prevent waste form degradation. Thermal constraints were developed for waste form interim storage for the time between production and disposal. The mass and decay heat limits for the four canister cases are summarized in Table 24.

Table 24. Glass Ceramic Waste Form (GCWF) Canister Mass and Decay Heat Limits

Diam. (in)	Diam. (cm)	Length (in)	Length (cm)	Mass of GCWF per Can* (kg)	Max. Decay Heat (Watts/Can)
9	22.9	90	229	285	6,280
12	30.5	120	305	676	10,420
16.9	42.9	52	133	480	4,750
24	61.0	180	457	4,057	24,700

* Density of 3.2 g/cm³

The impacts of these thermal limits were evaluated by selecting four fuel compositions and determining the maximum waste loading when applying the physical and thermal limits in Table 24. The four fuels selected were:

- 50 GWd/MT, 5 year cooled
- 50 GWd/MT, 50 year cooled
- 60 GWd/MT, 5 year cooled, and
- 60 GWd/MT, 30 year cooled fuel

Figure 134 summarizes the impact of canister diameter on waste loading for all 4 fuels studied.

2013 Accomplishments Report

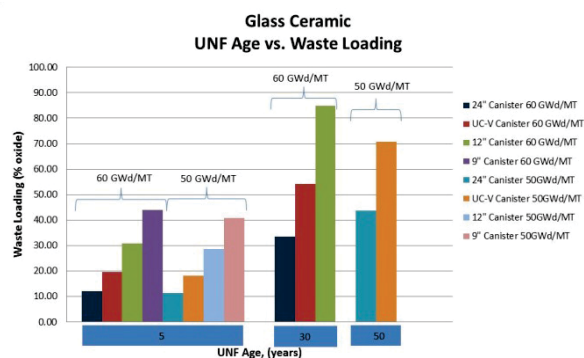


Figure 134. Waste Loading as a Function of Cooling Time

Glass Ceramic Waste Form Pre-Conceptual Cost Study

The report, entitled “Glass Ceramic Waste Form Pre-Conceptual Cost Study,” FCRD-SWF-2013-000267, developed a total project cost (TPC) estimate for a GCWF processing facility to process the HLW stream from a co-extraction recycling facility operating at a capacity of 800 MTHM/year. The pre-conceptual cost study was based on cost estimates prepared previously for the Engineering Alternative Studies (EAS) and the Follow-On Engineering Alternative Studies (FOEAS) as part of the Global Nuclear Energy Partnership program. The EAS and FOEAS evaluated a variety of recycling alternatives involving a variety of facility capacities and process technologies. Several sensitivity analyses were also conducted to evaluate the effects of process changes such as early receipt of used fuel, separation of Am and Cm, and production of a single borosilicate HLW glass. The sensitivity analysis for the single waste form was based on a recycling facility using a co-extraction process operating at a capacity of 800 MTHM/year. The cost estimate for the HLW fission products solidification facility associated with the single waste form sensitivity analysis case was used as a basis for the glass ceramic waste form pre-conceptual cost study. The prior estimate was modified based on technical input from the process flow diagrams and material balance previously developed for the glass ceramic waste form process. The facility space to contain the major process equipment was defined as part of the technical basis for this cost study. The difference between the reference FOEAS and

GCWF facility requirements provided the means for adjusting the FOEAS total project cost estimate to derive a total project cost estimate for the GCWF facility. Table 25 shows the resulting low and high range TPC estimates for a GCWF facility with the capacity to process the HLW fission products from a co-extraction recycling facility operating at a capacity of 800 MTHM/year.

Table 25. GCWF Total Project Cost Estimate Summary

Process Facility/Building	GCWF	
	Low Range (\$ x 1,000)	High Range (\$ x 1,000)
Fission Products Solidification and Packaging Building	2,480,100	3,922,700
Cold Feeds	33,300	39,400
Waste Storage Building	144,100	216,000
Ventilation Stack	7,200	9,100
Total	2,664,700	4,187,200

Glass Ceramic Waste Form Durability Testing

Another element of the SRNL support to the glass ceramic waste form development program is to perform durability testing to assess the performance of the glass ceramic product. The multi-phase nature of the glass ceramic product makes assessing the relative durability difficult because the various phases can corrode differently, thus, releasing radionuclides of concern at varying rates.

In FY 2013, a corrosion testing methodology was developed in an attempt to evaluate the bulk dissolution behavior of the glass ceramic waste form and the corrosion of individual phases comprising the glass ceramic. To assess bulk dissolution, a crush powder tests is used. This part of the test is based on the PCT – Method B (ASTM C1285-02) where crushed glass ceramic powder of a specific particle size is subjected to ASTM Type-1 water at a ratio of 10 parts water to 1 part glass ceramic on a mass basis. The test is conducted at 90°C for varying durations. The corrosion performance of the individual phases is assessed using polished monolithic coupons where

2013 Accomplishments Report

part of the sample is masked to maintain that part of the sample in a pristine condition for comparison to the leached material. Following testing, the masking is removed and the samples are analyzed using varying microscopic, profilometry and interferometry techniques to assess corrosion damage. Calculations showed that inclusion of the monolith in the powder leach tests would only increase the total surface area of leached material by about 2%. The powder/monolithic leach test configuration is shown schematically in Figure 135.

Glass ceramic material representing 10 glass ceramic compositions was obtained from PNNL and crushed, sieved and washed. Additionally, monolithic specimens were cut and polished. Testing will commence in early FY 2014 for varying durations with exposures greater than 1 year anticipated.

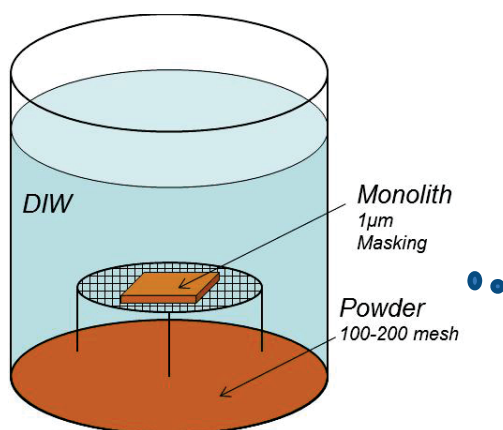


Figure 135. Schematic for powder/monolithic leach test configuration.

Characterization and Stability Test of Glass Ceramic Waste Forms

M. Tang, mtang@lanl.gov, and J. Crum

LANL is focusing on characterization and testing procedures on glass ceramics from the test matrix and melter testing to develop the glass ceramic waste form for immobilization of HLW raffinate stream. FY 2013 activities include: characterize glass ceramic waste forms from PNNL and INL and test their radiation stability, thermal stability. High-spatial resolution characterization uses TEM; electron and ion irradiation experiments are used to simulate self-

radiation and test the stability of glass ceramic waste form; the thermophysical property measurement capability is utilized to test thermal properties (including thermal conductivity, thermal diffusivity, specific heat capacity).

Characterization and Radiation Stability Testing of Glass Ceramics from PNNL

The long-term stability of nuclear waste forms is an important consideration in their selection for safe disposal of radioactive waste. The principal sources of radiation in HLW are β -decay of the fission products (e.g., ^{137}Cs and ^{90}Sr) and α -decay of the actinide elements (e.g., U and Pu). Beta-decay produces energetic β -particles, very low energy recoil nuclei, and γ -rays, whereas, α -decay produces energetic α -particles (4.5 to 5.5 MeV), energetic recoil nuclei (70 to 100 keV), and some γ -rays. Beta and alpha decay affect materials through the interactions of the β -particles, α -particles, recoil nuclei, and γ -rays with the target material. These interactions fall into two broad categories: the transfer of energy to electrons (ionization and electronic excitations) and the transfer of energy to atomic nuclei (displacement damage), primarily by ballistic processes involving elastic (billiard-ball-like) collisions. Our approach to simulate the self-radiation is to radiate the waste form with ion beams generated by accelerators, implanters, and electrons using TEM. Light ions and electrons provide a useful means to examine ionization effects because they deposit nearly all of their energy in solids via electronic loss processes; and heavy ion are used to simulate energetic recoil nuclei interaction which involves ballistic processes.

The purpose of this study is to assess the radiation stability of multi-phase glass ceramic waste forms, and researchers are targeting for these particular mineral phases within the glass matrix that incorporate a variety of waste components, including pollucite, celsian, oxyapatite, powellite, and lanthanide(Ln)-borosilicate phases. These mineral systems are selected because they all have been demonstrated to generally have high chemical durability (possibly with the exception of celsian due to moderate alkali release), high thermal stability, and good mechanical properties. The link between

Separations and Waste Forms

2013 Accomplishments Report

radiation tolerance of the above targeted phases in multiphase glass ceramics with the corresponding single phase oxides is necessary to fully understand the processes responsible for long-term performance of this waste form.

The radiation stability of two glass ceramics with different waste streams and waste loadings, was tested under various radiation environments in FY 2013. Glass ceramic composition GC-4 includes the combined CS+LN waste streams with a waste loading of 60 mass%. Glass ceramic composition Mo-6.25 is formulated with the combined CS+LN+TM waste streams at a waste loading of 45 mass% in which 6.25 mass% is MoO₃ in the final form. Both samples were subjected to 5 MeV alpha (He-light ion) beam with a fluence of 1×10^{17} ions/cm² (~ a dose of 7 GGy) and 600 keV Kr (heavy ion) with a fluence of 2.5×10^{15} ions/cm² (~ a dose of 3 dpa) sequentially at room temperature to provide preliminary insight into the radiation damage tolerance of the glass ceramic waste form. Energy dispersive X-ray spectroscopy and electron diffraction analysis were used to identify the phase compositions and crystalline structures. Five crystalline phase compositions including celsian, Ln-borosilicate, Ln-Al silicate, powellite, and oxyapatite, are identified in the observed area of these two glass ceramics. Overall, the present results indicate that these glass ceramics are radiation tolerant to the ionization damage induced by light ion irradiation, but susceptible to amorphization under recoil nuclei effects simulated by heavy ion irradiation. Specifically, different crystalline phases in these multiphase waste forms exhibit different radiation tolerance under various radiation damage environments (see Table 26).

Table 26. Summary of radiation stability of major crystalline phases in glass ceramic and ceramic waste forms.

Crystalline phase	Displacement damage (3 dpa)	ionization radiation (electron)
Ba-Al silicate (celsian)	Crystalline-Amorphous	2×10^{12} Gy, mostly
Ln-borosilicate	C-A	2×10^{13} Gy, partially
Ln-Al silicate	C-A	1×10^{13} Gy, partially
oxyapatite	C-A	1×10^{13} Gy, no amorphous
powellite	C-C	1.5×10^{13} Gy, mostly
hollandite	C-A	1.5×10^{13} Gy, mostly
zirconolite	C-C	

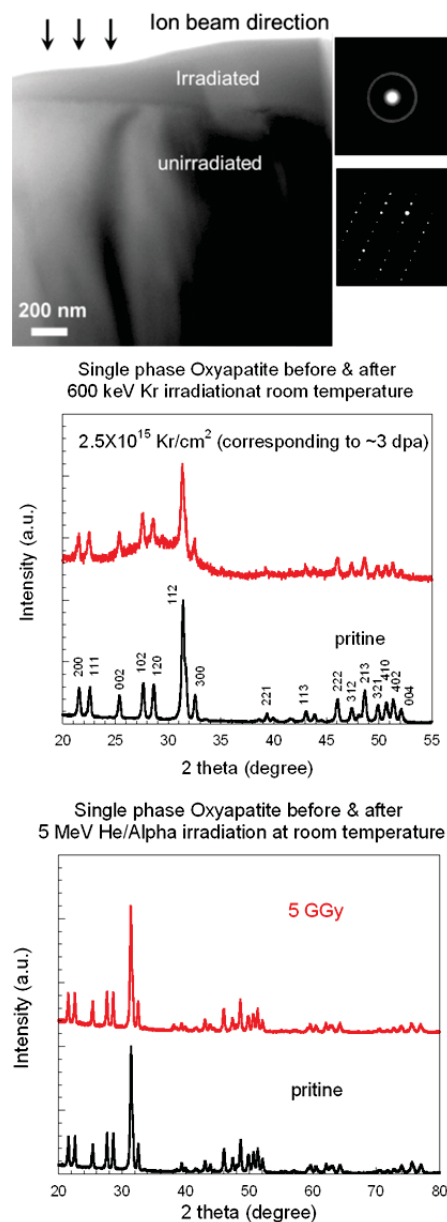


Figure 136. TEM and XRD observations of oxyapatite phase under irradiations.

Figure 136 (top) shows TEM observation of dual beam irradiated oxyapatite phase in Mo-6.25 glass ceramic, and it reveals that oxyapatite phase undergoes amorphization under radiations. Figure 136 (middle and bottom) shows XRD results of single phase oxyapatite before and after Kr or He irradiations. Amorphization is observed under Kr irradiation, while oxyapatite still remain crystalline under He irradiation. These identified crystalline phases in multiphase waste forms show

Separations and Waste Forms
2013 Accomplishments Report

the similar radiation response to the corresponding single phases under the similar radiation condition.

Thermophysical Property of Glass Ceramics from PNNL

Accurate thermophysical properties (thermal conductivity, heat capacity, thermal diffusivity) as a function of temperature are needed for engineering analysis of nuclear materials including waste forms. These properties are important in determining the thermal gradients in a waste form during its fabrication, storage, transport and geological disposal. Thermophysical properties of glass ceramic waste forms provide very useful information on the glass melting, forming process, and crystalline phase formation.

In this work, the thermophysical properties from room temperature to 1273 K were investigated for four different borosilicate glass ceramic compositions containing waste loadings from 42 to 60 weight percent in order to determine the sensitivity of these properties to waste loading, as-fabricated microstructure, and potential evolutions in microstructure brought about by temperature transients. The impact of increasing waste loading is shown to have a small but measurable effect on the thermophysical properties between the four compositions, contrasted to a much greater impact observed when transitioning from predominantly crystalline to glass.

The product of the density, specific heat capacity, and thermal diffusivity was calculated to determine the thermal conductivity of all four compositions, and the results are shown in Figure 137. Additionally, the thermal conductivity of both amorphous SiO₂ and a borosilicate waste glass are also plotted for comparison. All of these TM-containing samples exhibit increasing thermal conductivity with temperature as expected for systems dominated by glasses. This behavior is attributed to the fact that the phonon mean free path in amorphous (glass) systems is constant as a function of temperature; the thermal conductivity as a function of temperature is therefore dictated by the gradually increasing heat capacity. The GC-Mo 5.86, GC-Mo 6.25, and GC-Mo 6.94 samples

undergo a reduction in the thermal conductivity between 900 and 1000 K. This drop is again consistent with what would be expected for a system with a small fraction of liquid phase present in a solid matrix. After the samples transition through this region, the thermal conductivity of the samples again exhibits a positive temperature dependence. Conversely, the GC-4 sample displays a thermal conductivity curve that is generally the reverse of what would be expected of a system constructed of crystalline phases.

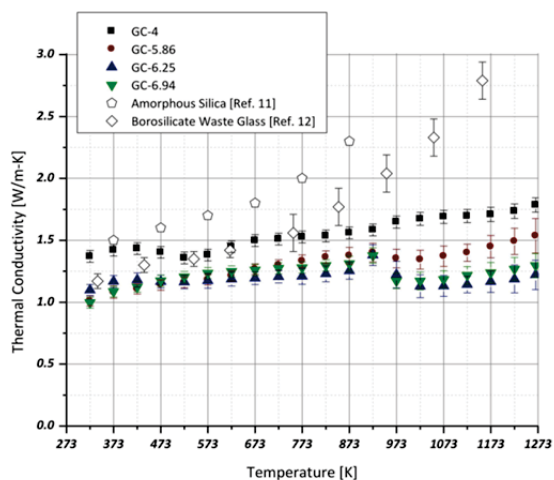


Figure 137. Thermal conductivity data calculated using the product of the thermal diffusivity, specific heat capacity, and density.

The presence of a glass transformation and melting of an amorphous phase dominate the properties of the GC-5.86, GC-6.25, and GC-6.94 samples at temperatures above 900K. The amorphous phase fractions present in the compositions synthesized with transition metals have been shown to largely dominate response. However, a more accurate understanding of the phases present as well as their individual thermophysical properties would be necessary to apply a more rigorous analysis of their individual contribution. Despite presence of a far lower phase fraction of amorphous constituents, GC-4 also exhibits thermophysical properties that are quite similar to those expected of an amorphous material. No melting was observed, but two smaller glass transitions are present.

Separations and Waste Forms
2013 Accomplishments Report

Publications

1. Kossoy, A., R. Schulze, M. Tang, D. J. Safarik, and R. J. McCabe (2013). “Nd–Mo–Borosilicate Glass–Ceramic: Synthesis, Characterization and Response to Ionizing Radiation.” *Journal of Nuclear Materials* 437 216-221.
<http://dx.doi.org/10.1016/j.jnucmat.2013.02.038>
2. Tang, M., A. Kossoy, G. Jarvinen, J. Crum, L. Turo, B. Riley, K. Brinkman, K. Fox, J. Amoroso, and J. Marra (2013). *Nuclear Instruments and Methods in Physics Research Section B*, accepted
3. Nelson, A. T., J. V. Crum, and M. Tang (2013). *Journal of the American Ceramic Society*, submitted

Cold Crucible Induction Melter

V. Maio, Vincent.maio@inl.gov

FY 2013 planned activities involving applied R&D into advanced HLW forms through testing in the INL’s integrated CCIM Pilot-Plant were to continue on the success of FY 2012’s proof-of-principle test. This FY 2012 test validated that a glass ceramics waste forms can be successfully fabricated in a CCIM. This was a significant accomplishment not previously demonstrated (see Figure 138, Figure 139, and Figure 140).

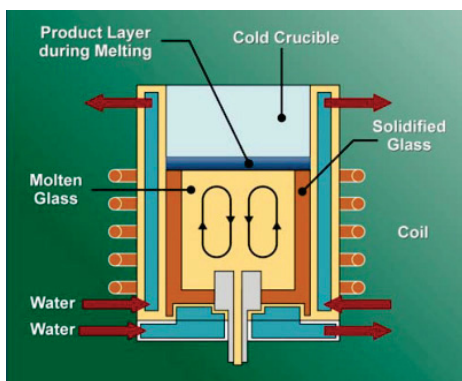


Figure 138 Schematic of a CCIM. Compared to a Joule-Heated-Melters, the lack of in-melt electrodes and refractory in a CCIM allow for greater mixing, less corrosion, longer life, greater throughput, less footprint and therefore melting temperatures exceeding 1700°C- which is 50% higher than that achievable with the JHMs.

Compared to previous glass –only melts using surrogates of slurry HLW feed based on legacy nuclear defense related processes, melt initiating, melting, tapping, pouring and controlled cooled curing occurred in the CCIM pilot plant with challenges when glass ceramic waste forms were required. The FY 2012 proof –of principle test was successful, but the challenges were expected and were a result of the diluted nature of the future UNF-recycled derived HLW raffinate surrogate, the relatively high resistivity of this melt, and the formation of crystals in the drain tube. Overall, however, the melt test gave performance as predicted based on earlier PNNL crucible-scale tests

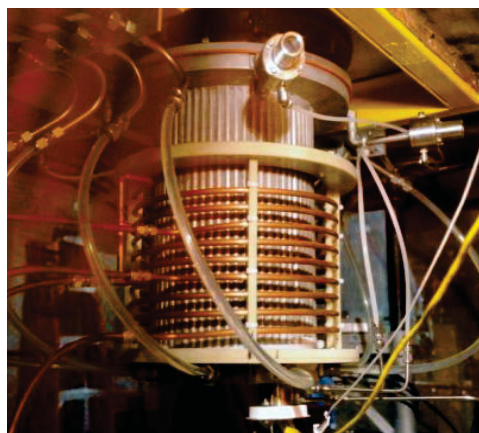


Figure 139 The INL’s CCIM Pilot Plant’s 26.5 cm dia. crucible, surrounded by its 6 –turn induction coil-all inside a Faraday cage

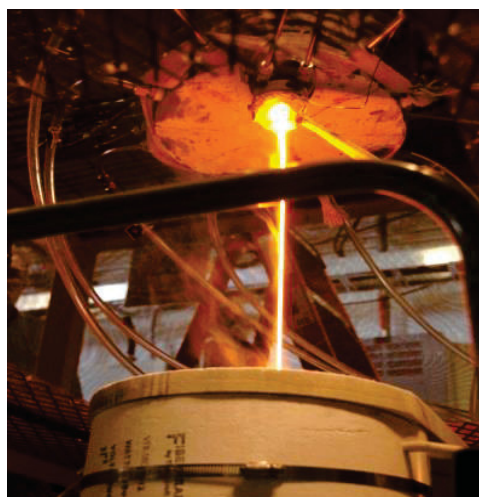


Figure 140. Glass Ceramic Melt Pouring from the INL CCIM during the FY2012 Proof-of-Principle Test.

Separations and Waste Forms
2013 Accomplishments Report

Prior to initiating FY 2013 duration tests with glass ceramics and FY 2014 proof-of-principle tests with titanate crystalline ceramic waste forms, key modifications to the CCIM pilot plant were required as an FY 2013 high priority objective. These modifications were necessary to measurably increase the CCIM technology's effectiveness for the resistive melts and surrogate melter feeds characteristic of the proposed composition of the recycled UNF – derived HLW raffinate. They were also necessary to ensure a reliable and robust new drain and drain heating system to accommodate the crystal (solid phase) formation that occurs in the drain tube after each tapping and pouring of the advanced waste forms. As shown in Figure 141 and Figure 142. Even though a bottom drain configuration is advantageous for crystals, the prolonged exposure to temperatures over 1100°C causes excessive corrosion to the upper part of the outer drain tube exposed to the melt and causes sagging and eventual breaking of the heating elements in the ceramic tube heater.



Figure 141. CCIM Drain Assembly as viewed from below the melter.



Figure 142. Observed damage to existing bottom drain tube and drain clamshell heater when exposed (for over an hour) at high temperatures (>1100°C) as required to melt solid crystals.

Results of CCIM Modifications and Testing

Robust CCIM bottom drain designs and drain heating systems are paramount to consistently tap and pour-in highly radioactive environments-melts containing ceramics (crystalline phases). Additionally, higher radio frequencies (RF) are necessary to couple to, initiate, and maintain the low conductivity (high resistivity) melts that are consistent with current advanced waste forms being developed by PNNL and SRNL; while still maintaining acceptable power capacity. These modifications are described below

- Bottom drain and drain heater design changes (Figure 143 and Figure 144), installation, and testing were completed to ensure the reliable and repetitive tapping and pouring of melts containing ceramic (solid) phases.

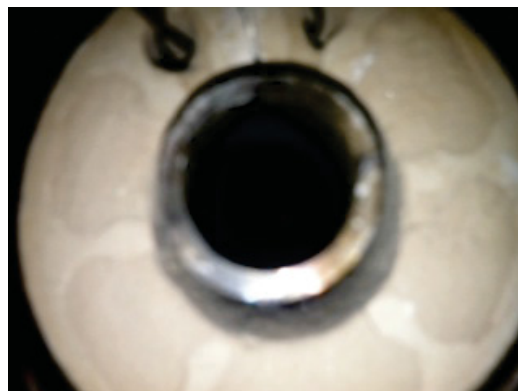


Figure 143 Tube shell heater with potted coils around a Hastelloy drain tube with a wider diameter. Drain tube diameter increased from 1/2" to 3/4".



Figure 144. Complete new drain assembly on test stand.

Separations and Waste Forms
2013 Accomplishments Report

- Two designs were considered: one involving traditional annular tube heaters potted to protect the electrical elements as well as a wider drain tube with nitrogen in-bed cooling; another based on a new crucible design (CFD modeled-per Figure 145) with a graphite susceptor drain tube (see Figure 146) coupled to an air operated remote arm for cooling as shown in Figure 147.
- Tests performed slowly cycled the heater temperature between 0 to 1100°C over three different periods by increasing the amperage to the heater via a rheostat. This had the effect of conditioning the elements-per manufactures recommendation- in the potted tube and as a result there was no heater tube failure after each cycle test.

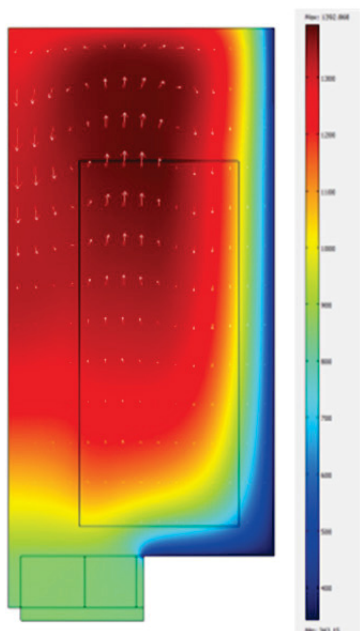


Figure 145. One dimensional CFD model of new crucible with the graphite susceptor drain (left – bottom green square) in the closed (cold) position.



Figure 146. Different sized test specimens for the new crucible's graphite susceptor bottom drain tube.



Figure 147. New CCIM Pilot Plant remote arm for graphite susceptor drain control and stopping with R, Z, and Θ range

- Both drains were enhanced with a new exhaust blower with greater vacuum and less flow to ensure pour control and immediate stopping (see Figure 148).



Figure 148. New exhaust blower.

2013 Accomplishments Report

- A new variable capacitor (Figure 149) was added and one fixed capacitor removed to increase the frequency of the RF generator damped L-C circuit, as required to couple to the more resistive melts. The new configuration was tested multiple times to understand complex relationships between melt properties, start-up conditions, and the CCIM's RF generator's electrical settings with regard to inductance, capacitance, and vacuum tube tuning.



Figure 149. New variable capacitor to replace one of two fixed capacitors.

The modifications described above have turned a CCIM originally designed for defense high-level waste glass fabrication into a test bed capable of testing a wide range of potential waste forms. This test bed will prove valuable to the United States in their development of advanced UNF treatment options. However, the cost and time required for the improvements were higher than originally planned. Therefore, the decision was made to post-pone the planned glass ceramic duration test to FY 2014, along with the all ceramic waste form proof-of-principle test.

Conclusions

The modifications to the INL CCIM test bed yielded several conclusions. These conclusions not only led to increasing the understanding of various electrical parameter relationships associated with the induction melting of resistive materials, but ensure greater confidence in planned future testing as well as aid in the advancement of the CCIM technology along the technical readiness levels (TRLs):

- Methods for improving the range of melt conductivity tolerance in a single, variable, melter test bed were developed. The variables of melt resistivity (as a function of temperature), RF generator power efficiency, and RF generator frequency (as a function of the damping LC circuit's conductance and resistance) of the new configuration are compared in Figure 150.

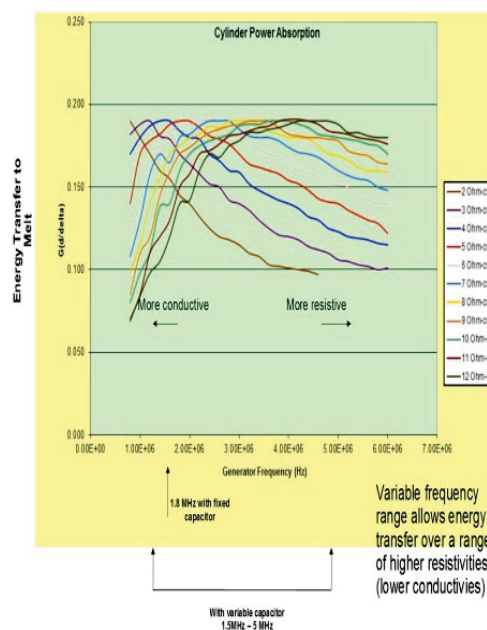


Figure 150. Power Efficiency vs. Frequency for various Resistances

- Advanced drain tube design that are flexible enough to allow for the reliable fabrication of both ceramic and glass-ceramic waste forms were developed. These designs will allow for higher crystal content in the drain while being stable to repeated heating and cooling cycles to temperatures over 1500°C.
- Calculations performed in FY 2013 regarding the concentration of simulated liquid HLW melter feed indicated that acceptable feeds (i.e., feed rates that take advantage of the CCIM's high temperature and high throughput) can be produced well below the azeotrope concentration for nitric acid.

Separations and Waste Forms
2013 Accomplishments Report

Concentration of the melter feed for FY 2014 testing is essential to validate the high CCIM GCWF production rate, which is expected to be 1500 kgs/m²Hr.

Publications

1. Maio, V. C. (2012). "Process-ability Advantages of Cold Crucible Induction Melter (CCIM) Technology for Immobilizing the HLW Fraction of Hanford Waste Tank AZ-101." INL/EXT-12-27749. Idaho National Laboratory, November 12.
2. Maio, V. C. (2012). "Glass-Ceramic High Level Waste (HLW) Form Process-ability with Cold Crucible Induction Melter (CCIM) Technology." INL/EXT-12-27750. Idaho National Laboratory, November 12.
3. Maio, V. C. (2013). "Test Plan II for Demonstrating the CCIM Stabilization of an (unsalted) Simulated HLW Raffinate into a Glass Ceramic Form via a Bench Scale CCIM with Advanced Drain Designs." INL/EXT-13-28250. Idaho National Laboratory, January 24.
4. Maio, V. C., and V. J. Rutledge (2013). "Concentration of HLW Raffinates from UNF Recycling." INL/EXT-13-28484. Idaho National Laboratory, February 19.
5. Ancho, M. (2011). "CCIM Plant Modification Plan." INL/MIS-11-23244. Idaho National Laboratory, September 7.
6. Maio, V. C. (2011). "Idaho National Laboratory Cold Crucible Induction Melter (CCIM) Test With a Glass-Ceramic Waste Form-FT121N030801." INL/MIS-11-23916. Idaho National Laboratory, November 9.
7. Maio, V. C. (2012). "Validation of the Completion of a CCIM Test Run to Produce a Glass Ceramic Waste Form." INL/MIS-12-26813. Idaho National Laboratory, July 31.

Epsilon Metal Waste Form Development

*J. V. Crum, jarrod.crum@pnnl.gov, D. M. Strachan,
M. Zumhoff*

Several components of UNF remain as undissolved solids (UDS; noble metals, Tc, Zr, and Mo) during aqueous reprocessing. The reference case is to combine all waste streams in to a single waste form, borosilicate glass. However in the reference case waste loading is severely limited by noble metals, which remain almost entirely undissolved in borosilicate glass. Alternatively, UDS and soluble Tc can be treated separately in a metal waste form without additives. Epsilon metal (ϵ -metal) is being developed as a waste form for treatment of UDS and soluble Tc generated during aqueous reprocessing of UNF. Natural analogs of the ϵ -metal phase have been shown to survive over extended geologic times scale (outperforming borosilicate glass).

Development work has focused on demonstrating that the ϵ -metal waste form can be produced using commercially available techniques and second, confirm the impressive corrosion resistance of the natural analogs using established testing methods in the laboratory.

Results of testing commercial processing technologies to produce ϵ -metal waste form were recently published in *The Journal of Nuclear Materials* this fiscal year ([Crum et al. 2013](#)). Results showed two viable technologies, SPS and HIP, for producing the waste form. With HIP having a significant edge in maturity over SPS both commercially and in nuclear wastes applications. Additional work is needed to optimize the process that is selected (SPS or HIP) in terms of the composition envelope and processing conditions that result in acceptable waste form performance.

The results of corrosion testing have been drafted into a journal article, to be submitted to the *Journal of Nuclear Materials*. Corrosion testing was performed by SPFT method at 90°C and pH 2.5, 5.6, and 7.8 and by electrochemical techniques (Tafel, linear polarization, and impedance spectroscopy) in a variety of potential

2013 Accomplishments Report

solution chemistries (basic, acidic, saline, and inert). Results of corrosion testing by both techniques are reported and compared in the article to be submitted. The average corrosion rate measured by the electrochemical tests was $\sim 1 \mu\text{m}/\text{y}$, or $3 \times 10^{-2} \text{ g}/(\text{m}^2 \cdot \text{d})$ in the units reported for SPFT. The electrochemical measurements of corrosion rate match the initial rates measured in the SPFT reasonably well. Over time the rate gradually drops 2 orders of magnitude to an equilibrium rate of $3 \times 10^{-4} \text{ g}/(\text{m}^2 \cdot \text{d})$ that is achieved between $\sim 60 - 80$ days, as measured by the SPFT method. SPFT tests were performed in diluted forward rate conditions in an oxidizing environment. The waste form performs quite well in oxidizing conditions and will perform even better in reducing environments.

These two articles demonstrate that ϵ -metal is a viable alternative waste form to immobilize UDS and soluble Tc that is very durable and can be produced with available technologies in a strait forward manner. Additionally, epsilon metal can be fabricated using only the waste and removes a large fraction of the noble metals and all the Tc from oxide waste form allowing higher waste loading; be it glass, glass-ceramic, or ceramic by a melt process.

Publication

1. Crum, J. V., D. Strachan, A. Rohatgi, and M. Zumhoff (2013). "Epsilon Metal Waste Form for Immobilization of Noble Metals from Used Nuclear Fuel." *Journal of Nuclear Materials* 441(1-3):103-12.

Zirconium Recycle

E. D. Collins, collinsed@ornl.gov, G. D. Del Cul, B. B. Spencer, R. R. Brunson, and J. A. Johnson

Introduction

Process development studies are being conducted to recover, purify, and reuse the zirconium ($\sim 98.5\%$ by mass) in UNF zirconium alloy cladding. The objective of the zirconium recycle task is to develop the technology to separate and recover purified zirconium from contaminated UNF zirconium alloy cladding, with the cost of the recovery process less than the

current compaction treatment and planned method of disposal of UNF cladding to a geologic repository. The recovered zirconium product must contain radionuclide concentrations that are inconsequential to the use of zirconium in future nuclear applications, recognizing that the recovered zirconium will inherently contain one radioactive isotope, ^{93}Zr , which has a half-life of ~ 1.5 million years and a weak beta radiation emission [Rolsten, 1961]. Alternatively, at a minimum, the recovered zirconium must meet specifications for disposal as low-level waste.

Traditional nuclear fuel recycling processes remove the fuel matrix from the zirconium alloy cladding in which it is sheathed. The cladding ($>98\%$ zirconium) is the second largest mass ($\sim 25\%$ on average, see Figure 151) in the U.S. inventory of LWR UNF [Collins, et al., 2010]. Generation of UNF assemblies in the United States is currently $\sim 2,700$ MT/year ($\sim 2,000$ MT/year of heavy-metal components) and may increase in the next 50 years.

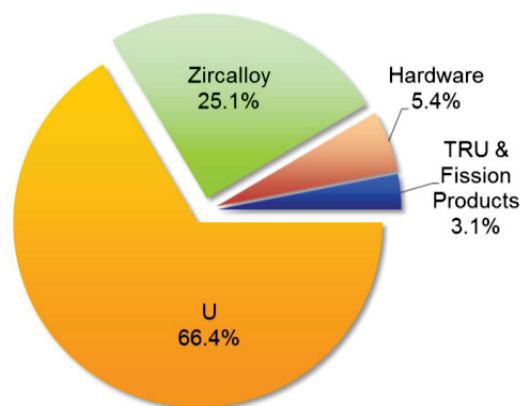


Figure 151. Recycle of zirconium from Zircaloy cladding is a major element of waste reduction.

Recovery and reuse of the zirconium would provide material cost savings that could exceed \$25 M/year. Even greater cost benefit can be obtained by diverting the zirconium from radioactive waste which is destined for emplacement in a geologic repository, since the volume of the compacted metal or grouted cladding waste is equal to or greater than the volume of vitrified high-level waste.

The goal of the recovery/purification processes is to remove chemical and radioactive

Separations and Waste Forms
2013 Accomplishments Report

element impurities from the zirconium contained in UNF zirconium alloy cladding. Radioactive impurities include uranium, transuranium elements, fission products, and activation products other than ^{93}Zr . Chemical impurities that will require removal for reuse in nuclear fuel cladding include alloying elements, such as tin, niobium, iron, nickel, and chromium, and non-metals, such as nitrogen, oxygen, and carbon [Collins, et al., 2012].

Feasibility studies began in FY 2010 using empty cladding hulls that were left after fuel dissolution or after oxidation to a finely divided oxide powder (pretreated). In FY 2012, two industrial teams, AREVA and Shaw-Westinghouse, were contracted by NE to provide technical assistance to the project.

In FY 2013, the NE FCRD Program requested development of a technology development roadmap to guide future work, and this was accomplished (Figure 152) [Collins, et al., 2013].

The first step in the roadmap development was to assess the starting point, that is, the state of the technology at the end of FY 2012, and the end goal for development of an industrial-scale process. The roadmap for process development will continue through process chemistry optimization studies, scale-up of the chlorination reactor design configuration, and product salt condensers. Methods and strategies must be developed to capture any volatile radioactive contaminants that are not easily condensable, such as tritium, from the off-gas stream and to disposition these materials as well as the non-volatile “ash.”

Based on results and observations from tests made in previous feasibility studies, development tests in 2013 and beyond were focused on using (1) chlorine as the chlorinating agent and (2) a process design that includes a chlorination reactor and dual ZrCl_4 product salt condensers. The likely need for a secondary purification step was recognized.

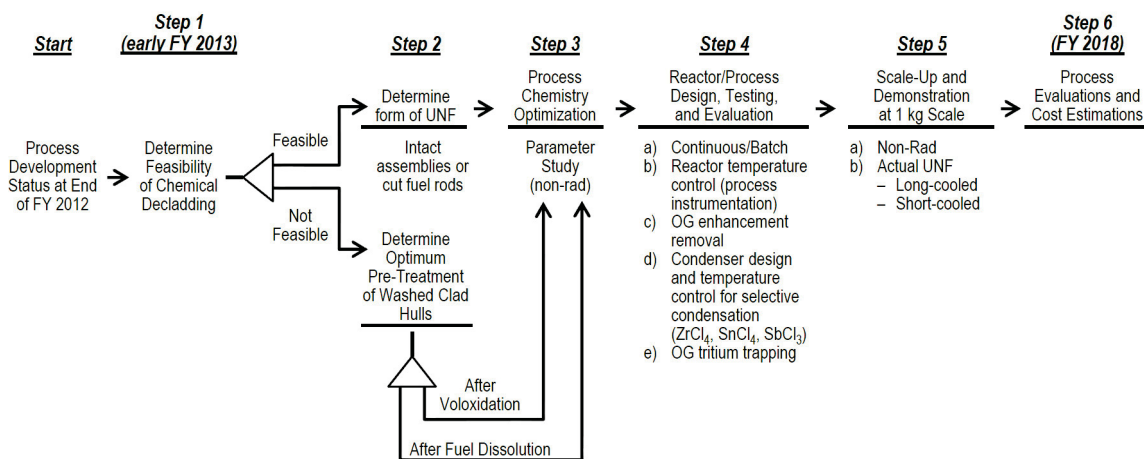


Figure 152. Roadmap for zirconium recovery/purification from UNF cladding.

State of Technology Development

Process development studies were begun in 2010 to assess the potential for recovering and recycling the zirconium contained in UNF zirconium alloy cladding using the iodination process for conversion of the zirconium to the volatile tetraiodide state which could then be volatilized for purification and re-converted to

metal. In 2012, technical assistance was obtained from two industrial expert teams with experience in the manufacture of Zircaloy fuel rod cladding. This was arranged by means of contracts with the industrial assistance program in NE.

The two industrial teams made site visits for observations of the experimental equipment and facilities, and for technical discussions with the

Separations and Waste Forms
2013 Accomplishments Report

experimenters. Both teams provided information describing the industrial-scale processes used to purify zirconium, convert it to zirconium tetrachloride salt, and then convert the salt to purified zirconium metal “sponge.” The purified metal is vacuum arc melted, and alloying agents are added. Finally, metallurgical processes (heating, extruding, rolling, and milling with intermittent annealing steps) are used to fabricate Zircaloy fuel cladding tubes (Figure 153).

Several advantages were identified for changing the process for zirconium recovery and purification from the initially considered iodination to hydrochlorination or chlorination. These advantages included (1) a direct connection to existing industrial processes by producing purified zirconium tetrachloride from the UNF cladding (Figure 152), (2) elimination of the need for the recovery process to include a process step to convert the purified zirconium salt to zirconium metal, and (3) use of gaseous HCl or Cl₂ at atmospheric pressure as reagents, permitting good flow rate control.

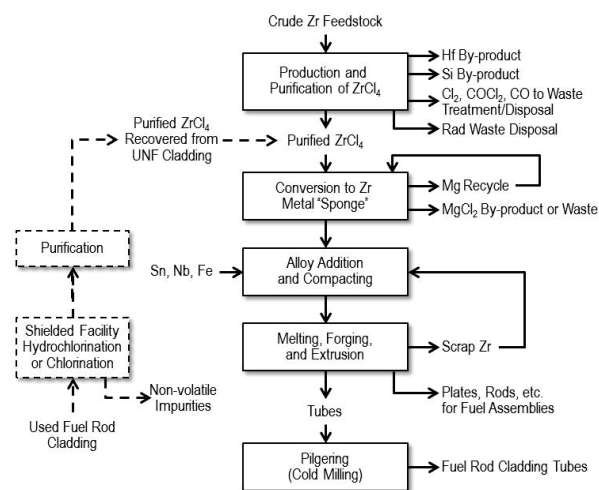
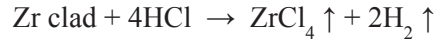
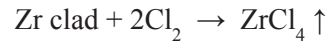


Figure 153. Potential insertion of purified recycle zirconium into the process for zirconium alloy cladding manufacture.

Even though the hydrochlorination process is less exothermic and does not create as many volatile impurity species as the chlorination process, an issue for an industrial application of the hydrochlorination process in a radiochemical operation is the hydrogen generated in the off-gas by the reaction



whereas hydrogen is not generated by reaction with the chlorination process



In addition, the hydrogen generated in the off-gas from the hydrochlorination process complicates the separation and retention of tritium that is released from the UNF cladding. Therefore, the chlorination process was selected for further development for recovery/purification of zirconium from UNF cladding.

Flowsheet Alternatives

Three alternative applications to UNF recycle flowsheets have been identified (Figure 154). These include (1) washed hulls after shearing and removal of the oxide fuel by dissolution in nitric acid as is done in current reprocessing plants; (2) washed hulls after shearing, voloxidation treatment to convert the ceramic UO₂-based fuel pellets to a finely divided U₃O₈- or UO₃-based fuel powder, separation of the fuel powder by screening, and acid washing of the hulls; or (3) chemical decladding of intact UNF assemblies or fuel rods.

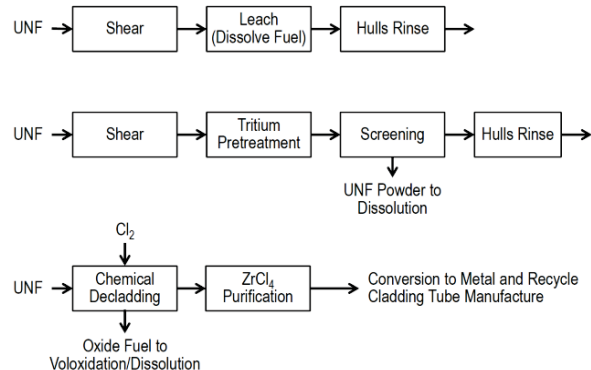


Figure 154. Potential flowsheet applications.

Two potential flowsheet applications begin with empty hulls after either fuel dissolution in nitric acid or electrochemical oxidation pretreatment for tritium management which dislodges the fuel as finely divided oxide powder. Both of these flowsheets were tested in FY 2012 using both non-rad and radioactive UNF and 10-15 gram cladding samples. Both were found to be feasible; however, the oxidation pretreatment caused formation of an excess layer of zirconium

Separations and Waste Forms

2013 Accomplishments Report

oxide on the cladding, and this resulted in an initial resistance to the chlorination reaction.

Chemical decladding is the favored application if it can be shown to be feasible. Even though it is more complicated because of the presence of UNF, this application is favored because it could eliminate or simplify the expensive and mechanically complex fuel shearing operation and equipment, eliminate the potential fire concerns due to the presence of zirconium fines, and simplify the process and equipment for subsequent tritium pretreatment of the fuel matrix.

Therefore, step 1 in the roadmap (Figure 152) was the chemical decladding feasibility tests which were accomplished in FY 2013. These tests used a segment of an actual fuel rod to determine if there is an increase in the amount of radionuclides carried with the ZrCl₄ product stream when oxide fuel is present in the ZrCl₄ formation reactor. As indicated by the test results shown in Figure 155, purified zirconium tetrachloride product salt was obtained. The purity was sufficient to enable the product salt to be handled without shielding.

Decladding Hot Tests	March-April 2013	August 2013		
Reactor → Condenser	Chlorine Down flow	Chlorine Up flow		
Reaction:				
Temperature	356-371°C	400°C		
Time	3.50 hours	10.5 hours ¹		
Unconverted clad	10.2 g	~0		
Converted Zr	5.5 g (35%)	~12 (~100%)		
%/hour	10%/hour	9.5%/hour		
	Bq/g Zr in Cladding			
Gamma Spectroscopy	<u>Fuel and Clad</u>	<u>Zr Cl₄ Product</u>	<u>Zr Cl₄ Product</u>	<u>Final DF</u>
²⁴¹ Am	1.8E+08	1.9E+03	9.4E+04	1.9E+03
²⁴³ Am	3.8E+06	<2.2E+01	<5.1E+01	>7.5E+04
¹³⁷ Cs	2.7E+09	3.7E+02	3.6E+03	7.5E+05
¹²⁵ Sb			4.7E+02	
⁶⁰ Co	< 4E+05	1.9E+01	<5.5E+01	
¹⁵⁴ Eu	1.2E+07	<2.9E+01	<7.4E+01	1.7E+05
¹⁵² Eu		<3.1E+01	6.3E+01	

¹Argon purge every 2 hours for ~ 30-45 min.

Figure 155. Chemical decladding test results, Dresden-1 BWR (24 Gwd/MT, discharge 1975).

Summary

A roadmap for development of the dry chlorination of UNF zirconium cladding to recover and recycle the zirconium was established. The roadmap will provide an efficient path to determining the process feasibility, optimization,

equipment requirements, scale-up capability, and overall performance.

Completion of feasibility testing required testing of a chemical decladding flowsheet option. This was accomplished during 2013. The processes used to volatilize and purify the zirconium during chemical decladding of the fuel, potentially eliminating or simplifying the expensive and mechanically complex fuel shearing operation will be given high priority in future work with used fuel samples with a wide range of burnup and decay aging time. The chemical decladding application would also eliminate potential fire concerns due to zirconium metal fines, and would simplify the process and process equipment for the subsequent component chemical separations of the fuel matrix.

References

- Rolsten, R. F. (1961). *Iodide Metals and Metal Iodides*. New York: John Wiley & Sons, Inc.
- Collins, E. D., G. D. Del Cul, J. E. Rushton, and K. A. Williams (2010). "A Practical Solution to Used Nuclear Fuel Treatment to Enable Sustained Nuclear Energy and Recovery of Vital Materials." ORNL/TM-2010/81. April.
- Collins, E. D., G. D. Del Cul, B. B. Spencer, R. R. Brunson, J.A. Johnson, D. S. Terehkov, and N. V. Emmanuel (2012). "Process Development Studies for Zirconium Recovery/Recycle from Used Nuclear Fuel Cladding." *Proceedings of Atalante 2012 International Conference, Process Chemistry 2012*. Elsevier, Montpellier, France. September.
- Collins, E. D., G. D. Del Cul, B. B. Spencer, R. R. Brunson, and J. A. Johnson (2013). "Establishment of a Roadmap for the Chlorination Process Development for Recovery/Recycle of Zirconium from Used Nuclear Fuel." *Proceedings of Global 2013 International Conference*, American Nuclear Society, Salt Lake City, Utah, October.

Separations and Waste Forms
2013 Accomplishments Report

This page intentionally left blank.

CHAPTER 10
WASTE FORM PERFORMANCE OVER
GEOLOGIC TIMESCALES

CHAPTER 10: WASTE FORM PERFORMANCE OVER GEOLOGIC TIMESCALES

W. Ebert, ebert@anl.gov

Alloy Long-term Corrosion

*W. Ebert, ebert@anl.gov J. Fortner, T. Cruse, ANL;
L. Olson, SRNL; D. Kolman LANL*

Work is in progress to develop a degradation model for steel-based metallic waste forms for immobilize reprocessing wastes that can be produced by directing melting the fuel wastes with either cladding hulls present in the waste stream or added steel. Fuel wastes dissolve in the molten steel and become incorporated into a small number of durable intermetallic and solid solution phases. A small number of phases form that can accommodate a wide range of waste stream compositions, which greatly simplifies performance modeling for long-term system assessments and waste form consistency requirements for waste acceptance. A conceptual degradation model has been developed for calculating the release of radionuclides from alloyed waste forms based on a two-step mechanism of oxidation and dissolution reactions. Experimental methodologies drawing on and combining standard electrochemical and immersion techniques are being coupled with microscopy to evaluate the corrosion behavior of these multi-phase alloys and their alteration products. The results of experimental activities in prior years have provided confidence in both the modeling and experimental approaches, and the main objective of FY 2013 testing was generating data bases needed to determine analytical forms, parameterize, and implement the initial degradation model. Several activities evaluated methods to characterize the development and stability of corrosion layers that passivate the surfaces and greatly attenuate the oxidation rate. These will be key analyses in corrosion tests conducted during FY 2014.

Most of the developmental work is being performed with alloys formulated to represent the immobilization of fuel wastes in the minimum amount of steel required to dissolve the wastes and incorporate the waste elements in durable iron

intermetallic phases. Other alloys have been made to represent a wide range of nominal waste stream compositions alloyed with various amounts of steel (e.g., cladding hulls), study the effects of key elements on the constituent phase assemblage and corrosion behavior, and study the effects of added corrosion inhibitors. In FY 2013, a series of alloys was made to study the effect of the Mo content on the formation of MoFe₂ intermetallic phases, which host Tc, and the overall corrosion resistance of the material. The Tc-bearing alloy EWF-1 having a composition similar to epsilon phases formed in oxide fuel was produced for testing. It represents direct processing of metallic fuel wastes (without steel cladding) and provides a bounding composition for evaluating the applicable range of the alloy waste form degradation model. Scoping tests were conducted with a surrogate made without Tc to verify the experimental methods were appropriate.

Testing Roadmap for Alloy Waste Forms

W. Ebert, ebert@anl.gov, and D. Kolman, LANL

The testing strategy (“roadmap”) being used to evaluate the performance and suitability for long-term isolation of multi-phase alloy waste forms was documented. The waste forms are generated by alloying predominantly metallic waste streams with cladding hulls and added trim metals. Alloy waste forms are currently used to immobilize metallic waste streams from the treatment of spent sodium-bonded fuel and are appropriate for use in future advanced reprocessing operations. The testing approaches and methods provide data required to address information needs pertinent to model development, waste form performance calculations, waste form production control, and acceptance of waste forms for disposal. Information needs related to waste form *performance* address developing a mechanistic understanding of waste form matrix degradation and radionuclide release modes, quantifying the effects of environmental variables on the degradation rate, etc., which are required to

Separations and Waste Forms
2013 Accomplishments Report

develop a mathematical model of waste form corrosion and radionuclide release that can be used in performance assessment calculations. Waste form production needs include understanding how changes in waste stream compositions and processing variables affect waste form performance and how process control limits can be used to ensure that all waste form products are sufficiently and consistently durable. Needs addressing waste form acceptance include measuring the intrinsic characteristics and attributes necessary to demonstrate that each waste package is qualified for disposal.

The strategy is based on the logic and high-level strategy codified in ASTM-International standard practice C1174 *Prediction of the Long-Term Behavior of Materials, Including Waste Forms, Used in Engineered Barrier Systems (EBS) for Geological Disposal of High-Level Radioactive Waste* [ASTM 2013a] and provides specific laboratory test and analytical methods to implement that strategy based on experience gained during the initial development of a metallic waste form for metal wastes from the electrometallurgical treatment of spent sodium-bonded nuclear fuel and from more recent experience with similar alloys formulated for reprocessing waste streams.

The test methods and test parameters were selected based on a conceptual model of the corrosion behavior, which is continuously verified and modified as insights are gained from the test results. The conceptual model for alloy waste form degradation is that the host phase and radionuclides must be oxidized and the resulting oxides dissolved for the radionuclides to be released to solution. Oxidation of the waste form occurs by electrochemical reactions with the solution contacting it. The goal is to link the electrochemical behavior measured under controlled conditions that can be interpreted mechanistically based on scientific theory with the release behaviors of ⁹⁹Tc and other radionuclides that are measured in long-term immersion tests to provide reliable radionuclide source term values for use in performance assessment calculations.

The performance measure for alloy waste forms is release of radionuclides from the waste form and its alteration products into the

environment. The release of radionuclides from the waste form requires oxidation of the host phase incorporating the radionuclide and oxidation of the radionuclide (except in the case of colloidal release) followed by dissolution of the oxide. The oxidized radionuclide may be released into the electrolyte (the solution supporting waste form corrosion) immediately or retained in an oxide layer at the surface, which may dissolve slowly. Waste form corrosion involves both electrochemical and chemical reactions with the electrolyte, and both affect the kinetics of radionuclide release. One or the other process may limit the release rate of a particular radionuclide; both processes are being studied experimentally and represented in the degradation model. The electrochemical behavior is modeled based on underlying electrochemical theory of mixed potential and electrode kinetics, although the complex behavior of the multi-phase waste forms precludes direct use of analytical forms, such as the Butler-Volmer equation for the dependence on the surface potential. The degradation model will require the use of empirical dependencies determined from experimental measurements guided by sound mechanistic understanding. An important aspect of those dependencies is that they will address the release of radionuclides (primarily Tc) into solution, not only the oxidation reactions.

Experiments completed to-date indicate that standard electrochemical techniques can be applied to study alloy waste form corrosion and identify oxidation mechanisms, the kinetics of contributing or competing processes, and the evolution of the corrosion behavior over time. The most important effect of time is the generation of passivating layers on the specimen surface that significantly decrease the corrosion rate. Standard electrochemical techniques have been modified to study chemical effects in parallel with the electrochemical effects, most importantly the release of ⁹⁹Tc and other radionuclides into solution. These methods are also coupled with surface analyses, such as those with SEM, to correlate changes in electrochemical behavior, solution concentrations, and the surface structure as the reactions proceed.

Scoping tests have demonstrated the importance of conducting electrochemical

Separations and Waste Forms
2013 Accomplishments Report

measurements with waste materials for long durations to evaluate the effects of evolving surface corrosion layers until steady state behavior is observed, which may require several weeks to months. Other experiments are needed to demonstrate the long-term stability of the layers and passivating effects, with the goal of linking the electrochemical behavior measured under controlled conditions that can be interpreted mechanistically based on underlying scientific theory with the ⁹⁹Tc release behavior that is measured in long-term immersion tests. Discussions of key laboratory experiments are discussed in the following sections.

References

1. Anderko, A., P. McKenzie, and R. D. Young. (2001). "Computation of Rates of General Corrosion Using Electrochemical and Thermodynamic Models." *Corrosion* 57 (3), 202-213.
2. ASTM (2013a). *Annual Book of ASTM Standards*, Vol 12.01. West Conshohocken, PA: American Society for Testing and Materials.

Publication

1. Ebert, W. L., and D. Kolman (2013). "Alloy Waste Form Testing Strategy Roadmap." FCRD-SWF-2013-000226.

Corrosion Experiments with RAW-1(Tc)

J. Fortner and W. Ebert, ANL

Corrosion experiments at 200°C with alloy RAW-1(Tc) that had been started in FY 2012 to provide insight into the Tc release kinetics from alloy waste forms in an oxidizing environment were completed. Several small samples of the alloy were immersed in demineralized water or suspended in humid air and the solutions were completely replaced every 2 or 3 weeks and the tests continued. The recovered solutions were analyzed to track the release of Tc and other components over time and evaluate the kinetics. Figure 156 shows the solution results for the immersion tests in terms of the cumulative fractional mass loss. The releases of Tc, Cr, and Mo in both the humid air and immersion tests slowed with time through about 100 days and then continued at nearly the same constant rate through

termination of the test after 313 days. The fraction release rate of Tc is 5×10^{-7} g Tc/g alloy is about 40X lower than the initial rate calculated from the first sampling.

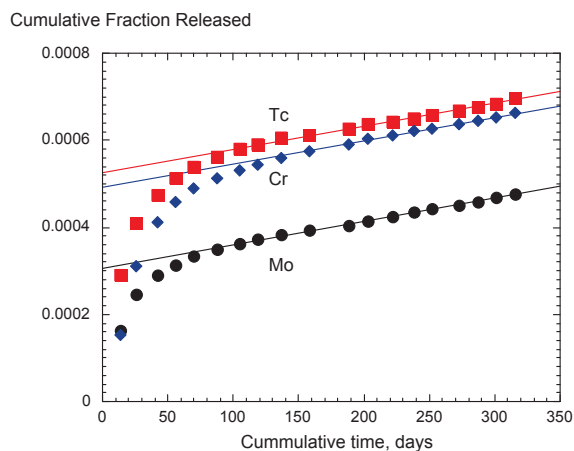


Figure 156. Results of solution exchange tests with RAW-1 under immersion conditions.

One of the specimens was removed from the test in humid air after 119 days for surface analysis; the test continued with the remaining samples. SEM examination of the cross sectioned specimen showed a thin layer $\sim 0.5 \mu\text{m}$ of predominantly iron oxide to have formed during the first 119 days. XANES identifies the oxidation state of the scattering atom and can reveal crystalline symmetry. Analysis of the iron K-absorption edge showed only small amounts of Fe(II) oxide at the surface. The Cr content of the layer was not determined, but the solution results show nearly stoichiometric release of Tc and Cr. More extensive corrosion in on-going or future tests may be required to measure the distribution of Cr in the surface layers, which is expected to be a key contributor to passivation. Other XANES analyses indicated the layer was depleted of Tc but contained oxidized Mo. This is consistent with the solution results showing a smaller fraction of the Mo inventory was released to solution.

Figure 157 shows the Fourier transform moduli (pseudo-radial distribution functions) determined from EXAFS analyses performed at grazing incidence (red curve) sensitive to the near-surface structure and normal incidence (green curve) sensitive to the underlying bulk. The presence of Mo-O and Mo-Mo bonds at the surface are evident. These data are consistent with

Separations and Waste Forms
2013 Accomplishments Report

a very thin (< 6 micrometer) layer of molybdenum oxide overlaying metallic molybdenum.

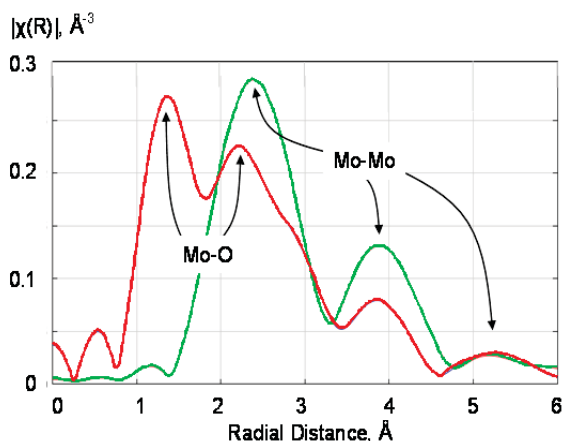


Figure 157. Pseudo-radial distribution function from EXAFS analysis of Mo K absorption edge for surface (red) and bulk (green) material.

Model Development and Corrosion Experiments with RAW-1(Tc)

W. Ebert and T. Cruse, and J. Fortner, ANL

Various experimental methods are being used to quantify the effects of environmental conditions on the performance of alloyed waste forms to support development and application of a waste form degradation model. The objective of the model is to provide source terms for radionuclides that are immobilized in alloyed waste forms for use in performance models for engineered disposal systems. The degradation model that is being developed is based on an oxidative dissolution mechanism in which metallic elements must first be oxidized to soluble oxidation states and then those oxides dissolve to release ions (including radionuclides) into solution in a transportable state. The oxidation step, the dissolution step, and the transport step can all limit the release of radionuclides, and all are sensitive to many environmental variables. The key variables for the oxidation step are the potential at the waste form surface, which is established by the environmental redox conditions (i.e., the Eh), and the chloride concentration (for steel-based alloys); the key variables for the dissolution step are pH, Eh, and temperature; the key variables for transport are groundwater advection, solubility, and sorption. The modeling and experimental work underway in the waste form behavior activities is focused on

the oxidation and dissolution steps, and on the release behaviors of Tc and U. Transport is being addressed in modeling and simulation activities within the S&WF and the Used Fuel Disposition Campaigns, and the results of those activities are being brought to bear in the modeling effort.

The alloyed waste forms of interest are multi-phase materials with four or five constituent phases. The approach taken in the degradation model is to represent waste form corrosion and radionuclide release as the sum of the contributions of the constituent phases. The current density that is measured in electrochemical tests is related to the sum of the corrosion rates of the constituent phases, where the current for each phase is related to its corrosion rate through Faraday's Law. Although it was originally planned that the dependence of the current density on the potential imposed at the alloy surface by the solution would be modeled using the Butler-Volmer equation using modeling methods developed for the active corrosion of stainless steels, the results of recent tests indicate this is not appropriate for these multi-phase alloys. Testing completed to date indicates the importance of passivation on the oxidation rate, which will likely dominate the degradation model. Many of the environmental effects on active corrosion become negligible upon passivation. An alternative approach focused on long-term stability of passivation effects is needed. The approach being pursued is to utilize electrochemical theory to provide the scientific basis for modeling the electrochemical effects of environmental variables (primarily the temperature, Eh, pH, and Cl⁻ concentration), but use empirical expressions to describe the coupling of oxidation reactions with the chemical effects of oxide dissolution under passivated conditions to calculate the fractional release rates of radionuclides. The degradation model is being developed as the product of terms for bare surface dependencies, an attenuation term representing the passivation layer effect measured at steady state, and another attenuation term representing the dissolution kinetics of the oxide layer. It is anticipated that the degradation model will have the generic form

$$FR(RN) = B(E, T, pH, Cl^-) \times P(t, Cl^-) \times D(RN)$$

Separations and Waste Forms
2013 Accomplishments Report

where the fractional release of a radionuclide RN depends on the effects of the surface potential E , temperature T , pH, dissolved chloride concentration Cl^- , and time t on the bare surface corrosion properties function $B(E, T, pH, Cl^-)$, passivation attenuation function $P(t, Cl^-)$, and oxide layer dissolution properties function $D(RN)$. The actual variables and functional dependencies remain to be determined from on-going experiments. The radionuclide release from the electrochemical model can be calibrated using the radionuclide release behavior measured in the simple immersion tests. In this way, the effects of the environmental variables on the oxidation kinetics and passivation measured in separate experiments can be taken into account analytically and the dissolution behavior empirically to provide the release rates of the radionuclides. Some dependencies will likely be taken into account within the set of lumped parameters and not quantified explicitly in the model, such as those for oxide layer dissolution on temperature and solution composition. Those effects are included in the B function determined for the conditions under which the radionuclide release (oxide dissolution) was measured.

The bare surface term remains important because it is expected to represent some effects of the waste form composition. The bare surface corrosion properties refer to the behavior of a prepared surface (polished and dried) in the electrolyte before appreciable alteration of the surface occurs. Some corrosion will inevitably occur when the alloy is first contacted by the solution. The surface may be electrochemically “cleaned” by imposing a cathodic potential prior to making a measurement or several measurements may be made sequentially. Sequential measurements are usually made in the order of increasing aggressiveness to minimize effects of prior measurements. The results of several hundred electrochemical experiments conducted at ANL to characterize the bare surface behavior alloys RAW-1 and RAW-2 have been compiled and entered into the Document Management System for the FCRD project as initial entries for the data base being assembled to support the degradation model. These include tests in the set of electrolyte solutions formulated to span the range of environmental pH and Eh

conditions in fresh groundwaters and brines. Electrochemical measurements include potentiodynamic scans, cyclic voltammetry, potentiodynamic Tafel scans, linear polarization resistance measurements, potentiostatic hold experiments, and electrochemical impedance spectroscopy measurements.

As an example, the results of potentiodynamic sweep measurements conducted with electrodes made from RAW-1(Tc) and RAW-2(UTc) conducted in various electrolytes under argon purge to provide anoxic conditions and equilibrated with air to provide oxidizing conditions are shown in Figure 158. The corrosion potentials (the potentials at which the net current density drops to zero) fall within a narrow range in all conditions (vertical dashed lines are drawn at 0 V vs. saturated calomel electrode [SCE] to aid visual comparisons) and the estimated alloy corrosion currents (the anodic current estimated at the corrosion potential) are similar; horizontal dashed lines are drawn at about 6×10^{-7} A cm^{-2} . Differences seen in the top and bottom plots reflect the use of different electrodes for each series of tests, and are thought to be due to different relative areas of constituent phases that are exposed. Experiments are being conducted using several electrodes made from the same ingot of alloy to take this variance into account.

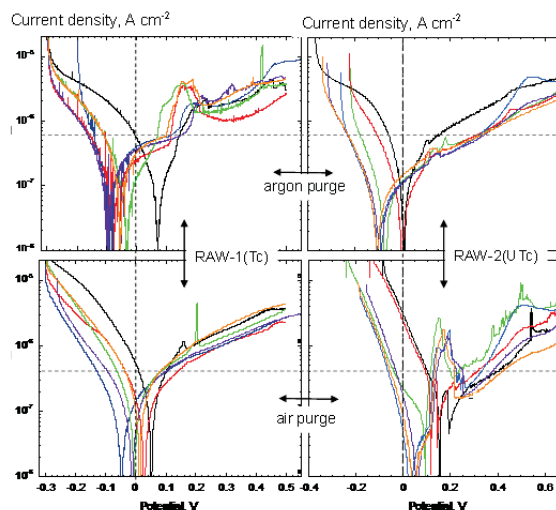


Figure 158. Comparison of potentiodynamic responses of (left) RAW-1(Tc) and (right) RAW-2(UTc) under conditions of (top) argon purge and (bottom) air in standard solutions: acidic (black), acid brine (red), neutral (blue), brine (green), alkaline (violet), and alkaline brine (orange).

Separations and Waste Forms
2013 Accomplishments Report

In addition to the standard solutions shown above, tests were conducted in solutions with added H_2O_2 to represent radiolysis products. Figure 159 shows the results of potentiodynamic sweep measurements for the surrogate EWF alloy (Mo-Ru-Pd-Rh-Re) in a 1 mmolal NaCl solution with various amounts of added H_2O_2 . The general shape of the curve and corrosion potentials are similar to those measured in tests with RAW-1 and RAW-2, but the corrosion currents are about 10X higher. Although the bare surface behavior appears to be similar, passivation of the EWF materials is not expected due to the absence of Cr, although Mo and dissolved Tc may attenuate the corrosion rate somewhat. Tests with Tc-bearing EWF material are planned for FY 2014 to measure the corrosion behavior over longer durations and determine if active or passive corrosion behavior is controls the release of Tc.

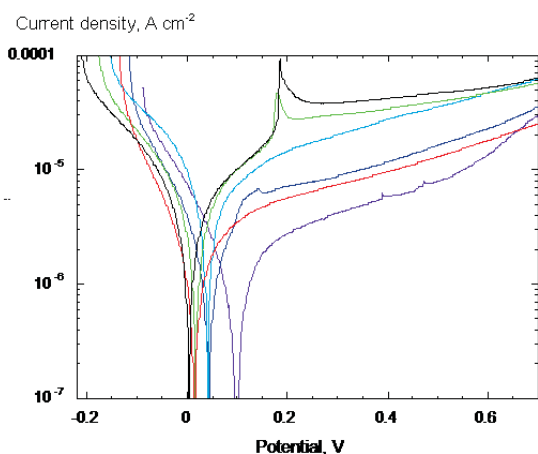


Figure 159. Comparison of potentiodynamic responses of surrogate EWF in 0.1 mmolal NaCl solutions spiked with: 1×10^{-2} M H_2O_2 , (violet), 1×10^{-4} M H_2O_2 , (blue), 1×10^{-2} M H_2O_2 , (aqua), 1×10^{-6} M H_2O_2 , (green), 1×10^{-8} M H_2O_2 , (red), and without H_2O_2 , (black).

Potentiostatic hold and open circuit experiments were performed to measure the release of Tc, U, and other constituents in the alloys to solution as they corrode under various conditions. These experiments provide correlations between the oxidation reaction measured electrochemically and dissolution of the oxidized species measured chemically. In addition, microscopic characterization of the electrode surface before and after test intervals provide chemical and physical changes to the surface that may indicate which phase(s) corrode

during the experiment and what alteration phases form. By conducting potentiostatic experiments over a range of potentials and in various electrolyte solutions, researchers are mapping out the corrosion behavior over the range of possible environmental conditions in disposal systems of interest. Conducting tests with several well-characterized alloys provide a range of relative surface areas of the constituent phases and may provide a waste form composition term that can be included in the degradation model.

The development of corrosion layers (films) that can passivate the alloys is being studied in detail using several methods. Figure 160 shows the results of scanning electrochemical spectroscopy with RAW-1 reacted in 0.1 mmolal H_2SO_4 . In this experiment (which was performed at Western University, Ontario, Canada), the probe was rastered across the surface to measure the corrosion current at different locations.

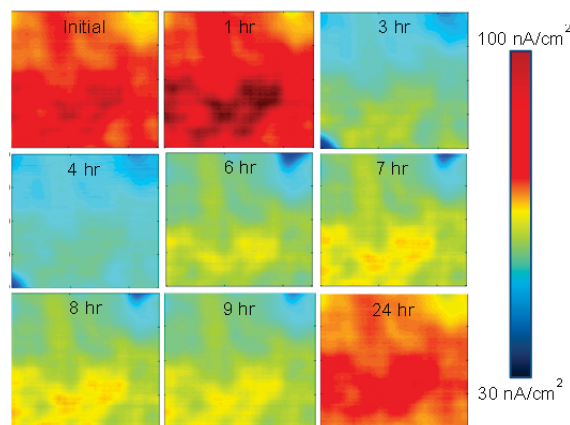


Figure 160. Results of SECM of RAW-1 surface during corrosion in 0.1 mmolal H_2SO_4 .

Images are shown for an area of 1 mm^2 collected soon after the sample was immersed (initial) and after several reaction times. The color of the pixel represents the corrosion current, and regions with different color indicate different constituent phases in the waste form. Note that the currents show the underlying phase distribution in most images. (A corresponding electron image of the surface was not taken.) The key point is that the corrosion currents at all locations decrease between 1 and 4 hours of corrosion, but increase to near the initially-measured values by 24 hours. This is interpreted to be due to the instability of the passivating layers that form over each phase

Separations and Waste Forms
2013 Accomplishments Report

during the first 4 hours in the acidic solution. However, the region having the highest current initially (most obvious after 1 hour) is evident at 8 hours but not seen after 24 hours. It is possible that the most reactive phase seen initially had dissolved within 24 hours.

References

1. Anderko, A., P. McKenzie, and R. D. Young (2001). "Computation of Rates of General Corrosion Using Electrochemical and Thermodynamic Models." *Corrosion* 57 (3), 202-213.

Publications

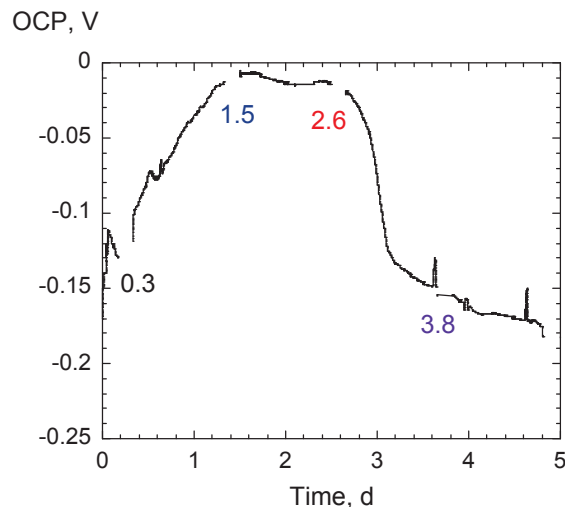
1. Ebert, W. L., and T.A. Cruse (2013). "Data Base for Electrochemical Corrosion Measurements." FCRD-SWF-2013-000306.
2. Fortner, J. A., A. J. Kropf, and W. L. Ebert (2013). "Characteristics of Metal Waste Forms Containing Technetium and Uranium." *Proceedings: Global 2013: International Nuclear Fuel Cycle Conference*, Salt Lake City, UT, September 29–October 3.

Electrochemical Impedance Spectroscopy of Alloy Waste Form

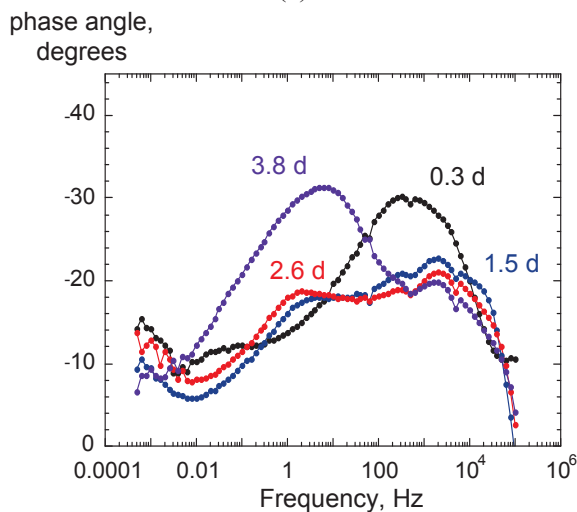
D. Kolman, kolman@lanl.gov, LANL

Electrochemical experiments were conducted with RAW-2(UTc) to independently assess the applicability of various methods for characterizing the corrosion behavior for later comparison with results obtained at other participating laboratories. This hands-on experience with one of the multi-phase alloy materials being used in the testing activities was utilized to provide critical review of the approach developed at ANL with the expectation of reaching technical consensus regarding the methodologies followed for electrochemical testing and interpretation of the results. Electrochemical impedance spectroscopy (EIS) measurements provide the best insights into the passivation of the alloys as they corrode and quantify key parameters in the degradation model. The results of a key experiment are summarized in Figure 161. An electrode made with a piece of RAW-2(UTc) material supplied by ANL from the same source ingot as samples being studied at ANL was corroded in 0.1 mmolal H_2SO_4 solution

exposed to air. The sample was allowed to corrode under open circuit conditions, interrupted to perform EIS, then continued corroding without an imposed potential.



(a)



(b)

Figure 161. (a) Evolution of open circuit potential as RAW-2 corrodes in 1 mmolal H_2SO_4 and (b) EIS measurements made after various reaction times.

The value of the OCP plotted in Figure 161a reflects the potential at which the anodic and cathodic reactions balance to zero net current. Changes in the OCP over time indicate changes in one or more of these reactions as the alloy corrodes, most likely due to changes in the surface. The OCP increases from that of the clean surface during the first day, remains nearly constant for about three days, then decreases to the

Separations and Waste Forms
2013 Accomplishments Report

clean surface potential and lower. In the EIS experiment, sinusoidal voltages with different frequencies are imposed on the specimen and the current is measured. The frequency dependence of differences in the amplitudes and phases of the voltage and current waves correspond to impedances provided by the solid/solution interface and any corrosion layers. These can be described in terms of resistance and capacitance of electrical circuits. In fact, the system can be modeled as an electronic circuit to analyze contributions of various physical features; most importantly, the passivation layer. The phase angles in the EIS spectra collected after the sample corroded for 0.3, 1.5, 2.6, and 3.8 days are plotted for comparison in Figure 161b. These provide the most visible indication of changes occurring as the specimen corrodes. The black, blue, red, and violet curves were measured after 0.3, 1.5, 2.6, and 3.8 days, respectively. The black curve for 0.3 days has a dominant peak at about 1000 Hz and the violet curve for 3.8 days has a dominant peak at about 1 Hz.

Electrochemical impedance measurements are expected to provide key information for the developing the passivation attenuation term in the alloy waste form degradation model. Analysis of the experimental response using circuit analysis is well-established and has been summarized in the testing strategy roadmap report. The coupling of solution analyses to quantify released radionuclides and microscopic surface analyses to characterize the chemical and physical nature of alteration layers that form during corrosion to passivate the surface and mitigate corrosion will provide a description of alloy waste form degradation with a firm scientific basis.

Publication

1. Ebert, W. L., and D. Kolman (2013). "Alloy Waste Form Testing Strategy Roadmap." FCRD-SWF-2013-000226.

Effects of Waste Stream Composition on Phases Formed in Alloy Waste Forms

L. Olson, luke.olson@srnl.doe.gov, SRNL

Alloys were produced with 1.8, 5.2, 6.7, 8.3, and 9.8 at% Mo as variations of the RAW-3 formulation (which has 1.8 at% Mo) to evaluate the point at which the Mo content became sufficient to form measurable quantities of the MoFe₂ phase, which is known to sequester Tc-99, and measure the effects of the phase(s) on the morphological and corrosion properties of the alloy. Other alloys were made with additional Ni and Ti to represent cladding coated to control chemical interactions and with lower concentrations of Pd, Rh, and Ru than used in RAW-3 to evaluate the effect on the U distribution. The alloys were made in a tube furnace by heating at 1650°C for 1.5 hours and annealing at 1100°C for 1.5 hours. Samples were prepared for analysis using standard metallography techniques.

The chemical compositions and areal fractions of the constituent phases were measured using SEM/EDXS. Figure 162 shows the microstructure of the alloy with 6.7% total Mo showing many MoFe₂ phase domains distributed in steel matrix along with ZrFe₂ and ZrFe₂ inclusions. Two Mo-containing phases could be distinguished by contrast in with the SEM and by composition with EDXS, which are given in Table 27. The lighter phase occurs in the interiors of large domains of the darker phase. In each alloy, the darker phases had slightly lower Mo contents than the lighter phases, and higher Fe, Cr, and Zr contents. The compositions of both phases are essentially the same in all alloys, with only small differences in the concentrations of minor components. The total Mo content affects the amount of MoFe₂ phases, but not the compositions. Neither phase was detected in the alloy made with 1.8 at% Mo, and only a trace amount of the darker phase was detectable in the alloy made with 5.2 at% Mo. The areal fractions of the MoFe₂ phases (total) were about 0, 2, 34, 45, and 48% for the alloys with 1.8, 5.2, 6.7, 8.3, and 9.8 at% total Mo, respectively.

Separations and Waste Forms
2013 Accomplishments Report

Table 27. Compositions of MoFe₂ Phases in Alloys, in at%

Total Mo,at%	Fe	Cr	Ni	Mn	Zr	Mo	Ru	Rh	Pd	Re	U
Darker Phase											
1.8	Phase not detected										
5.2	63	13	0.3	0.4	0.5	19	1.6	0.6	0.2	2.3	0.1
6.7	63	14	0.2	0.4	0.2	17	1.4	0.6	0.8	1.4	0.2
8.3	63	14	0.2	0.4	0.7	18	1.3	0.5	0.4	1.3	0.2
9.8	64	13	0.3	0.4	0.6	18	1.2	0.6	0.3	1.2	0.1
Lighter Phase											
1.8	Phase not detected										
5.2	Phase not detected										
6.7	47	10	0.6	0.4	2.5	24	1.5	2.8	6.4	1.6	2.7
8.3	56	11	0.2	0.4	2.0	27	1.3	0.2	0.2	1.9	0.2
9.8	56	11	0.3	0.4	1.3	27	1.2	0.2	0.2	1.7	0.3

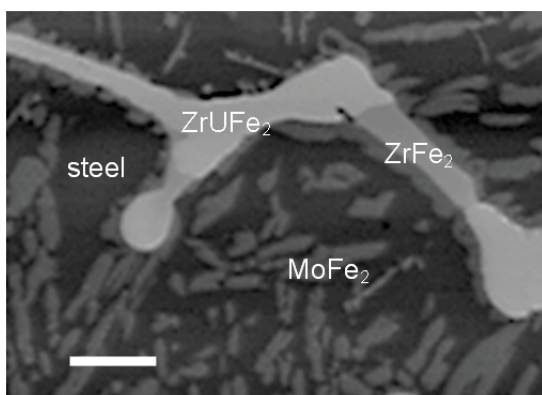


Figure 162. SEM photomicrograph of alloy made with 6.7 at% Mo showing MoFe₂ phases distributed in steel matrix. (scale bar = 20 μm)

Electrochemical tests were performed on coupons of the alloys with 1.8 at% Mo, which is the base RAW-3(URE) composition, and the 6.7 at% Mo in the reference alkaline brine solution. As shown by the cyclic potentiodynamic polarization scans in Figure 163, the alloys behaved similarly under anodic polarization, with near identical corrosion currents and corrosion potentials (about -0.05 V vs. SCE).

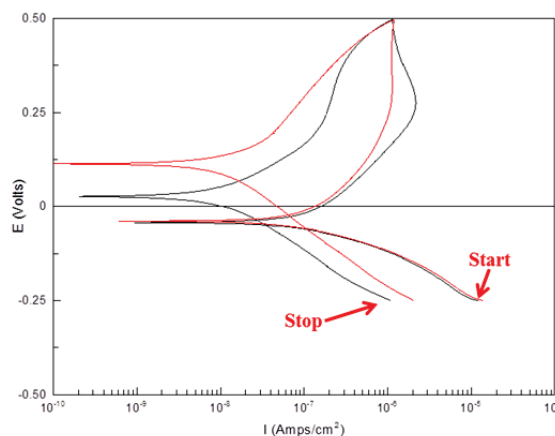


Figure 163. Cyclic potentiodynamic polarization scans of alloys with 1.8 at% Mo (red) and with 6.7 at% Mo (black).

The polarization behavior differed with further anodic polarization between about 0 and 0.50 V and during the return polarization. After passivation at 0.50 V vs. SCE, the alloy with 1.8 at% Mo had a more electropositive corrosion potential (about 0.10 V) than the alloy 6.7 at% Mo (about 0.02 V), indicating a more highly passivated surface. The corrosion currents were reduced by about an order of magnitude for both alloys (from about 2×10^{-7} A cm⁻² to about 2×10^{-8} A cm⁻²), and the corrosion potentials were both more electropositive in the initial (bare surface) potentials signifying some passivation did occur. More thorough and quantitative analyses

Separations and Waste Forms
2013 Accomplishments Report

are planned for FY 2014, including measurements of the dissolved U and Re concentrations.

An alloy was made to evaluate the effects of higher Ni and Ti concentrations on the waste form; fuel cladding may be coated with Ni and Ti to control chemical interactions. About 2 at% each Ni and Ti were added to the RAW-3(URe) formulation to simulate waste forms made with coated cladding. About twice as much Ti entered the $ZrFe_2$ phase regions as entered the ferrite steel phase. The majority of the Ni entered the $ZrFe_2$ phase. No other differences from the additional Ni or Ti were observed in comparison to the baseline RAW-3(URe) waste formulation.

Current waste forms being made with EBR-II treatment wastes have significantly lower precious metal contents than many of the formulations currently being studied. Because phases containing Pd, Rh, and Ru also incorporate significant amounts of U, a waste form was made with HT9 and a simulated waste stream with no precious metals to evaluate how this affects the disposition of U. When Pd, Rh, and Ru are completely eliminated from the composition, the resultant alloy is similar to that expected for a low waste loading metallic fast reactor fuel made with HT9 cladding with no additional Ni. With the low Ni content of the HT9 (compared with the Type 316L stainless steel in EBR-II waste forms), the $ZrFe_2$ composition range has several sub-compositions having distinct phase boundaries, as shown in Figure 164. Similar to the distributions in alloys made with Type 316L stainless steel, these phases can be distinguished as having high U contents (Zr+U about 10 at% for 1 and 2) and low U contents (Zr+U about 3.3 at% for 3 and 4). The low Pd content in the waste stream decreases the amount of $ZrPd_2$ that forms, which is another important host phase for U. The importance of these results is that essentially the same constituent phase hosts U over a very wide range of U contents in the waste streams.

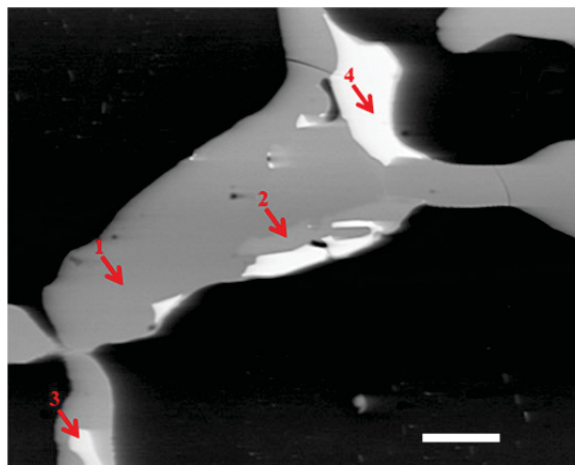


Figure 164. Alloy made with HT9 steel and simulated waste having a low Pd content showing four compositionally distinct $ZrFe_2$ phases. (scale bar = 20 μm)

Publications

1. Olson, L. (2013). "Formulation of Test Plan for Study of Mo Content in RAW-3 for FY 2013." FCRD-SWF-2013-000060.
2. Olson, L. (2013). "Effect on Morphology and Corrosion Behavior of Mo Content Variation in RAW-3 Alloys." FCRD-SWF-2013-000355.

Glass Long-term Corrosion

J. Ryan, joe.ryan@pnnl.gov, S. Kerisit, D. Strachan, and J. Neeway, PNNL; W. Ebert and J. Fortner, ANL; C. Crawford and C. Jantzen, SRNL

Borosilicate glass is being used to immobilize HLW in the United States and internationally and is the most mature technology for reprocessing of commercial UNF. The release of radionuclides from borosilicate glass waste forms into the environment requires the initial degradation of the glass structure during corrosion in groundwater. Subsequent transport is determined by environmental factors including advection, sorption, precipitation, colloid formation, size exclusion, etc. Transport is being addressed in the Used Fuel Disposition campaign. The source term for radionuclide release being addressed in the S&WF campaign is the product of the radionuclide inventory, the glass dissolution rate, and the glass surface area. The objective of activities in this control account is to develop the

Separations and Waste Forms
2013 Accomplishments Report

scientific data base and mechanistic understanding of glass degradation necessary to reach an international consensus on how to model the corrosion behaviors of glass waste forms over geologic time scales and calculate radionuclide source terms for a variety of relevant disposal environments.

Waste glass corrosion is conveniently illustrated by the simplified reaction progress diagram shown in Figure 165, where an overall progress variable is used to represent several parallel, sequential, and coupled reactions between glass and groundwater that result in the glass being replaced by an assemblage of more stable secondary phases in a solution that is saturated with respect to those phases.

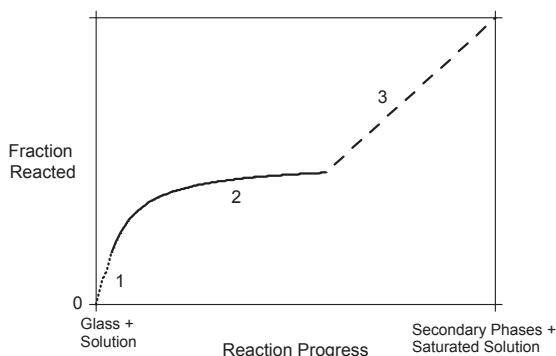


Figure 165. Schematic reaction progress plot for glass corrosion.

Corrosion can be described as occurring in three stages in which different reactions or sets of reactions dominate the reaction progress and the kinetics. Stage 1 represents glass dissolving into a dilute solution through hydrolysis and ion exchange reactions with no transport or reaction affinity limitations. Stage 2 represents the combined slowing effects of a decreasing reaction affinity due to increasing solution concentrations and mass transport limitations imposed by developing surface alteration layers, which can result in very low residual rates. Stage 3 represents an increase in the reaction rate that is observed in some systems and is thought to be due to positive feedback accompanying the precipitation of some secondary phases. The glass dissolution kinetics is related to the slope of the curve (not always linearly), which changes significantly as the reaction progresses in the different stages. The activities in this control account address the

processes, kinetics, and couplings that contribute to and control corrosion within the different stages and transitions between stages. The corrosion stages addressed by work in each activity are identified in the summaries.

A detailed integrated plan for understanding these and other aspects of long-term glass behavior and developing international consensus on the glass dissolution rate law was developed in fiscal year 2011 and subjected to an independent peer review [Ryan, et al., 2012]. That plan includes experiments designed to address particular aspects of glass corrosion with modeling efforts performed at the atomic and continuum scales to help interpret the experiments, apply the results to the degradation model, and interface the degradation model with disposal system performance assessment calculations. The initial results of those collaborations have been documented in review papers (Gin et al. 2013, Vienna et al. 2013). Two major issues addressed in FY 2013 are (1) quantifying the relative roles of chemical reaction affinity and mass transport control on the glass degradation under various and changing conditions (primarily in Stages 1 and 2) and (2) identifying the mechanism by which the precipitation of secondary phases couples with the glass dissolution rate and quantifying the effect (transitioning from Stage 2 to Stage 3 and dissolution in Stage 3). Work is in progress to quantify these effects within a rate law that can be used to calculate glass degradation and radionuclide release rates over geologic times. There is general agreement that the rate law must include terms representing the effects of glass composition, temperature, pH, ionic strength, mass transport through surface alteration layers, and feedback effects from the solution. The primary tasks that remain are determining analytical forms to quantify the effects of mass transport and solution feedback over the relevant range of disposal conditions and as the contributions of different processes change as corrosion progresses. Uncertainties in quantifying mass transport stem from the effect of the solution composition on the effectiveness of the transport barrier and identification of the physical layer providing the transport resistance, and from changes in both as corrosion proceeds. Uncertainties in quantifying the solution effects

Separations and Waste Forms
2013 Accomplishments Report

include the analytical forms of the reaction affinity term that occur in concentrated solutions (negative feedback) and the presence of secondary phases (positive feedback). Experimental and modeling activities are in progress to address these factors in the glass dissolution rate law.

The research performed to understand and quantify the glass corrosion is jointly sponsored by DOE-EM and DOE-NE. Most of the activities in this study benefit from collaborations with NEUP-funded research being conducted at several universities in the United States, jointly sponsored research by DOE-EM, and with research being conducted in France (CEA, Subatech, AREVA), Belgium (SCK-CEN), U.K. (NNL, Amec, Sheffield), Japan (Kyushu University, JAEA), and Germany (University of Bonn). Additional collaborations are being initiated with researchers in other countries (Russia, India, Switzerland). These collaborations are yielding scientific advances more quickly and fostering consensus in the scientific understanding of waste glass corrosion and the development of an effective mechanistic rate law. The work completed in FY 2013 addressed processes contributing to potential mechanisms and enabled development of a holistic model that accounts for observed glass degradation behavior. Summary descriptions of experimental and modeling results follow in the same order as the reaction stages they address.

References

1. Gin, S., A. Abdelouas, L. J. Criscenti, W. L. Ebert, K. Ferrand, T. Geisler, Harrison, M. T. Y. Inagaki, S. Mitsui, K. T. Mueller, J. C. Marra, C. G. Pantano, E. M. Pierce, J. V. Ryan, J. M. Schofield, C. I. Steefel, and J. D. Vienna (2013). "An international initiative on Long-Term Behavior of High-Level Nuclear Waste Glass." *Materials Today* 16, 243-248`.
2. Ryan, J. V., W. L. Ebert, J. P. Icenhower, D. M. Strachan, C. I. Steefel, L. J. Criscenti, I. C. Bourg, R. E. Williford, K. A. Murphy, E. M. Pierce, C. J. Jantzen, D. K. Shuy, G. A. Waychunas, J. C. Marra, J. D. Vienna, and P. Zapol (2011). "Technical Program Plan for the International Technical Evaluation of Alteration Mechanism (I-Team)." PNNL-21031.
3. Vienna, J. D., S. Gin, J. V. Ryan, and Y. Inagaki (2013). "Current Understanding and Remaining Challenges in Modeling Long-Term Degradation of Borosilicate Nuclear Waste Glasses." *International Journal of Applied Glass Science*, accepted for publication.

Small-Angle X-ray Scattering

J. Fortner, ANL

Several experiments conducted previously with SON-68 and Advanced Fuel Cycle Initiative (AFCI) glass targeted the early interactions between glass and water (Stage 1), when some components are preferentially removed from the glass through a combined hydration/ion-exchange process that removes highly-soluble components such as alkali metals in exchange with water. These reactions open percolation pathways through which water can enter the glass. Little is known about the structural changes that occur in the surface of the glass during this process, as it is difficult to probe with electron microscopy. After extensive hydration and ion exchange, alteration layers may form by condensation reactions involving these relict glass components (Stage 2 after transition from Stage 1). Several reacted monolithic specimens of SON-68 and AFCI glass were analyzed using small-angle x-ray scattering (SAXS) to probe changes in short- and medium-range structure during the initial stages of corrosion. A pinhole SAXS camera at the Advanced Photon Source Sector 15ID was used to examine qualitative changes in glass structure, observing differences among different glasses and as a single type of glass reacts with water. Figure 166 shows a comparison of the SAXS responses for the 20-component AFCI glass and the 6-component International Simple Glass. The more complex AFCI glass exhibits higher intensities at all wavenumbers, which indicates a more ordered distribution of constituents within the glass structure.

Separations and Waste Forms
2013 Accomplishments Report

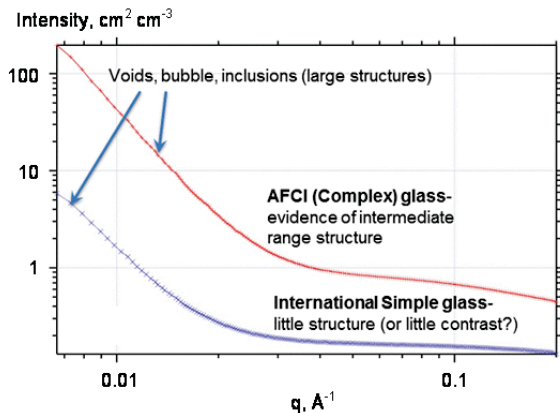


Figure 166. Small angle X-ray scattering from AFCI glass and International Simple Glass.

Figure 167 shows the results of SAXS measurements with SON 68 glass reacted in static ASTM C1220 tests at pH 10 or pH 11 for various durations. The measured degree of structure increases with the extent of corrosion, as measured by the B release. (The values on the plot give NL(B) in gm^{-2} ; higher values indicate greater extents of corrosion.) This is interpreted to represent the development of an alkali metal and B-depleted surface alteration layer having more intermediate range structure than the underlying glass. The red curve shows the spectrum for AFCI glass reacted for 77 days in an ASTM C1308 solution exchange test performed in a pH 8.5 solution at 90°C with a 7-day exchange interval.

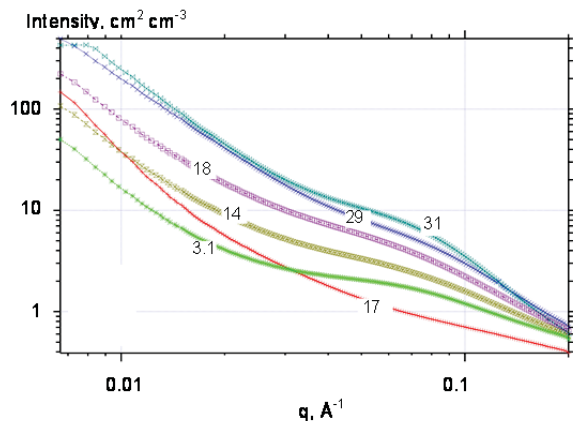


Figure 167. SAXS analyses of SON68 glass reacted in ASTM C1220 tests at pH 10 for 1.5 day (green) and 20 days (turquoise) and pH 11 for 9 days (gold/brown), 11 days (violet), and 19 days (blue). Red curve for AFCI glass reacted in C1308 test for 77 days at pH 8.5 with 7-day exchange interval.

The value gives the cumulative value of NL(B) after 10 solution exchanges. Comparison with the spectrum for unreacted AFCI glass in Figure 166 shows only a small increase in the amount of intermediate range structure (note the shapes of the curves). A thinner layer is developed under the ASTM C1308 test conditions because solution replacements maintain lower Si concentrations that develop under static conditions. Researchers are currently modeling this scattering data and will couple those findings with insights from electron microscopy to better understand structural changes in the glass as corrosion proceeds.

Publication

1. Fortner, J. A. (2013). Advanced Photon Source User's Meeting poster presentation.

Examinations of Surface Alteration Layers

J. Ryan, J. Neeway, Z. Zhu, D. Schreiber, A. Mitroshkov (PNNL)

Some glass degradation models include the effects of a transport barrier that forms during the corrosion process and that limits dissolution; however, neither the location of the barrier nor the critical species that are affected by it are definitively identified. Detailed knowledge of the location, composition, evolution, and sensitivity to the solution composition of such a transport barrier layer is required to incorporate its effects into performance models. Tests have shown the efficiency of the barrier is related to the solution composition [Jollivet, et al., 2012]. This is important because changes in the structure and composition of surface alteration layers will not be tracked in disposal system performance assessments. Studying surface alteration layers is challenging because they develop slowly, are easily damaged by handling drying, and are sensitive to changes in solution chemistry. Multi-year isotope swap experiments have provided a detailed view of the interfacial region where glass corrosion is occurring and new insights to possible mass transport barriers. For example, APT data demonstrated the presence of two reaction areas: a very sharp interface locating the depth to which boron was released and another interface closer to the solution where the network silica have rearranged due to condensation reactions. A study

Separations and Waste Forms
2013 Accomplishments Report

of changing silicon isotope ratios showed little resistance to silica transport into and out of the gel area, which suggests the gel material is not an effective transport barrier. In addition, lithium from solution was found to have penetrated far beyond the depth of boron release. In general, many ions form their own discrete concentration profiles as the glass interacts with the solution, giving the appearance of many discernable layers having different transport properties and participating in different properties or reactivity. From the solution in, a corroded glass often exhibits the following alteration layers: crystallized precipitates, a porous, restructured alteration layer, often referred to as the gel, a series of reaction fronts, and an area of glass affected by ion exchange and/or water diffusion

To study the effects of the formation of these alteration layers on lithium diffusion into the glass, a glass specimen was immersed into a volume of the non-reactive solvent DMSO that had been spiked with the trackable isotope ^6Li and the lithium penetration into the glass was measured as a function of time and temperature. Specimens of the lithium-containing glasses CJ-6 and SON68 were placed in the ^6Li /DMSO solutions at three temperatures (25, 90, and 150 °C) for time periods ranging from 3 days to 9 months. By running the reaction in the non-aqueous solution, no glass dissolution occurred and no alteration layers were formed. The ^6Li profiles measured with time-of-flight secondary ion mass spectrometry (ToF-SIMS; see Figure 168) showed considerably deeper penetration (faster diffusion) than had been observed for specimens of the same glasses that formed alteration layers during the isotope swap experiments. The data in Figure 168 demonstrate this phenomenon for the SON68 glass where ^6Li was allowed to diffuse at 90°C. This suggests that the alteration layers do attenuate the diffusion of ^6Li . The data, which are still being collected, will be used to quantify the diffusivity of Li in the layers and the glass.

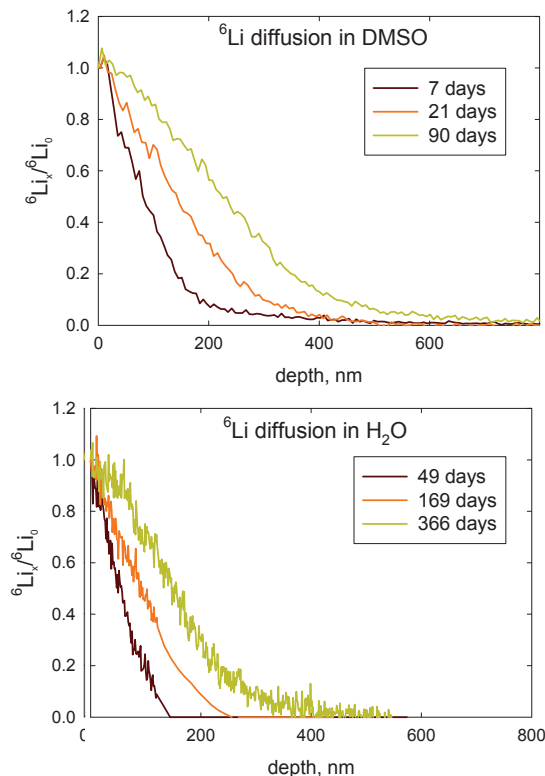


Figure 168. ToF-SIMS profiles of lithium diffusing into CJ-6 glass

One of the major problems with the APT analysis, which was used to directly image the layer theorized to cause the slowing of corrosion for the first time last FY, is that its success is strongly dependent on the type of glass being analyzed, e.g. highly porous material like the gel are unstable during analysis. Therefore, a novel sample preparation technique was developed to improve the depth resolution of nano secondary ion mass spectrometry (NanoSIMS) for analyzing cross sections of interfaces in materials not amenable to APT analysis (such as the ancient roman glasses). Preparing a wedge-shaped specimen by using a FIB was demonstrated to provide a five-fold increase in depth resolution compared to a perpendicular cross-section usually used in NanoSIMS. The improved depth resolution reveals the silicon and boron reaction fronts (see Figure 169) in the isotope swap sample discussed above are separated by less than 20nm, similar to measurements with APT. Although this experiment was performed on a sample whose composition could be confirmed with APT, this technique should be applicable to any material

Separations and Waste Forms
2013 Accomplishments Report

appropriate for examination with NanoSIMS. The technique enables examination of narrow and rough interfaces, and will be used to further characterize these potentially critical alteration layers. This capability will also enable further characterization of ancient glass samples that have been challenging to analyze.

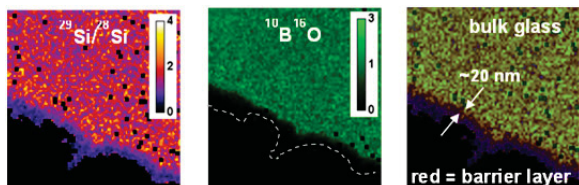


Figure 169. Nano-SIMS cross-section of corroded SON68 glass showing (left) uptake of ^{29}Si from solution, (center) total depletion of B, and (right) inner layer theorized to act as a transport barrier

References

1. Jollivet, P., P. Frugier, G. Parisot, J. P. Mestre, E. Brackx, S. Gin, and S. Schumacher (2012). "Effect of clayey groundwater on the dissolution rate of the simulated nuclear waste glass SON68." *Journal of Nuclear Materials* 420, 508-518.

Publications

1. Gin, S., J. V. Ryan, D. K. Schreiber, J. Neeway, and M. Cabié (2013), "Contribution of Atom-Probe Tomography to a Better Understanding of Glass Alteration Mechanisms: Application to a Nuclear Glass Specimen Altered 25 Years in a Granitic Environment." *Chemical Geology*, 349–350, June 29. pp. 99–109.
2. Strachan, D. M., J. V. Crum, J. V. Ryan, and A. Silvestri. "Characterization and Modeling of the Cemented Sediment Surrounding the Iulia Felix Glass." *Applied Geochemistry*, in revision.
3. Murphy, K.A., N. M. Washton, J. V. Ryan, C. G. Pantano, and K. T. Mueller (2013). "Solid-State NMR Examination of Alteration Layers on Nuclear Waste Glasses", *Journal of Non-Crystalline Solids* 369, 44-54.

Determining the Analytical Form of the Reaction Affinity Term in Concentrated Solutions

C. Crawford (SRNL)

Experimental methods are being developed to quantify the effects of specific solution species on glass dissolution rates to determine the form of the reaction activity term in concentrated solutions in Stage 2 prior to and during the transition to Stage 3. Several previous tests have indicated significant changes in the Al concentration immediately before the dissolution rate increases [Ebert, et al., 2011; Fortner, 2012]. Many studies of incongruent mineral dissolution have shown the reaction affinity terms are different under far-from-equilibrium and near-equilibrium conditions due to changes in the reaction mechanism, and the same effect has been hypothesized to explain the effects of secondary phase formation on the glass dissolution rate (see Section 11.2.8). The tests described in this section are being conducted to assess the mechanistic and analytical form of the reaction affinity term for concentrated solutions prior to secondary phase formation. An SPFT test apparatus was constructed as described in ASTM method C1662. The apparatus and procedure were verified by measuring the forward dissolution rate of the reference LRM glass under the same conditions used in an earlier round robin study to measure the intra-laboratory precision of the method.

Initial tests are being conducted with AFCI glass to utilize insights from prior testing, and the concentrated solution of initial interest is the solution generated during a 7-day PCT. Previous tests showed that solution was similar to the solution composition prior to formation of secondary phases and transition to Stage 3. The plan is to conduct SPFT experiments using leachants having slightly higher or lower Al and Si concentrations to measure the effect on the dissolution rate at the same pH attained in the 7-day PCT, which was pH 10.3, and determine the analytical forms of the affinity term before and after the transition to Stage 3. Scoping SPFT tests were conducted with AFCI glass to estimate the forward rate at 90°C and pH 10.3. The forward rate was estimated to be less than 3 g/(m²·d) based on the release of B, although steady state

Separations and Waste Forms
2013 Accomplishments Report

conditions were not attained. PCTs were also conducted for 14 and 21 days to estimate the dissolution rate in the more concentrated solutions. The cumulative B releases between 7 and 14 days were used to estimate the instantaneous dissolution rate in the 7-day PCT solution, which was 0.002 g/(m²·d) at about the same pH. This is approximately 3 orders of magnitude lower than the estimated forward rate. The test conditions necessary to measure those very low dissolution rates were determined based on insights gained from the scoping tests, including glass particle size, leachant flow rates, and sampling intervals.

Recent work at LBNL has demonstrated the effectiveness of measuring the loss of thickness from dissolution test coupons to obtain dissolution data in the absence of feedback rather than the traditional method of analyzing the test solutions. Such an approach would allow many glasses to be studied simultaneously in the same reaction cell, dramatically increasing the capacity to parameterize models for various glass compositions. Unfortunately, this approach would be inappropriate for the anticipated low dissolution rates anticipated in the concentrated solutions.

Future tests using several leachant solutions having Al and Si concentrations similar to those attained in the 7-day PCT-A tests are planned to evaluate the dependence of the rate (and the sensitivity of the affinity term) to each of these species. Scientists at PNNL performed calculations using GeoChemist's Workbench to assess the stabilities and help formulate solution compositions for those more complicated tests. Results showed that stable solutions could be achieved by lowering concentrations or increasing temperature. These modifications should allow for investigation of the effects of Al and or Si on the dissolution rates of the AFCI glass at the desired pH and temperature. These tests are designed to supplement similar tests to be conducted at ANL in FY 2014 using leachants representing test solutions measured after secondary phases have precipitated. This series of tests will indicate changes to the reaction affinity term that occur as glass corrosion progresses from highly dilute ground waters to highly concentrated solutions.

The resulting model will be evaluated using test data recently compiled in the Accelerated Leach Testing of Glass (ALTGLASS) database (see the following subsection).

References

1. Ebert, W. L., J. A. Fortner, A. L Billings, C. and Crawford (2011). "Glass Testing Activities at ANL and SRNL: FY11 Progress Report." FCRD-WAST-2011-000404.
2. Fortner, J. A. (2012). "Effects of Alteration Phase Precipitation on Glass Dissolution." DOE/NE report FCRD-SWF-2012-000266.

Publications

1. Crawford, C. (2013). "Letter Report on Initiation of Flowthrough Tests at SRNL." FCRD-SWF-2013-000119.00.
2. Crawford, C. (2013). "Letter Report on Completion of Flowthrough Tests." FCRD-SWF-2013-000331.
3. Strachan, D. M., J. J. Neeway, and J. V. Ryan (2013). "Modeling of the Solutions to be Used for the SRNL 'Super Flow' Experiments." FCRD-SWF-2013-000106.

ALTGLASS Database

C. Jantzen (SRNL)

Data from time-sequenced ASTM C1285 PCT with HLW and low activity waste glasses performed at variety of national and international laboratories were compiled into the ALTGLASS database. This database can be used to evaluate geochemical, thermodynamic, kinetic, and glass composition/structural approaches developed to predict long-term nuclear waste glass durability. The test durations range from 2 days to more than 20 years for some glasses (see Table 28). The ALTGLASS database contains 2123 rows representing the average of duplicate or triplicate test responses for 213 different glasses. It provides the solution compositions (Si, B, Ca, Li, Na, K, Al, Fe, Mo, Mg, Ti, Zn, Zr, and U when available) and pH from the PCTs, the glass composition, measured glass density, and the nominal test parameters (see Table 28).

Separations and Waste Forms
2013 Accomplishments Report

Table 28 - Maximum/minimum values of selected durability test parameters for tests in the ALTGLASS database

Parameter	Minimum	Maximum
Test Duration (days)	2	7,426
SA/V (m ⁻¹)	1081	39,113
(SA/V)·time (days/m)	3,914	69,423,179
Glass Density (kg/m ³)	2,370	2,810
Temperature (°C)	25	200

If secondary phases were analyzed by the researchers, the identification of these phases is given with the methodology used for phase identification. The database is given in tabular form and is available on request electronically to all national/international modeling groups from SRNL as a Microsoft Excel file. The database will help evaluate models relating corrosion rates and behavior to the compositions of the glass, test solution, and assemblage of secondary phases. It will be utilized to evaluate the revised dissolution rate model that is being developed with different reaction affinity terms before and after secondary phases form.

Publication

- Jantzen, C. (2013). "SRNL Modeling Database: Accelerated Leach Testing of GLASS (ALTGLASS)." FCRD-SWF-2013-000339.

Characterization of Extensively Corroded Glass and Secondary Phases

C. Crawford and J. Marra (SRNL)

Several experimental activities are being conducted within this study to identify the assemblages of secondary phases formed when glass corrodes for use in the models. Analyses continued to characterize solids recovered from very long-term PCT that were conducted previously at SRNL with the AFCI and SON-68 reference glasses at 200 °C. The high temperature was used to promote the conversion of glass to secondary phases to study advanced reaction progress in Stage 3 within a reasonable test duration. The solution results indicated that the AFCI glass particles were completely reacted and

replaced by alteration phases within 90 days (as evidenced by the releases of B and Mo); this was confirmed by analysis of the reacted solids. The release of Mo to solution suggested the SON-68 particles were completely reacted within 509 days, but the release of B corresponds to only about 50% of the glass reacted in those conditions. Solids analyses are needed to determine if Mo was selectively leached from the glass or if B precipitated into an alteration product (the two most likely causes for the differences). Solids analyses confirmed the AFCI glass was completely reacted within 308 days and that the each glass particles had fully transformed isovolumetrically into a clay, with no residual reacted glass cores detected. Solids analyses of SON-68 glass reacted 509 and 791 days had a very different appearance than the AFCI glass. As revealed in the SEM photomicrograph of cross-sectioned particles Figure 170, a coarse 2-µm layer of clay identifies the original perimeter of each particle with the glass in the interior having been completely replaced by various non-descript secondary phases. Only the outer clay layer had been observed in tests with SON-68 glass conducted for short durations and at lower temperatures.

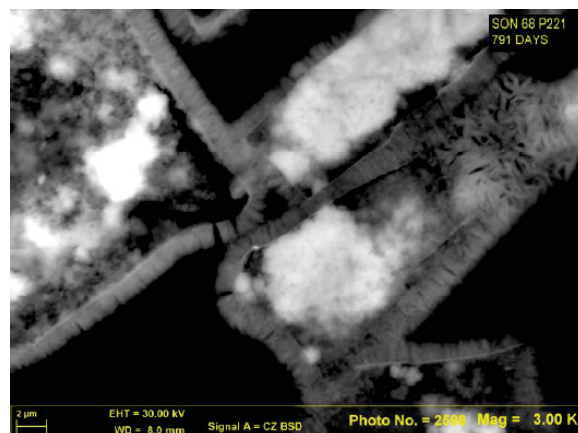


Figure 170. SEM photomicrograph of SON-68 glass reacted 791 days at 200°C.

The morphology of the reacted grains is consistent with the glass corrosion model of slow dissolution prior to the formation of secondary phases and fast dissolution after secondary phases precipitate. For AFCI glass and other glasses, most of the crystalline secondary phases are seen to precipitate on the outer surface of the clay layer

Separations and Waste Forms
2013 Accomplishments Report

and the glass at the interior transforms to clay. Analcime, clinotobermorite, montmorillonite (clay), and lithium silicate were detected in XRD analyses of AFCI glass reacted 7 days and longer at 200°C. XRD analyses of SON-68 glass reacted 28 days and longer at 200°C detected analcime, sillimanite, nontronite (clay), nacrite, and a sodium-aluminum silicate. These analyses confirm the different corrosion behaviors of AFCI and SON-68 glass seen in other tests and indicate solution results may belie the actual extent of corrosion in Stage 3.

Publication

1. Crawford, C. L. (2013). "Completion of S3D Tests Series 3 and Characterization of Glass Solids from Long-Term Corrosion Testing." FCRD-SWF-2013-000157.

Incorporating Monte Carlo Techniques into Corrosion Modeling

S. Kerisit, and J. Ryan (PNNL)

A Monte Carlo code of glass corrosion in aqueous conditions, which has been developed at PNNL over the last several years, was modified further to incorporate a simple model for simulating secondary phase formation. This new development allowed for investigating the influence of aluminum on the rate and mechanism of corrosion of sodium borosilicate glasses in static conditions. The glasses studied were in the compositional range (80-2x-2y)% SiO₂ y% Al₂O₃ (10+x)5% B₂O₃ (10+x+y)% Na₂O, where 0 ≤ x, y ≤ 15%.

Initial simulations without secondary phase formation allowed showed that increasing the amount of aluminum in the glass slows dissolution, as determined from the rate of boron release. However, the extent of corrosion based on the final B leached thickness (see Figure 171) increased with increasing Al₂O₃ content up to a threshold Al₂O₃ concentration. This is because the glass corrodes over a longer period of time in this regime when Al₂O₃ is present in the pristine glass. Indeed, the MC simulations revealed that this behavior is due to aluminum slowing the kinetics of hydrolysis/condensation reactions that drive the reorganization of the glass surface to form a protective surface layer [Cailleteau, et al., 2008; Kerisit and Pierce, 2012]. This phenomenon is in

agreement with experimental observations [Ledieu, et al., 2005].

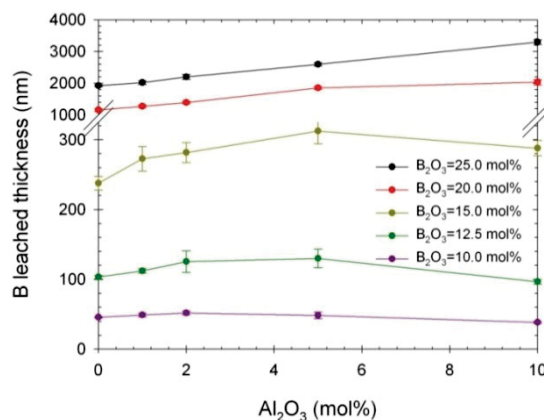


Figure 171. Boron leached thickness as a function of Al₂O₃ content for a series of aluminoborosilicate glasses with varying B₂O₃ content.

Once the threshold Al₂O₃ concentration is reached, further addition of Al₂O₃ leads to the opposite effect, i.e. a decrease in the extent of glass corrosion (see Figure 171 for B₂O₃ contents of less than 20 mol%). This phenomenon arises because the presence of aluminum creates small, hard-to-dissolve clusters of network formers that begin to form extended networks once the concentration threshold is reached. This effect strengthens the glass framework sufficiently to extend the lifetime of the outer part of the altered layer, which in turn facilitates formation of a blocking/protective layer and thus reduces the corrosion time. Such behavior is observed experimentally for addition of insoluble oxides, such as ZrO₂ [Cailleteau, et al., 2011], that do not have a tendency to form secondary phases, but not for Al₂O₃. This difference between Al₂O₃ and ZrO₂ is due to yet another process in the presence of aluminum, namely, secondary phase formation.

Indeed, a second series of Monte Carlo simulations with secondary phase formation allowed showed a continuous increase in final B leached thickness with increasing Al₂O₃ content. This finding was explained by the diminishing rate of condensation in the altered layer when a secondary phase is formed, which delays the formation of a blocking/protective layer and thus increases the corrosion time [Kerisit, et al., 2013]. In summary, the Monte Carlo model allows us to elucidate the interplay of elementary mechanisms

Separations and Waste Forms
2013 Accomplishments Report

that give rise to experimental observations of glass corrosion behavior. Additionally, the model was successfully incorporated into the model testing toolbox developed under the Fundamental Science and Methods Development Campaign's Comprehensive Corrosion Model task. Details on this effort can be found in Chapter 7.

References

1. Cailleteau, C., F. Angeli, F. Devreux, S. Gin, J. Jestin, P. Jollivet, and O. Spalla (2008). "Insight into silicate-glass corrosion mechanisms." *Nature Materials* 7, 978-983.
2. Kerisit, S., and E. M. Pierce (2012). "Monte Carlo simulations of the dissolution of borosilicate glasses in near-equilibrium conditions." *Journal of Non-Crystalline Solids* 358, 1324-1332.
3. Ledieu, A., F. Devreux, and P. Barboux (2005). "The Role Of Aluminium in the Durability of Alumino-Borosilicate Glasses." *Physics and Chemistry of Glasses* 46, 12-20.
4. Cailleteau, C., F. Devreux, O. Spalla, F. Angeli, and S. Gin (2011). "Why Do Certain Glasses with a High Dissolution Rate Undergo a Low Degree Of Corrosion?" *Journal of Physical Chemistry C* 115, 5846-5855.
5. Kerisit, S., J. V. Ryan, and E. M. Pierce (2013). "Monte Carlo Simulations of the Corrosion of Aluminoborosilicate Glasses." *Journal of Non-Crystalline Solids* 378, 273-281.

Publications and Reports

1. Kerisit, S., J. V. Ryan, and E. M. Pierce (2013). "Monte Carlo Simulations of the Corrosion of Aluminoborosilicate Glasses." *Journal of Non-Crystalline Solids* 378, 273-281.
2. Pierce, E. M., P. Frugier, L. J. Criscenti, K. D. Kwon, and S. Kerisit. "Modeling the Glass-Water Reaction from Interface to Pore Scale: Recent Advances and Current Limitations." *International Journal of Applied Glass Science*, accepted for publication.
3. Williford, R. E., J. V. Ryan, P. C. Rieke, Y. Minet, P. Frugier, and S. Gin. "Inverse

Modeling to Extract Rate Constants from Nuclear Waste Glass Corrosion Data: An Example Case for the GRAAL Model." *Journal of Nuclear Research*, in revision.

Modeling the Effects of Secondary Phase Precipitation on Glass Dissolution Using a Linear Rate Law

J. Neeway, D. Strachan (PNNL)

Previous modeling studies have shown that the durability of a glass is related to its composition. For example, glasses with high-alumina contents may show good short-term durability but poorer long-term durability. This is due to the composition effects that cause a glass to enter stage 3 corrosion, which has been attributed to the formation of analcime (ideally $\text{NaAlSi}_2\text{O}_6$) as a secondary phase that consumes the surrogate glass phase, $\text{SiO}_2(\text{am})$ [Van Iseghem and Grambow, 1988; Strachan and Croak, 2000]. However, those studies considered only the thermodynamics of the system and neglected important kinetic considerations. Those previous modeling studies were extended by using a linear affinity term model to represent the glass dissolution and secondary phase precipitation kinetics. The modeling results showed that the kinetics of both reactions are important when considering the effect of the secondary phase precipitation on glass dissolution. The calculations predicted that, although glasses with reasonably high alumina contents do show poor durability at the onset of analcime formation, in the absence of a gel layer the rate of glass dissolution will eventually slow because the amount of dissolved Al that is available to form analcime becomes limited by the glass dissolution rate. As a result of the slowing of analcime precipitation due to the lack of dissolved Al, the consumption of dissolved silica in the form of orthosilic acid (H_4SiO_4) slows and, through the affinity model, the glass dissolution rate decreases. At some point as reaction progresses, a steady-state is reached for the coupled glass dissolution and analcime precipitation reactions. The calculations also showed that increases in the glass dissolution rate (assumed to be solely influenced by an inverse relationship to orthosilic acid) could occur with increasing pH even when the total amount of silica in solution increases. This is because between the

Separations and Waste Forms
2013 Accomplishments Report

pH (90°C) values of 8.2 and 9.0, there is a significant increase in the HSiO_3^- species as a fraction of the total Si in solution and a concomitant decrease in the fraction of H_4SiO_4 , which is the rate controlling species assumed in the linear affinity model for glass dissolution. Thus, even as total Si in solution increases the glass dissolution rate increases both from a pH effect in the kinetic term of the model and a decrease in Q that affects the thermodynamic affinity term of the model.

The linear affinity term model was also used to investigate the importance of the relative rates of glass dissolution and alteration product precipitation. It was found that, while the relative rates are important, the rate of glass dissolution ultimately limited the precipitation of analcime. This prediction is a consequence of the linear form of the affinity term. However, the prediction is consistent with results seen in vapor hydration conditions at relatively high temperatures. These results suggest that Stage 3 may be a transient condition and glass corrosion will ultimately slow again to a new steady state rate. There are limited experimental evidence for the slowing of the rate after stage 3 was obtained. However, most experimental results suggest that the higher rate will continue until the glass completely reacts. The potential discrepancy between these modeling results and the observed behavior of glass suggests that the assumptions made for these models, primarily the linear affinity term, may lack some necessary details, mainly the absence of the gel layer. Regardless, the use of kinetics in modelling the effects of secondary phase formation on glass dissolution has been demonstrated to be very important. The use of coupled kinetics and a non-linear affinity term to model glass behavior is discussed in the following subsection.

References

1. Strachan, D.M., and T. L. Croak (2000). "Compositional Effects on Long-Term Dissolution of Borosilicate Glass." *Journal of Non-Crystalline Solids* 272, 22-33.
2. Van Iseghem, P., and B. Grambow, (1988). "The Long-Term Corrosion and Modeling of Two Simulated Belgian Reference High-Level Waste Glasses." *Scientific Basis for Nuclear*

Waste Management XI. Material Research Society Symposium Proceedings 112, 631-639.

Publication

1. Strachan, D., and J. Neeway, "Effects of Alteration Product Precipitation on Glass Dissolution." *Applied Geochemistry*, submitted.

Modeling the Onset of Secondary Phase Precipitation and Effect on Glass Dissolution Using Non-Linear Rate Laws

W. Ebert, ANL

Arguably the most important uncertainties in projecting the performance of geologically disposed waste glasses are the cause and relevancy of the sudden increase in the dissolution rates of many surrogate waste glasses observed in laboratory tests transitioning to Stage 3. Although the sudden increase referred to here as Stage 3 has been known for about 30 years to occur during the dissolution of some glasses in several test methods, the process causing the increase and controlling the rate are not understood. Not all glasses and not all testing conditions result in stage 3 "acceleration." Modeling the source term for radionuclide release over time requires the mechanism underlying the increase be understood and, if it is relevant to disposed waste glass, quantified and incorporated into the glass degradation model used to calculate radionuclide source terms.

The approach taken to address this issue has been to generate a database of experimental results for relevant borosilicate glasses with a variety of test methods and conditions that highlight different aspects of corrosion behavior and can be used for internal comparisons. This has included work by researchers within the FCRD project and by collaborators outside the project. The available data have been evaluated with regard to past and current models used by glass scientists and geochemists and the scientific bases and assumptions underlying those models and technical approaches that were taken have been reassessed. In addition, the insights from recent progress in modeling incongruent mineral dissolution were applied to modeling glass

Separations and Waste Forms
2013 Accomplishments Report

corrosion. This required reassessing some aspects of glass corrosion modeling and key assumptions, reconsidering sometimes tightly held theories that are contrary to recent experimental observations. The evaluations have been documented in a project report and an open-literature paper describing a new conceptual model is under review. The conclusions that were reached require further technical evaluations and debate, but appear to be qualitatively consistent with observed glass corrosion behavior, particularly with regard to the effects of secondary phase formation on the glass dissolution rate.

In general, the new conceptual model attributes the slow residual rate (Stage 2) to the reaction affinity between the solution and alteration phases formed on the glass surface, not between the solution and the glass. The chemical reaction affinity model is appropriate for describing this interaction based on consideration of underlying scientific principles and insights provided by recent studies of incongruent mineral dissolution. Most recent criticisms of applying reaction affinity model to glass corrosion address assumptions and how the model is applied to glass rather than the model itself [Gin, et al., 2008; Curti, 1991]. These include simplifying assumptions used by Grambow and others [Grambow and Strachan, 1988; Grambow and Muller, 2001] based on partial equilibrium theory not being consistent with the observations in laboratory tests with many surrogate waste glasses when secondary phases that cause Stage 3 corrosion precipitate, namely, the increased glass dissolution rate accompanied by increasing silica concentrations and the variance in equilibrium constant (K) with test conditions. Application of the affinity model without the restrictive assumptions in the partial equilibrium approach is consistent with experimental observations if the coupling between glass dissolution and secondary phase precipitation reactions leading to either negative or positive feedback are taken into account.

Briefly, the conceptual model differs from the Grambow model in that the reaction affinity term is determined by disequilibrium between the solution and alteration or secondary phases rather than between the solution and a pseudo-glass

phase. Initially, the depleted surface layer formed by incongruent dissolution during Stage 1 behaves as a separate phase that interacts with the solution as a thermodynamically stable phase. The disequilibrium between the solution and this phase establishes the reaction affinity for the system, including the glass. The kinetics of glass dissolution and alteration layer formation are coupled by the transfer of silica, which can be tracked through the dissolved silica concentration. (Note that this behavior was seen in the outer layer discussed in the previous subsection) This results in the same form of the rate law as the Grambow model for initial corrosion in Stage 2, but the affinity term is defined differently. Based on the lithium penetration data discussed in the "Examinations of Surface Alteration Layers" subsection, it is evident that the alteration layer also provides a mass transport barrier that further influences glass dissolution, and that different regions of the alteration layer likely contribute affinity and transport effects. Whereas the equilibrium constant (K) is considered to represent an intrinsic property of the glass defining the silica solubility limit in the Grambow model, it represents the alteration phase in the proposed model. The steady-state condition between glass dissolution and alteration layer formation kinetics establishes a dissolved silica concentration that depends on the test conditions, as observed in experiments. As new secondary phases form, new steady state conditions between glass dissolution and formation of those phases are established resulting in a different glass corrosion rates.

The kinetics of glass dissolution and secondary phase precipitation are coupled through the transfer of species from the glass to the secondary phases. This may occur through solution or by surface migration. In the new conceptual model, the form of the reaction affinity term is redefined to represent the disequilibrium between the solution and the thermodynamically most stable secondary phase allowed to form in the system, which changes as the reaction progresses. The coupled glass dissolution and secondary phase precipitation reactions establish a steady state condition through the species transferred from the glass to the secondary phase that maintains a nearly constant glass dissolution rate until the glass is completely consumed or a

Separations and Waste Forms
2013 Accomplishments Report

more stable secondary phase forms to establish a new steady state. The reactive surface areas of glass and secondary phases will affect the kinetics. Changes in the affinity-controlling phases as the reaction progresses requires the use of a non-linear rate law in which different forms of the reaction affinity term apply for different stages of reaction progress because the reactions change. These changes may include different phases and dissolved species determining the saturation index and different functional dependencies of the rate on the affinity. The same approach has recently been used to model mineral transformation.

The conceptual model provides frameworks for (1) laboratory studies to identify solution conditions under which rate-affecting secondary phases nucleate and measure the dependencies of the kinetic and affinity terms on the solution composition after they form, and (2) modeling long-term waste form performance as corrosion conditions evolve. Knowledge of the effects of the solution composition on the nucleation and growth of rate-affecting secondary phases and on the glass dissolution rate is required to accurately model long-term waste glass degradation. Owing to the empirical nature of the kinetic and reaction affinity terms, their analytical forms and parameter values must be determined experimentally. This approach will incorporate the effects of other processes that are not modeled explicitly, such as mass transport through surface layers, within the values that are measured. For example, the qualitative sensitivity of the protective nature of the surface layers to the solution composition allows the effect of transport limitations on the glass dissolution rate to be expressed in terms of the solution composition effects, albeit empirically rather than analytically.

The new conceptual model provides an approach to take the coupled dissolution and precipitation reactions into account when modeling the long-term corrosion behavior of a borosilicate waste glass in a disposal environment. The Stage 3 behavior observed in some laboratory experiments suggests the glass dissolution rate and tectosilicate precipitation rates both contribute to the coupled rate under those conditions, and that the transfer of Al to the secondary phases limits the conversion rate [Ebert, et al., 2013]. The affinity for glass dissolution might not be affected

by the Al concentration, but the precipitation of clays and tectosilicates will be affected. Transfer of Al is required to form the secondary phase that consume Si and affect glass dissolution, and this couples the reactions. Simple laboratory tests can be used to measure model parameter dependencies and values at several stages of reaction progress, such as those described in the “Characterization of Extensively Corroded Glass and Secondary Phases” subsection.

References

1. Curti, E. (1991). “Modeling the Dissolution of Borosilicate Glasses for Radioactive Waste Disposal with the PHREEQE/GLASSOL Code: Theory and Practice.” Paul Scherrer Institut-Bericht Report 86.
2. Ebert, W., J. Fortner, C. Crawford, and J. Marra (2013). “Test Methods to Study Secondary Phase Formation and the Resumption of Glass Alteration.” *International Journal of Applied Glass Science*, submitted.
3. Gin, S., C. Jégou, P. Furgier, and Y. Minet (2008). “Theoretical Consideration on the Application of the Aagaard-Helgeson Rate Law to the Dissolution of Silicate Minerals and Glasses.” *Chemical Geology* 255, 14-24.
4. Grambow, B., and D. M. Strachan (1988). “A Comparison of the Performance of Nuclear Waste Glasses by Modeling.” PNL-6698. Pacific Northwest National Laboratory.
5. Grambow, B., and R. Müller (2001). “First-Order Dissolution Rate Law and the Role of Surface Layers in Glass Performance Assessment.” *Journal of Nuclear Materials* 298, 112-124.
6. Strachan, D. M., and T. L. Croak (2000). “Compositional Effects on Long-Term Dissolution of Borosilicate Glass.” *Journal of Non-Crystalline Solids* 272, 22-33.
7. Van Iseghem, P., and B. Grambow (1988). “The Long-Term Corrosion and Modeling of Two Simulated Belgian Reference High-Level Waste Glasses.” *Scientific Basis for Nuclear Waste Management XI. Material Research*

Separations and Waste Forms
2013 Accomplishments Report

Society Symposium Proceedings 112, 631-639.

Publication

1. Ebert, W. L. (2013). "A Conceptual Model for the Effects of Secondary Phase Precipitation on Waste Glass Dissolution." FCRD-SWF-2013-000303.
2. Ebert, W., J. Fortner, C. Crawford, and J. Marra (2013). "Test Methods to Study Secondary Phase Formation and the Resumption of Glass Alteration." *International Journal of Applied Glass Science*, submitted.
3. Fortner, J. A. (2013). "Rapid Glass Dissolution Reaction Coupled to Aluminosilicate Precipitation," *American Ceramic Society 10th Pacific Rim Conference on Ceramic and Glass Technology*. San Diego, CA, June 2-7.

Collaborations

As mentioned above, progress in these activities is greatly enhanced by a strong team of collaborators, both international and domestic. Through two international workshops associated with major conferences in May/June, representatives from eight countries shared data, techniques, and theories. The plan to use a standard simplified glass to provide a common baseline has been implemented, with twenty institutions incorporating experiments with that glass into their test plans. Additional partners working on the topic were contacted in May when research as part of the IAEA "Coordinated Research Program" with the Japanese, Belgian, and French partners was presented. Several projects funded through the NEUP program have been especially valuable to this effort. Partners at Penn State University, Washington State University, and Alfred University have on-going efforts addressing structural characterization, the examination of near-field chemistry effects, and in-situ interrogation, respectively, that are pertinent to the project goals. These efforts provide more opportunities to identify, understand, and parameterize the rate-limiting steps in glass corrosion. Additionally, the modeling work performed by the three

Fundamental Science, Modeling and Simulation tasks (see respective portions of Chapter 7) has been of critical importance to the overall effort, including the first principles studies of bond strength (ANL), microcontinuum modeling (LBNL), and the development of a versatile testing platform for the various models being developed (PNNL), all of which are described in Section 1..

As part of the CEA/DOE direct collaboration, a renowned corrosion scientist from France's CEA laboratory, Stéphane Gin, served a 12-month appointment at PNNL ending this past August 2013. Having Dr. Gin working directly with us was extraordinarily helpful, as 5 papers were written with 5 more still in draft. The jointly designed and executed experiments of the past year made use of his years of experience with the subject and, in some cases, 10+ year old samples he brought over from France. Additionally, Dr. Gin partnered with Drs. Vienna and Ryan from PNNL to be guest editors for an issue of the *International Journal of Applied Glass Science* that deals exclusively with the state-of-the-art of glass corrosion science. This journal issue is expected to be published around the end of 2013.

Last fiscal year, PNNL made use of the Office of Science Visiting Faculty Program to provide a professor and student from a non-research university the chance study the effect of geometry on the dissolution of glass in dilute solutions. The project was a success, conclusively finding that dissolution proceeded in a geometric fashion and that particle shape can indeed affect the observed dissolution rate. This year, the project returned the same professor and a new student to continue the research, with the student taking second place at the Materials Science and Technology Conference undergraduate poster session. The team developed a much more sophisticated model to incorporate quantitative analysis of real glass particles based on 2-dimensional images. Particles of simulated waste glass reacted following the SPFT procedure were imaged in 2D and modeled to see how the observed dissolution rate would relate to the forward rate. The apparent dissolution rates of realistic single particles were found to be bounded between certain aspect ratios of rectangular shapes. The computational work on batched

Separations and Waste Forms
2013 Accomplishments Report

particles demonstrated that the effect of particle shape was largely averaged out, but with a significant offset from the true rate. An initial push to extend the model to three dimensions, however, revealed that crushed particles are heavily biased to have a flake shape: much larger in 2D area than in thickness. This predilection to high aspect ratio was modeled to have a large effect on observed dissolution rate, particularly at long times. A map to a correction factor is thus perceived and can be refined through further development of 3-D modeling.

Publications and Reports

1. Gin, S., A. Abdelouas, L. J. Criscenti, W. L. Ebert, K. Ferrand, T. Geisler, M. T. Harrison, Y. Inagaki, S. Mitsui, K. T. Mueller, J. C. Marra, C. G. Pantano, E. M. Pierce, J. V. Ryan, J. M. Schofield, C. I. Steefel, and J. D. Vienna (2013). "An International Initiative on Long-Term Behavior of High-Level Nuclear Waste Glass." *Materials Today* 16, 243-248.
2. Vienna, J. D., S. Gin, J. V. Ryan, and Y. Inagaki (2013). "Current Understanding and Remaining Challenges in Modeling Long-Term Degradation of Borosilicate Nuclear Waste Glasses." *International Journal of Applied Glass Science*, accepted for publication.
3. Senecal, J., (2012). "Parameterization of a General Glass Dissolution Model: Accounting for Shape Effects in Dilute Dissolution Conditions." 2nd place undergraduate student poster award at *MS&T 2012*.

Conclusions

Results of the various testing and modeling activities within the control account that have focused on particular aspects of the glass corrosion behavior summarized in Figure 1 have together provided a fairly complete description of the processes contributing to overall glass corrosion. It is now evident that mass transport and chemical reaction affinity act in concert and that both must be included in the rate law for waste glass dissolution to account for all phenomena that are observed experimentally. This has led to formulation of a new conceptual model that is consistent with experimental and modeling results

and provides the basis for an improved quantitative rate law for waste glass corrosion and radionuclide source terms. Future work remains to develop quantitative analytical expressions for including the coupled effects of mass transport, reaction affinity, and reaction kinetics in the rate law. As a collaborative group, it appears that researchers are approaching the consensus regarding a mechanistic model that has been a goal of the group from the start. This is a direct result of coordinating research with common objectives and materials, sharing data and test materials, debating experimental and analytical methods, and coming to agreement regarding data interpretations at regularly-held technical workshops.

Discussions between participating researchers continue to identify experimental and modeling activities to further quantify aspects of mass transport through alteration layers and the coupled kinetics of glass dissolution and secondary phase precipitation. For example, Japanese colleagues have offered to host a workshop at the end of 2014 to compare and critically assess models being developed for the dissolution of SON-68 glass in a static solution. The major FY 2014 milestone for researchers in this control account will be documenting an up-dated glass degradation model. That will include refining the new conceptual model, linking available experimental results to aspects of that model, and designing experiments to parameterize the model. The majority of FY 2014 efforts, including experiment, theory, and computational modeling, will target that goal.

Publications and Awards

1. Gin, S., A. Abdelouas, L. J. Criscenti, W. L. Ebert, K. Ferrand, T. Geisler, M. T. Harrison, Y. Inagaki, S. Mitsui, K. T. Mueller, J. C. Marra, C. G. Pantano, E. M. Pierce, J. V. Ryan, J. M. Schofield, C. I. Steefel, and J. D. Vienna (2013). "An International Initiative on Long-Term Behavior of High-Level Nuclear Waste Glass." *Materials Today* 16, 243-248.
2. Gin, S., J. V. Ryan, D. K. Schreiber, J. Neeway, and M. Cabié (2013). "Contribution of Atom-Probe Tomography to a Better Understanding of Glass Alteration Mechanisms: Application to a Nuclear Glass

Separations and Waste Forms
2013 Accomplishments Report

- Specimen Altered 25 Years in a Granitic Environment.” *Chemical Geology* 349–350, pp. 99–109. June 26.
3. Murphy, K. A., N. M. Washton, J. V. Ryan, C. G. Pantano, and K. T. Mueller (2013). “Solid-State NMR Examination of Alteration Layers on Nuclear Waste Glasses.” *Journal of Non-Crystalline Solids* 369, 44-54.
 4. Pierce, E. M., P. Frugier, L. J. Criscenti, K. D. Kwon, and S. Kerisit. “Modeling the Glass-Water Reaction from Interface to Pore Scale: Recent Advances and Current Limitations.” *International Journal of Applied Glass Science*, accepted for publication.
 5. Kerisit, S., J. V. Ryan, and E. M. Pierce (2013). “Monte Carlo Simulations of the Corrosion of Aluminoborosilicate Glasses Journal of Non-Crystalline Solids.” *Journal of Non-Crystalline Solids*, accepted for publication.
 6. Vienna, J. D., S. Gin, J. V. Ryan, and Y. Inagaki (2013). “Current Understanding and Remaining Challenges in Modeling Long-Term Degradation of Borosilicate Nuclear Waste Glasses.” *International Journal of Applied Glass Science*, accepted for publication.
 7. Ebert, W., J. A. Fortner, C. Crawford, and J. Marra (2013). “Test Methods to Study Secondary Phase Formation and the Resumption of Glass Alteration.” *International Journal of Applied Glass Science*, submitted.
 8. Williford, R. E., J. V. Ryan, P. C. Rieke, Y. Minet, P. Frugier, S. Gin. “Inverse Modeling to Extract Rate Constants from Nuclear Waste Glass Corrosion Data: An Example Case For the GRAAL Model.” *Journal of Nuclear Research*, in revision.
 9. Strachan, D. M., J. V. Crum, J. V. Ryan, Alberta Silvestri. “Characterization and Modeling of the Cemented Sediment Surrounding the Iulia Felix Glass.” *Applied Geochemistry*, in revision.
 10. Wang, Y.-C., D. K. Schreiber, K. Jin, J. Neeway, J. V. Ryan, W. Wei, Z. Zhu, “NanoSIMS Imaging Alternation Layers of a Leached SON68 Glass via a FIB-Made Wedged Crater.” *Proceedings of the 19th International Conference on Secondary Ion Mass Spectrometry – SIMS XIX*, submitted.
 11. Strachan, D., and J. Neeway, "Effects of Alteration Product Precipitation on Glass Dissolution." *Applied Geochemistry*, submitted.
 12. Ebert, W. L. (2013). “A Conceptual Model for the Effects of Secondary Phase Precipitation on Waste Glass Dissolution.” FCRD-SWF-2013-000303.
 13. Crawford, C. (2013). “Letter Report on Initiation of Flowthrough Tests at SRNL.” FCRD-SWF-2013-000119.
 14. Crawford, C. (2013). “Letter Report on Completion of Flowthrough Tests.” FCRD-SWF-2013-000331.
 15. Crawford, C. L. (2013). “Completion of S3D Tests Series 3 and Characterization of Glass Solids from Long-Term Corrosion Testing.” FCRD-SWF-2013-000157.
 16. Jantzen, C. (2013). “SRNL Modeling Database: Accelerated Leach Testing of GLASS (ALTGLASS).” FCRD-SWF-2013-000339.
 17. Strachan, D. M., J. J. Neeway, and J. V. Ryan (2013). “Modeling of the Solutions to be Used for the SRNL ‘Super Flow’ Experiments.” FCRD-SWF-2013-000106.
 18. Senecal, J., (2012). “Parameterization of a General Glass Dissolution Model: Accounting for Shape Effects in Dilute Dissolution Conditions.” 2nd place undergraduate student poster award at *MS&T 2012*.)

CHAPTER 11
FUEL RESOURCES

CHAPTER 11: FUEL RESOURCES

K. Felker, felkerlk@ornl.gov

The Fuel Resources Program completed an independent review of the work performed. The reviewer panel consisted of Prof. Charles W. Forsberg (MIT), Dr. Paul B. Glaser (GE Global Research), Prof. William M. Landing (Florida State University), and Prof. Robert T. Paine (University of New Mexico). The initial three-year target to develop adsorbents that can extract uranium at twice the capacity of adsorbent developed by researchers at the Japan Atomic Energy Agency was met and exceeded.

Thermodynamic and Kinetic Studies (U from Seawater)

L. Rao, lrao@lbl.gov

Objectives

To improve the extraction efficiency and reduce the extraction cost, fundamental understanding of the coordination chemistry of the extraction process is necessary. Systematic thermodynamic studies were conducted to determine the stability constants of the complexes of uranium with amidoxime-type ligands.

Complexation of U(VI) with Phthalimidedioxime in Comparison with Glutarimidedioxime

In FY 2013, the stability constants of the U(VI) complexes with two phthalimidedioxime ligands (Figure 172) were determined by potentiometric and spectrophotometric titrations, and compared with those of the U(VI) complexes with glutarimidedioxime previously studied. Density functional theory calculations were performed to identify the most probable protonation sites of the ligand and help to interpret the trend in the binding strength of the ligands.

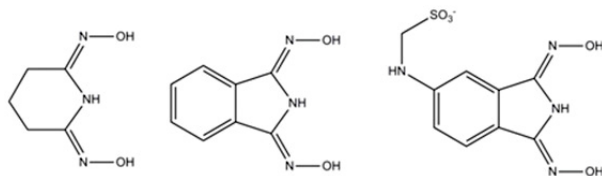


Figure 172. Amidoxime-related ligands (from left to right: $H_2^{II}L$, glutarimidedioxime; $H_2^{II}L$, phthalimidedioxime; and $H_2^{III}L$, 2-(1,3-bis(hydroxyimino)isoindolin-5-ylamino)ethane-sulfonate (^{III}L was prepared at ORNL).

The protonation constants, the stability constants and enthalpy of complexation of U(VI)

with phthalimidedioxime were determined by potentiometry and calorimetry (Table 29).

Table 29. Thermodynamic parameters of the protonation and complexation of phthalimidedioxime ($H_2^{II}L$) and 2-(1,3-bis(hydroxyimino)isoindolin-5-ylamino)ethanesulfonate ($H_2^{III}L$) with U(VI), in comparison with glutarimidedioxime ($H_2^I L$). 25 °C, $I = 0.5 M$ (NaCl).

Reaction	$\log \beta^*$		
	$H_2^I L$	$H_2^{II} L$	$H_2^{III} L$
$H^+ + L^{2-} = HL^-$	12.06 ± 0.23	11.18 ± 0.10	11.28 ± 0.10
$2H^+ + L^{2-} = H_2L(aq)$	22.76 ± 0.31	21.56 ± 0.10	21.78 ± 0.10
$3H^+ + L^{2-} = H_3L^+$	24.88 ± 0.35	23.30 ± 0.15	23.32 ± 0.10
$UO_2^{2+} + L^{2-} = UO_2L(aq)$	17.8 ± 1.1	15.5 ± 1.1	14.4 ± 0.4
$H^+ + UO_2^{2+} + L^{2-} = UO_2(HL)^+$	22.7 ± 1.3	21.2 ± 1.2	
$UO_2^{2+} + 2L^{2-} = UO_2L_2^{2-}$	27.5 ± 2.3		25.0 ± 0.2
$H^+ + UO_2^{2+} + 2L^{2-} = UO_2(HL)_2^+$	36.8 ± 2.1	35.0 ± 1.5	34.6 ± 0.1
$2H^+ + UO_2^{2+} + 2L^{2-} = UO_2(HL)_2(aq)$	43.0 ± 1.1	40.5 ± 1.7	40.3 ± 0.2

* Values for $H_2^I L$ are from ref.1; values for $H_2^{II} L$ are from spectrophotometry in this work; values for $H_2^{III} L$ are the average from spectrophotometry and potentiometry in this work.

The U(VI)/phthalimidedioxime complexes were found to be 2–3 orders of magnitude weaker than the corresponding U(VI)glutarimidedioxime complexes, which was attributed to the difference between phthalimidedioxime and glutarimidedioxime in their electronic and structural properties. The incorporation of the aromatic ring in phthalimidedioxime reduces the electron density on the donor atoms of the ligand and makes the imidedioxime moiety less complementary for binding UO_2^{2+} via its equatorial plane. DFT calculations performed at ORNL support these explanations.

Separations and Waste Forms
2013 Accomplishments Report

Though being weaker than glutarimidedioxime, phthalimidedioxime still forms fairly strong U(VI) complexes and can still effectively compete with carbonate for the complexation of U(VI) at seawater pH and carbonate concentration. Due to its higher chemical stability in acidic solutions than that of glutarimidedioxime, phthalimidedioxime is a valuable ligand that could have potential use in the extraction of U(VI) from seawater.

Complexation of U(VI) with Glutarimidecarbonyloxime (Ligand C) in Comparison with Ligands A and B

In the radiation-grafting process for preparing the amidoxime-based sorbent, three possible configurations could form, including glutarimidedioxime (Ligand A), glutardiamidoxime (Ligand B), and glutarimidecarbonyloxime (Ligand C), as shown in Figure 173. The studies of the complexation of U(VI) with A and B have been completed and the results have been published.^{1,4} Starting in the second part of FY 2013, complexation of U(VI) with Ligand C has been conducted. A comparison of the binding strength of the three ligands provides a structure-property relationship that could serve as guidance for optimizing the conditions of the radiation-grafting process.

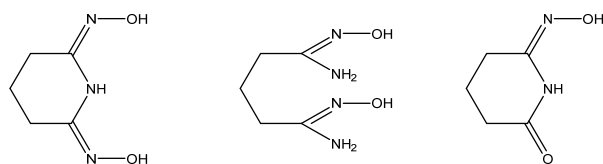


Figure 173. A series of amidoxime-related ligands. (from left to right) A – glutarimidedioxime; B – glutardiamidoxime; C – glutarimidecarbonyloxime.

A series of potentiometric and spectrophotometric titrations, using NaOH to titrate a solution of uranyl in the presence of Ligand C, were carried out in order to study the formation of complexes of uranyl with Ligand C. Difficulties were encountered in these experiments, mainly due to the weak binding strength of ligand C with U(VI), the strong tendency of U(VI) hydrolysis, and the limited solubility of U(VI) hydrolyzed species. No quantitative values of the stability constants of U(VI)/Ligand C complex(es) could be obtained by

these experiments. However, results of these experiments did suggest that Ligand C is much weaker in binding U(VI) than Ligands A and B. The upper limit of the stability constant of the 1:1 U(VI)/Ligand C complex is around 8.5–9 (log β).

To minimize the experimental hindrances of the U(VI) hydrolytic processes, researchers tried to assess the formation of uranyl – Ligand C complexes by a competition method using ethylenediaminetetraacetic acid (EDTA) as a competing agent. EDTA was used to prevent (or reduce) the effect of U(VI) hydrolysis. Based on the literature, EDTA forms two stable U(VI) complexes: $[\text{UO}_2\text{edta}]^{2-}$ (log β = 12.1) and $[\text{UO}_2(\text{Hedta})]^-$ (log β = 16.7) in 0.5 M NaCl.⁵ A series of competition potentiometric titrations were performed with varying concentrations of reagents. The experimental data can be fitted with a speciation model including the formation of a 1:1 uranyl-Ligand C complex, $[(\text{UO}_2)\text{C}]^+$, with a calculated log β = 8.7 \pm 0.1 (Table 30). This complex seems to form in the pH region of 3.5–5.5 and maximize at pH \sim 5, which probably explains why Ligand C cannot compete with the hydrolysis of U(VI) at higher pH.

In conclusion, Ligand C is a much weaker complexant for U(VI), in comparison with Ligand A and B. In the radiation grafting process for preparing the amidoxime-based sorbents, the grafting and reaction conditions should be chosen to minimize the formation of Ligand C. For example, the molar ratio of –CN groups to hydroxylamine should be kept low so that the yield for Ligand C is minimized.

Table 30. Protonation and complexation of Ligand C with U(VI) (25 °C, I = 0.5 M NaCl)

Reaction	log β (3 σ)	ΔG (3 σ) kJ/mol	ΔH (3 σ) kJ/mol	$T\Delta S$ (3 σ) kJ/mol
$\text{H}^+ + \text{C}^- = \text{HC}$	10.85(3)	-61.9(2)	-35.7(2)	26.2(3)
$\text{H}^+ + \text{HC} = (\text{H}_2\text{C})^+$	12.0(3)	-69(2)	-41.3(6)	27(2)
$\text{UO}_2^{2+} + \text{C}^- = \text{UO}_2\text{C}^+$	8.7(3)			

Publications

- Sun, X., C. Xu, G. Tiam, and L Rao (2013). “Complexation of Glutarimidedioxime with Fe(III), Cu(II), Pb(II), and Ni(II), the Completing Ions for the Sequestration of

Separations and Waste Forms
2013 Accomplishments Report

- U(VI) from Seawater.” *Dalton Trans.* 42, 1462114627.
2. Tian, G., S. J. Teat, and L. Rao (2013). “Thermodynamic Studies of U(VI) Complexation with Glutardiamidoxime for Sequestration of Uranium from Seawater.” *Dalton Trans.* 42, 5690-5696.
 3. Tian, G., S. J. Teat, Z. Zhang, and L. Rao (2012). “Sequestering Uranium from Seawater: Binding Strength and Modes of Uranyl Complexes with Glutarimidedioxime.” *Dalton Trans.* 41 (38), 11579-11586 (Journal Cover October 2012).

Absorbent Development, Ligand Design, and Nanosynthesis

K. Felker, felkerlk@ornl.gov

Advanced Adsorbent Development

In FY 2013, key accomplishments in the Advanced Adsorbent Development subtask included the following: (1) the conditions for radiation induced graft polymerization (RIGP) of acrylonitrile and methacrylic acid onto high surface area polyethylene fibers was determined; (2) developed an approach to prepare high-performance fiber adsorbents without RIGP; (3) produced a high capacity adsorbent based on alternative monomers through RIGP that exceeded the capacity of the initial ORNL adsorbent; and (4) produced initial braided high surface area fibers at Steeger, USA (Inman, SC) for flow testing at the PNNL Marine Sciences Laboratory (MSL).

The parameters for RIGP of acrylonitrile with methacrylic acid were optimized and repeatable on high surface area fiber. The polyethylene fiber used consisted of a hollow gear shape. The monomers have been demonstrated to graft throughout the polymer fiber. The 70:30 ratio of acrylonitrile to methacrylic acid in DMSO results in a grafted copolymer consisting of a 50:50 mixture of acrylonitrile and methacrylic acid. These parameters were utilized to graft the acrylonitrile-methacrylic acid copolymer onto a braided high surface area fiber. The braids were generated at Steeger, USA and grafted with the acrylonitrile-methacrylic acid copolymer at the

NEO Beam irradiation facility. The braids were sent to the MSL at the end of FY 2013.

In addition to RIGP, controlled radical polymerization was developed. Through atom transfer radical polymerization (ATRP), the need for radiolysis is decreased. By utilizing halide initiators with a copper-ligand catalyst system, polyacrylonitrile can be grown onto the polymeric support. This decreases the cost of the adsorbent while allowing the polymerization of long polyacrylonitrile chains.

Methacrylic acid was replaced by other acid monomers to increase the capacity through enhanced hydrophilicity or through complementary chelation sites. The capacities of the vinylphosphonic acid and itaconic acid copolymers resulted in significant enhancements of capacity. The capacity of the acrylonitrile-methacrylic acid copolymer is 3.2 mg-U/g-ads, while that of the acrylonitrile-itaconic acid copolymer was 4.6 mg-U/g-ads. Braided adsorbents consisting of acrylonitrile-itaconic acid copolymers were generated and are in queue for marine testing.

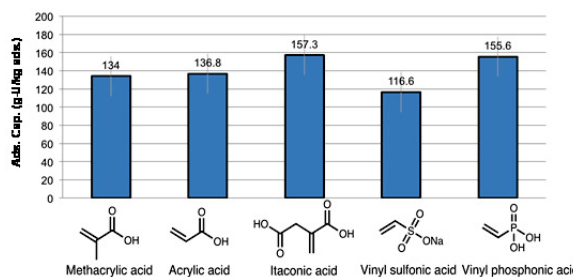


Figure 174: Screening capacities of different monomers that add hydrophilicity.

Functional Ligand Development

The pKa of several ligands were predicted and verified. A bisamidoxime ligand was synthesized with a procedure to anchor the ligand onto the polyethylene support. Click chemistry is used in the anchoring step. The ligand is functionalized with an alkyne while the polyethylene support, starting with vinylbenzyl chloride grafted polyethylene was converted to an azide. The coupling is quantitative and can be tracked gravimetrically.

Separations and Waste Forms
2013 Accomplishments Report

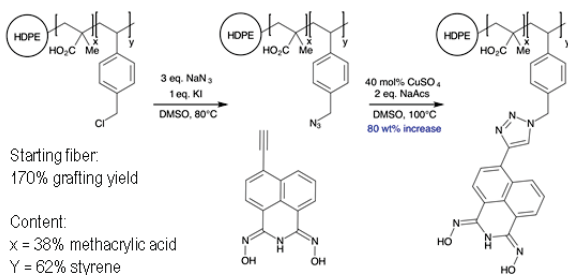


Figure 175: The grafting methodology using "Click" chemistry for designed ligands.

Nanosynthesis

A nanoporous polymeric adsorbent was generated that consisted of a hierarchical pore structure of micropores and mesopores. In addition to the porosity, the polymer represented the first mesoporous ATRP initiator. Halides, specifically chlorides, were embedded in the framework of the mesoporous polymer allowing polyacrylonitrile to be grown in the pores. Grafting yields exceeded 400 % with laboratory screenings exhibiting an 80 mg-U/g-ads. capacity. Figure 176 shows the uranium concentration decay in seawater screening under batch conditions in five gallons of seawater suggest a high capacity, 1.99 mg-U/g-ads., at 30 days (Yue, et al., 2013). The initial uptake rate was higher than that of the polymer fibers.

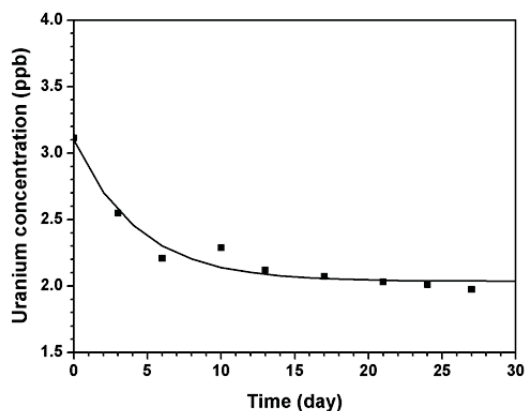


Figure 176: Batch seawater analysis with the nanoporous polymer adsorbent.

Grafting onto carbon remains a primary challenge. However, through the utilization of a support polymer, high grafting yields can be obtained. The use of glycidyl methacrylate as a support for an ATRP initiator from which polyacrylonitrile can be grown has been

successful. Through this technique (Figure 177), a seawater capacity exceeding 5 mg-U/g-ads. has been demonstrated.

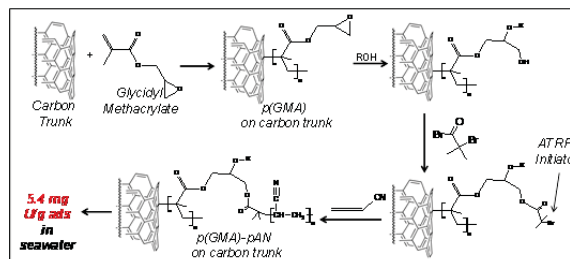


Figure 177: Scheme for producing high capacity sorbents with carbon trunks.

Reference

1. Yue Y., R. T. Mayes, J. Kim, P. F. Fulvio, X. G. Sun, C. Tsouris, J. Chen, S. Brown, and S. Dai (2013). "Seawater Uranium Sorbents: Preparation from a Mesoporous Copolymer Initiator by Atom-Transfer Radical Polymerization." *Angew. Chem. Int. Ed.* 52(52); 13458-62. December 9. DOI: 10.1002/anie

Publications

1. Grant, C. D., S. O. Kang, and B. P. Hay (2013). "Synthesis of a Hydrophilic Naphthalimidedioxime." *J. Org. Chem.* 78, 7735-7740.
2. Vukovic, S., and B. P. Hay (2013). "De Novo Structure-Based Design of Bis-Amidoxime Uranophiles." *Inorg. Chem.* 52, 7805-7801.
3. Górká, J., R. T. Mayes, L. Baggetto, G. M. Veith, and S. Da (2013). "Sonochemical Functionalization of Mesoporous Carbon for Uranium Extraction from Seawater." *J. Mater. Chem. A* 1, 3016.
4. Kim, J., Y. Oyola, C. Tsouris, C. R. Hexel, R. T. Mayes, C. J. Janke, and S. Dai (2013). "Characterization of Uranium Uptake Kinetics from Seawater in Batch and Flow-Through Experiments." *Ind. Eng. Chem. Res.* 52, 9433-9440.
5. Kim, J., C. Tsouris, R. T. Mayes, Y. Oyola, T. Saito, C. J. Janke, S. Dai, E. Schneider, and D. Sachde (2013). "Recover of Uranium from Seawater: A Review of Current Status and

Separations and Waste Forms
2013 Accomplishments Report

Future Research Needs.” *Sep. Sci. Technol.* 48, 367-387

- Sun, X., G. Tian, C. Xu, L. Rao, S. Vukovic, S. O. Kang, and B. P. Hay (2013). “Quantifying the Binding Strength of U(VI) with Phthalimidedioxime in Comparison with Glutarimidedioxime: Implications in the Extraction of U(VI) from Seawater with Amidoxime-Based Sorbents.” *Dalton Trans.* Accepted September.

Patents/Invention Disclosures

- Janke, C. J., S. Dai, and Y. Oyola. “Fiber-Based Adsorbents Having High Adsorption Capacities for Recovering Dissolved Metals and Methods Thereof.” U.S. Patent Application 2013/0071659.
- Dai, S., J. Górka, and R. T. Mayes. “Surface-Functionalized Mesoporous Carbon Materials.” U.S. Patent Application 13/851,523.

Thermodynamic, Kinetic, and Structural Studies

K. Felker, felkerlk@ornl.gov

The binding of uranyl to cyclic and non-cyclic forms of glutardiamidoxime was studied under seawater carbonate conditions. It was found that the cyclic form effectively competes with carbonate for complexation of the uranyl while the non-cyclic form did not. However, the cyclic form of glutardiamidoxime is not acid stable [Tian, et al., 2013]. Work with the major competing ions is currently on-going. Understanding the binding constants for the major competing ions in seawater provides insight for tailoring the selectivity.

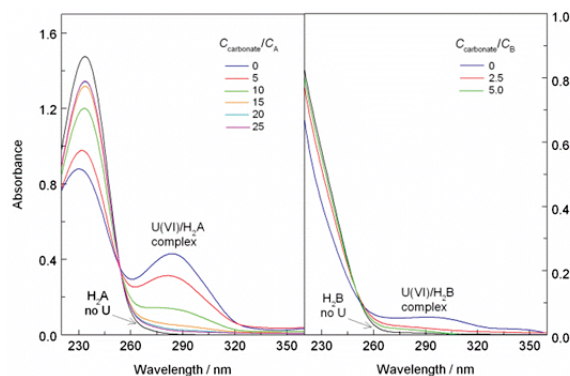
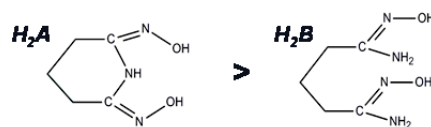


Figure 178: Uranium(VI) complexation with the cyclic (H2A) and non-cyclic (H2B) forms of glutardiamidoxime.

Reference

- Tian, G., S. J. Teat, and L. Rao (2013). “Thermodynamic Studies of U(VI) Complexation with Glutardiamidoxime for Sequestration of Uranium from Seawater.” *Dalton Trans.* 42 (16), 5690 – 5696

Marine Testing and Durability Studies

G. Gill, gary.gill@pnnl.gov

Introduction

The marine testing program is part of the Fuel Resources effort to develop advanced absorbent materials for the extraction of uranium from seawater. The program is being conducted at the MSL, a part of PNNL located on the Olympic Peninsula in Washington State. The project began in FY 2012 and is being conducted in coordination with ORNL, LBNL, University partners (City University of New York, University of Alabama, and the University of Maryland), and an international collaboration with Japan and China.

PNNL receives uranium adsorbent materials developed by program participants and conducts independent testing with natural seawater at realistic marine conditions. PNNL is also conducting tests to characterize the adsorbent materials durability, its toxicity, and other critical features related to use of an adsorbent to remove uranium from seawater. Studies have also been conducted to investigate the impact of a farm of

Separations and Waste Forms
2013 Accomplishments Report

adsorbent material deployed in the coastal marine environment on current flow. The marine testing program also serves to validate the results reported by the international program participants.

Adsorption Capacity and Adsorption Rate Determinations

PNNL has developed a marine testing system and program using natural seawater to independently determine the adsorbent capacity of and adsorption rate of uranium (and other elements) on candidate adsorbent materials. The major testing program is being conducted at MSL, but additional marine testing sites have been established at Woods Hole Oceanographic Institution and also at the Rosenstiel School of Marine and Atmospheric Sciences at the University of Miami. By establishing multiple testing sites it is possible to confirm adsorbent characteristics and verify performance in different marine water bodies. In FY 2012 and 2013, 37 separate investigations were conducted of adsorption capacity and/or adsorption rate from adsorbent materials received from program participants. To date, the best adsorption capacity observed was for the ORNL AF1 adsorbent material which had an capacity of 5200 $\mu\text{g U/ g}$ adsorbent (normalized to a salinity of 35 psu). This level of capacity exceeds the Uranium Extraction from Seawater program's goals of producing a high capacity material that is double that the Japanese adsorbent material, which was evaluated to have a capacity of approximately 1060 $\mu\text{g U/ g}$ of adsorbent material (normalized to a salinity of 35 psu).

Illustrated in Figure 179 below is a summary of the kinetic and adsorption capacity tests conducted on the ORNL 38H adsorbent with filtered natural seawater conducted in FY 2012. A one-site ligand saturation model applied to these data predicts that the adsorption capacity is $4890 \pm 830 \mu\text{g U/ g}$ of adsorbent material (normalized to a salinity of 35 psu). The model also predicts that the half-saturation time for this material is 28 ± 10 days.

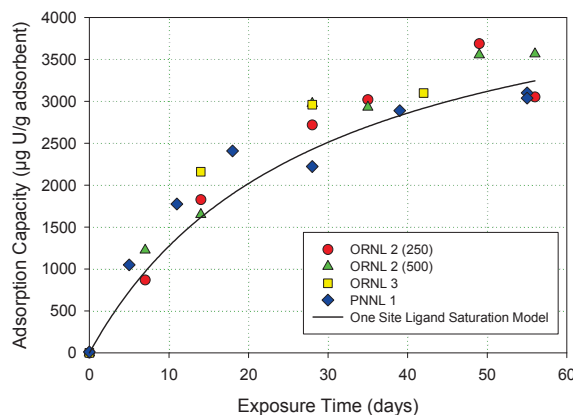


Figure 179. Summary of seawater exposure experiments conducted at PNNL with the ORNL 38H amidoxime-based uranium adsorbent material to determine adsorption capacity and kinetic uptake rate. One-site ligand saturation modeling indicates an adsorption capacity of $4890 \pm 830 \mu\text{g U/ g}$ adsorbent (when normalized to a salinity of 35 psu and a half-saturation time of 28 ± 10 days).

Adsorbent Characterization

In addition to determining capacity and uptake rate for candidate adsorbents, PNNL also has been characterizing the adsorbents for their ability to extract elements from seawater other than uranium. Understanding the competition between uranium and other seawater for binding sites on the adsorbents will lead to development improvements in adsorption performance. Other adsorption characterization includes determining the effect of temperature on adsorption capacity and evaluating how flow-rate (linear velocity) affects adsorption rate. This information is critical for identifying what marine conditions, especially temperature and flow-rate, are optimal for extraction performance.

Shown in Figure 180 are the adsorption capacity and adsorption rate of selected trace elements (e.g. Cu, Ni, V, and Zn) along with uranium for the ORNL 38H adsorbent material. Note that vanadium has a higher adsorption capacity than uranium and that the adsorption capacity and adsorption rate varies with each element.

Separations and Waste Forms
2013 Accomplishments Report

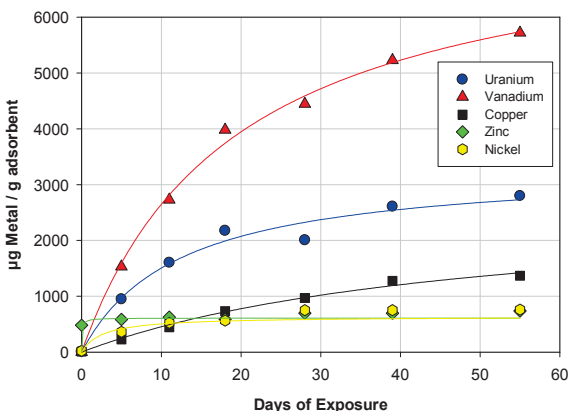


Figure 180. Time series measurements of selected trace element adsorption on the ORNL 38H adsorbent material.

The decrease in rate of adsorption with time suggests a dynamic equilibrium (i.e. a reversible reaction). The adsorption of other elements onto the 38H adsorbent material is given in Table 31.

Table 31. Adsorption capacities for several trace elements on the ORNL 38H uranium adsorbent material

Element	µg Metal/g adsorbent
V	5720
U	2798
Fe	1973
Cu	1365
Ni	760
Zn	736
Sr	313
Cr	203
Mn	140
Pb	111
Co	84.2
Sn	34.3
La	30
Nd	26

Uranium exists in seawater as the uranyl ion (UO_2^{2+}) bound to carbonate - $\text{UO}_2(\text{CO}_3)_3^{4-}$. When interacting with the amidoxime-based adsorbent material the uranyl ion binds to two adjacent amidoxime ligands on the adsorbent material to form a chelate complex. The overall reaction can be written as:



Where H_2A represents two adjacent binding sites on the amidoxime adsorbent material. Thermodynamic modeling predicts the interaction between the uranyl ion and the amidoxime ligand to be endothermic ($\Delta\text{H} = 35 \text{ kJ/M}$) in seawater; hence higher temperatures should yield enhanced adsorption capacity (Tian et al., 2012). PNNL has undertaken preliminary testing in FY 2013 which suggests that adsorption capacity does indeed increase with increasing temperature.

Preliminary testing was also undertaken in FY 2013 to determine the effect of flow-rate (linear velocity) on adsorption capacity and adsorption kinetics for the ORNL amidoxime-based polymeric materials. Additional work on characterizing the temperature and flow-rate effects on uranium adsorption kinetics and capacity will continue in FY 2014.

Toxicity Testing

Use of uranium adsorbent materials at viable scales will require deployment of expansive “farms” of adsorbent material. Prior to such a deployment it will be necessary to demonstrate that the deployment materials are not harmful to marine biota and the marine ecosystem. PNNL has been conducting toxicity tests of adsorbent materials using the well accepted standard “Microtox[®]” aquatic toxicity test to assess potential environmental impacts to marine organisms. Tests were conducted with both solid adsorbent materials and effluent seawater that passed through columns containing adsorbent materials.

Three out of the six tested adsorbent materials were found to have potential toxicity, but only when the very high concentrations of adsorbent material were used for the assay. The three adsorbent materials which showed toxicity were:

- YF130226C Copolymer-PAN (ORNL-Richard Mayes) at a concentration > 25mg/ml
- CA-4139: Porous Titanium Dioxide (North Carolina, Carter Abney/Lin Group) at 1.1mg/ml
- MC-Phosphate (612), Phosphoryl-Functionalized Mesoporous Carbon (North

Separations and Waste Forms 2013 Accomplishments Report

Carolina, Carter Abney/Lin group) at a concentration > 5mg/ml

An example of the concentration effect on adsorbent toxicity is shown in Figure 181 with the adsorbent material received from the University of North Carolina.

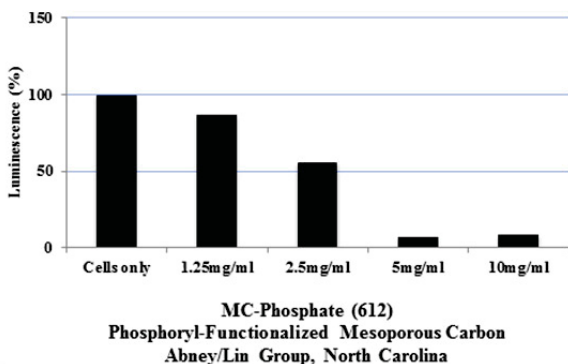


Figure 181. Example of a Microtox Test conducted with solid uranium adsorbent material obtain from the University of North Carolina. Toxicity was observed only when the concentration of the adsorbent reached levels concentration levels greater than 5 mg/mL.

The concentration levels of exposure where toxicity was observed are extremely high and not likely to be realistic of conditions when the material is used in the marine environment. More realistic exposures, applicable to marine deployments, are to test water in contact with the adsorption material. Testing of seawater effluents collected from 15 different flow-through columns (see section on marine testing) containing adsorbent material did not exhibit and toxic behavior.

Material Durability

A major cost in mining uranium from seawater is manufacturing of the adsorbent material. The more times that the material can be re-used (deploy, strip of uranium, and re-deploy), the lower the overall cost. PNNL has been assessing the durability of adsorbent materials to marine conditions, focusing on developing optimal chemical extraction pathways for removal of uranium from adsorbent material and understanding the impact of biological fouling on adsorbent capacity and kinetics for re-use. Initial studies with different acid strengths suggest that uranium can be removed from the amidoxime-based adsorbent with mild acid (1 M) with a short duration of exposure (Figure 182).

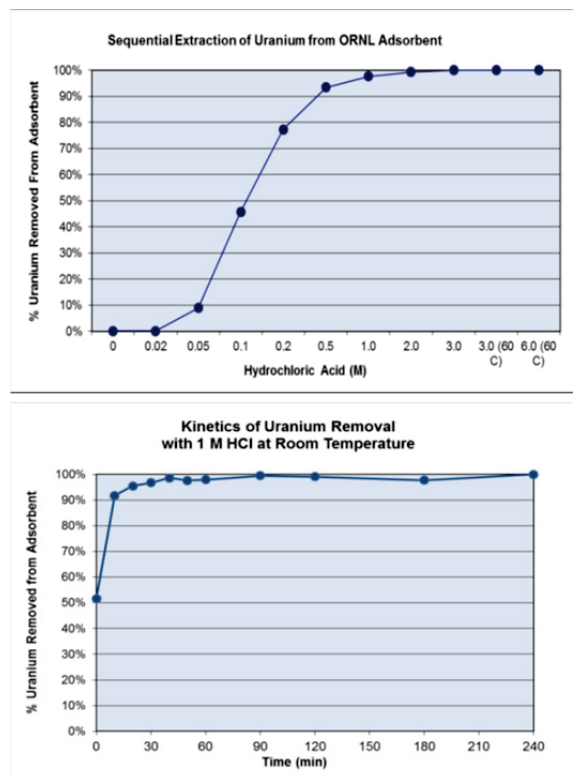


Figure 182. Characteristics of the removal of uranium from the ORNL amidoxime-based adsorbent material with HCl. Top Panel: Sequential extraction of uranium from the adsorbent using increasing HCl acid concentrations. Bottom Panel: Kinetics of uranium removal as a function of time at room temperature.

FY 2014 work will address other approaches to uranium extraction from the adsorbent material and test the adsorption capacity loss due to the repeated re-use of the adsorbent.

Potential Impact of Adsorbent Deployment on Ocean Current and Tidal Circulation

G. Gill, gary.gill@pnnl.gov

PNNL has been identifying environmental issues and information needs, from an engineering and hydrological perspective, associated with marine deployment of an adsorbent material "farm" in the coastal marine environment. Choice of an optimal site for deployment of a farm of adsorbent material will require locating an appropriate site based on an understanding of the optimal water quality and physical conditions. In addition, a key decision factor in choosing a site will also be identifying the physical infrastructure

Separations and Waste Forms
2013 Accomplishments Report

needed to deploy the adsorbents. It is also critical to understand how deployment of a farm of adsorbents will impact flow in coastal marine systems.

A major concern expressed by many is whether deployment of a farm of “kelp-like” adsorbent materials will impact natural currents and lead to ecosystem damage. PNNL is addressing this concern by assessing the form drag from a braid adsorbent farm using hydrodynamic modelling. To simulate the effect of moorings anchored to the bed or suspended from the water surface extending over a majority of the water depth, a new formulation was developed within the Finite Volume Coastal Ocean Model [Chen, et al., 2003]. The module is based on the classic momentum sink approach and approximates the retardation effect of structures on flows as additional drag force in the momentum equations that is applied in the occupied layers in the water column. The model was calibrated using information on current flow through a kelp forest. Applying the model to an adsorbent farm with a spacing density of 0.00178 moorings/ m², as described in Tamada [2009], results in the reduction in ambient currents of 4-10% (Figure 183).

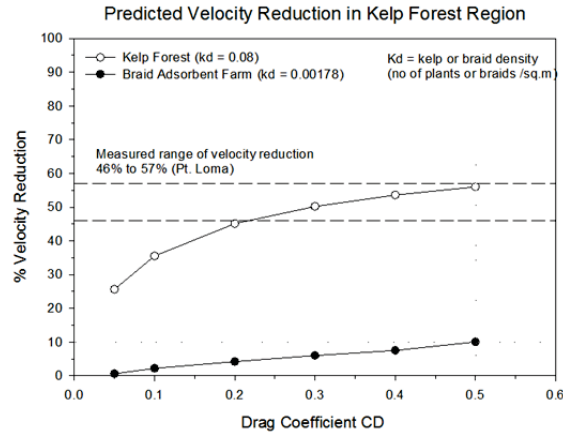


Figure 183. Predicted reduction in ambient velocity through (a) kelp forest with a frond density of 0.08 fronds / m² and (b) braid adsorbent uranium extraction farm with a mooring density of 0.00178 moorings/ m²

This reduction in currents is fairly minor by comparison to the reduction in currents observed through a kelp forest (up to 50%). In the open ocean this level of reduction is not anticipated to be significant, however, in an enclosed embayment, such as Puget Sound, such a reduction could have significant impacts on tidal flushing and water residence times, leading to environmental impacts.

References

1. Chen, C., H. Liu, and R. C. Beardsley (2003). “An Unstructured, Finite-Volume, Three-Dimensional, Primitive Equation Ocean Model: Application to Coastal Ocean and Estuaries.” *Journal of Atmospheric and Oceanic Technology* 20:159–186.
2. Tian, G., S. J. Teat, Z. Zhang, and L. Rao (2012). “Sequestering Uranium from Seawater: Binding Strength and Modes of Uranyl Complexes with Glutarimidedioxime.” *Dalton Trans.* 41, 11579-11586.

APPENDIX ACRONYMS

Separations and Waste Forms
2013 Accomplishments Report

APPENDIX: ACRONYMS

3AMS	3A molecular sieve
A&AC	Advisory and Assistance Contract
ACSEPT	Actinide reCycling by SEParaTion
AES	Atomic Emission Spectroscopy
AFCI	Advanced Fuel Cycle Initiative
ALSEP	Actinide-Lanthanide Separation
ALTGLASS	Accelerated Leach Testing of GLASS
AMUSE	Argonne Model of Universal Solvent Extraction
APT	atom probe tomography
ASTM	American Society for Testing and Materials
ATRP	atom transfer radical polymerization
BCNECAP	China–United States Bilateral Civil Nuclear Energy Cooperation Action Plan
R	Belgian Reactor
CA	chronoabsorptometry
CCIM	Cold Crucible Induction Melter
CDCOCP	constant deposition coulombs open circuit potential chronopotentiometry
CDCSC	constant deposition coulombs stripping chronoamperometry
CDPOCP	constant deposition potential open circuit potential chronopotentiometry
CDTSC	constant deposition time stripping chronoamperometry
CEA	Commissariat à l'Énergie Atomique (France)
CFD	Computational Fluid Dynamics
CNWG	Civil Nuclear Working Group
COEX™	co-extraction of uranium and plutonium (French)
CRIEPI	Central Research Institute of the Electric Power Industry (Japan)
CV	curved vanes
DFT	Density Functional Theory
DOE	U.S. Department of Energy
-EM	Office of Environmental Management
-NE	Office of Nuclear Energy
-SC	Office of Science
EAS	Engineering Alternative Studies
EBR	Experimental Breeder Reactor
EDL	Engineering Development Laboratory

Separations and Waste Forms
2013 Accomplishments Report

EDXS	energy dispersive x-ray spectroscopy
EIS	electrochemical impedance spectroscopy
ESI-MS	Electrospray Ionization-Mass Spectrometry
EU	European Union
EXAFS	Extended X-Ray Absorption Fine Structure
FCRD	Fuel Cycle Research and Development
FIB	focused ion beam
FOEAS	Follow-On Engineering Alternative Studies
FP	fission products
FTIR	Fourier transform infrared spectroscopy
GCMT	glass corrosion modeling tool
GCM	glass composite material
GCWF	Glass Ceramic Waste Form
GIT	Georgia Institute of Technology
GRAAL	Glass Reactivity with Allowance for the Alteration Layer
GSTA	Generalized Statistical Thermodynamic Adsorption
HAADF	high-angle annular dark-field
HEF	High Exposure Facility
HFDA	Hot Fuel Dissolution Apparatus
HFEF	Hot Fuels Examination Facility
HIP	hot isostatic pressing
HLW	high-level waste
HP	hot pressing
HUP	hot uniaxial pressing
IAEA	International Atomic Energy Agency
ICP-MS	Inductively Coupled Plasma-Mass Spectrometry
ICP-OES	Inductively Coupled Plasma-Optical Emission Spectroscopy
IDIQ	indefinite delivery/indefinite quality
INL	Idaho National Laboratory
JAEA	Japan Atomic Energy Agency
JNFL	Japan Nuclear Fuel Limited
LANL	Los Alamos National Laboratory
LBNL	Lawrence Berkeley National Laboratory
LCC	liquid cadmium cathode

Separations and Waste Forms
2013 Accomplishments Report

LET	linear energy transfer
LRM	low-activity reference material
LWR	light-water reactor
MOF	metal organic framework
MOOSE	Multi-physics Object Oriented Simulation Environment
MOU	Memorandum of Understanding
MTHM	metric tons heavy metal
MTZ	mass transfer zone
MWCNT	multi-wall carbon nanotube
NAA	neutron activation analysis
NanoSIMS	nano secondary ion mass spectrometry
NEUP	Nuclear Energy University Programs
NNL	National Nuclear Laboratory (UK)
NTD	National Technical Director
OCP	open circuit potential
OECD	Organization for Economic Cooperation and Development
ORNL	Oak Ridge National Laboratory
OSPREY	Off-gas SeParation and REcoverY (
PCT	product consistency test
PDE	partial differential equations
PI	Principal Investigator
PLS	partial least squares
PNNL	Pacific Northwest National Laboratory
PRI	Porous Reactive Interface
PSA	Pressure Swing Adsorption
PUREX	plutonium uranium reduction extraction
R&D	research and development
RF	radio frequency
RIGP	radiation induced graft polymerization
RT	retention time
S&WF	Separations and Waste Forms
SACSESS	Safety of ACTinide SEparation ProceSSes
SANEX	Selective Actinide Extraction
SAXS	small angle s-ray scattering

Separations and Waste Forms
2013 Accomplishments Report

SCE	saturated calomel electrode
SEM	scanning electron microscopy
SF	separation factor
SPFT	single pass flow through
SPS	spark plasma sintering
SRIM	Stopping and Range of Ions in Matter
SRNL	Savannah River National Laboratory
SSPM	Separations and Safeguards Performance Model
SSRL	Stanford Synchrotron Radiation Laboratory
STEM	scanning transmission electron microscope
STMAS	Sigma Team for Minor Actinide Separation
SX	solvent extraction
TALSPEAK	Trivalent Actinide - Lanthanide Separation by Phosphorous reagent Extraction from Aqueous Komplexes
TEM	transmission electron microscopy
TGA	thermal gravimetric analyzer
TRA	Technology Readiness Assessment
TRIGA	Training, Research, Isotopes, General Atomics (reactor)
TRL	Technology Readiness Level
TRLIFS	time resolved laser induced fluorescence spectroscopy
TMP	Technology Maturation Plan
TPC	total project cost
TRU	transuranic
TRUEX	transuranic extraction
TSA	Thermal Swing Adsorption
TST	Test of Significant Toxicity
UDS	undissolved solids
UK	United Kingdom
UNC	University of North Carolina
UNF	used nuclear fuel
UREX+	Uranium Extraction Plus
UV-vis	ultraviolet-Visible
UV-vis-NIR	ultraviolet-visible near-infrared
VPO	Vapor Pressure Osmometry
WG	working group

Separations and Waste Forms
2013 Accomplishments Report

XANES	X-ray absorption near edge structure
XAS	X-ray Absorption Spectroscopy
XPS	x-ray photoelectron spectroscopy
XRD	X-ray Diffraction

Chemical Compounds

ADU	ammonium diuranate
Ag ⁰ Z	silver substituted mordenite
AgA	silver nitrate impregnated alumina
AgS	silver nitrate impregnated silica
AgZ	silver exchanged mordenite
AgZ-PAN	silver exchanged mordenite in an engineered form sorbent
BP18C6	<i>N,N'</i> -bis[(6-carboxy-2-pyridyl)methyl]-4,13-diaza-18-crown-6
CMPO	octyl(phenyl)- <i>N,N</i> -diisobutylcarbonoylmethyl-phosphine oxide
DAAP	diamylamylphosphonate
DMSO	dimethyl sulfoxide
DPA	dipicolinic acid
DPAH	dithiophosphinic acid
DTPA	diethylenetriamine- <i>N,N,N',N'',N'''</i> -pentaacetic acid
EDTA	ethylenediaminetetraacetic acid
H ₂	hydrogen
H ₂ MEHP	mono-(2-ethylhexyl) phosphoric acid
H ₂ O	water
H ₂ O ₂	peroxide
H ₄ SiO ₄	orthosilic acid
HDBP	di- <i>n</i> -butyl phosphoric acid
HDEHP	bis-(2-ethylhexyl) phosphoric acid
HEDHP	di(2-ethylhexyl) phosphoric acid
HEDTA	<i>N</i> -(2-hydroxyethyl)ethylenediamine- <i>N,N,N'</i> -triacetic acid
HEH[EHP]	2-ethylhexylphosphonic acid mono-2-ethylhexyl ester
HMDPA	hydroxymethyl-DPA
HNO ₃	nitric acid
KSICON	KZr ₂ P ₃ O ₁₂
K-TSP	HK ₃ Ti ₄ O ₄ (SiO ₄) ₃ ·4H ₂ O

Separations and Waste Forms
2013 Accomplishments Report

LA	lactic acid
LBLTO	$\text{Li}_6\text{BaLa}_2\text{Ta}_2\text{O}_{12}$
mor-DPA	4-morpholino- DPA
mPIP-DPA	4-methyl-piperidinyl-DPA
NaSICON	Na Super Ion CONductor: $\text{NaZr}_2\text{P}_3\text{O}_{12}$
NO_2	nitrogen dioxide
O_2	oxygen
PAN	polyacrylonitrile
QDPA	quaternary methyl ammonium-DPA
SFM	perovskite structured $\text{Sr}_2\text{Fe}_{1.5}\text{Mo}_{0.5}\text{O}_{6-\delta}$
TBP	tributyl phosphate
TcO_4^-	pertechnetate anion
TEDGA	tetraethyl diglycolamide
TOPO	tri- <i>n</i> -octylphosphine oxide
UOX	uranium oxide (fuel)
$\alpha\text{-Fe}_2\text{O}_3$	hematite
$\alpha\text{-FeOOH}$	goethite
vC-CO ₂	deprotonated lactate
vC-COOH	protonated lactic acid